Advancing Single-Molecule Localization Microscopy: Quantitative Analyses and Photometric Three-Dimensional Imaging

DISSERTATION ZUR ERLANGUNG DES
NATURWISSENSCHAFTLICHEN DOKTORGRADES
DER JULIUS-MAXIMILIANS-UNIVERSITÄT
WÜRZBURG

vorgelegt von

Christian Franke

geboren in Halberstadt

Würzburg, 2017

Eingereicht am: ....

Mitglieder der Promotionskommission:

Vorsitzender: ....

Gutachter: Prof. Dr. Markus Sauer

Gutachter: Prof. Dr. Ricardo Benavente

Gutachter: ....

Tag des Promotionskolloquiums: ....

Doktorurkunde ausgehändigt am: ....

DIE MASSE BESTEHT AUS INDIVIDUEN

Abstract

Since its first experimental implementation in 2005, single-molecule localization microscopy (SMLM) emerged as a versatile and powerful imaging tool for biological structures with nanometer resolution. By now, SMLM has compiled an extensive track-record of novel insights in sub- and intercellular organization.
Moreover, since all SMLM techniques rely on the analysis of emission patterns from isolated fluorophores, they inherently allocate molecular information *per definitionem*.
Consequently, SMLM transitioned from its origin as pure high-resolution imaging instrument towards quantitative microscopy, where the key information medium is no longer the highly resolved image itself, but the raw localization data set.
The work presented in this thesis is part of the ongoing effort to translate those *per se* molecular information gained by SMLM imaging to insights into the structural organization of the targeted protein or even beyond. Although largely consistent in their objectives, the general distinction between global or segmentation clustering approaches on one side and particle averaging or meta-analyses techniques on the other is usually made.

During the course of my thesis, I designed, implemented and employed numerous quantitative approaches with varying degrees of complexity and fields of application.

In my first major project, I analyzed the localization distribution of the integral protein gp210 of the nuclear pore complex (NPC) with an iterative k-means algorithm. Relating the distinct localization statistics of separated gp210 domains to isolated fluorescent signals led, among others, to the conclusion that the anchoring ring of the NPC consists of 8 homo-dimers of gp210.
This is of particular significance, both because it answered a decades long standing question about the nature of the gp210 ring and it showcased the possibility to gain structural information well beyond the resolution capabilities of SMLM by crafty quantification approaches.

The second major project reported comprises an extensive study of the synaptonemal complex (SNC) and linked cohesin complexes. Here, I employed a multi-level meta-analysis of the localization sets of various SNC

proteins to facilitate the compilation of a novel model of the molecular organization of the major SNC components with so far unmatched extend and detail with isotropic three-dimensional resolution.
In a second venture, the two murine cohesin components SMC3 and STAG3 connected to the SNC were analyzed. Applying an adapted algorithm, considering the disperse nature of cohesins, led to the realization that there is an apparent polarization of those cohesin complexes in the SNC, as well as a possible sub-structure of STAG3 beyond the resolution capabilities of SMLM.

Other minor projects connected to localization quantification included the study of plasma membrane glycans regarding their overall localization distribution and particular homogeneity as well as the investigation of two flotillin proteins in the membrane of bacteria, forming clusters of distinct shapes and sizes.

Finally, a novel approach to three-dimensional SMLM is presented, employing the precise quantification of single molecule emitter intensities. This method, named TRABI, relies on the principles of aperture photometry which were improved for SMLM.
With TRABI it was shown, that widely used Gaussian fitting based localization software underestimates photon counts significantly. This mismatch was utilized as a z-dependent parameter, enabling the conversion of 2D SMLM data to a virtual 3D space. Furthermore it was demonstrated, that TRABI can be combined beneficially with a multi-plane detection scheme, resulting in superior performance regarding axial localization precision and resolution.
Additionally, TRABI has been subsequently employed to photometrically characterize a novel dye for SMLM, revealing superior photo-physical properties at the single-molecule level.
Following the conclusion of this thesis, the TRABI method and its applications remains subject of diverse ongoing research.

Zusammenfassung

Seit ihrer ersten experimentellen Umsetzung in 2005 hat sich die Einzel-Molekül Lokalisations-Mikroskopie (*engl.* single-molecule localization microscopy (SMLM)) als vielseitig einsetzbares Verfahren in der biologischen Bildgebung etabliert, vor allem aufgrund ihres hohen Auflösungsvermögens im Nanometer Bereich. Bis heute wurde eine Reihe neuer Erkenntnisse bezüglich der sub- und inter- zellulären Organisation durch den Einsatz der SMLM erlangt.

Aufgrund der Tatsache, dass alle SMLM Techniken auf dem Prinzip basieren, isolierte Fluorophore zu detektieren und zu analysieren, beinhalten SMLM Daten *per definitionem* molekulare Informationen.

Folgerichtig entwickelte sich das Feld der SMLM vom reinen Bildgebungsinstrument mit Nanometer-Auflösung hin zu quantitativer Mikroskopie, bei welcher der Fokus nicht länger vornehmlich auf dem hochaufgelöstem Bild, sondern vielmehr auf den Lokalisationsdaten liegt.

Die vorliegende Arbeit ist als Teil der anhaltenden Bestrebungen zu sehen, aus den *per se* molekularen Informationen der SMLM weiterführende Erkenntnisse über die strukturelle Organisation der markierten Proteine zu gewinnen. Obwohl mit der gleichen prinzipiellen Zielsetzung versehen, unterscheiden sich hierbei globale oder Segmentierungs- Clusteranalysen von Lokalisations-Meta-Analysen oder so genannten *particle averaging* Ansätzen.

Während meiner Doktorarbeit habe ich verschiedene Quantifizierungs Ansätze entworfen, implementiert und angewendet, mit unterschiedlichen Graden an Komplexität und Breite des Anwendungsgebietes.

In meinem ersten wesentlichem Projekt analysierte ich mit einem iterativen k-means Algorithmus die Lokalisationsverteilung des integralen Proteins gp210, welches Teil des Kernporenkomplexes ist (*engl.* nuclear pore complex (NPC)). Durch den Vergleich der charakteristischen Lokalisations-Statistik von separierten gp210 Domänen mit isolierten Fluoreszenzmarkern konnte unter anderem festgestellt werden, dass der Verankerungsring des NPC aus acht gp210 Homodimeren bestehen muss.

Diese Erkenntnis beantwortet zum einen eine jahrzehntealte Frage nach der Zusammensetzung des gp210 Rings und zum anderen liefert sie ein Beispiel dafür, dass durch eine geschickte Analyse der Lokalisationsstatistik strukturelle Informationen erlangt werden können, die jenseits des räumlichen Auflösungsvermögens von SMLM liegen.

Das zweite hier vorgestellte wesentliche Projekt beinhaltet eine umfassende Studie des Synaptonemalen Komplexes (*engl.* synaptonemal complex (SNC)) und damit verbundenen Cohesin Komplexen. Um die molekulare Organisation des SNC zu untersuchen, implementierte ich eine multi-level Meta-Analyse der Lokalisationsdaten mehrerer SNC Komponenten. Aus dessen Ergebnissen konnte ein neues drei dimensionales molekulares Modell des SNC erstellt werden.
Nachfolgend wurden die beiden murinen Cohesine SMC3 und STAG3 mit adaptierter Methodik untersucht. Hierbei musste die starke intrinsische Dispersion der Cohesin-Signale berücksichtigt werden. Die Analyse ergab deutliche Hinweise auf eine Polarisation der Cohesine innerhalb des SNC. Zudem zeigte sich eine mögliche Substruktur in der Organisation von STAG3, die unterhalb der Auflösungsgrenze von SMLM liegt.

Weitere Nebenprojekte im Zusammenhang mit quantitativer Lokalisationsanalyse umfassten die Untersuchung der Lokalisationsverteilung von Plasma-Membran Glykanen, sowie zweier Flotillin Proteine in den Membranen von Bakterien, welche Cluster unterschiedlicher Form und Größe aufzeigten.

Schließlich wird ein neuartiger Ansatz für dreidimensionale SMLM vorgestellt, die auf der genauen Bestimmung von Einzel-Molekül Intensitäten basiert. Diese Methode, genannt TRABI, stützt sich auf die Prinzipien der Apertur Photometrie, welche für die SMLM angepasst und verbessert wurden.
Mit TRABI konnte gezeigt werden, dass weit verbreitete Lokalisations-Software, die auf $Gaussian - Fitting$ basiert, die Photonenzahl von Emittern oftmals stark unterschätzt. Diese Diskrepanz kann als z-abhängiger Parameter verwendet werden um z.B. einen 2D SMLM Datenatz in einen virtuellen 3D Raum zu überführen. Außerdem wird gezeigt, dass TRABI vorteilhaft mit einem multi-plane Detektionsschema kombiniert werden kann und dabei höhere axiale Lokalisationsgenauigkeiten und Auflösungen erreicht.
Zudem wurde TRABI eingesetzt, um einen neuen Fluoreszenzfarbstoff für SMLM zu charakterisieren und dessen verbesserte photo-physikalische Eigenschaften auf Einzel-Molekül Basis zu demonstrieren.
Auch nach Abschluss dieser Arbeit ist die TRABI Methode und deren Anwendung weiterhin Gegenstand diverser Forschungen.

Contents

1 Introduction and Theory

Seeing is believing. This was not only the slogan of the first scientific conference I have ever attended, but also expounds the nimbus of microscopy in general society and science. Being able to observe an object, static or dynamic, e.g. stars and planets in the night sky (albeit technically not microscopy but rather astronomy, the slogan and underlying optical principles apply just as well) or microorganisms and even sub-cellular structures, with one's own eyes is probably the most powerful insight experience one could have. It allows us to build a direct context from our, i.e. *human*, dimension to the object scale.

The latter applications were largely popularized by the invention of fluorescence microscopy, whose advent was interestingly enough mostly an annoyance for its discoverer August Köhler, who tried to enhance the microscopic resolution by using ultraviolet light (UV). He felt that it was almost impossible for him to see the actual UV image in his photographs, since it was overshadowed by visible fluorescent signal originating from the sample [1]. In the following decades, fluorescence microscopy became one of the prime tools to investigate (sub-) cellular structures, due to its drastically improved contrast and structural specificity compared to classical transmission light microscopy. However, classical fluorescence microscopy is not able to provide access to cell organelles, protein assemblies or molecular scales, since its optical resolution is limited by diffraction to roughly the half wavelength of the observed light [2], i.e. ≈200 nm laterally for '*dry*' objectives and visible light, which was the initial reason for Köhler to use light of smaller wavelengths (UV).

The key transition to sub-diffraction imaging that had to occur was from detecting all fluorescent probes in a sample at once with one specific feature, i.e. emission wavelength, to detect single molecules, circumventing the problem of overlapping emission patterns. The crucial concepts descended from spectroscopic approaches to optically detect single molecules by probing their absorption in solid matter in 1989 [3] and by sensing their emitted fluorescence in crystals and solution in 1990 [4][5], albeit the single molecule

state was manufactured by strong dilution of the molecules of interest, removing the ensemble aspect somewhat artificially.
Driven by the proposal of confocal sub-diffraction imaging by Hell and Wichmann in 1994 [6] and a more general idea for super-resolution microscopy by Betzig in 1995 [7], several far-field microscopic techniques have been developed trying to utilize additional distinguishable spectroscopic features like fluorescence lifetime, absorption or shifted emission to detect two or more otherwise identical fluorophores within one diffraction limited area (DLA) [8][9]. Nevertheless, the pool of applicable discrete spectroscopic characteristics was way too small to uniquely separate a set of fluorophores labeled to a typical biological structure, resulting in often thousands of emitters per *DLA*. However, these approaches pioneered methods still used today, e.g. determining the precise position of single emitters by centroid fitting (see section 1.1.1). Given the limitation in separation power of spectroscopic features, the seemingly only way to detect single molecules out of a huge ensemble is the spatio-temporal separation of emitters, allowing only a sparse subset of emitters to be active at any given time and *DLA*.
In modern day far-field super-resolution microscopy, there are two basic principles for this premise to be accomplished. Deterministic methods like stimulated emission depletion (STED)[6][10] or structured illumination microscopy (SIM) [11][12] utilize manufactured light patterns, preventing fluorophores in certain areas of the sample to emit. STED is based on the general idea of confocal microscopy and limits the effective laser focus by overlaying the excitation beam with a second, *'donut'*-shaped and red-shifted pattern, leading to stimulated emission apart from the inner, smaller than the *DLA*, zone. SIM applies spatially periodical excitation patterns in a widefield manner, which allows to extract subdiffraction information in the form of moire-fringes. Therefore, several shifted and rotated patterns are applied sequentially to finally generate a reconstructed high resolution image, possibly in all three spatial dimensions [12]. Both techniques are capable of reaching lateral resolutions of $\leqslant$100 nm with different benefits and drawbacks regarding laser intensities, temporal resolution and applicability to biological samples.
On the other hand, there is the class of methods that rely on stochastically modulating the emission of individual molecules by photo-activation, -conversion and -switching. First experimental advance was made in 2005 by Lidtke et al. [13], utilizing the intrinsic emission intensity fluctuation of semi-conductor quantum dots, therefore enabling the nanometer precise localization of isolated emitters. The method was named pointillism, because the final, super resolved, image consisted of the sum of all local-

ization points over time. However, since quantum dots exhibit an unpredictable and less-than-ideal blinking behaviour, alternate approaches and fluorophores were applied shortly after. Photoactivated localization microscopy (PALM)[14, 15], using fluorescent proteins as dyes, started the ongoing commotion in biological microscopy in 2006. Shortly after, stochastic optical reconstruction microscopy (STORM)[16] and *direct* STORM [17] were introduced, employing synthetic organic fluorophores. Collectively with related methods they form the universe of single-molecule localization microscopy (SMLM) in which this thesis resides.

In the following sections, I will give an initiation into the technical aspects of fluorophore switching, the localization idea and process, the extension of SMLM into the third spatial dimension as well as the transition to quantitative super-resolution microscopy. Further, I will introduce two biological structures, both multi-protein complexes, that were analyzed during this thesis by quantitative *d*STORM in combination with meta-analysis algorithms based on single molecule localization data.

1.1 Single-Molecule Localization Microscopy

" In order for the light to shine so brightly, the darkness must be present. "

Single-molecule localization microscopy (SMLM) relies on the basic principle of spatio-temporal separation of the emission of fluorophores within a diffraction limited area. That means, at any given time, only a small number of fluorophores is allowed to emit, enabling the nanometer precise localization of the emitter's position. Throughout the duration of this thesis there has been great controversy in the field about the precise denomination of the technique, or plainspoken, which member of the ever-growing zoo of acronyms and names should predominantly be used to represent the same underlying principle. I will use the acronyms of two techniques that are essential for the work depicted in the thesis, namely *direct* stochastical optical reconstruction microscopy (*d*STORM) and photoactivated localization microscopy (PALM). For an comprehensive overview of the timeline of optical super-resolution techniques with respect to similarities and distinctions I recommend the review article written by my colleagues Klein, Proppert and Sauer in 2014 [18].

Although PALM and *d*STORM rely on the same premise of detecting single molecules out of a huge ensemble, the photo-chemical and -physical implementation slightly differs. PALM was first proposed with photo-activatable fluorescent proteins (PAFP), whereas *d*STORM was introduced with standard organic fluorophores. In respect to SMLM the main difference of the two dye classes is, which state is used for the actual imaging. Although most PAFPs exhibit fluorescence in their native state, it is not a necessary requirement. To tune the emitter density to single molecule levels the native state of single PAFPs is photo-converted to another, usually red shifted, fluorescent state that is then read out subsequently until photobleaching. The conversion process is stochastic, while its rate is adjustable by the conversion light power density. Therefore the native state is used as the *dark state*, albeit possibly fluorescent, and the converted as the *bright state*, as Fig. 1.1 illustrates.

Contrary, the native fluorescent state of organic fluorophores is used as the *bright state* and read out. Here, the bulk of emitters is photo-chemically reduced to a non fluorescent *dark state* with very long lifetimes, relative to the fluorescence lifetime. Therefore a repetitive switching between the *bright* (*ON*) and *dark state* (*OFF*) can occur, that can comprise tens of temporally separated emission events until photobleaching.

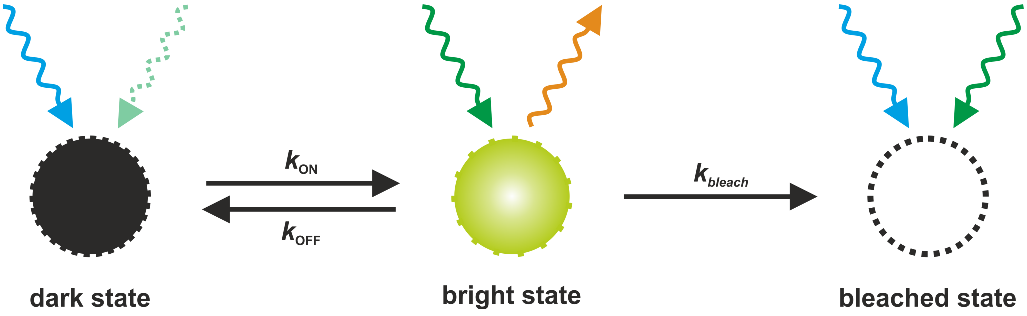

Figure 1.1: General scheme of the most common photoswitching mechanisms involved in SMLM. In PALM like imaging approaches fluorophores are (photo-) converted from a non fluorescent *dark state* (left) to a fluorescent *bright state* (middle), whose extinction is usually red shifted to the dark state. Afterwards the fluorescence is read out until the fluorophore is (photo-) bleached (right), i.e. a permanent inability to fluoresce regardless of the extinction wavelength. In *d*STORM like imaging approaches most of the fluorescent emitters (middle) undergo a repetitive cycle of photoswitching to a (chemically reduced) *dark state* (left), whose extinction is usually blue shifted to the *bright state*, and back until photobleaching (right).

This is of great importance for quantification approaches relying on *d*STORM, since there is not always a clear correlation between the number of detected ON states and the number of causing emitters, which is elucidated in section 1.1.3.

1.1.1 Estimating Single-Molecule Coordinates with Nanometer Precision

Once the transition to the single-molecule level is accomplished by above described means, the key task is to determine the precise position of a fluorophore that is detected through an optical microscope on a pixel array, generally referred to as *localization*. Albeit, almost all fluorophores used for SMLM are smaller than the diffraction limit (one can assume them as virtual point emitters), they appear as blurred shapes on the detector. This transformation is described by the point spread function (PSF) of the microscope, which is a complex mathematical function, incorporating every transition on every optical element in the detection path. Important factors are the numerical aperture of the objective used, immersion media and dipole influences, both from the extinction light source and fluorophore emission. Furthermore, several noise and background factors also play a

crucial role to the final emission pattern [19]. Although this emission pattern on the detector, i.e. a *spot*, is technically speaking not equal with the analytical PSF, it is employed synonymously. There are several approaches of localizing a spot, of which the most commonly applied (and for this thesis only relevant) is fitting a model function to the PSF. Of course, the straight forward way to accomplish that task would be to utilize model functions, that incorporate many optical parameters of the system like the Richards-Wolf [20] or the even more sophisticated Gibson-Lanni PSF model [21], and fit them directly to the raw data. Despite the existence of open access software like the 2013 released ImageJ plug-in by Kirshner et al. [22], the formulas remain complicated and computationally very expensive [23]. This is because fitting algorithms are iterative and require a pixel based evaluation, besides high-accuracy PSF models rely on a vast multitude of parameters making it impractical to apply to real data sets [24].
Therefore, more convenient PSF models like the Airy function (Besselian) were applied, performing well both in accuracy and computation speed [25][26]. Anyway, it has been shown, that the even more manageable Gaussian PSF model operates equally well for near focus isotropic emitters, which is the case for most SMLM applications [27]. Therefore the Gaussian PSF according to

$$I(x,y) = I_0 \cdot \exp\left[-a \cdot \left(\frac{(x-x_0)^2}{\sigma_x^2} + \frac{(y-y_0)^2}{\sigma_y^2}\right)\right] + b \tag{1.1}$$

and variations of it is today's prime model for SMLM fitting. Here, I_0 is the peak intensity proportional to the emitters photon emission rate per frame, a a scaling factor, $\sigma_{x,y}$ equivalent to the width of the PSF and b the average background per pixel. Finally (x_0, y_0) are then the spots coordinates, i.e. the localization.
At this point, only one aspect of the core principle of SMLM is missing, i.e. the collection and summation of every emitter's localization. Therefore, typical SMLM image stacks contain tens of thousands of individual images, all comprising just a few active emitters to avoid overlapping PSFs and therefore fitting artifacts. After the evaluation of the whole image stack, leading to often millions of individual localizations, a high resolution image is then constructed by summing up all localizations.

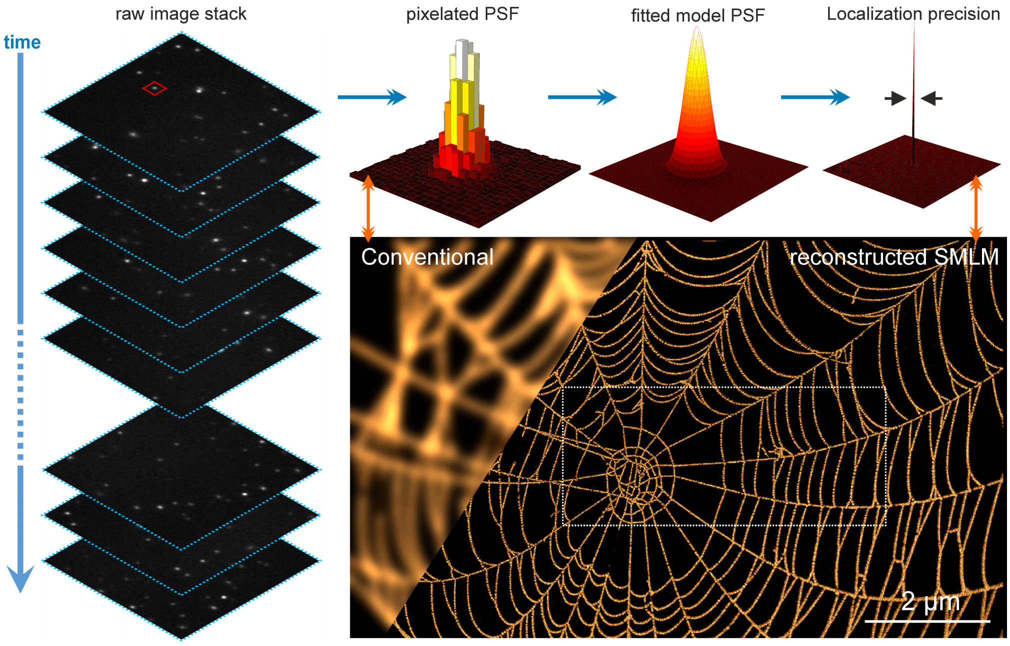

Figure 1.2: General schematic overview of the SMLM principle. *Left*: The fluorophore ensemble is tuned to the single molecule level, so that in every individual camera frame only a sparse subset is allowed to be active. To collect all emitters, usually tens of thousands of frames are gathered while fluorophores switch between the On and Off state stochastically. *Top*: The pixelated emission pattern (PSF) is fitted with a model function, allowing the nanometer precise determination of the center of mass, i.e. the localization. *Bottom*: All collected localizations are assigned to a pixel array with significantly lower pixelsize than the raw images, which leads to a much superior spatial resolution then the conventional, diffraction limited fluorescence image. The target pixel size should hereby scale with the projected localization precision for an optimal representation [28].

There is a multitude of possibilities on how to exactly depict the localization data, reaching from simple scatter plots to blurring the scattered data with a measure of their ensemble or individual uncertainty (see next section). The most common and intuitive way, however, is to construct a two dimensional histogram, i.e. a pixel grid, with significantly smaller edge length then the source pixel size. This is justified by the sub-pixel localization precision of individual spots. Usually values in the 10 nm range are used, sorting localizations according to their sub-nanometer defined coordinates into them, often times weighted with their individual intensity with all kinds of possibilities to blur, weight or color-code the result.

To illustrate the whole procedure in Fig. 1.2, I assumed and simulated a model structure, seemingly similar to a spiders web, but on a sub-microscopic scale. Here, the popular localization software rapidSTORM [24] was used with standard parameters, so that the final image was constructed with 10 nm pixel size and a pixel-intensity, derived from the number of localizations per pixel, weighted with their individual localization intensity and color-coded with a logarithmic scale. This remains, with variations, the most popular way to display SMLM images, since it already encodes a certain amount of quantitative information in the image, regarding structural density and coherence, which is further discussed in section 1.1.3.

The Significance of Emitter Intensities in SMLM

As mentioned above, a key parameter for SMLM fitting routines is the intensity of the spot. First of all, the localization uncertainty $\mu_{x,y}$, i.e. the localization precision, and therefore the potential structural resolution capability of fitting based SMLM methods, scales according to

$$\mu_{x,y} = \sqrt{\frac{\sigma_a^2}{N}\left(\frac{16}{9} + \frac{8\pi\sigma_a^2 b^2}{Na^2}\right)} \tag{1.2}$$

with $\sigma_a^2 = \sigma_{PSF}^2 + a^2/12$, a^2 the pixel area, b^2 the background per pixel, σ_{PSF} the width of the PSF and most importantly N the photon number, i.e. the emitter's intensity. For reasonable experimental parameters this expression can be approximated to

$$\mu_{x,y} \propto \frac{\sigma_{PSF}}{\sqrt{N}} \tag{1.3}$$

leaving the emitter's brightness as the prime parameter for the potential quality of SMLM imaging [19][26][29].
Furthermore, there is a great number of SMLM related techniques that rely on the usage of localization intensities, such as multicolor spectral demixing approaches [30][31], interferometric PALM with superior three-dimensional resolution [32] or (super) critical angle fluorescence microscopy [33][34]. Also, the method that I invented together with Sebastian van de Linde (see section 3.2 and **P6**,[35]) utilizes the precise determination of single molecule intensities to obtain three dimensional information.

1.1.2 Expanding SMLM into the Third Dimension

Life is three-dimensional, ... This simple statement is as naïvely true as far-reaching for microscopists in the life sciences, especially when utilizing SMLM. Unlike confocal microscopy, where it is possible to measure the three-dimensional shape of the PSF directly by scanning the focus through different axial planes, widefield microscopy usually provides 2D slices of the PSF. In principle, it would also be feasible to perform an axial scan of the image in a widefield setup, but since SMLM depends on the fast switching of the fluorophores, it is practically impossible and undesireable to preserve fluorophores in their ON-state for an entire z-scan. Additionally, in pure widefield approaches, the PSF is highly symmetric around the focal plane, resulting in ambiguous z-position assignments for emitters evenly spaced below and above the focus. In the last ten years several approaches have been introduced to obtain the three-dimensional localization of single molecule emitters, most of them applying amendments to the standard setup, resulting in an ever-growing technical complexity. The bulk of these alterations can be classified into general groups, of which the two most commonly used are [36]:

1. PSF engineering methods, where the detection PSF of the microscope is tuned by an additional (optical) device introduced to the emission path
2. Multiplane methods (mostly *Bi*plane), where at least two different focal planes are imaged simultaneously

During my thesis I developed a novel 3D method for SMLM, which, in its most powerful application, is based on the Biplane imaging scheme, while enhancing the axial localization precision dramatically by applying a photometric approach, called TRABI, that does not rely on fitting the PSF shape unlike the above mentioned methods [35];**P6**. I will give a brief overlook of the two major 3D imaging classes in the following paragraphs, to put TRABI into context with state of the art techniques.

PSF Engineering Methods

The PSF of any microscope is a three dimenional mapping function of a given point emitter. Due to the fact that common microscopic detectors are flat (EMCCD or CMOS chips) one can usually only measure the two dimensional projection of an emission pattern, commonly described as the 2D PSF (from here on called PSF). In the field of single molecule detection techniques there is a concept of encoding the emitter's axial position in the shape of the PSF. In general, this is achieved by introducing (phase-) aberrations into the detection path of the microscope. The simplest implementation was realized by inserting a relatively weak cylindrical lens inducing a z-dependent ellipticity of the PSF, being zero in focus and orthogonal non zero above and below the focal plane. This approach was applied as early as 1994 in single particle tracking experiments [37] and adapted for SMLM in 2008 [38][39]. A more versatile, albeit technically more demanding, approach is the utilization of an adjustable phase modulator like a deformable mirror [40] or a spatial light modulator [41]. Generally speaking, the PSF can be changed to any desired shape at the image plane by backtracking the target PSF to the measured native PSF and adding a phase curvature at the Fourier plane of the microscope. The main goal of PSF engineering is to encode the z position into the 2D PSF, enabling the robust precise determination of the encoded feature, mainly though fast fitting algorithms while keeping a high signal to noise and background ratio. Over the years numerous implementations of phase encoded PSFs emerged both for single particle tracking as well as SMLM.

A condensed overview of a couple of important engineering approaches is given in Fig. 1.3, namely *Astigmatism*, rotating *Double-Helix PSF* [42], *Corkscrew PSF* [43] and various forms of the *Tetrapod PSF* [44]. Additionally shown are exemplary phase patterns for the generation of Astigmatic-, Double-Helix- and Tetrapod- PSF.

For a more detailed overview of PSF engineering approaches, including a mathematical description of the PSF backtracking as well as Fisher information calculations benchmarking some of the approaches I recommend the excellent review by Diezmann, Shechtman and Moerner [36], on which the bulk of this section is based.

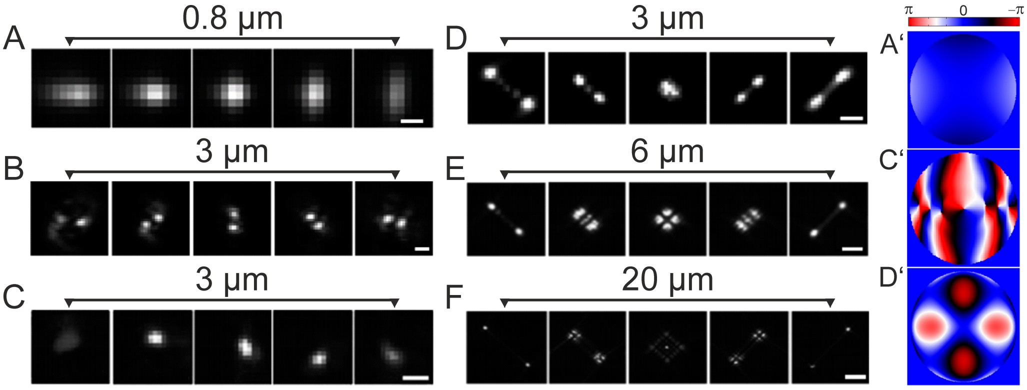

Figure 1.3: Overview of several PSF engineering approaches for 3D SMLM. *Left:* PSF shape as a linear function of the axial emitter position (the applicable z-range is indicated above each panel). (A) Astigmatism. Scale bar 500 nm. (B) Double helix. Scale bar 2 µm. (C) Corkscrew. Scale bar 1 µm. (D-F) various Tetrapod PSFs. Scale bars 1, 2 and 5 µm respectively. *Right:* Corresponding phase patterns for astigmatic PSF (A, A'), double-helix PSF (C,C') and lower range Tetrapod PSF (D, D'). Adapted from [36] with permission of ACS publishing.

All of the engineered PSF-forms display a spatially distinct, relatively easy to determine feature, e.g. eccentricity, angular rotation, splitting and recombination that allows the calculation of the lateral and axial position with varying degree of precision and range. It is worth noting, that the principle of trading range and precision is also valid here. While astigmatism allows for relatively low axial ranges, it requires manageable photon budgets, while the latest Tetrapod PSF permits huge z-ranges (up to 20 µm) but warrants very bright emitters since the PSF is spread to the multi micrometer range out of focus. Therefore it is not surprising that it is mainly used for tracking experiments, while in SMLM astigmatism is still the most commonly used PSF engineering technique. Nevertheless, very recently a phase mask design was released, that was not only successfully applied for large range SMLM but also encoded axial and spectral information simultaneously, allowing for two-color, 3D SMLM and stands as a guide, where modern day PSF engineering, possibly combined with other techniques, could lead the field of SMLM [45].

Multiplane Methods

As mentioned above, ideally one would like to measure the whole three-dimensional shape of the PSF to directly calculate its center in $x - y$ and z, e.g. by fitting an experimentally determined or theoretically derived model to the data, like it is already done with the lateral position from 2D PSF slices. Refraining from that for obvious reasons, i.e. fast blinking emitters, leaves the idea to measure several, slightly axially shifted, 2D PSF slices simultaneously. Thus, one would not get a whole volumetric expression for the PSF, but a very discretized 3D footprint.

The technically simplest and most convenient implementation is the introduction of a 50:50 image splitter into the detection path that splits the signal evenly onto two detectors (either two cameras or two areas on the same camera chip), while shifting one detector relative to the other, resulting in two distinct focal imaging planes [46][47]. Typical inter focal distances are in the range of 0.1 - 1 µm, where the optimal spacing for a given application can be calculated via the Fisher information, as a compromise between axial range and three dimensional localization precisions [48]. For a focal shift of 500 nm, Biplane provides an axial working range of $\approx$ 1.5 µm with an axial localization precision of $\leqslant$40 nm, while preserving the lateral localization precision [49].

Usually the relation of the fitted FWHMs of the PSFs in each plane is used as axially defining parameter, breaking the focal symmetry of the single plane case and bypassing the relatively low parametric change for near focus fluctuations. An exemplary illustration of the linked defocusing behavior of a PSF split onto two focal planes separated by 500 nm is given in Fig. 1.4, where PSFs were simulated according to the Gibson-Lanni model [21].

Besides its application for 3D SMLM, multiplane imaging was also successfully applied to the field of single particle tracking, where its overall axial range was increased up to 10 µm by introducing four distinct focal planes [50], while there is no strict technical limitation prohibiting the use of even more planes.

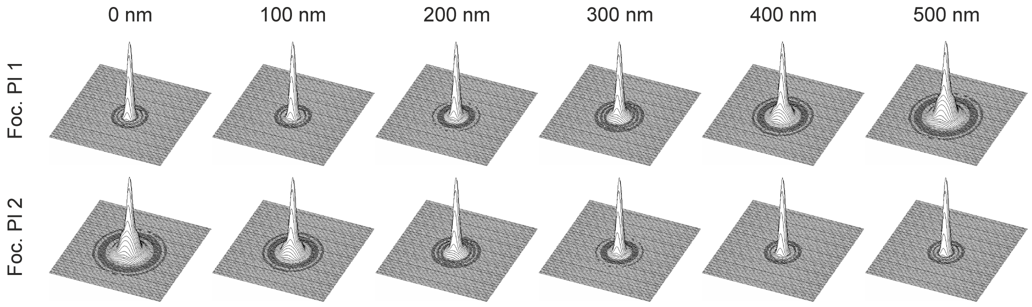

Figure 1.4: Exemplary PSF characteristics for Biplane based microscopy. PSFs were simulated according to the Gibson-Lanni model as a function of the axial position of the emitter relative to the respective focal plane. The second plane (Foc. Pl 2) is hereby axially shifted with 500 nm regarding the 'master' plane (Foc. Pl 1). Around the focus, the PSF only slightly changes when moving in z, whereas further from the focus a drastic deviation from a Gaussian model function is visible.

Interestingly enough, Biplane imaging provides the best localization precision performance compared to the widely used astigmatism- and double helix-PSF approaches (see 1.1.2), when dealing with relatively low signal strengths. In case of very bright emitters, which is common for single particle tracking techniques utilizing beads but not for most SMLM experiments, Biplane and double-helix are virtually equal, while in all cases astigmatism performs the worst for all three dimensions [51]. This is not trivial to grasp, since Biplane splits the photon budget for each individual PSF in half, therefore worsens the respective localization precisions. Seemingly, the correlation of the two independently fitted FWHM values compensates for that. Recently, there have been combinational approaches of multiplane and astigmatic imaging [52][53] and it seems logical to explore more combinations of multifocal imaging with PSF engineering to achieve an optimal balance between axial range and localization precision and therefore resolution.

An overview of various calibration curves for 3D SMLM imaging regarding FWHM based as well as the novel photometry based Biplane imaging can be found in [35];**P6**. Further, an experimental comparison in terms of axial localization precision and applicability is also given.

1.1.3 From *Pretty Pictures* to Quantitative SMLM

Life is three-dimensional, ... and begins with molecules [54]. Due to the inherent pinpointing nature of SMLM, i.e. localizing single fluorescent molecules, one could assume that it should be straight forward to translate the total localization count in a given structure to a quantitative number of target proteins. However, this naive approach is almost always forbidden due to a number of reasons. First, as mentioned earlier, PAFPs and even more so organic fluorophores used for SMLM exhibit transient repetitive On/Off switching (blinking), possibly leading to a re-counting of the same fluorophore [55][56]. Additional over-counting can arise from fluorophores being active over several frames. Although the latter can be adjusted by temporal tracking approaches, this has to be taken into account, especially when dealing with densely labeled samples, that make reasonable tracking approaches impossible. Further, dense samples are prone to a variety of fitting artifacts due to overlapping emission patterns, which make any attempt of quantifying localization densities and counts obsolete [57].

Since therefore a direct deduction of protein amount from localization count is highly inadvisable, one could suggest calibration experiments with isolated fluorophores, measuring the mean amount of localizations one could expect from a single fluorophore, taking photo-blinking and -bleaching into account and therefore being able to calculate the number of fluorophores in a given sample by dividing the total number of localizations by the standard previously set.

Unfortunately, it has been shown, that those approaches are also largely invalid, since the photo-physical behavior, like switching performance, strongly depends on the nano-environment of fluorophores, leading to changed localization counts per fluorophore in calibration- and target-sample [58]. Still, isolated emitters can be used as benchmark to calibrate the total number of localizations to a certain target protein count, as long as they are in the same experimental environment [59], or imaged simultaneously.

As discussed in section 3.1, one can extract single emitters out of a bulky data set, if strict control mechanisms are in place, e.g. algorithmically as published in [60],**P2**. Another, experimentally very challenging, option to assure quantitative dependability is to perform measurements on the same sample type but with different label concentrations. Those kind of titration experiments, mostly done by varying the ratio of primary and secondary antibody, reduce the impact of possible switching ratio artifacts as well as ensuring quantitative labeling [61].

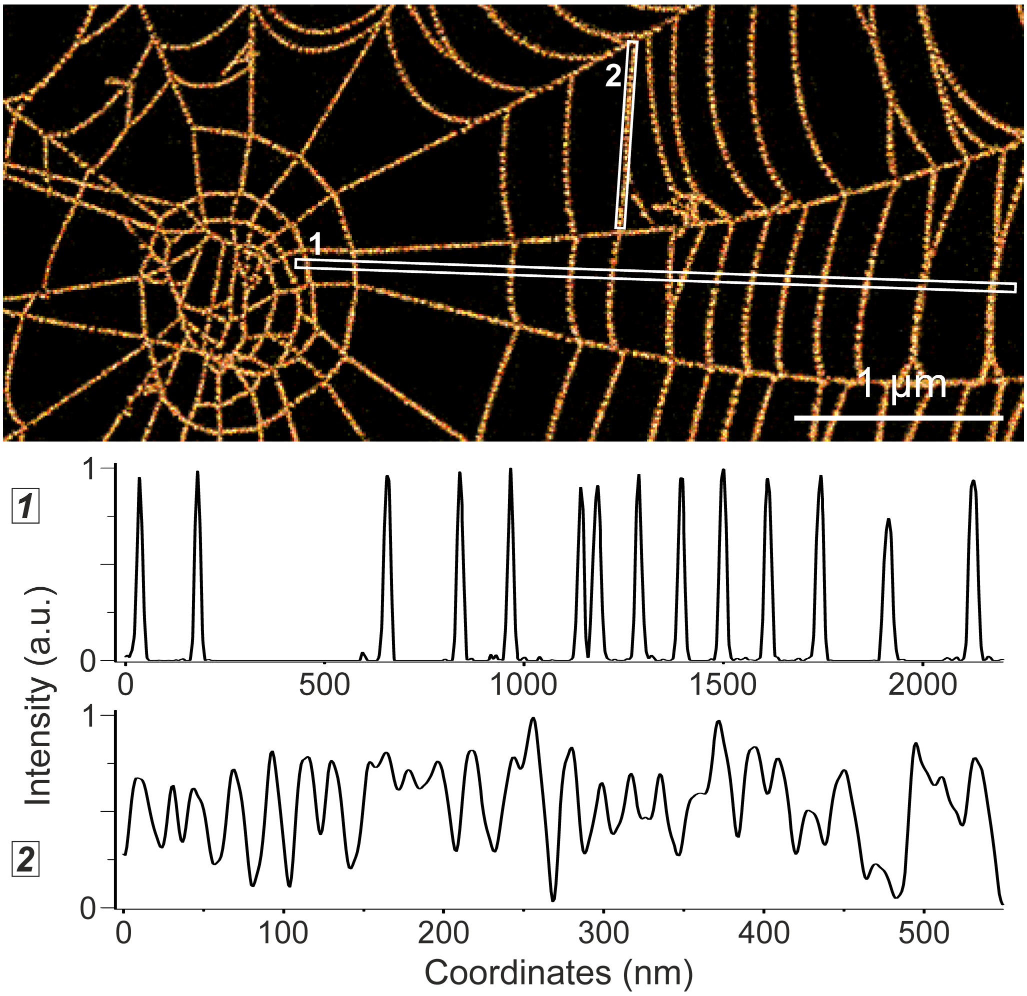

Figure 1.5: Image based quantitative analysis of SMLM data. *Top*: Magnified view of the region indicated in Fig. 1.2 with different line-profiles across (**1**) and along (**2**) a structure of interest. *Bottom*: Intensity distributions along the indicated line-profiles, allowing possible further analysis of distances and patterns across and along the target structure, revealing information depending on rendering method and parameters.

Assumed those issues can be accounted for, one can further operate in the native data type of SMLM, namely the set of localizations, treating them as the main source of information rather than the prelude to a high-resolution image [62]. Nevertheless, the superior spatial resolution of rendered images allows for some degree of quantitative analysis of organization and pattern that eluded diffraction limited microscopy, which is exemplarily shown in Fig. 1.5.

There is an extensive toolbox of classical image analysis methods, almost all applicable to super-resolved images, with varying degree of complexity and sophistication, but the necessary image rendering step (from localization data to a pixelated image) can conceal or even lose important information of the underlying structure, depending on rendering method and parameters [60],**P2**,[63].

As mentioned SMLM data is by itself a multidimensional array of fitting parameters, which is the starting point for any quantitative analysis in modern day SMLM. One of the driving forces in super-resolution based quantitative biology is the question, whether an imaged set of target proteins is organized other than randomly, commonly referred to as clustered. Especially in membrane biology this is of special significance, since the (non-) clustering of membrane proteins are supposed to control and regulate cell- physiology, -function, -stability and inter-cellular recognition [64][65][66],**P3**.

In recent years, a number of different approaches to localization clustering have been deployed with varying perks and drawbacks. In general there are two classes of clustering analysis:

1. Global, ensemble approaches, that can elucidate the general state of spatial clustering in a localization data set. Those methods include several approaches of nearest neighbor analysis, Ripley's K & H function and pair correlation

2. Local segmentation approaches, including density-based methods like DBSCAN and k-means clustering, as well as mesh representation based techniques like Voronoi diagrams and Delaunay triangulation

Some of those widely used concepts are schematically shown in Fig. 1.6, taken from the intriguing *perspective article* written by Nicovich, Owen and Gaus earlier this year [62].

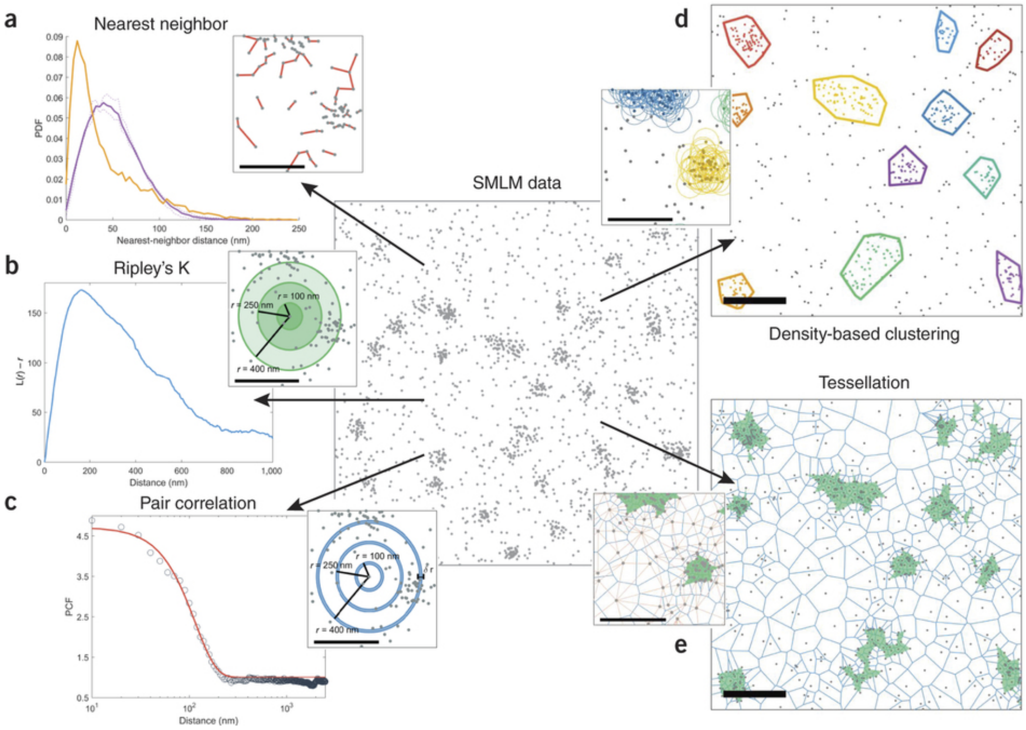

Figure 1.6: Global (*left*) and segmentation based (*right*) cluster analysis approaches on simulated data (*middle*). **(a)** Nearest Neighbor analysis measures the closest pairwise distance between neighboring localizations. The ensemble histogram (orange) shows a significant deviation from randomized data set (purple). **(b)** Ripley's functions measure the area dependent localization density around every localization (inset). Averaging over all points in the data set leads to a peaked curve, indicating clustering, whereas a randomized data set would show a flat line. **(c)** Pair correlation is conceptually closely related to the Ripley functions, but utilizes circular segments instead of full circles to determine an area density metric. **(d)** Assumed a minimal number of points constituting a cluster and a confidence interval, DBSCAN groups localizations into clusters and background. Colored lines indicate the convex hulls of individual clusters. **(f)** Tessellation approaches like the displayed Voronoi diagram facilitate segmentation by another form of density metric, via the inverse relation between local density and area tile size. From [62] with permission of Nature Publishing Group.

Global Clustering

The common ground of all global approaches is their relatively straight forward implementation and the necessity to compare the resulting metric with a random distribution to assess, whether the underlying data set exhibits clustering. The most intuitive way of measuring global clusterization degrees is the generation of nearest neighbor (NN) statistics.

In short, the pairwise distance between the closest localizations are determined throughout the whole dataset. A random distribution of localizations of same size is then used as a benchmark, often connected with some sort of NN-index, as it is shown in Fig. 1.6a (e.g. according to the Clark-Evans statistic a random distribution gets a NN-index of 1, whereas clustered data deviates substantially from that [67]).

Ripley's functions also emerged as popular tools in quantitative SMLM, decreasing the impact of so called self clustering on length scales of the localization precision, originating from the previously mentioned repetitive detection of the same fluorophore over an extended period of time. As Fig 1.6b illustrates, Ripleys functions measure the amount of surrounding localizations for possibly every point in a data set. Averaging over the ensemble at any desired length scale results in a flat baseline for randomly distributed points, whereas for clustered data a peaked distribution appears. The position of this peak can function as an indicator of the potential cluster size, whereas the amplitude serves as metric for the degree of clustering [68].

Localization based pair correlation statistics can lead to very similar results as Ripley's functions (1.6c), although it tends to distinguish better between self- and structural induced clustering. Although Ripley's functions and other global approaches have been applied successfully to SMLM data, inherently, they represent ensemble measurements without insight in possible subpopulations. Therefore they often serve as preparatory step for further analysis like cluster segmentation approaches.

Segmentation Clustering

The ultimate benefit of SMLM is the generation of *single molecular* information. This in itself is almost trivial but gets undercut by the application of ensemble quantification approaches described earlier. Subpopulations and features of distinct clusters disappear in the overall average. Especially in quantitative biology it is often the case that knowledge of subpopulations yield the most valuable information about the system. As mentioned, global approaches may deliver sensible parameters for a more detailed analysis by segmenting the bulk of data into actual individual clusters. Fig. 1.7 illustrates the general idea, that if one would be able to assign distinct domains in a sample, one could then subsequently extract parameters of interest. Also one would be able to judge the effect of a treatment in molecular detail.

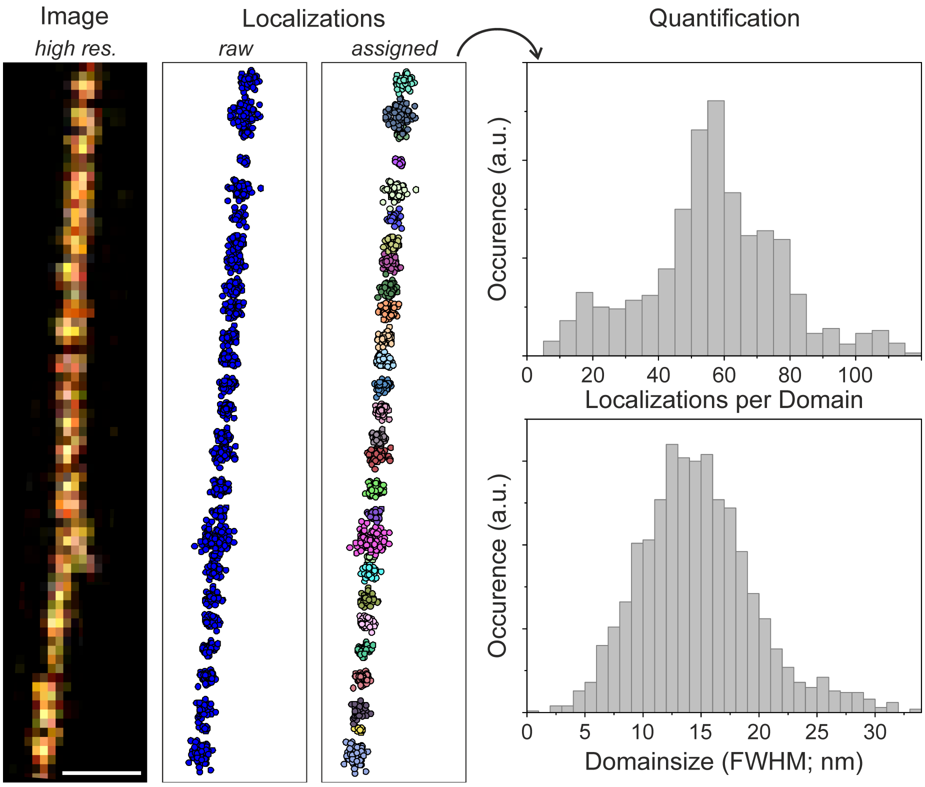

Figure 1.7: General idea of segmentation based cluster analysis of SMLM localization data. The localization set of a possibly preselected area is assigned to distinct nano-domains, i.e. clusters. Further analysis steps may include area and density calculations, NN-assignments between clusters and comparative studies of differently treated samples. Scale bar 100 nm.

Popular segmentation approaches are density based methods like the relatively straight forward to implement *density-based spatial clustering of applications with noise* (DBSCAN) [69] (see 1.6d).
DBSCAN accounts for clusters of different shape, size and content and it does not rely on an assumed total number of clusters. The only external premise is the minimal count of organized points constituting a cluster and a certain confidence interval when not meeting this parameter. Obviously that requires *a priori* knowledge about the data set, which is possible to obtain from pre-analysis (s.o.) or, as recently demonstrated, via a Bayesian estimator [70].
Another, novel, approach is the application of mesh based segmentation, of which the most commonly used is the Voronoi diagram [71] (see 1.6e). There is a great overlap between those methods and modern computer graphics, which, in my opinion, is a direction the field of quantitative microscopy has to evolve in even further, since analysis methods are already existing and very fast.
Voronoi diagrams (V.d.) and the closely related Delaunay triangulation (D.t.) transform localization sets to polygonic meshes. V.d. create many-sided polygons, where each localization sits in the middle and edges are equidistant bisectors between different localizations. D.t. builds a mesh of triangles, where localizations are the corner points. Both methods therefore stand as a mixture of the ideas of NN-based and density based methods and have been successfully applied to SMLM data [71].
During my thesis, I applied a number of different techniques described above, that I would summarize under the term *classic cluster analysis.* In **P3** I used NN-filters as well as Ripleys functions to analyze localization data of membrane glycans. In **P5** I applied a modified form of a DBSCAN as a pre-analysis step for nanodomains in bacteria samples.

Localization based k-means Algorithms

In **P7** I designed another NN-filter and a subsequent k-means separation algorithm to analyze clusters of sub-domains in a larger ultra structure. k-means clustering is an alternative method of cluster segmentation, that is ideologically related to the above described approaches [72]. I also used it to separate single nano-domains of the nuclear pore complex, utilizing the strong symmetry of the overall structure **P2**. As discussed earlier there are a number of different classical clustering algorithms for more or less sparse data sets, adaptable for SMLM. k-means clustering aims to the minimization of the variation of allocated localizations within one cluster. The main advantage of k-means clustering is, that it is computationally fast and often pre-implemented in many coding languages. However, there are drawbacks, like meaningful initialization of k, both in number and starting position. The double-edged sword like nature of k-means clustering is illustrated in Fig. 1.8, which shows simulated localization data, stemming from 3 distinct centers.

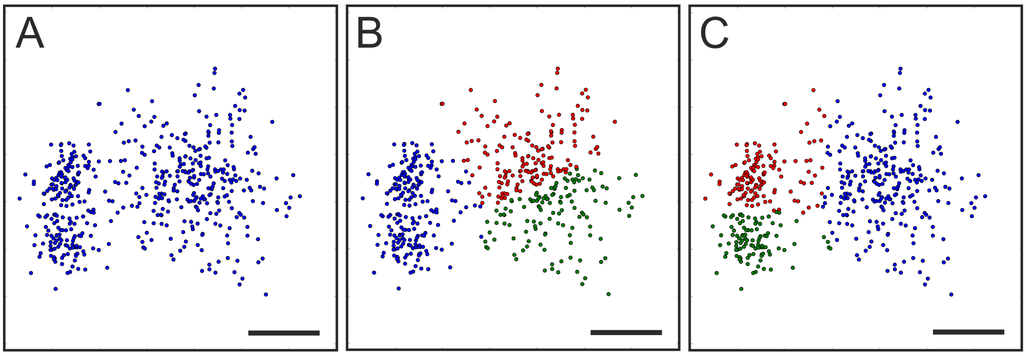

Figure 1.8: k-means based clustering of localization data. If k-means is applied to localization data (A) without a priori knowledge it tends to split the input data into even partitions (B). If one can provide meaningful starting points, it performs well to separate the simulated three domains from each other (C). Scale bar 100 nm

If the k-means algorithm is applied without a priori knowledge, it tends to split the input data into even partitions (Fig. 1.8 B). Nevertheless, if one is able to provide sensible starting points, the algorithm is fast, robust (Fig. 1.8 C) and applicable to large data sets, common for SMLM. Two major incidents, where I used k-means clustering are published in **P2** & **P7**, whereas the detailed description of the overall methods can be found in sections 3.1.2 & 3.1.3.

1.2 Analysis of Multi-Protein Complexes with quantitative *d*STORM

In the greater context of all the different optical SR-techniques the so far unmatched power and distinction of SMLM is its ability to give us molecular information about the target structure, because every localization is *per definitionem* derived from a single (fluorescent) molecule. As I discussed in the previous section 1.1.3, there has been a number of approaches to benefit from this potential over the years, some of which are an integral part of my thesis. Apart from classical cluster analysis, which is probably the most applied form of quantitative SMLM, I was fortunate enough having the opportunity of designing and applying localization based multi-level analysis algorithms for two major multi-protein complexes. In the following sections I will give a brief introduction focusing on the biological and microscopy context of the nuclear pore complex and the synaptonemal complex, whereas the ideas and concepts for the actual computational analysis are described in section 3.1.

1.2.1 The Nuclear Pore Complex

The nuclear pore complex (NPC) is one of the largest molecular machines in cells, consisting of multiple replicates of more than 30 nucleoporins, shaped in a highly symmetrical structure, exhibiting an overall molecular mass of ≈120 MDa. All nucleo-cytoplasmic transport involves the NPC as conduit, i.e. the central channel with a diameter of 35-50 nm, whereas the NPC is anchored in the nuclear envelope by an outer ring of ≈150 nm. The NPC is a continuously studied object in electron microscopy (EM) for decades and also recently gained more attention in fluorescence microscopy, especially for dynamic receptor studies, which is a field inaccessible for EM for obvious reasons [73]. However, the spatial resolution capabilities of conventional fluorescence microscopy can not compete with EM, thus providing the opportunity to introduce SMLM to the NPC community. In a first work done by my colleague Anna Löschberger (et al.[74]), *d*STORM could be benchmarked against the long standing results of EM, displaying the eight fold symmetrical structure of the integral protein of the outer ring gp210 and furthermore resolve the central channel to ≈40 nm (Fig. 1.9).

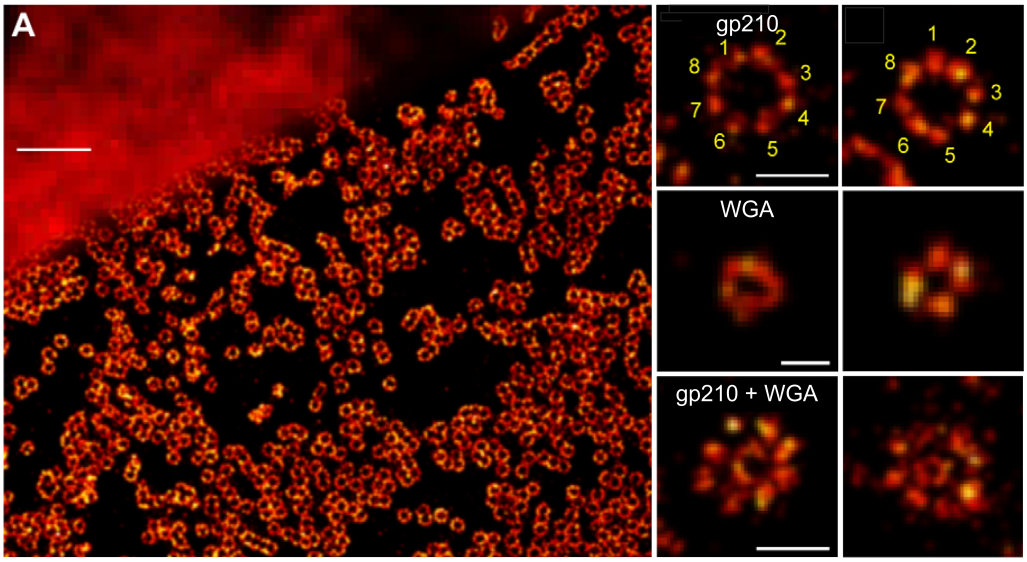

Figure 1.9: The nuclear pore complex as seen by *d*STORM. (A) The anchoring protein gp210 was immuno-labeled with Alexa647 and displays ring like structures when imaged with *d*STORM (lower right region), whereas due to diffraction blur no such details can be observed with classical fluorescence microscopy (upper left corner). (*Right*) Higher magnifications of structures, where at *top* the eightfold symmetrical arrangement of gp210 proteins is visualized, *middle* shows the circular shape of the inner channel via WGA and *bottom* demonstrates the overlay. Scale bars: 1 µm (A), *Right* 150 nm (*top, bottom*), 50 nm (*middle*); modified from [74]

Finally, the concept of particle averaging was introduced to SMLM and implemented (here one whole nuclear pore represents a single particle) for localization microscopy to determine statistically very precise diameters both for the outer (164±7 nm; mean±s.d) and inner channel (41±7 nm; mean±s.d) of the NPC (Fig. 1.10).

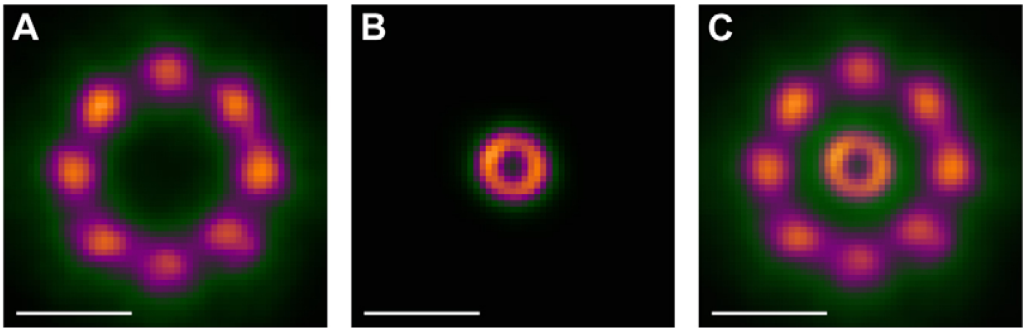

Figure 1.10: Particle averaging for SMLM data on the example of the NPC. (A) The overlay of 426 individual gp210 rings containing ≈160,000 localizations results in a high precision representation of the outer ring (mean diameter 164±7 nm; mean±s.d).(B) For WGA, 621 rings containing ≈40,000 localizations were combined (mean diameter 41±7 nm; mean±s.d). (C) Superimposed image of both structures. Scale bars: 100 nm. From [74].

Following that inaugural work, the NPC emerged as one of the prime model [75][76] and target [77][78] structures for super-resolution imaging and data analysis. Since the NPC is a traditional EM subject, the idea of correlative light, i.e. SMLM, and electron microscopy (CLEM) was an almost obvious next step to illustrate the power of *d*STORM while benefiting from the respective perks of both imaging modes. Together with Anna (et al.) I was able to further investigate the molecular organization of gp210, by applying a multilevel quantification approach, resulting in structural insights beyond the resolution capabilities of *d*STORM. Furthermore, due to the context of the ultrastructure given by EM, we could demonstrate the highly effective and specific labeling strategy applied for *d*STORM. A detailed description of the findings can be found in [60];**P2**, and a comprehensive description of the quantification algorithm is specified in 3.1.

1.2.2 The Synaptonemal Complex

The synaptonemal complex (SNC) is a meiosis-specific multi-protein complex and interestingly enough like the NPC a structure of interest for electron microscopy (EM) for nearly half a century [79][80]. Albeit sparse, information about the molecular organization of SNC's, that play a key role in the pairing of homologous chromosomes, has been mainly obtained so far by EM, mostly by labeling particular SNC components with immunogold. This lead to the general view, that SNCs have a ladder-like structure, consisting of two lateral elements (LEs) $\approx$200 nm apart, comprising a central element (CE). The CE itself is made up of several transversal filaments (TF) that connect the LEs and is therefore responsible for the overall chromosomal cohesion. So far, seven distinct proteins have been identified building the SNC, namely SYCP2 and SYCP3 in the LE, SYCP1 representing the TF and the CE situated SYCE1, SYCE2, SYCE3 and TEX12 [81].
Nevertheless, EM could not provide a molecular model describing the altogether assembly of these components and their relative relations. This is owed to the tedious sample preparation and the insufficient levels of labeling densities in common immunogold EM. Since structure dictates function, the lack of a comprehensive molecular map is the reason, why the complex process of synapsis, recombination and segregation of homologous chromosomes remains elusive on the molecular scale.
Another key player in chromosome synapsis and recombination are cohesin axes, whose formation is strongly (inter-) dependent on the SNC. But like the SNC, the molecular organization of cohesin complexes and their relationship to distinct components of the SNC is also poorly understood.

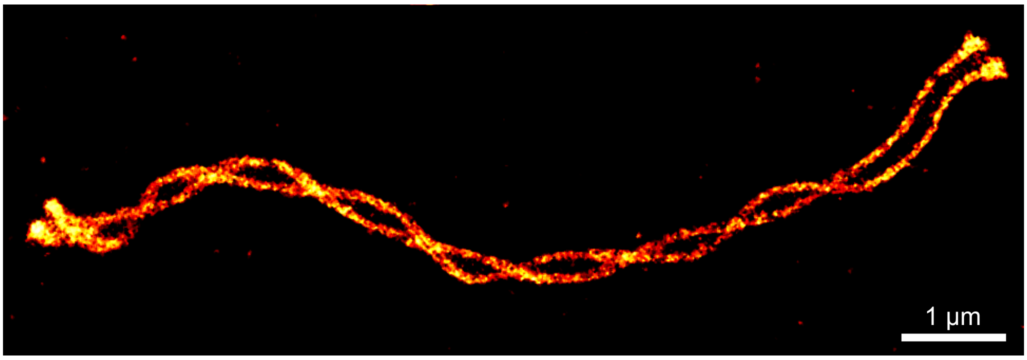

Figure 1.11: The synaptonemal complex imaged by *d*STORM exemplary illustrated with the LE protein SYCP3.

Together with Katharina Schücker and Ricardo Benavente I had the chance to investigate those questions with quantitative *d*STORM. In a first work we could compile a novel molecular model of the SNC based on a meta-analysis of localization data from six of the seven SNC proteins (excluding TEX12). Fig. 1.11 gives an impression of the appearance of the SNC imaged by *d*STROM exemplary for the LE protein SYCP3. Further details of the findings can be found in the published paper from 2015 ([81],**P4**) and in section 3.1.3, where I describe the applied quantification approach precisely. In a second paper, which is currently under review (**P7**), we could further clarify the molecular organization of the murine cohesin components SMC3 and STAG3 by again applying *d*STORM imaging and a custom-built post processing algorithm. A short overview of the technical aspect of this particular quantification procedure can also be found in section 3.1.3.

2 Publications

This thesis is based on the following publications:

P1 van de Linde S, Aufmkolk S, Franke C, Holm T, Klein T, Löschberger A, Proppert S, Wolter S, Sauer M (2013) Investigating cellular structures at the nanoscale with organic fluorophores. *Chemistry & Biology* 20(1):8-18, 2013

P2 Löschberger, A., Franke, C., Krohne, G., van de Linde, S., and Sauer, M. (2014). Correlative super-resolution fluorescence and electron microscopy of the nuclear pore complex with molecular resolution. *J. Cell Sci.* 127(Pt 20), 4351–4355. doi: 10.1242/jcs.15662

P3 S. Letschert, A. Göhler, C. Franke, N. Bertleff-Zieschang, E. Memmel, S. Doose, J. Seibel and M. Sauer, Super-Resolution Imaging of Plasma Membrane Glycans, *Angew. Chem., Int. Ed.*, 2014, 53, 10921–10924.

P4 Schücker K, Holm T, Franke C, Sauer M and Benavente R, 2015, Elucidation of synaptonemal complex organization by super-resolution imaging with isotropic resolution, *Proc. Natl. Acad. Sci. USA*, 112, 2029 – 33

P5 Schneider J, Klein T, Mielich-Suss B, Koch G, Franke C, Kuipers OP, et al. Spatio-temporal remodeling of functional membrane microdomains organizes the signaling networks of a bacterium. *PLoS Genet.* 2015; 11(4):e1005140. doi:10.1371/journal.pgen.1005140

P6 Christian Franke, Markus Sauer & Sebastian van de Linde, Photometry unlocks 3D information from 2D localization microscopy data, (11/2016) AOP *Nat. Methods* 14, 41–44, (2017), doi:10.1038/nmeth.4073

P7 Katharina Schücker*, Christian Franke*, Rolf Jessberger, Markus Sauer and Ricardo Benavente, *equal contribution, Super-resolution imaging of cohesin organization in meiotic chromosome axes, *in revision* (2017)

P8 Megan S. Michie, Ralph Götz, Christian Franke, Matt Bowler, Nikita Kumari, Valentin Magidison, Marcia Levitus, Jadranka Loncarek, Markus Sauer, Martin J. Schnermann, Cyanine Conformational Restraint in the Far-Red Range, *in revision* (2017)

Patent Registration

The TRABI algorithm and its application for photon counting in SMLM, as well as for 3D imaging has been patented together with *Carl Zeiss Microscopy GmbH* as "Verfahren und Mikroskop zum Ermitteln einer Fluoreszenzintensität" (Nummer 10 2016 014 133.6). The authors of [35];**P6** are listed as equal and only inventors.

I presented the bulk of this work at the following conferences:

T1 20th International Workshop on “Single Molecule Spectroscopy and Ultrasensitive Analysis in the Life Sciences”, Picoquant, Berlin, Germany, Sept. 2014, **Talk**

T2 The Quantitative BioImaging, Paris, France, Jan. 2015, **Talk & Poster**

T3 14th Conference on Methods and Applications of Fluorescence, Würzburg, Germany Sept. 2015, **Talk**

T4 22nd International Workshop on “Single Molecule Spectroscopy and Super-resolution Microscopy in the Life Sciences”, Picoquant, Berlin, Germany, Sept. 2016, **Talk**

T5 The Quantitative BioImaging, College Station, TX, USA, Jan. 2017, **Talk**

2.1 Short Summaries and Own Share

In the following section I will reference all main manuscripts with a short contentual summary and an accurate specification of my own share to the overall work. The published manuscripts, together with the accordance form from every co-author, are reproduced in Appendix B in the original typeset from the publishing journal.

P1 - Investigating cellular structures at the nanoscale with organic fluorophores

van de Linde S, Aufmkolk S, Franke C, Holm T, Klein T, Löschberger A, Proppert S, Wolter S, Sauer M (2013). *Chemistry & Biology* 20(1):8–18

Short Summary

This review article focuses on the utilization of organic fluorophores for super-resolution imaging. First a historic overview of fluorescence microscopy is given with emphasis on super-resolution, especially single molecule localization microscopy (SMLM). The photo-chemical and -physical mechanisms of single molecule photo-switching is summarized with respect to buffer conditions and excitation power density. Furthermore the possibilities and restrictions of live-cell SMLM with organic fluorophores are discussed. Also the quantification capabilities of SMLM are demonstrated, as well as possible complications and challenges. The article closes with a comprehensive outlook of the possible future of SMLM. [82]

Own Share

- Compilation and supplementation of raw data
- Discussion of the manuscript draft

P2 - Correlative super-resolution fluorescence and electron microscopy of the nuclear pore complex with molecular resolution

Löschberger, A., Franke, C., Krohne, G., van de Linde, S., and Sauer, M. (2014). *J.Cell Sci.* 127(Pt 20), 4351–4355. doi: 10.1242/jcs.15662

Short Summary

This work presents a correlative approach between scanning electron microscopy (SEM) and *direct* stochastic optical reconstruction microscopy (*d*STORM). Here, the nuclear pore complex from the envelope of *Xenopus leavis* oocytes, i.e. the inner channel visualized by dye labeled WGA and the immuno-labeled integral membrane protein gp210, is subsequently imaged by *d*STORM and SEM. A method to straight forward superimpose images from both microscopy modes is presented, utilizing the highly symmetrical structure of the NPC as intrinsic landmark. Furthermore, a localization based automated quantification approach of gp210 subunits is presented and utilized. Major results include the verification of the used labeling technique as highly specific and efficient, the existence of subpopulations of pores with 9-fold symmetry and the insight, that the gp210 ring is composed of eight homo-dimers based on the analysis of the localization statistics. Also the general validity of correlative microscopy is indicated. [60]

Own Share

- Conceptual design, implementation and execution of the described quantification approach
- Analysis of gp210 localization data
- Contribution to the manuscript draft, especially Figure 3 and section 'Quantification of *d*STORM data'

P3 - Super-Resolution Imaging of Plasma Membrane Glycans

S. Letschert, A. Göhler, C. Franke, N. Bertleff-Zieschang, E. Memmel, S. Doose, J. Seibel and M. Sauer, *Angew. Chem., Int. Ed.*, 2014, 53, 10921–10924.

Short Summary

In this work, a novel labeling strategy to investigate membrane specific glyco-conjugates is reported. The technique is deployed to enable super-resolution imaging of cell membranes of different cell lines via modified glycans, labeled with organic fluorophores, i.e. 'click chemistry'. The key finding is the homogeneous distribution of differently modified glycans (N-acetylmannosamine, N-acetylgalactosamine, O-linked N-acetylglucosamine) over large areas of the membrane. A straight forward localization based quantification approach is described with emphasis on the areal localization density and distribution. [66]

Own Share

- Design and implementation of early stage data analysis tools
- Analysis and discussion of preliminary results

P4 - Elucidation of synaptonemal complex organization by super-resolution imaging with isotropic resolution

Schücker K, Holm T, Franke C, Sauer M and Benavente R, 2015, *Proc. Natl. Acad. Sci. USA*, 112, 2029 – 33

Short Summary

In this work the so far unknown molecular organization of the synaptonemal complex (SNC) is investigated by *d*STORM. Holistic labeling of one or two SNC components at the same time enables spatially high-resolved *d*STORM imaging of all major components (excluding TEX12). Due to rare turning events, a differentiation between a virtual lateral and frontal view could be made, leading to an isotropic three-dimensional representation of the SNC. A localization based automated quantification approach for all investigated 6 components is presented and utilized. Major results include the three-dimensional representation of the SNC with isotropic resolution although only 2D *d*STORM measurements were performed and the compilation of a novel three-dimensional molecular model with nanometer precision, stemming from the meta-analysis of the localization data ensemble. [81]

Own Share

- Conceptual design and execution of the described quantification approach
- Implementation of the used software
- Meta-analysis of all reported 6 SNC component localization data
- Contribution to the manuscript draft, especially Figure 4 and section 'Postprocessing of *d*STORM Data for Average Protein Position Determination'

P5 - Spatio-temporal remodeling of functional membrane microdomains organizes the signaling networks of a bacterium

Schneider J, Klein T, Mielich-Suss B, Koch G, Franke C, Kuipers OP, et al., *PLoS Genet.* 2015; 11(4):e1005140. doi:10.1371/journal.pgen.1005140

Short Summary

This work presents a holistic approach to investigate functional membrane micro-domains (FMM) in the prokaryotic model organism *Bacillus subtilis.* Here, two families of micro-domains, both containing different kind of scaffolding flotillin proteins, are examined with various fluorescence microscopic techniques, including conventional and super-resolution microscopy (PALM). Other applied techniques include *flow cytometry*, *whole-genome microarray analysis*, *BN-PAGE and immunoblotting*, *bacterial two-hybrid analysis* and *physiological assays.* [83]

Own Share

- Conceptual design, implementation and execution of the described quantification approach of SMLM data
- Analysis of SMLM data
- Minor contribution to the manuscript draft; Figures 3 and 4E; section 'Photoactivated localization microscopy'

P6 - Photometry unlocks 3D information from 2D localization microscopy data

Christian Franke, Markus Sauer & Sebastian van de Linde, (11/2016) AOP
Nat. Methods 14, 41–44, (2017), doi:10.1038/nmeth.4073

Short Summary

This work presents a photometric method termed TRABI, enabling the precise determination of photon numbers from single molecule emitters. The method improves upon the principles of aperture photometry by utilizing the switching behavior of fluorescent dyes commonly used for SMLM. The work includes an extensive characterization of the algorithm via custom written simulation software and benchmark measurements with widely used localization software. Major results include the finding, that common localization software, based on Gaussian fitting, underestimates single molecule intensities systematically. A general method, based on TRABI, to utilize this photonic mismatch to construct an axially dependent parameter is presented and deployed to several 2D SMLM data sets, transforming them into virtual 3D data. Furthermore, TRABI is combined with a classical multi-plane imaging scheme and benchmarked against FWHM-based Biplane imaging, leading to substantially improved axial localization precisions down to 10 nm. [35]

Own Share

- Idea, design, development and evaluation of the TRABI algorithm (collaboratively)
- Analysis of pre-published data concerning the *virtual 3D* method
- Preparation of samples (single molecule surfaces and microtubules)
- Design and execution of experiments
- Implementation, execution and evaluation of all Biplane post-processing steps
- Implementation, execution and evaluation of single molecule simulations
- Contribution to the manuscript draft and revision process

P7 - Super-resolution imaging of cohesin organization in meiotic chromosome axes

Katharina Schücker*, Christian Franke*, Rolf Jessberger, Markus Sauer and Ricardo Benavente, *equal contribution, *in revision* (2017)

Short Summary

In this work, super-resolution imaging and average protein position determination is applied to the murine cohesin components SMC3 and STAG3 in context of the synaptonemal complex (SNC). First confocal laser scanning microscopy (CLSM) and structured illumination microscopy (SIM) was applied to obtain a contextual overview of the cohesins with the lateral element protein SYCP3. Next *d*STORM was deployed to further investigate the structural organization. A twofold localization based quantification approach is presented. First to calculate distribution parameters as previously reported, secondly to analyze the discontinuous distribution of STAG3.

Own Share

- Conceptual design, implementation and execution of the described quantification approach
- Analysis of SMLM data
- Contribution to and discussion of the manuscript draft, including several figures

P8 - Cyanine Conformational Restraint in the Far-Red Range

Megan S. Michie, Ralph Götz, Christian Franke, Matt Bowler, Nikita Kumari, Valentin Magidison, Marcia Levitus, Jadranka Loncarek, Markus Sauer, Martin J. Schnermann, *in revision* (2017)

Short Summary

This work reports a synthetic strategy that blocks the major internal conversion pathway of Cy5. The transformation process is described extensively. The resulting molecules exhibit over 3 times improved quantum yield and extending fluorescence lifetime on the ensemble level. Moreover, these compounds recover from hydride reduction with dramatically improved efficiency.

Finally, a phalloidin bound form of the compound is employed in a PALM like imaging fashion. Two- and three-dimensional (TRABI-Biplane) SMLM measurements are performed in PBS buffer. Single molecule emitter intensities are calculated with TRABI, indicating a similar to slight superior single molecule photon yields compared to common Cy5, but with the major advantage of convenient buffer compositions, hinting at possible live-cell applications.

Own Share

- Execution of SMLM experiments (collaboratively)
- TRABI - analysis of SMLM data
- TRABI-Biplane post-processing and evaluation
- Contribution to the manuscript draft, including several figures

3 Design, Development and Application of Methods for Quantitative Microscopy

Microscopy inherently relies on images and their interpretation. As discussed earlier, microscopy in general and SMLM in particular have potential not only to be used as merely visual imaging techniques, but rather as powerful quantitative toolbox. This thesis comprises a number of instances, where the transition from pure imaging to quantitative microscopy was facilitated by the development of computational analysis tools. In the following sections, I will give an comprehensive overview of the approaches I designed and implemented to study the molecular organization of the nuclear pore- and the synaptonemal complex as well as a photometric approach to SMLM, enabling precise photon counting and several modes of three-dimensional imaging.

3.1 Quantification of Localization Data by Meta-Analyses

3.1.1 Canny Edge Detection for Image based Separation of Target Structures

Although SMLM provides a unique data structure amongst microscopic techniques, i.e. the localization data set, an image based pre-analysis of the data can be beneficial, due to the superior spatial resolution. One of the main tasks in SMLM post-processing, and also during my thesis, was the separation of target structures from their surrounding to analyze them on a single particle level. Here, a 'particle' can be an isolated fluorophore, a protein cluster, a single nuclear pore complex (NPC) or an extensive coherent structure like the synaptonemal complex (SNC).

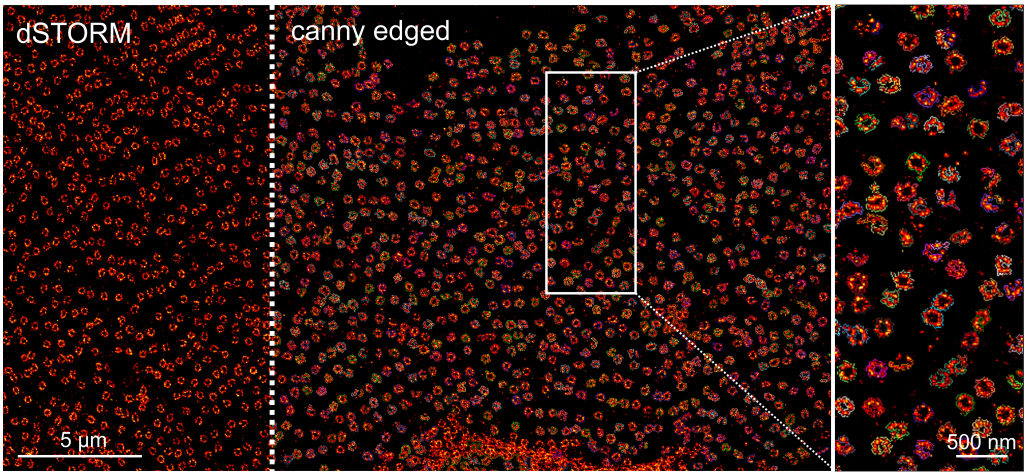

Figure 3.1: Application of the Canny-Edge-Detector (CED) to super-resolved images of the nuclear pore complex. *Left:* Conventional *d*STORM image of gp210 with 10 nm pixelsize. *Middle:* Result of the *CED* with a Gaussian-Kernel of size (9,9) px, $\sigma = (3,3)$ px and a lower area threshold of 0.01 µm^2. Solid outlines represent particle candidates, where colors are chosen randomly. *Right:* Two fold magnification of the area indicated shows the robust pre-separation of whole pores.

Since by hand separation or selection can lead to a substantial bias, I employed an automated pre-analysis routine based on the *Canny-Edge-Detector* (CED) [84], which requires very little human input and is robust against imprecise or biased choice of parameters. The basic principle of the *CED* as implemented can be broken down to just two major steps.

First, the source image is blurred with a Gaussian kernel, whose size is set by the user and should scale approximately with the target structure size. Afterwards, the blurred image is binarized via a hard coded intensity threshold and contours are searched. Coherent contours are then assumed to be particle candidates, while an area bandpass is applied to discard 'obvious' not sufficiently separated structures or unspecific background.

Here, the second and more sensitive user input is required, i.e. the smallest and largest sensible structure size to be allowed. Naturally, a priori knowledge of the target structure is of huge help, but since there is an already existing super resolved image, the estimate of the structure size proves to be relatively straight forward. Figures 3.1 and 3.2 illustrate the transition from the super-resolved image (pixelsize 10 nm) to pre-separated target structures via the *CED*.

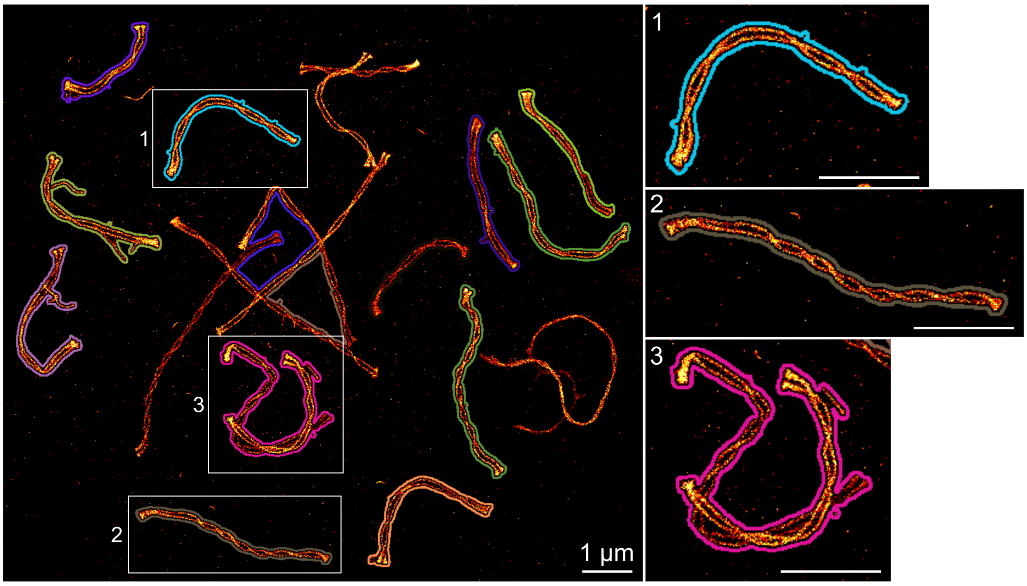

Figure 3.2: Application of the Canny-Edge-Detector (CED) to super-resolved images of the synaptonemal complex (SNC). *Left:* Conventional *d*STORM image of SYPC3 with 10 nm pixelsize, overlayed with the result of the CED with a Gaussian-Kernel of size (25,25) px, σ = (9,9) px and a lower area threshold of 0.5 µm^2. Solid outlines represent particle candidates, where colors are chosen randomly. *Right:* Two fold magnification of the areas indicated shows well separated single SNC candidates (**1**&**2**) and also crossing or interlaced candidates (**3**), that can be filtered out in further processing.

In case of the NPC (Fig. 3.1) a Gaussian-Kernel of size (9,9) px and σ = (3,3) px was applied with a lower area threshold of 0.01 µm^2, while for the SNC (Fig. 3.2) a Kernel of size (25,25) px and σ = (10,10) px was used with a lower area threshold of 0.5 µm^2.

That way derived contours of target structure candidates function as a spatial mask filter, in that their vertices are used to crop the according localizations from the whole data set. All further analysis steps, described in the following sections, are purely based on the localization data. Therefore, the pre-analysis via the CED is robust against 'human error', since *faulty* target structure candidates can be screened and discarded based on their localization distribution.

3.1.2 Utilizing the highly symmetrical NPC

As discussed in section 1.1.3, k-means clustering can be a versatile and robust separation tool for SMLM localization data sets, if provided with sensible starting points. Within the already highly symmetrical NPC structure, the gp210 domains protrude due to their eightfold circular periodicity, as shown in chapter 1.2.1.

During the analysis for **P2**, I reasoned, that this symmetry could be used to apply k-means clustering to single pore localization sets to effectively separate individual gp210 domains from each other. At that point in time, it was unclear, whether 8 monomers or 16 homo-dimers of gp210 form the anchoring ring around the central channel of the NPC [85][86]. Since SMLM allocates molecular information, it seemed the perfect microscopic tool to elucidate this long standing question.

Therefore I designed a multistage localization analysis beginning with just one imaged based separation step described above, namely the canny edge detection of single pore candidates (see 3.1.1). After that, every step of the analysis is purely localization based and is schematically shown in Fig. 3.3. First, for every single pore candidate, a mean component analysis (MCA) was performed serving two general purposes (Fig.3.3 b). In case of strong ellipticity, i.e. the absolute values of the *MCA* eigenvectors form a ratio of larger than two, the pore candidate was discarded from further analysis, since this would indicate strong overlapping signals from different pores. In that rare case the canny edge detector would fail to separate the signal to individual pores. If the ellipticity was sufficiently small, the *MCA* parameters, such as center of mass and both normal vectors indicating the principal orientation of the localization cloud, were used to fit an ellipse to the data (Fig.3.3 c).

We expected the majority of NPCs to be of eightfold symmetry, but also had to account for deviations. To apply k-means clustering, starting points were set equidistantly along the fitted ellipse. In case of an ideal pore candidate, i.e. eight gp210 domains, the first two starting points would then be on 'the end' of prominent *MCA* eigenvector (±1 from the center of mass) as indicated in Fig. 3.3 b&c. This also constitutes the shortest analysis pipeline, since the starting points would be close enough to the actual domain center to successfully perform a k-means assignment (Fig.3.3 e). Hereby 'successfully' is constituted by whether the resulting localization cloud passes the last analysis step, i.e. the Anderson-Darling test for 'Gaussianess' (ADT) (Fig.3.3 f) [87].

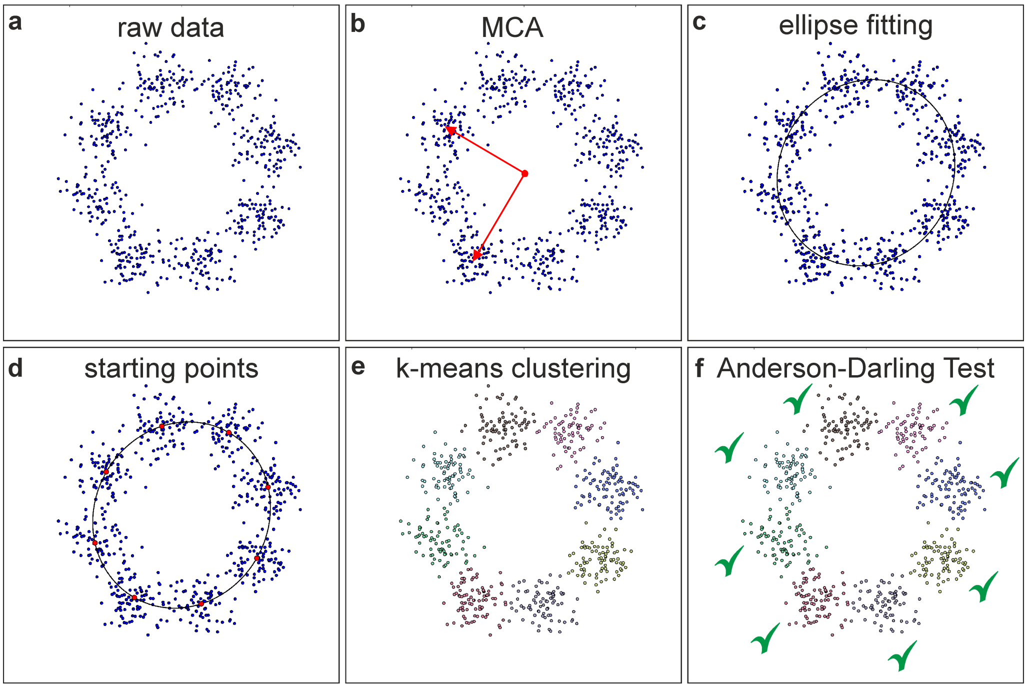

Figure 3.3: General scheme of an optimal multi-level k-means algorithm applied in **P2** to separate individual gp210 domains from the whole pore raw data (**a**). To test the ellipticity of the pre-separated data, originating from a canny edge filtering, a mean component analysis of the localizations is performed (**b**). If sufficiently non elliptical, MCA parameters are used to fit an ellipse to the data (**c**) and settting starting points equidistant along the ellipse (**d**). With those, a k-means analysis is performed and the result tested for 'Gaussianess' via an Anderson-Darling test (**e&f**). If all domains pass this test, sufficient separation is assumed which allows further analysis of localization statistics as further described in **P2**.

The premise of my reasoning was, that if all existing domains were to be separated sufficiently accurate, i.e. all localizations are allocated to the right domain, the resulting localization clouds should comply with two-dimensional Gaussian distributions. This assumption is a direct consequence of the inherent nature of *d*STORM, where single fluorophores are usually localized several times, leading to scattered point clouds around the actual fluorophore position, following a two dimensional Gaussian distribution with a standard deviation represented by the localization precision.
Albeit, there is possibly just one single underlying gp210 protein, the chosen labeling approach (immunostaining with secondary antibodies with degrees of labeling $\geqslant$1) will always lead to an extended Gaussian point cloud. This

is true as long as switching artifacts are negligible and the imaging time is large enough that most fluorophores can be active at least once. Obviously the larger the individual localization statistics, the more accurate the result of the Anderson-Darlin test will be.

To account for instances where one or several gp210 domains are missing, either due to deficient labeling or to actual structural causes, the initial number of starting points was set to 5. In preliminary calculations it turned out, that there were almost never single pore candidates exhibiting less than 5 gp210 domains; even 5 very rarely occurred. The remainder of the analysis proceeded in an iterative manner. The result of the k-means clustering underwent the ADT, where, if at least one of the separated point clouds failed, starting points were turned with an angle $\alpha = \pi k^{-1}$ and repeated.

If after turning the ADT fails again, k is then iteratively increased up to 8, while turning with α in between if necessary. If at any configuration a completely successful ADT occurs, sufficient domain separation is assumed. If the last possible configuration does not pass the ADT, the candidate is discarded. The iterative character of the analysis is illustrated in Fig. 3.4 with a pore, missing two gp210 domains, since a fully projected pore, proved to be relatively straight forward for the algorithm (see Fig. 3.3).

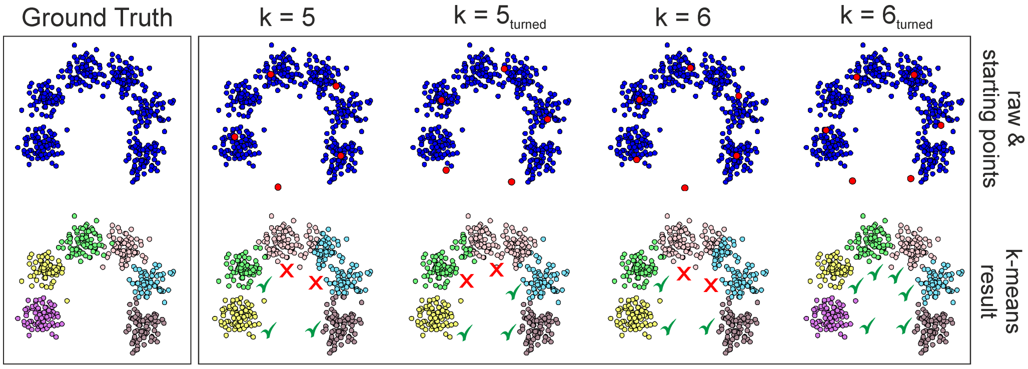

Figure 3.4: Iterative k-means separation of gp210 domains. *Left*: Simulated ground truth localization set, representing a NPC with only 6 gp210 domains (*top*), color-coded according to their actual affiliation (*bottom*). *Right*: Iterative k-means process, based on starting points calculated from the *MCA* (indicated as red circles in the upper panel). Beginning with $k = 5$, the configuration is iteratively changed dependent on the *ADT* of each domain candidate (domains passing the test are indicated with a green check mark; failing candidates with red crosses, *bottom* panel). Configuration changes may include the simultaneous turning of starting points or increasing k. Once all candidates pass the test, sufficient domain separation is assumed.

As reported in **P2**, the vast majority of NPCs showed an eightfold symmetrical distribution of gp210 signal, which is one of the results of the described analysis and naturally makes the k-means separation easier. To quantify possible false positive allocated localizations I generated a set of simulated pores with properties matching the experimentally found parameters. It can be shown, that for localization precisions of 30 nm upper bound, which is already much worse than usual *d*STORM values, there is an allocation error of ≈3%. Since the miss-allocations are not directed, the overall error in domain size and localization count is negligibly low. A typical example is shown in Fig. 3.5.
This approach was applied to hundreds of single pore candidates and allowed further statistical analysis of the localization distribution of separated gp210 domains. As benchmark, isolated secondary antibody signal was also quantified and compared to the distinct localization distribution of gp210 domains. This lead to the conclusion, that the anchoring ring has to consist of eight homo-dimers of gp210. In other words, the quantitative analysis of the localization set, generated by *d*STORM imaging, revealed structural information well beyond the spatial resolution capabilities of the method itself, which is, along other findings, reported in **P2**, [60].

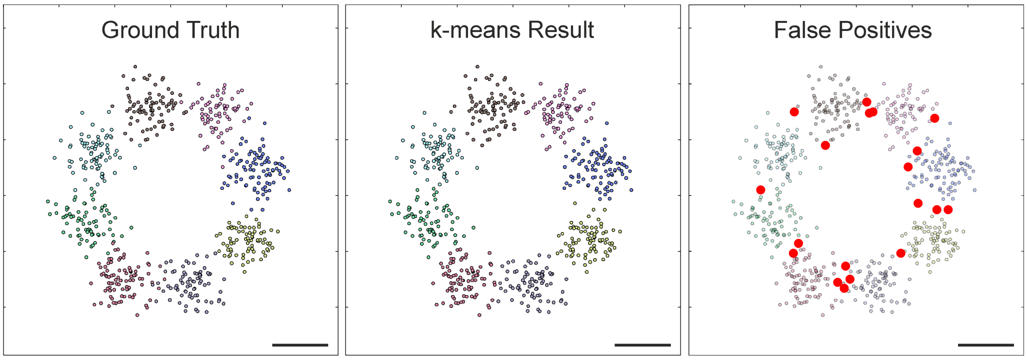

Figure 3.5: The impact of false positive allocated localizations in the iterative k-means separation algorithm. *Left*: Simulated localization set, color-coded according to their real affinity. *Middle*: The result of the iterative k-means separation process, color-coded analogously to *Left* according to their calculated domain affinity. *Right*: Falsely allocated localizations indicated as bigger red circles. Of the total 638 simulated localizations, only 19 are not in the right domain, which corresponds to a non-directed allocation error of 2.98%. Scale bar 100nm.

Nuclear Pore Complex Ground Truth Data Simulation

To test the algorithm described above, I took the previously reported parameters of size and shape (from [74]) as starting premise and assumed a slight elliptical shape ($r_1 = 170$ nm, $r_2 = 155$ nm). Then, I allowed all possible rotational states of that ellipse, drawing a random angle to rotate the pore. The number of domains was preset between 5 and 8 for every run, while the number of localizations per single domain was randomly drawn from a Poissonian with mean 80.

Center points for the domains were set along the ellipse, if eight domains exist equidistantly, otherwise points are chosen randomly from the eight possible positions. Localizations were then distributed around each domain center with a two-dimensional Gaussian with varying sigma (default 25 nm). Various parameter runs were then performed and evaluated with the analysis algorithm with excellent recall of the initial ground truth parameters (data not shown).

3.1.3 Automated Analysis of the SNC Meta-Data

Measuring a cross section profile is easy. This statement is as true as incomplete. In fact, the main issue is not so much as *how to* but *where to* scale a widespread structure, if the task is to quantify a characteristic feature. In case of the synaptonemal complex (SNC) the features of interest were the widths of individual strands and even more important the distance between two strands, if existent. It turned out, that measuring both parameters manually in a statistically meaningful quantity is not just a tedious task, but highly susceptible to subjective assessments. Those include the choice or dismissal of SNCs, seeming suitable or not for general representation. Also, once a SNC is selected, the precise positioning of cross sections strongly relates to the result, since two different appraisers would chose slightly divergent places to measure.

The prime goal in context of the SNC was to generate a quantitative chart of several different proteins building and associated to the SNC. Since here structure translates to function, precise determination of mean protein location and distribution was imperative. Therefore I designed a multilevel analysis of the SNC metadata of all eight imaged proteins, starting with the pre-selection of SNC candidates via the canny edge detector (see 3.1.1). Again, all subsequent analysis steps are purely localizations based and the evaluation of the overall method relies on simulated ground truth data.

Sliding Window Scan along the Polynomial Bisector

The first step after canny edge pre-separation is a general shape test including area thresholding, MCA and trying to fit a high order polynomial to the localization data set. Area thresholding gets rid of connected or overlapping SNCs due to the two-dimensional projection of three-dimensional data. The MCA provides a metric for the curvature of the candidate structure. Extreme curvatures close to a full ellipse are inherently inaccessible to analytical approximation and were therefore discarded.

Finally, a high order (n=20) polynomial fit was attempted. If not successful, i.e. no convergence, the localization set was transposed or rotated around its center of mass with another subsequent fitting attempt. In the rare case of repeated fit failure, the candidate was discarded from further analysis. The resulting polynomial approximation of the SNC was then used as a bisector guideline along the data cloud (Fig. 3.6 c-d',e,e').

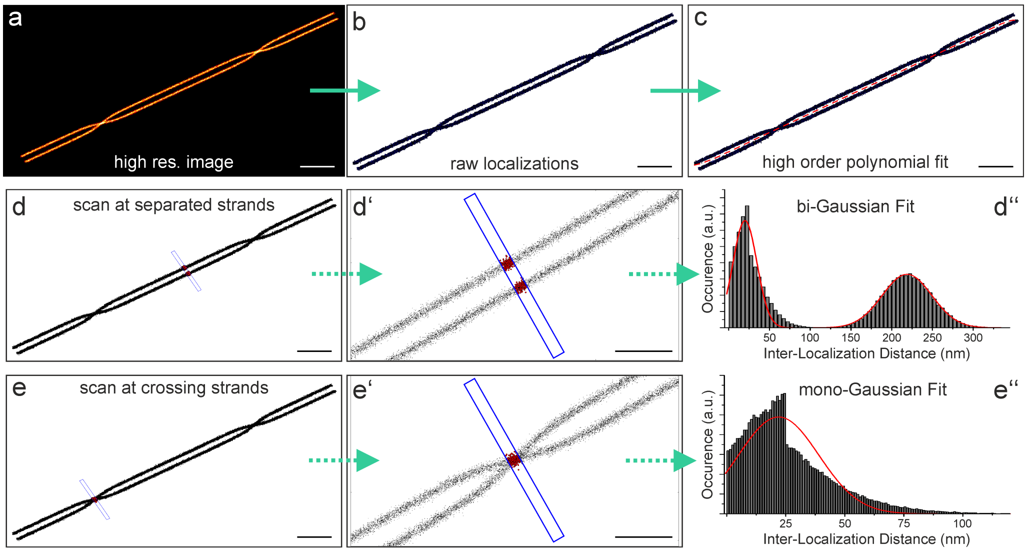

Figure 3.6: General overview of the automated analysis of the SNC exemplified with simulated ground truth data. **a**: Super-resolved image of a simulated SNC, preselected via the canny edge filter. **b**: Representation of the raw localization set used for the analysis. **c**: A high order (n = 20) polynomial is fitted to the localization data as precise bisector guideline. **d&e**: The polynomial fit is used to apply a sliding window scan orthogonal along the SNC. Localizations are allocated from the ensemble according to the window borders (d’,e’) and all inter-localization distances are calculated and histogrammed (d”,e”). A bi-Gaussian fit to the histogram is attempted to calculate the inter-strand distance and strand diameter simultaneously. If the try is successful, i.e. the scan resides at a point where strands are separated, both peak values are recorded (d’,d”). Else, a mono-Gaussian fit is attempted, assuming the scan resides at a point of strand crossing, and if successful, the peak value is recorded as strand diameter (e’,e”). All recorded peak values are finally combined to calculate the mean inter-strand distance and diameter (see **P4**,**P7**,[81]). Scale bars 1 µm (a-e), 500nm (d’,e’).

A sliding window scan was applied, where windows are orthogonal to the current polynomial gradient and the shift between two adjacent windows was 50 percent. The Window length was set large enough to cover all localizations in the vicinity of the SNC (15 times the width of the scanning window, but at least 1μm) and the width was set in a range of usually 10-250 nm, dependent on localization density and application. Localizations were allocated from the ensemble according to the window borders ((Fig. 3.6 d,d’,e,e’) and all inter-localization distances were calculated.

To avoid projection artifacts, especially in wider scan windows, i.e. the diagonal measurement of localization distances would lead an overestimation of the strand distances, the angle of inter-localization conduits in respect to the current polynomial gradient was calculated. If the absolute value of the conduit was larger than 50 nm, i.e. it is likely that the two contributing localizations reside in opposing strands, the angular projection was corrected. For every individual scanning window all inter-localization distances were then histogrammed (Fig. 3.6 d",e"). In the further analysis, two cases had two be handled.

If a region of the SNC is scanned, where two opposing cables exist (Fig. 3.6 d-d") the histogram would show a bimodal distribution. One peak stemming from inter-localization distances of same cable localizations, representing a measure of standard deviation in a single strand. This would be in the scale of 0.426·FWHM, translatable to the width of one strand. A second peak stemming from inter-localization distances of different cable localizations would also be apparent, representing the orthogonal inter-strand distance. In case of scanning an overlap region (Fig. 3.6 e-e") the latter peak would disappear and only one distribution around FWHM scale would exist. To account for that, a multilevel fitting approach was implemented, starting with an attempt to fit a bi-Gaussian function to the histogrammed data. If successful, i.e. convergence, both peak values are stored (the bigger as distance, the smaller as diameter) and the window shifted. Else, a mono-Gaussian fit is attempted; if successful the peak value is stored as single strand diameter. If both approaches fail, the scan is marked as defect and discarded. In rare cases the majority of scans failed, leading to an insufficient statistic regarding the strand parameters and therefore a total dismissal of the candidate.

Finally all diameter and distance values are histogrammed and peak-fitted to determine the mean parameters for a single SNC. Due to the extensive nature of this method, i.e. getting hundreds of cross-section scans from a single SNC, usually the overall sample size could be kept low, i.e. a single cell preparation.

Since this precise method can be applied automated, I was able to analyze localization data of 6 different proteins constructing the SNC (excluding TEX12). Together with Katharina Schücker and Ricardo Benavente we were able to compile a novel model of the molecular and microscopic architecture of the SNC as a result of this meta-analysis. The experimental (all measurements were performed by Katharina) and consequential details can be found in **P4**, [81], published in 2015.

Synaptonemal Complex Ground Truth Data Simulation

To test the above described approach, I simulated artificial SNCs according to the experimental results for SYCP2 and SYCP3, i.e. an interstrand distance **dist** ≈220 nm and strand diameters of ≈50 nm. Therefore I created an ambiguous Boltzmann function $\mathrm{B}_{\mathrm{SNC}}$ according to

$$B_{\mathrm{SNC}}(x, x + dl) = \pm \left(\frac{\mathbf{dist}}{1 + e^{\frac{x - x_0}{dx}}} \right) \tag{3.1}$$

where dx represents the crossover gradient, set to be 200 nm and the typical definition range l was 10 μm (length of the synthetic SNC; $dl = 0.5l$). The data density was set to represent one simulated antibody every 5 nm. Those starting points where then rotated around the center of the SNC by 30°. Finally, each starting point functioned as the center of a two-dimensional Gaussian to generate localization data, with $\sigma = 21$ nm (≈ 50 nm FWHM) and the number of localizations drawn from a Poissonian with mean 10. Final synthetic SNCs were then fed to the described analysis algorithm with excellent recall of the initial ground truth parameters (data not shown).

Analysis of Cohesin Complexes associated to the SNC

Following up on the initial work of quantitative *d*STORM imaging of the SNC, we explored the possibility to apply the described method to other players in the process of meiotic division in context of the SNC, namely cohesin complexes (see section 1.2.2).

In general, the analysis of the two murine cohesin components SMC3 and STAG3 was conceptually analogous with the above described approach, concerning the strand diameters and distances, since they are associated to the lateral elements of the SNC. However, due to strong background, i.e. localizations not strictly associated to either of the lateral cables, stemming from cohesin complexes in the chromatin surrounding the SNC, there was the need to prefix a sort of mask filter, discarding of unwanted unspecific signal.

Furthermore, during the analysis of the STAG3 component we realized that the localization distribution along the individual strands seemed to follow an underlying periodicity, resulting in a *spotty* signal.

Localization based Mask Filter

To analyze solely cohesin signal within the SNC, a mask-filter based on the previously reported properties of the lateral element protein SYCP3 was applied (interstrand distance $\mathbf{dist}_{\text{SYCP3}}$ 221.6 ± 6.1 nm [81]), i.e. only inter-localization distances $\mathbf{d}$ were kept, fulfilling the condition:

$$\mathbf{dist}_{\text{SYCP3}} - \boldsymbol{n}\cdot\sigma_{\mathbf{dist}_{\text{SYCP3}}} \leqslant \mathbf{d} \leqslant \mathbf{dist}_{\text{SYCP3}} + \boldsymbol{n}\cdot\sigma_{\mathbf{dist}_{\text{SYCP3}}} \tag{3.2}$$

Here, $\boldsymbol{n}$ defines the variation allowed in factors of standard deviations $\boldsymbol{n}$ of $\mathbf{dist}_{\text{SYCP3}}$. Values of $\boldsymbol{n}$ [1, 2, 3, 5, 10, 15, 20, 50, unlimited] were applied, results histogrammed and fitted with a Gaussian (for $\boldsymbol{n}$ = 1, 2, 3, 5, 10) or Bi-Gaussian function (for $\boldsymbol{n}$ = 15, 20, 50, unlimited) to determine the mean values. Obviously, allowing just a few $\boldsymbol{n}$ distorts the actual statistical strand distance to values close to $\mathbf{dist}_{\text{SYCP3}}$. Since the measured strand distance showed to be a function of $\boldsymbol{n}$, plus the appearance of a second peak at lower $\mathbf{d}$ values, which becomes visible from $\boldsymbol{n}$ = 15 on, I calculated the $\boldsymbol{n}$ - dependent peak positions and derived a pseudo asymptotic behaviour

for the high - value peak after the splitting into two distinct peaks.
I therefore reasoned, that the interstrand diameter can be derived from the bimodal fit of the unfiltered data, whereas the larger peak value represents the actual distance between the strands, and the lower peak value is a product of the significant background signal, which blurres the strand specific signal. This accentuates the twisted regions in which the strand distance is gradually reduced and can thus explain the appearance of the second peak.

k-means based Quantification of a possible STAG3 sub-resolution Organization

To investigate the possible sub-organization of STAG3, a k-means based separation approach was designed and applied to the raw localization data. Contrary to the gp210 ring (see section 3.1.2), no distinct upper limit in k can be assumed. Therefore a semi-automated initiation of starting points was deployed, either by setting starting points with an image based maximum finder, or by manually selecting starting point centers. In both cases, an Anderson-Darling test was performed, assuming fully separated STAG3 domains to produce Gaussian localization clouds.
Starting points of domains passing the test were fixed, while starting points from failing ones were split into two equidistant 'children'. This procedure was then repeated iteratively until a full separation was achieved. Afterwards, the 'left' and 'right' nearest neighbor of every domain was determined and inter-domain distances calculated. Those were then histogrammed, but since the resulting histogram did not show a sharp peak but rather a broad, albeit distinctively jagged distribution, the result was then subject to an autocorrelation analysis to identify any possible regularities in interspot distances. The autocorrelation curve showed a peak at 12.5 nm, which suggests that STAG3 molecules are separated on average by 12.5 nm along the LE albeit the interspot distance is clearly below the spatial resolution provided by dSTORM.
This work is, at this moment, still in revision **P7** and further broadened by additional experiments. Therefore I refrain from giving a more detailed dipiction of results as well as a final conclusion to this project.

3.2 TRABI

***T**emporal **R**adial **A**perture **b**ased **I**nstensity estimation* (TRABI) is a photometric method, whose core function is to determine single molecule brightness from SMLM movies. Together with Sebastian van de Linde I designed, developed and applied this method not only for pure intensity estimation in single molecule data, but more importantly, to extract three-dimensional information encoded in two-dimensional SMLM data sets, previously unused. Additionally, we combined TRABI with a multiplane detection scheme, facilitating quantitative 3D-SMLM imaging with superior axial precision and resolution than conventional Biplane SMLM under the exact same conditions.

Since we published a methodical paper in *Nature Methods* earlier this year (**P6**, [35]) with extensive supplementary information, I desist from giving an in-depth description of the method and its applications. Nevertheless, as TRABI is, in my opinion, the most important single component of my works, I will draw up a quick review of its methodical foundation. Some points may also be of more general interest apart from their TRABI context, namely the generation of 3D calibration curves and the benchmark simulations of single molecule emitters from different models.

A review and correction of the published PSF-averaging approach, to characterize the photon mismatch under different experimental conditions, can be found in chapter 4.

3.2.1 The TRABI Principle

TRABI, as its name already implies, is based on aperture photometry (AP), a method commonly applied in astronomical research to robustly determine the brightness of astronomical features [88] like stars, or more recently even in single molecule FRET applications [89]. In classical AP the raw intensity of an object is measured in a circular aperture around the center of mass. If the premise of that measurement is to cover all photons of the emitter it was shown, that a radius of 2-3 units of the expected FWHM of the spot is needed to cover a sufficient area [35][88]. To then correct this raw intensity for the background (BG) portion, a second, larger aperture is plugged to the central circle. The area-normed mean BG-intensity is determined and subtracted from the raw intensity.

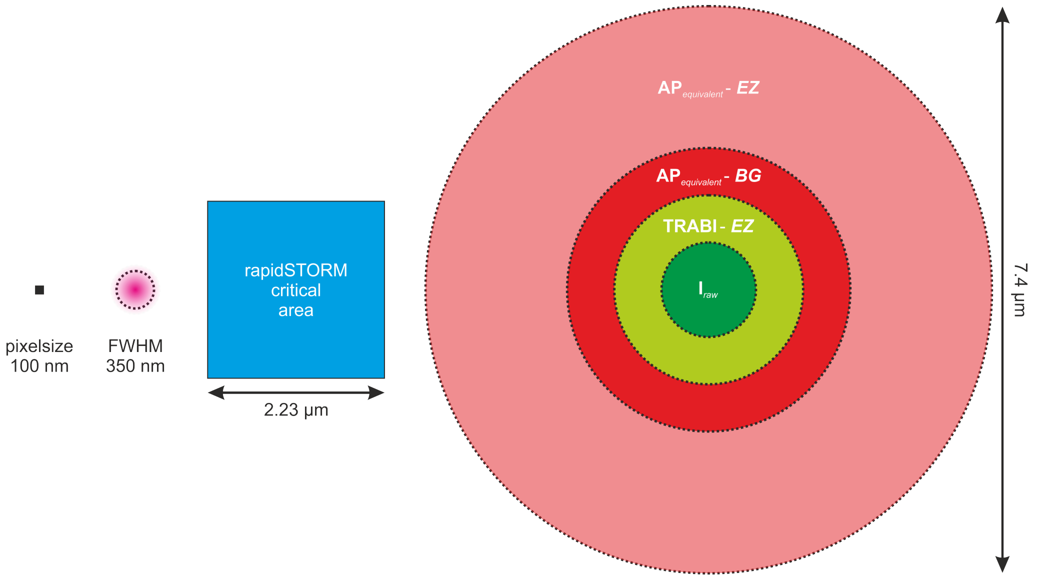

Figure 3.7: Different aperture area sizes in context of the critical emitter density (for rapidSTORM). *Left*: Assuming a pixelsize of 100 nm (black square) and an *in focus* FWHM of an emitter of 350 nm (red circled spot), the critical emitter density (CEmD) for rapidSTORM translates to area of the blue square in which only one active emitter is allowed to avoid fitting errors (0.2 localizations · µm^{-2} or 1 emitter per 5 µm^{2}). *Right*: Comparison of the covered area concerning different AP and TRABI modes. The optimized TRABI analysis relies on a diameter of 13 camera pixel (1300 nm) for the raw intensity estimation and a doubled *exclusion zone* (EZ; 2600 nm), which complies with the CEmD (1 emitter per 5.3 µm^{2} or 0.19·µm^{-2}). In case of the BG-area equivalent AP, an BG zone diameter of 37 camera pixel (3700 nm) and doubled EZ (7400 nm) is needed so that the covered area of the EZ increases dramatically to 43 µm^{2}. The resulting target emitter density (≈0.02·µm^{-2}) is therefore an order of magnitude smaller than the rapidSTORM limit and unusually low for SMLM experiments.

This method in itself is already applicable to SMLM data but has a severe drawback in the overall area covered by the aperture. Although in SMLM most fluorophores reside in their dark state, a significant number is active at all times. If handled with care, fitting artifacts originating from overlapping emission patterns can be avoided [57][90], but AP decreases the allowed emitter density by an order of magnitude, when an equivalent to TRABI BG estimation quality is targeted [35], as Fig 3.7 illustrates. That means that even neighboring PSFs that are apart several micrometers can interfere with the raw intensity and/or background measurement.

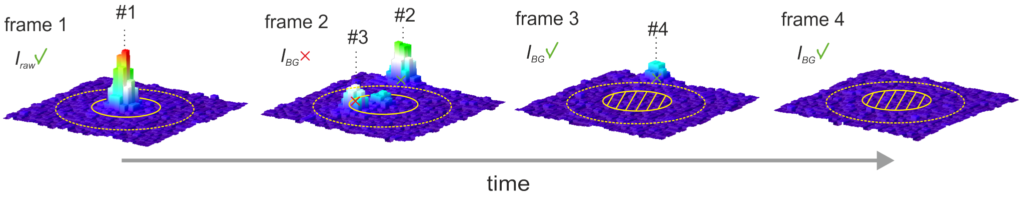

Figure 3.8: Principle of TRABI, which uses a circular aperture with radius r_1 (solid circle) and the EZ defined by $2r_1$ (dashed circle). I_1 is determined by subtracting background (I_{BG}) from raw intensity ($I_{\mathrm{raw},1}$). $I_{\mathrm{raw},1}$ and I_{BG} are not estimated in frames in which localizations from neighboring spots interfere. Modified from [35],**P6**.

The most significant difference between astronomical and SMLM data sets is the blinking behavior of SMLM emitters. TRABI utilizes the fact, that one can simply wait a couple of frames until the fluorophore of interest is switched off, enabling raw intensity and BG measurement at the exact same spatial position. Naturally, one has to take care of interfering emitters as well, but since there is no need for a second large aperture, the critical spot density decreases significantly. Fig. 3.8 illustrates the principle of the BG averaging approach and density filter, i.e. the exclusion zone (EZ).

To avoid interference from close-by emitters, we introduced an EZ in which no other active emitter is allowed. Assuming, that 100% of one emitter's intensity is included in the initial aperture, emitters that are two times the radius away from its center cannot contribute to the central aperture. Consequently, the BG measurement has to fulfill the same requirement. Therefore, the radius of any EZ should be two times the inner aperture. If at any point in the analysis, at least one spot other than the initial one is apparent, the current measure is discarded.

We showed, that averaging more than one BG frame increases the accuracy of the BG estimation significantly. Choosing 7 BG frames proved to be the optimal compromise between precision and applicability. With this basic principle it was possible to acquire accurate photon numbers from single molecule emitters, both simulated and experimentally measured. It turned out, that commonly used Gaussian fitting based SMLM algorithms systematically underestimate those intensity values, and in addition, that the mismatch between the true intensity value, stemming from TRABI, and the fit parameter is dependent on the axial position of the emitter.

This issue has great implications for SMLM, since the evaluation of novel dyes, buffers and imaging techniques is often judged by the emitter intensity, usually calculated by a Gaussian fit. More details on those findings and other important TRABI parameters can be found in [35], **P6**.

3.2.2 Photometric Three-Dimensional Imaging

Apart from the actual photon counting, we adapted TRABI to calculate an axially changing parameter, i.e. the photonic mismatch between the total intensity determined by TRABI and an inner, smaller aperture measure, as illustrated in Fig. 3.9.

Hereby, the inner aperture can be a classical circle with $r_2 < r_1$ or an intensity value stemming from the preceding fitting algorithm, since they tend to underestimate intensities. The best approach to generate the z-dependent P value ($P = I_2 {I_1}^{-1}$) was to use a stiff Gaussian fit with fixed width in rapidSTORM to determine I_2 [35], which resulted in superior working range and precision in P.

As also can be seen in Fig. 3.9, $P(z)$ is symmetric around $z = 0$, so it can be ambiguous for a particular axial range if the focal plane is well inside the structure. To achieve uniqueness, the focal plane can be predominantly set above or below the sample, so that the steep flank of the z-dependence can be used for three-dimensional imaging above the coverslip. Albeit, that reduces the axial range of the method, it but makes single-plane 3D TRABI instantly applicable to any conventional 2D SMLM setup.

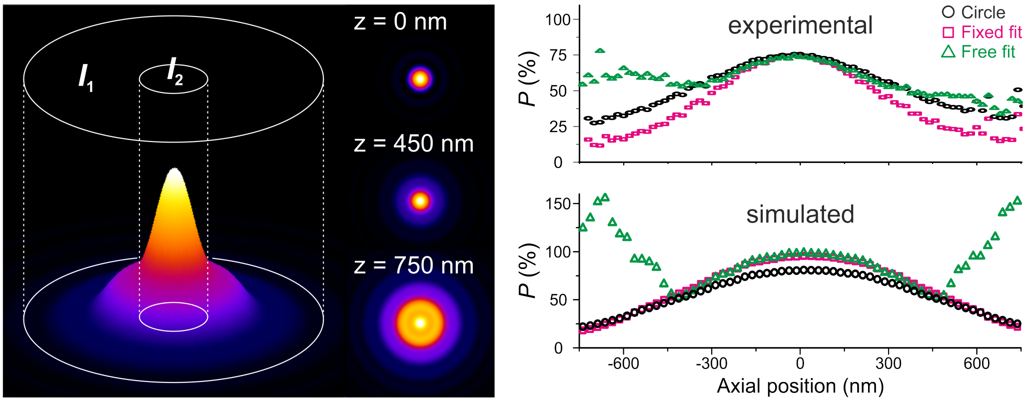

Figure 3.9: Principle of 3D single-plane TRABI imaging. *Left*: The z-dependent photometric parameter P is determined by the intensities in two apertures of the molecule's emission pattern according to $P = I_2 {I_1}^{-1}$. *Right*: P as a function of the axial position calculated from experimental (top, 133 nm pixelsize) and simulated data (bottom, 100 nm pixelsize). Dots represent the median of the distribution; I_1 was determined by TRABI ($r_{1,\,\text{exp}} = 865$ nm, $r_{1,\,\text{sim}} = 750$ nm), and I_2 was determined either by TRABI ($r_{2,\,\text{exp}} = 333$ nm, $r_{1,\,\text{sim}} = 250$ nm, black circles) or through free (green) or fixed fitting (magenta, $FWHM = 300$ nm) in rapidSTORM. Modified from [35],**P6**.

3.2.3 TRABI Biplane Imaging

Another way to break the symmetry around the focus is to apply a biplane detection (BP) scheme (see chapter 1.1.2). Here, we followed the standard procedure of placing the two planes ≈300 nm apart and relating the sample signal to a previously measured calibration curve. In our original work, we achieved axial ranges of > 1 µm while improving upon classical BP up to a factor of 2 in axial localization precision, measured for the exact same data set, reaching 10 nm (s.d.) under optimized conditions. This is coherent with the larger gradient in the TRABI calibration curves compared to BP-curves where the FWHM information of the spots was used.

Modifications to the standard SMLM Setup

It is worth noting, that most SMLM setups, build for two color applications (mostly red and green), exhibit already an axial shift between the two detection planes of ≈ 300 nm when operated monochromically, which makes the conversion from two color to three dimensional imaging via BP or TRABI-BP most convenient. One basically just has to exchange the dichroic with a 50/50 beamsplitter without any need to major adjustments apart from the 3D calibration procedure. Naturally, if one uses two separate cameras for detection, those have to be synchronized. This can either achieved by triggering one camera with the other, at which a temporal shift of exactly one frame between the two cameras can occur, or, as reported, by utilizing an external signal (e.g. from a pulse generator) to evenly trigger both cameras. This fact can further be used advantageously to trigger a (re-) activation laser pulse (e.g. 405 nm), as often done in SMLM with organic fluorophores or PAFPs.

3D Calibration

In order to generate 3D calibration curves we employed a single molecule surface (SMS) as sample and moved the objective with a piezo scanner (Pifoc, Physik Instrumente) driven with a LVPZT servo controller (E-662, Physik Instrumente) typically in a range of ±2 µm around the SMS. In general, all kinds of SMS could be used, but it is advisable to use as similar parameters for calibration and sample as possible. Especially fluorescent beads, quantum dots or other very stable probes commonly used for SMLM calibration purposes are not recommendable if one wants to apply TRABI, since those usually do not exhibit blinking with long lived dark states, which makes the temporal BG calculation impossible.

Therefore, SMS based on immunofluorescence or the common surface modification consisting of a system of BSA-Biotin-NeutrAvidin-Biotin-DNA-Dye is favorable.

The usual processing routine included application of a fitting algorithm (usually rapidSTORM with fixed FWHM), a subsequent TRABI analysis of both channels (transmitted and reflected) and a nearest neighbor (NN) assignement between the channels to calculate the z-dependent parameter P(z) by

$$P(z) = (P_{\text{transmitted}} - P_{\text{reflected}})(P_{\text{transmitted}} + P_{\text{reflected}})^{-1} \tag{3.3}$$

Usually, the calibration curve is then smoothed with a median filter and fitted with a polynomial which then serves as lookup-table.

Nearest Neighbor Assignement

Since both channels are imaged with the same spectral information, the is no expected chromatic aberration. Therefore, a linear least square shift is applied to the localization data to achieve a coarse alignment of both channels. Afterwards a frame by frame screening is performed, where every localization in the predefined master channel (usually the transmitted) is checked for an equivalent in the slave channel with an allowed error margin of up to 500 nm. Effectively, the nearest neighbor of every localization is searched in the other channel.

3.2.4 Simulating Ground Truth Single-Molecule Data

An important aspect in evaluating novel analysis approaches is to test them with ground truth data. In the case of TRABI, that would mean knowing an emitters photon yield a priori and compare its result with it. Surely, the only practical possibility to achieve that is to create a simulation of single molecule raw data with adjustable parameters. As is discussed in section 1.1.1, the Gaussian- (eq. 1.1.1) or Besselian-model PSF (eq. 3.2.4) [91] is not accurate, but sufficient for most *in focus* PSF approximations.

$$PSF_{Besselian}(D) \quad = \quad \left(\frac{2J_1(D)}{D}\right)^2 \; ; \quad D(r, \lambda, NA, n) = \frac{2\pi \;\; NA \;\; r}{\lambda \;\; n} \qquad (3.4)$$

Here, J_1 is the Bessel function of first kind and first order, r the radial distance from the emitter position, NA the numeric aperture of the objective, λ the (discrete) emission wavelength and n is an effective scaling factor for the PSF FWHM. Interestingly enough, if one calculates the theoretical FWHM for a red dye like Cy5 (λ_{max} = 670 nm) according to

$$FWHM(\lambda, n, NA) \quad = \quad \frac{0.514 \;\; n \;\; \lambda}{NA} \qquad (3.5)$$

one would get unrealistically (regarding experimentally recorded in focus FWHMs) low values for $n = 1$:

	NA$_{oil}$ = 1.45	NA$_{water}$ = 1.15
theor. FWHM$_{in\ TIRF\text{-}zone}$	237 nm	300 nm
theor. FWHM$_{above\ TIRF\text{-}zone}$	258 nm	300 nm
exper. FWHM	310 - 340 nm	355 nm

To ensure simulated PSFs with FWHM consistent with experimental data we employed a scaling factor of n = 1.33 for all Besselian-PSF simulations. This is of major significance, since these simulations were then used to determine optimal AP and TRABI parameters. Furthermore, for three dimensional PSF implementations, the Gibson-Lanni model supplies an excellent approach, accounting for the vector nature of light and interfaces between sample and objective lense, e.g. coverslips [21][23].

Simulations with pseudo Realism

In order to closely reconstruct experimental conditions, one has to take into account the discrete nature of the photon stream to the detector, i.e. single photons hitting the pixelated chip. Therefore I took the analytical form of each simulation model and converted it into a discrete 2D probability distribution, pre-pixelated with 1 nm resolution and translated it to a coordinate map. Then, single pseudo-photons were randomly drawn from this map until the target amplitude was reached. After binning to the target pixel size (usually 100 nm), noise was added according to a theoretical model (e.g. Poisson) or experimentally measured camera noise.

To ensure the applicability of TRABI, pure noise frames were inserted in between the emitter frames. This could either be the exact same noise pattern from the emitters frame or another set of randomly drawn values from the same model. For TRABI, typically 1,000 frames each (emitter and pure noise) were simulated with distinct parameters.

We also tested a number of more extensive approaches, including taking the real emission spectrum of fluorophores into account, since the usual models only deal with one discrete emission wavelength. Considering weighted shares of different wavelengths naturally also leads to a spatial re-distribution of photons, but we found no significant divergence in terms of the photonic (mis-) match compared to TRABI, i.e. at least in the Gaussian and Besselian model case. Still, the inclusion of fluorophore specific spectral properties should be kept in mind.

Furthermore, we created data sets that emulate the *real* blinking behavior of fluorophores under SMLM conditions, meaning unsynchronized (dye to camera) On and Off switching, leading to distorted overall intensity distributions. Therefore I assumed exponential On/Off time statistics, where the switching ratio R can be adjusted by $R = \tau_1 {\tau_2}^{-1}$. Then a virtual time-trace for every emitter is constructed by randomly pulling On and Off times alternating until the desired stack length is reached. The On/Off time are hereby oversampled (usually a factor of 100-10000) and then re-sampled to the targeted frame duration.

Alternatively, a set of initial *active* emitters can be generated, assigning a distinct first On time to those, and a distinct Off time for all remaining emitters. Once the end of the initial time period is reached for an emitter, the respective different state will be set with an appropriately pulled time period value, and so on. Because there was no significant influence to the TRABI relevant results, we did not use that simulation mode for **P6**, but it is worth noting for general SMLM simulation approaches.

Finally, if the most possible realism for simulated data is desired, one also has to involve the intrinsic intensity distribution of real fluorophores. Therefore I included the possibility to draw randomly amplitude values from a Poissonian or Log-Normal distribution for each fluorophore and distinct On state.

Summarizing, I created a framework from which 2D and 3D (Gibson-Lanni model) PSFs with realistic On/Off blinking behavior, including desynchronized switching, can be generated. This includes the possibility to convolve distinct spectral properties, including experimental emission spectra, and intensity distributions together with model (Poisson etc.) or experimentally recorded noise.

However, for the purpose of TRABI characterization and quality control the full range of this methods was not necessary, nevertheless all features are implemented and were tested with different localization software and TRABI itself.

Finally, for the sake of transparency, it has to be mentioned, that the practical implementation of simulated PSFs for the published TRABI manuscript may include an effective cutoff of the PSF beyond the second side minimum. Also, to achieve most realistic PSF simulation data, complex full vectorial models have to be explored and tested. These issues are currently under investigation and further discussed in section 5.4.

4 Ongoing Work

TRABI follow up Projects

Following the original publication of the TRABI algorithm and the connected results ([35];**P6**), the research on several aspects of that work was continued. In the following sections, I will give a comprehensive overview of the two most advanced projects that are not yet published, but are either in review or in preparation. First an application of TRABI and TRABI-BP is presented, characterizing a novel dye for SMLM.

Afterwards a conceptual overview of the progression in quantitative single plane TRABI, BP-TRABI and their application is given. Here the improved techniques are employed in the study of cellular membrane topology with various membrane markers.

Furthermore, I will start with a description of recent advancements regarding the PSF-averaging approach, which was revised and enhanced to allow the TRABI analysis of the averaged PSF. Hence, new results lead to modified interpretations of the original data and a better understanding of the data.

A forward-looking overview of current and potential subsequent work is given in chapter 5.

4.1 Advanced PSF-averaging for TRABI

One of the most far-reaching findings for principled SMLM in the original TRABI work was the fact that even *in focus* PSFs show a substantial photonic deviation from a 2D-Gaussian model, when analyzed with TRABI [35];**P6**. This effect only occurred in experimentally recorded, but not in standard simulations, independent of the sophistication of the simulation method (Gaussian-, Besselian-, Gibson-Lanni-PSF; see chapters 1.1.1&3.2.4).
However, we were recently advised that the implemented simulation may have introduced an effective PSF cutoff, that possibly hides the apparent *in focus* photonic mismatch in our simulations, which is further commented upon in section 5.4.
In the original work, we performed PSF-averaging analyses, which led to supplementary Fig. 12 in [35];**P6** and the conclusion that the *in focus* photon mismatch between Gaussian-fitting and TRABI is substantially reduced in the averaged PSFs.

During our ongoing research we revised the PSF-averaging method applied in [35];**P6** and extended it. The improved procedure allows for a TRABI analysis of the averaged data by also averaging the according background information for every singular PSF. Additionally we introduced the possibility of an iterative analysis after every averaging step, therefore making the process traceable and more transparent. Hereby the main motivation was to quantify how many singular PSF would be sufficient to get an improved photonic mismatch.

However, while re-analyzing the original data with the improved algorithm, we came to a divergent conclusion regarding the effect of PSF averaging on the P-value, that can be summarized as:

The averaged PSF does not differ in terms of the photon mismatch from the ensemble of singular PSFs, i.e. the photometric P-value is virtually the same for singular PSFs (median) and for the averaged PSF. Therefore it can be stated, that the averaging has a negligible effect on the photometric measure.

Following that finding, we could identify three main differences between the published and the improved averaging procedure (in descending order of impact):

1. Insufficiently small AP radius used in [35];**P6**
2. Imprecise comparison of the TRABI-P_{ensemble} value with the AP-P_{average} value
3. Possible pixel coordinate interpolation error, due to different coordinate-origin definitions in rapidSTORM and other software

Insufficiently small AP radius

The first and most significant bias, of choosing a too small AP-radius, was effectively an oversight during the analysis process and can be straight forwardly corrected by using a sufficient radius.
Fig. 4.1 shows a comparative graph, illustrating the divergence of the P-value compared to rapidSTORM with different fit-window (FW) sizes (400 nm & 1500 nm) in free FWHM mode.
As it turned out, an AP-radius of 600 nm as suggested by simulations in **P6** is insufficient to cover the complete area of the averaged PSF, thus leading to an overestimation of the P-value (dashed lines in Fig. 4.1). Using a sufficient AP-radius of 900 nm results in an almost perfect accordance of the ensemble median P-value (dotted lines in Fig. 4.1) and the asymptotic P-value of the averaged PSF (solid lines in Fig. 4.1).
The published value of $P = 96.2\%$ after averaging (dashed blue line in Fig. 4.1) is therefore clearly explainable as the result of this ambiguity, seemingly indicating a substantial influence of the PSF-averaging approach on the photonic mismatch.

In summary, the averaging curves show no significant trend dependent on the number of averaged singular PSFs nor a divergence from the ensemble P_{AP} value (median).

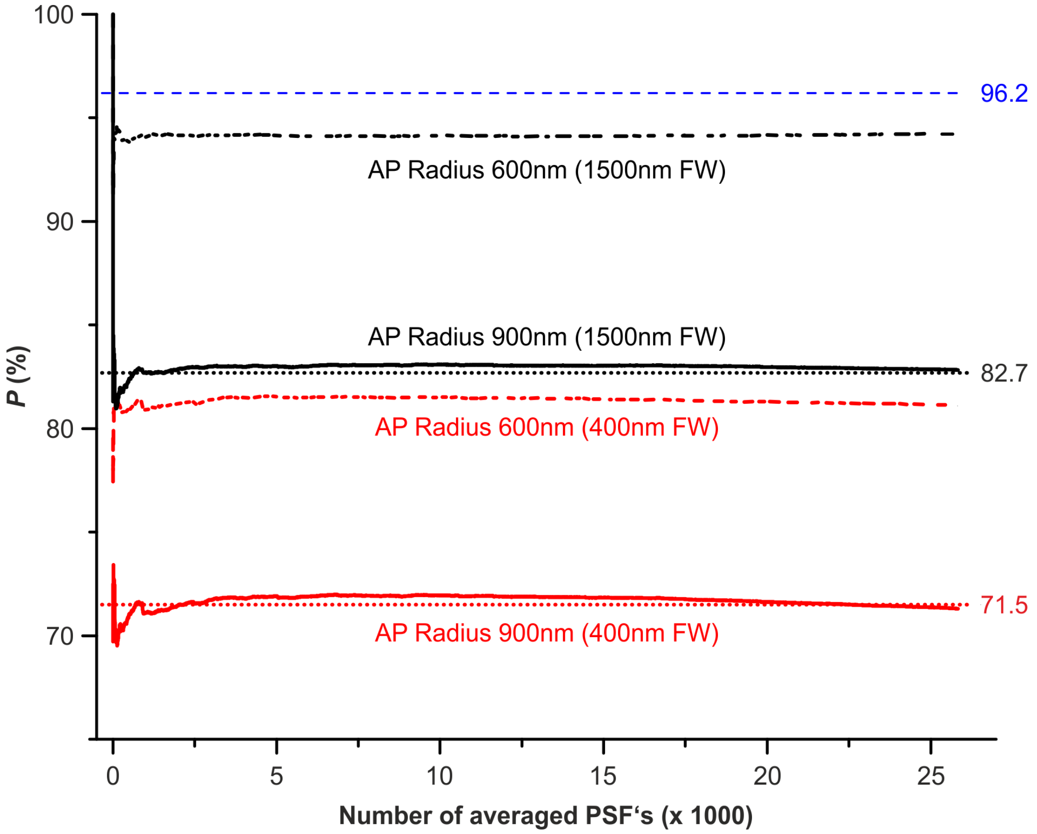

Figure 4.1: The effect of insufficiently small AP-radii on PSF averaging. The AP-analysis of the averaged PSF constructed from up to 26000 single PSFs shows no significant overall trend, independent of rapidSTORM fit-windows (FW) sizes (400 nm FW, red lines; 1500 nm FW, black lines) or AP-radii. Asymptotic average values with a sufficient AP-radius of 900 nm (solid lines) virtually coincide with the AP ensemble P-median values (dotted lines; ensemble median values indicated). Using an AP-radius of 600 nm as in **P6** a virtual shift to larger P-values than the ensemble median is observable (dashed lines). The published averaged P-value of 96.2% is indicated as blue dashed line, which is close to the asymptote value originating from AP-radius 600 nm at FW 1500 nm.

The mismatch between TRABI and AP

The second bias in the averaging analysis was more subtle, albeit also substantial. Due to computational convenience, the averaged PSF was analyzed once the whole averaging process was concluded, not after every averaging step. Also the averaged PSF was not accessible by TRABI, since we only averaged single PSFs but did not carry their related background information. Therefore AP was used to analyze the final average PSF.

By introducing an incremental averaging approach that also includes the complete background information of each spot we not only improved the traceability of the process, but also enabled a TRABI analysis of the averaged PSFs and therefore facilitating a more accurate analysis. Since AP systematically underestimates the photon number compared to TRABI [35];**P6** (see also section 5.4), it is evident, that comparing the ensemble P_{TRABI} with P_{AP}, originating from of the averaged PSF will lead to deviations, as illustrated in Fig. 4.2.

Considering the findings described in the previous paragraph, a sufficient AP- and TRABI- radius of 900 nm was chosen. Also, we conducted analyses with different rapidSTORM FW sizes as before and calculated the ensemble median P-value (indicated as dotted lines in Fig. 4.2).

As can be seen with the improved approach, every averaging run in itself shows almost perfect consistency between the ensemble median and the average P-value. However, there is an offset of 5-6% between the TRABI and AP value. Consequently, even when choosing the right analysis parameters one observes a virtual effect of PSF averaging when comparing the ensemble TRABI-P-value with the AP-P-value of the averaged PSF, as previously done.

On the contrary, comparing the ensemble median and averaged P-value with consistent methods, no significant effect of PSF averaging is observable regarding the photonic mismatch between Gaussian fitting and AP and TRABI respectively.

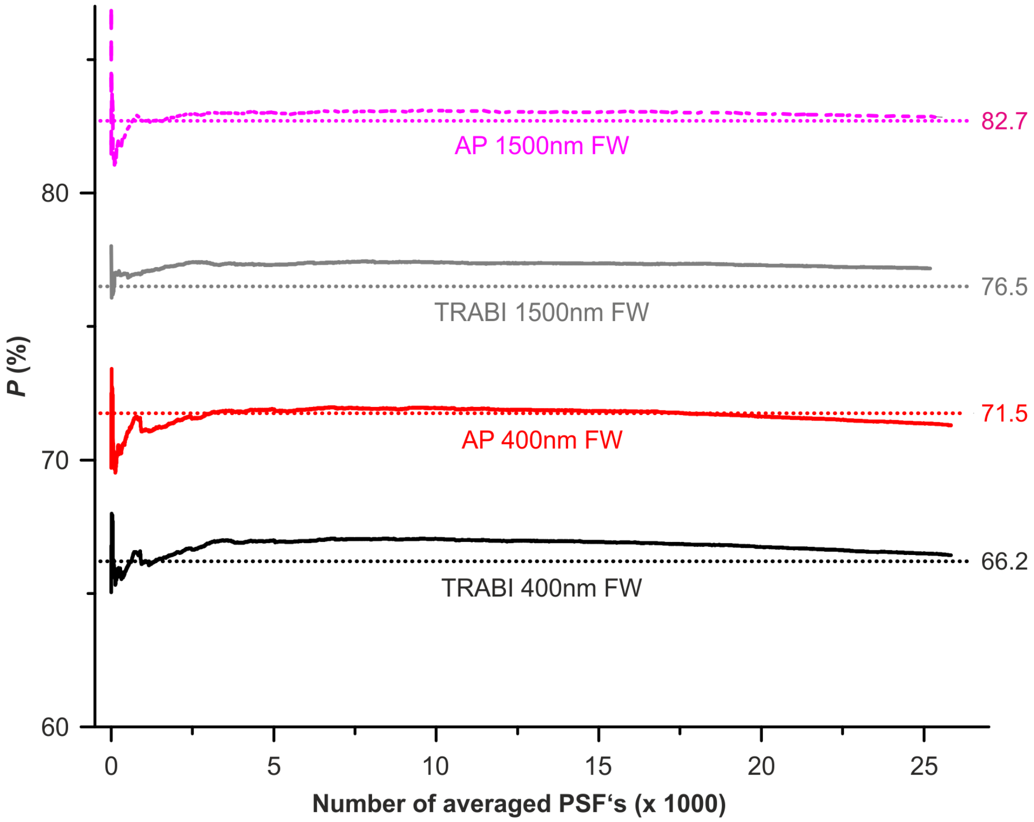

Figure 4.2: The effect of analyzing the averaged PSF with AP and TRABI. AP (solid red and magenta lines) underestimates the true photon number of the averaged PSF compared to TRABI (solid black and grey lines), using a sufficient radius in both cases (900nm). Consistent with Fig. 4.1 there is an almost perfect match between the ensemble median P-values (dottet lines) and the averaging asymptote, thus underlining the lack of an effect of PSF-averaging on the photon mismatch. However, there is a substantial difference in AP and TRABI P-values, causing a virtual effect of PSF averaging.

Pixel coordinate interpolation error

The third inaccuracy in the averaging analysis has almost no substantial effect on the actual result and its interpretation, but has more general implications when using rapidSTORM as a localization sofware.
During the reanalysis of the averaging data as described above, we realized an oddity that slipped by before. Contrary to all of our in-house written analysis tools (especially TRABI and AP) and other localization sofware that we used (ThunderSTORM [92], peakfit [93]), rapidSTORM defines the {0.5, 0.5}-pixel-coordinate as the lower right corner of the pixel, whereas the more common and intuitive definition is the center, i.e. the middle. Thus, using rapidSTORM together with other software, a coordinate shift between rapidSTORM and TRABI of ∅ 0.5 source pixel can occur, which is illustrated in Fig. 4.3.

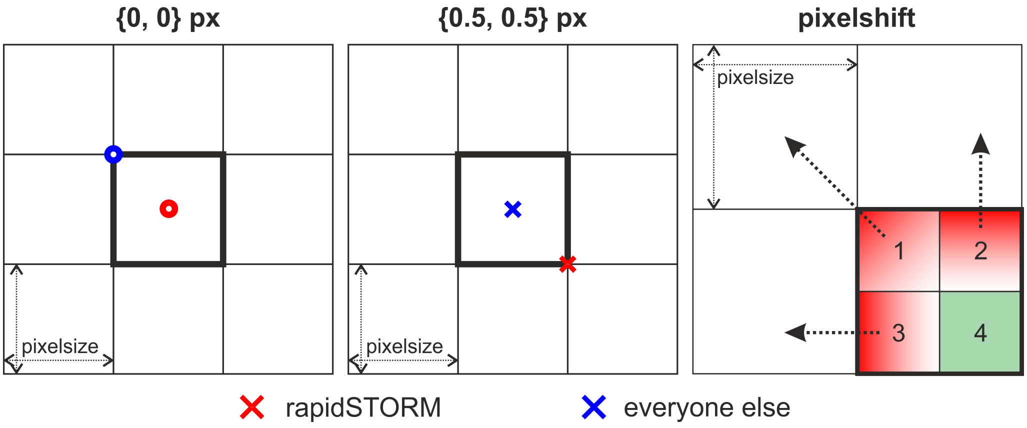

Figure 4.3: Coordinate shift between rapidSTORM and other software. *Left*: Diverging definition of the origin of a pixel, i.e. the {0, 0}-pixel-coordinate, between rapidSTORM (*center*, red marker) and all other used software (*upper left corner*, blue marker). *Middle*: Consequential difference in definition of the {0.5, 0.5}-pixel-coordinate, i.e. usually the center of the pixel. *Right*: Resulting possible pixel-coordinate shift. Only if a fluorophore ’truly’ resides in quadrant 4 of the pixel, there is no difference in its pixel-coordinate. In every other case, there is an apparent shift between the ’true’ and the rapidSTORM localization to adjacent pixels (indicated by arrows).

Only if a fluorophore ’truly’ resides in the lower right quadrant of a source pixel, there is no impact on its virtual pixel-coordinate. In every other case, there is an apparent shift between the ’true’ and the rapidSTORM localization to adjacent pixels (indicated by arrows in Fig. 4.3).

As Fig. 4.4 shows, this led to a very small (AP) to negligible (TRABI) effect on the averaging data, when using sufficient radii (900 nm). It is still worth noting, since the whole TRABI- (and AP-) principle relies on the precise determination of pixel intensities, where a (virtual-) shift of one pixel can make a substantial difference in the overall value, especially when working with borderline small radii, e.g. in the case of high emitter densities.

Following the realization of this issue, the updated TRABI versions 1.1 and higher are now factoring in the diverging coordinate origin definitions [94].

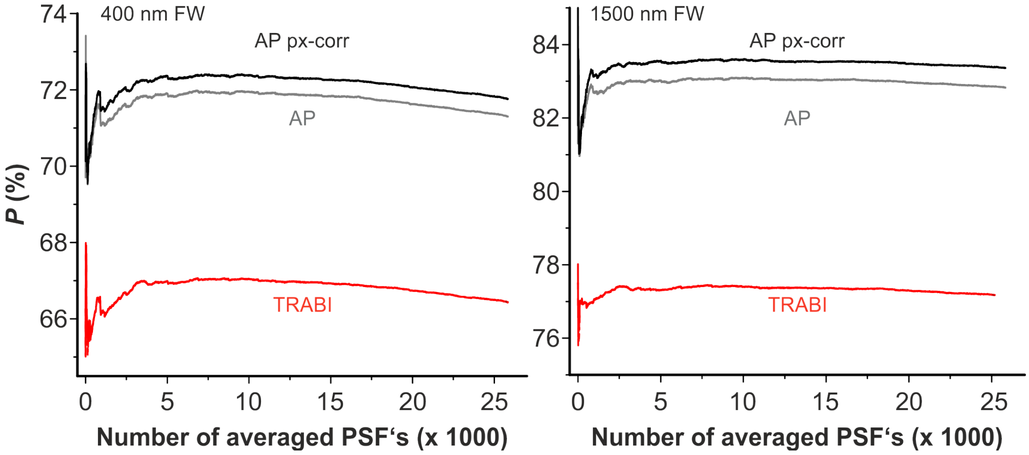

Figure 4.4: The effect of the pixel coordinate shift on PSF averaging. There is no substantial impact in the TRABI case (red curves, virtual match), whereas a small offset <1% can be observed between the uncorrected and the corrected pixel-coordinates analyzed by AP (grey lines).

4.2 Characterization of novel Dyes for SMLM with TRABI

One of the main applications and original purpose of TRABI was to determine accurate photon numbers from fluorophores, suited or tested for SMLM. Hereby TRABI provides a robust intensity measure independent of the axial emitter position, contrary to Gaussian fitting based approaches [35]. I discussed the basics and intricacies of emitter intensities in SMLM in 1.1.1, where the main implications of emitter brightness are localization precision and resolution (see eq. 1.2 & 1.3).

The first opportunity of employing TRABI in that manner was presented to us by the group of Martin Schnermann (*NIH, Center for Cancer Research*) in the form of a Cy5 derivative internally called *MM3*. In short, *MM3* is a chemically *bridged* form of the native Cy5, which leads to a significantly higher quantum yield and better photo-stability on the ensemble level (for a more detailed description see **P8**).

To validate these results on the single molecule level, the phalloidin-linked dye was tested in SMLM experiments, trying to resolve the demanding structure of actin filaments in U2OS cells (all shown data was gathered together with Ralph Götz, where Ralph prepared all *MM3*-samples, the imaging was largely done corporately, while calibration experiments and data analysis were performed by myself).

By reducing the dye *in vitro* with NaBH$_4$ into a dark state and gradually activating it with just the readout laser ($\lambda_{640\mathrm{nm}}$), we where able to perform high-quality SMLM in a PALM like fashion, which is shown exemplarily in Fig. 4.5. Since TRABI was applied to the data to extract the true photon statistics of the dye, the super-resolved image is displayed in virtual 3D (x-y-P), which is an instant benefit of the TRABI analysis. It is worth noting, that the imaging took place in pure PBS buffer and show remarkable quality both in labeling density, which is an issue in actin imaging, and resolution. The inset and cross sections in Fig. 4.5 illustrate single filaments exhibiting FWHMs of less than 20 nm and two adjacent filaments that are 40 nm apart can be resolved comfortably, which corresponds to the high single molecule intensity of more than 3500 photons per localization or 5000 photons per *ON-state* (median, Fig. 4.10).

Consequently, lateral localization precisions of 5 nm were calculated by tracking single emitters over subsequent frames, determining first mean and standard deviation (std) of the track and then fitting Gaussians to the histogrammed std-data (Fig. 4.6).

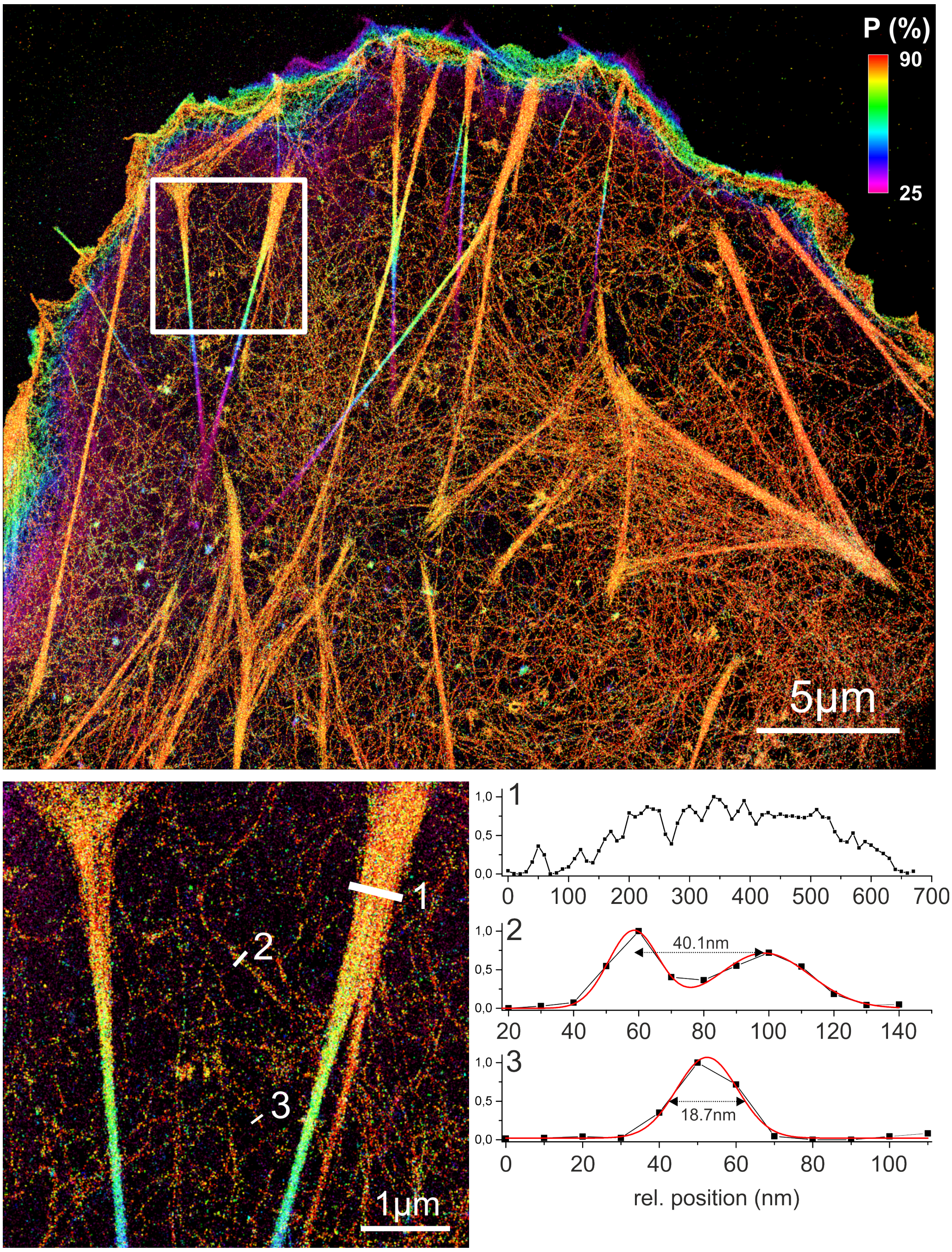

Figure 4.5: High-quality SMLM with MM3-phalloidin. *Top*: Virtual 3D-SMLM image of F-Actin in U2OS cells stained by MM3-phalloidin in single plane imaging mode. *Bottom left*: Magnified view of the selection shown in top. *Bottom right*: Cross sections of the regions indicated left. Black squares represent data points, solid black lines should guide the eye and solid red lines represent Gaussian fits to the data. **(2)** Two filaments, separated by 40 nm can easily be resolved laterally. **(3)** The FWHM of a single filament is well beyond 20 nm.

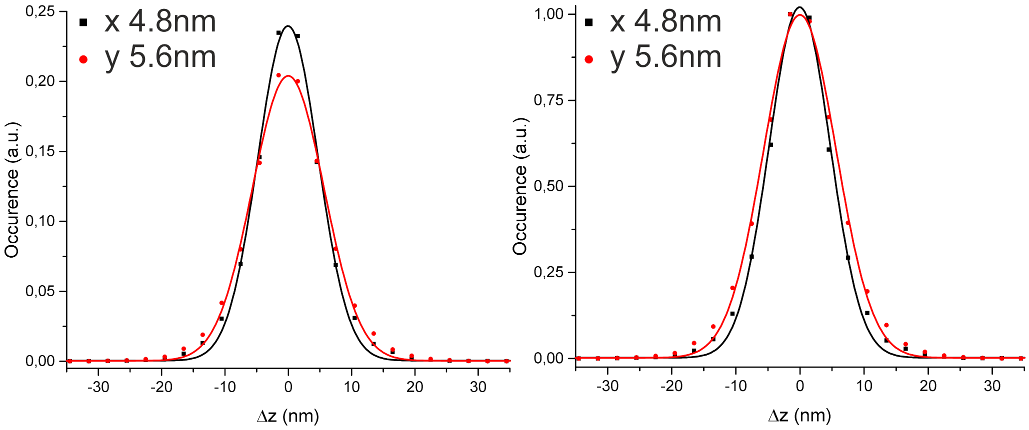

Figure 4.6: Lateral localization precision calculated from the data shown in Fig. 4.5. Unnormed *(left)* and peak-normed *(right)* histograms of x-y localization precisions. Black squared and red circles represent the x- and y- data points respectively, whereas solid lines represent Gaussian fits to the data.

Next, we performed TRABI-Biplane (TRABI-BP) as described previously in detail (**P6**) to further test the 3D-SMLM capabilities of *MM3*.
In brief we used a two-channel image splitter with twofold magnification (TwinCam, Cairn Research) equipped with a 50/50 beamsplitter (Cairn Research) and two EMCCD cameras (Ixon 897 and Ixon Ultra 897, Andor), whose focal planes were separated by 300 nm. Cameras were synchronized by a pulse generator (DG535, Stanford Research Systems).
3D calibration curves were gathered by moving the objective with a piezo scanner (Pifoc, Physik Instrumente) driven with a LVPZT servo controller (E-662, Physik Instrumente). Z-coordinates from TRABI-Biplane imaging were corrected for the refractive index mismatch by a scaling factor of 0.71 (refractive index of buffer $n_b = 1.34$ and substrate (glass) $n_s = 1.52$, numerical aperture of NA = 1.45).
As Figures 4.7 & 4.8 illustrate, high quality 3D super-resolution imaging can be achieved in pure PBS buffer conditions, with localization precisions of 6-8 nm (lateral) and 20 nm (axial), hinting at the possibility, that *MM3* could possibly be used under life-cell conditions by pre-reducing the dye ex-vitro and subsequent sample staining and imaging.
Preliminary live-cell experiments conducted by Ralph showed promising results, although still in need of improvement, mainly due to the very dense actin-phalloidin labeling and therefore spot density limitations (data not shown).

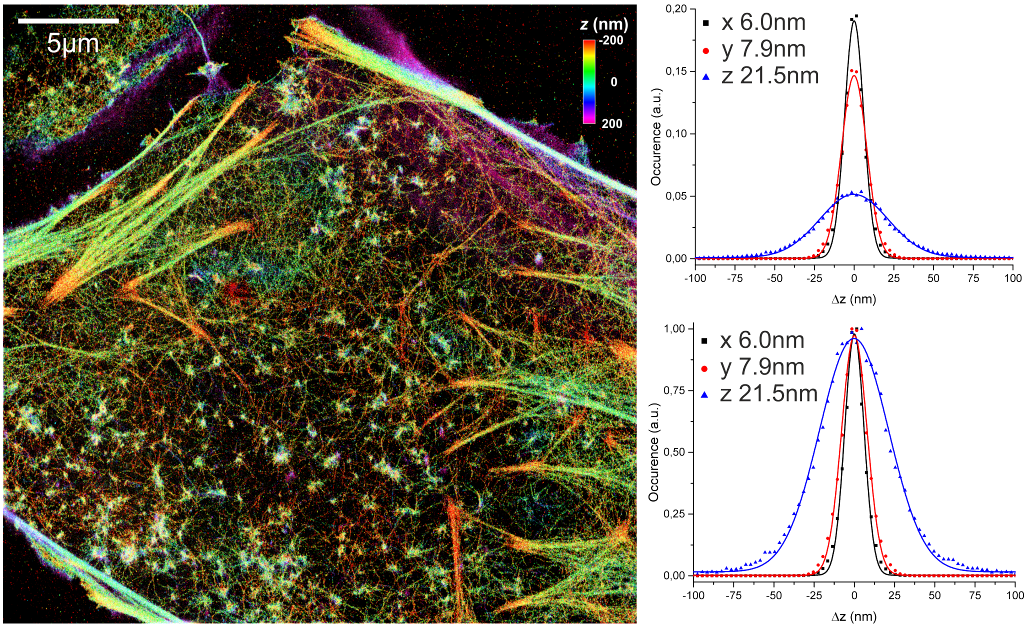

Figure 4.7: Three-dimensional SMLM utilizing BP-TRABI of MM3-phalloidin stained F-Actin in U2OS cells. *Left:* 3D PALM-like image using BP-TRABI, color-coded in z. *Right:* Measured lateral and axial localization precisions from the data *left*. Native (*top*) and peak-normed *bottom* localization precision distributions lead to 6-8 nm lateral and ≈20 nm axial, where marks indicate histogrammed data points and solid lines Gaussian fits to the data.

Another interesting aspect of *MM3* is its apparent absorption redshift. On most common SMLM setups, there is a 640 nm laser as 'red' excitation medium, which is therefore not optimal for *MM3* and possibly lessens the gain in photon numbers. Hence, we performed a comparative measurement, i.e. alternating excitation with 640 nm and 660 nm every 5000 camera frames at the exact same sample spot, while adjusting the respective excitation power density to match in the sample plane.
A subsequent TRABI analysis shows that there is indeed the expected slight raise in single molecule intensities when exciting with 660 nm while decreasing the mean duration of the *ON-state* slightly (Fig. 4.9). It is worth mentioning that the experiment was performed with a suboptimal detection filter set, leading to a slight bleed-through of the 660 nm laser. While this obviously effects the actual SMLM quality, TRABI filters out the additional constant background, thus leading to reliable single emitter intensities in Fig. 4.9.

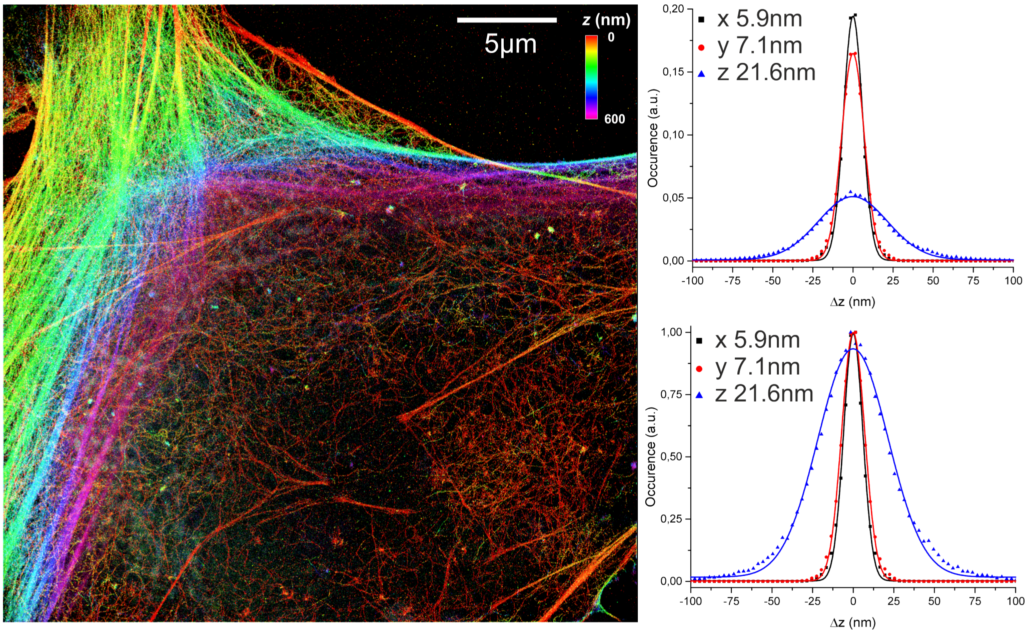

Figure 4.8: Three-dimensional SMLM utilizing BP-TRABI of MM3-phalloidin stained F-Actin in U2OS cells. *Left:* 3D PALM-like image using BP-TRABI, color-coded in z. *Right:* Measured lateral and axial localization precisions from the data *left*. Native (*top*) and peak-normed *bottom* localization precision distributions lead to 6-7 nm lateral and ≈20 nm axial, where marks indicate histogrammed data points and solid lines Gaussian fits to the data.

Finally, we performed a benchmark experiment with Cy5-phalloidin under dSTORM buffer conditions and otherwise matching imaging modalities, to class the new dye with its native form, i.e. the most commonly used dye in the dSTORM realm.
Like before, we determined single emitter intensities with TRABI and their mean *ON-time*. As Fig. 4.10 shows, there is a substantial increase in single emitter intensities when using *MM3* compared to Cy5. This gain is observable in single frame intensities (Fig. 4.10 a & b) and even more so when comparing the *ON-time*-corrected values (Fig. 4.10 d).
Therefore we tracked single emitters in subsequent frames and determined the distribution of uninterrupted fluorescent states and applied the geometric mean (*geom*) as metric for the *ON-time*. We then multiplied the single frame intensities stemming from TRABI with the mean *ON-time* as a measure of the total number of photons the respective dye allocates. In case of the Biplane data, we took the sum of both channels to determine the total photon number of each fluorophore, taking into account the slight difference in photo-sensitivity and conversion of each camera.
Interestingly enough, we observed the highest photon counts for both TRABI-BP *MM3* measurements almost doubling the value of the single plane Cy5 sample, whereas the single plane *MM3* acquisition exhibits 20-25% less than the TRABI-BP, but is still more than 25% brighter than Cy5, when comparing the *On-time* corrected intensities.
In summary, *MM3* is a promising new dye for SMLM, especially because its switching capability under physiological conditions. TRABI analyses of various data sets show, that *MM3* exhibits considerably higher single molecule photon counts than Cy5 under comparable conditions, which results in high quality 3D-SMLM images of very dense actin structures.
It is also the first case of TRABI as a characterization tool for novel dyes, which was its original purpose.

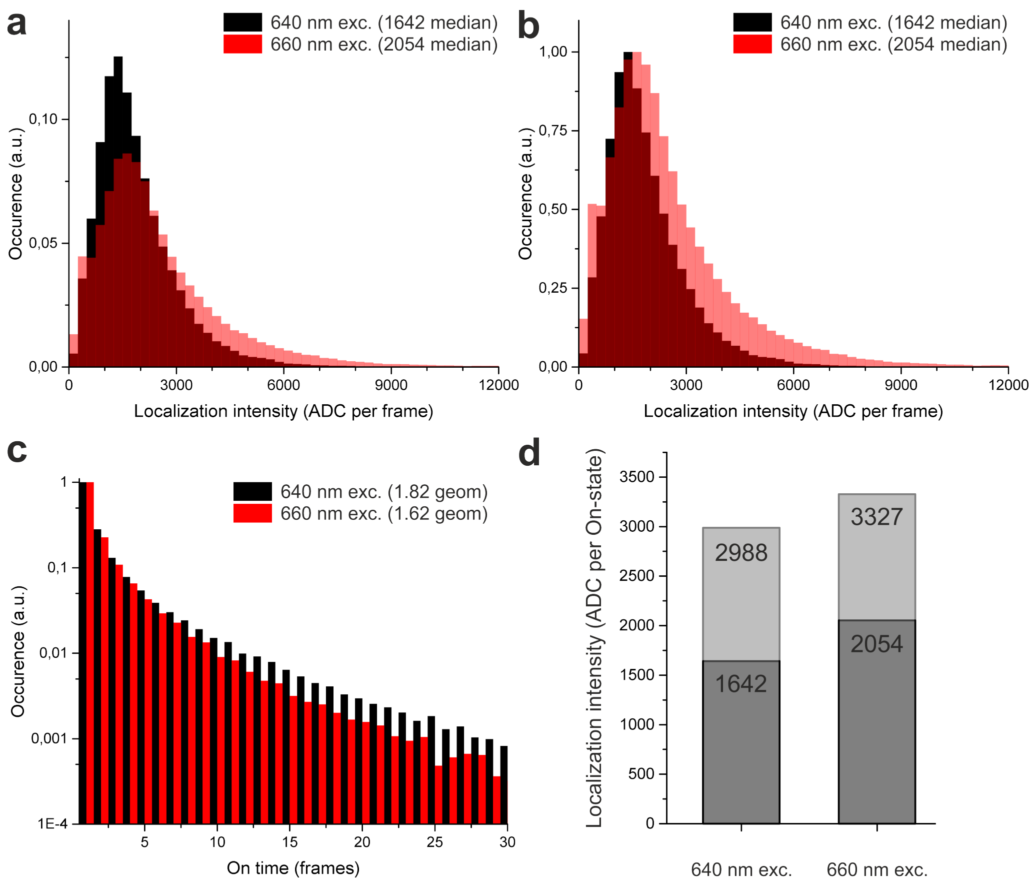

Figure 4.9: Comparison of MM3 single molecule emitter intensities at different excitation wavelengths. Unnormed **(a)** and normed **(b)** histogram of single molecule emitter intensities determined by TRABI. Excitation with 640 nm (black) or 660 nm (transparent red) leads to a median emitter intensity of 1642 ADC/frame and 2054 ADC/frame respectively ($\approx$ 25% intensity increase). **(c)** Distribution of On-state lengths of the two imaging modalities. The geometric mean of the distributions can be calculated to 1.82 frames in case of 640 nm excitation and 1.62 frames in case of 660 nm excitation. **(d)** Overview of single molecule emitter intensities based on single frames (dark grey) and On-time corrected (light grey).

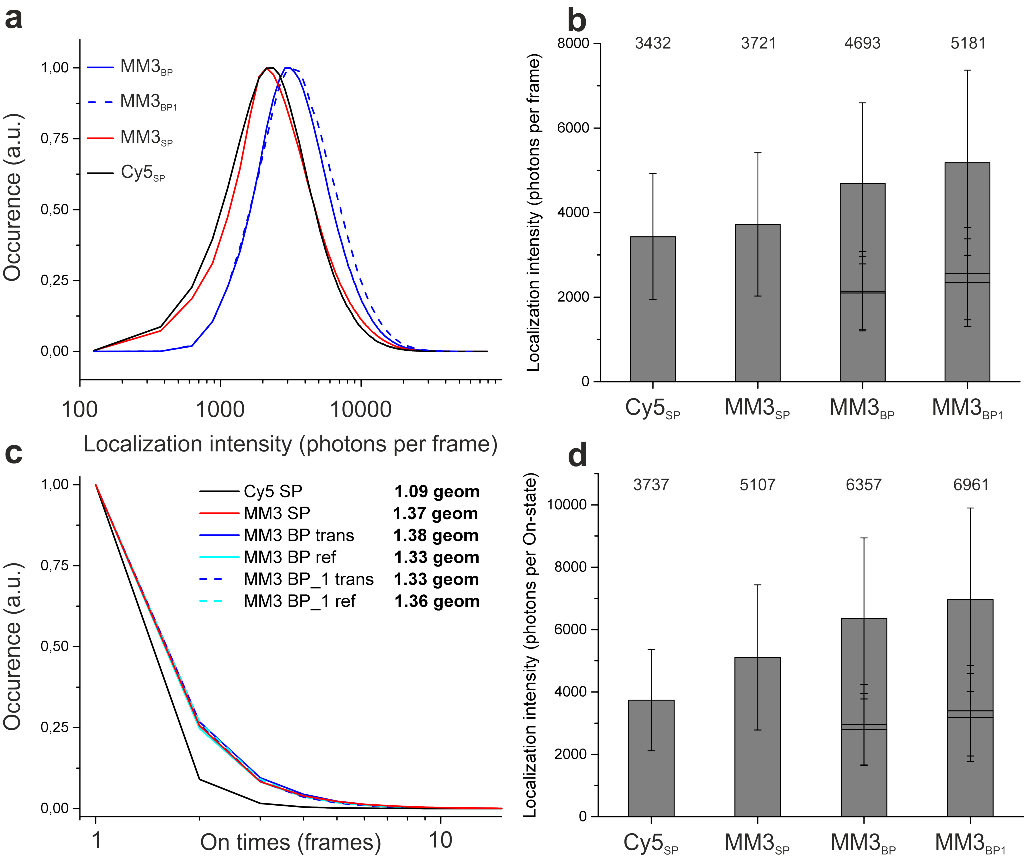

Figure 4.10: Comparison of single molecule emitter intensities of MM3 and Cy5 in different imaging modalities. **(a)** Histograms of single molecule emitter intensities obtained with TRABI in respect to one camera frame. Conventional Cy5-phalloidin (black line) serves as standard in single plane (SP) *d*STORM imaging. Compared to SP MM3-phalloidin in PBS (red line), apparently no intensity difference is observable, whereas the combined photon count from both Biplane (BP) channels (blue lines) is substantially shifted to higher values. **(b)** Bar-chart of the median intensities of the distributions shown in **(a)**, while error bars represent the MAD (median absolute deviation). For BP measurements, the single channel intensities are indicated. **(c)** Histograms of single emitter On-times obtained with rapidSTORM. Whereas Cy5 seems is in photo-saturation, MM3 shows On-times of $\geqslant$1.3 frames in all imaging modalities, where *ref* and *trans* denote the respective BP-channels. **(d)** On-time (T_{ON}) corrected median intensities of Cy5 and MM3 under different imaging modalities ($I_{\text{On-time}} = I_{\text{frame}} \cdot T_{\mathrm{ON}}$).

4.3 Studying Plasma Membrane Morphology with TRABI

Apart from the actual photon counting in SMLM, TRABI can be utilized in different ways as a tool for three-dimensional imaging. When dealing with already existing SMLM data, there is the possibility to transform a localization data set from 2D to virtual 3D which was explicitly shown in [35],**P6** with the synaptonemal complex, the active zone protein *Bruchpilot* and the actin cyto-skeleton of U2OS. Another option is to combine TRABI with a Biplane imaging scheme beneficially to create high precision quantitative 3D molecular coordinates, as shown with immuno-labeled microtubules in the original work and with the actin cyto-skeleton of U2OS in the previous section.

Another important target structure for todays SMLM is the cellular plasma membrane, which one could naively assume to be flat, sheet-like structures, especially for adherent cells. Nevertheless, there are many instances of three-dimensional membrane curvature, either due to intrinsic mechanisms or to extrinsic factors [95].

In the following sections I will give a conceptual overview of an ongoing methodical work on how to study membrane morphology and topography with TRABI and TRABI-BP. Here we apply classical TRABI to elucidate the three-dimensional nature of the basal membrane of U2OS cells labeled with click chemistry [96]. Further, an improved version of the TRABI-BP approach is implemented and a novel concept for fiducial free axial drift correction is employed.

With those techniques, the glycoprotein CD4 is investigated, directly immuno-labeled on the plasma membrane of Jurkat cells. This project is part of a collaboration between Zuzana Kvicalova, Marek Cebecauer (both J. Heyrovsky Institute of Physical Chemistry, Prag), Pablo Mateos-Gil (University of Crete), Sebastian van de Linde (University of Strathclyde) and myself, where Zuzana and Marek established the CD4 transfection and labeling protocol, Pablo provided raw data and Sebastian and I conceived the general project. Measurements related to CD4 were done collaboratively (Zuzana and I), while all post-processing and analyses where performed by myself. The here reported figures and results are an excerpt of the ongoing work.

4.3.1 TRABI on two-dimensional SMLM Data of Membrane Proteins

The plasma membrane with its rich molecular composition emerges as a prime target structure for todays SMLM [97][98]. Hereby, quantification approaches of specific membrane proteins play a huge role in its popularization, including global homogeneity measurements and statistical analyses of (non-) clustering.

One aspect that might shift the perception of these approaches and their results is the possible three-dimensional nature of the imaged membrane. Although it has been shown, that two-dimensional imaging artifacts can originate from high emitter densities caused by three-dimensionally overlapping signal [57], the impact of two-dimensional projection on the various quantification approaches and therefore the biological conclusions have not been discussed yet.

Two examples are shown in Fig. 4.11, where the standard 2D *d*STORM image of the basal membrane of U2OS cells labeled with Alexa647 via click chemistry ($Ac_4GalNAz$, [96]) suggests a very homogeneous distribution of localizations and therefore target protein.

However, the virtual 3D image obtained by TRABI analysis reveals a layered three-dimensional structure with convexities in the $\geqslant$100 nm scale. Since this could have an impact on localization density calculations, which are usually two-dimensional, we suggest an amended form of the widely used Ripley's functions, factoring in a third spatial coordinate, either virtual (P_{TRABI}) or quantitative (e.g. originating from TRABI-BP imaging, see next section).

Especially in cases where the basal and apical plasma membrane are imaged simultaneously, e.g. at the edges of cells, or in instances where the membrane forms adhesion induced structures (see next section), the distinction between the two-dimensional projection and the actual three-dimensional reality might be of utmost importance for the biological interpretation of the data.

Comparative studies of conventional and three-dimensional Ripley's functions, as well as 3D-NN analyses on various data sets are in progress (data not shown).

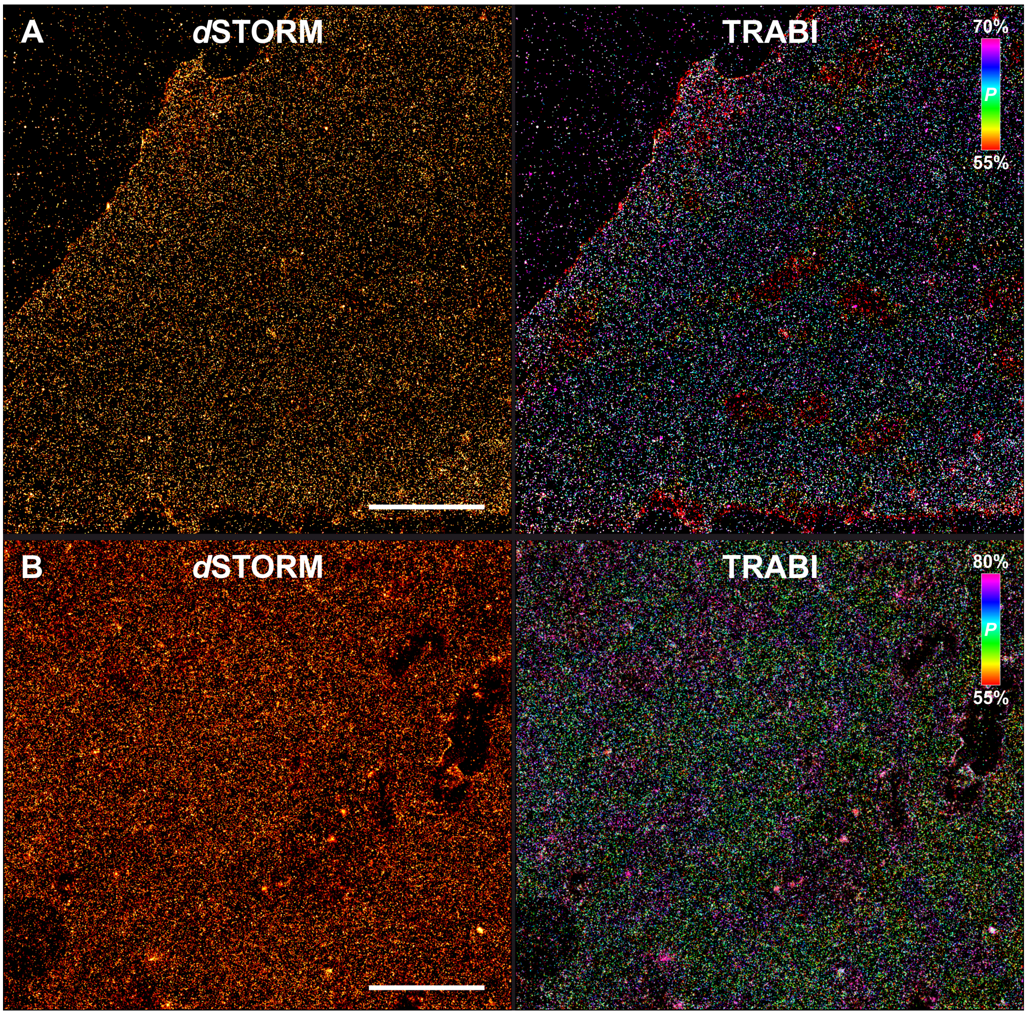

Figure 4.11: The effect of TRABI on the visibility of membrane topology. The standard 2D *d*STORM image suggests a very homogeneous localization distribution (*left*), whereas the virtual 3D visualization achieved by TRABI analysis reveals a layered 3D nature of the membrane with convexities in the ⩾100 nm scale (*right*). Scale bars 5 µm.

4.3.2 Advanced TRABI-BP Imaging of CD4

The three-dimensional distribution and structural formation of CD4 on the basal membrane of Jurkat cells is very diverse as Fig. 4.12 illustrates. Structures range from ring-like nanodomains in the $\geqslant$100 nm scale to almost filamentous structures of CD4 assemblies away from the adhesion plane.

To characterize the wild-type CD4 together with two functional mutants (data not shown) we employed an improved TRABI-BP version as well as an fiducial free drift correction approach, described in the following sections.

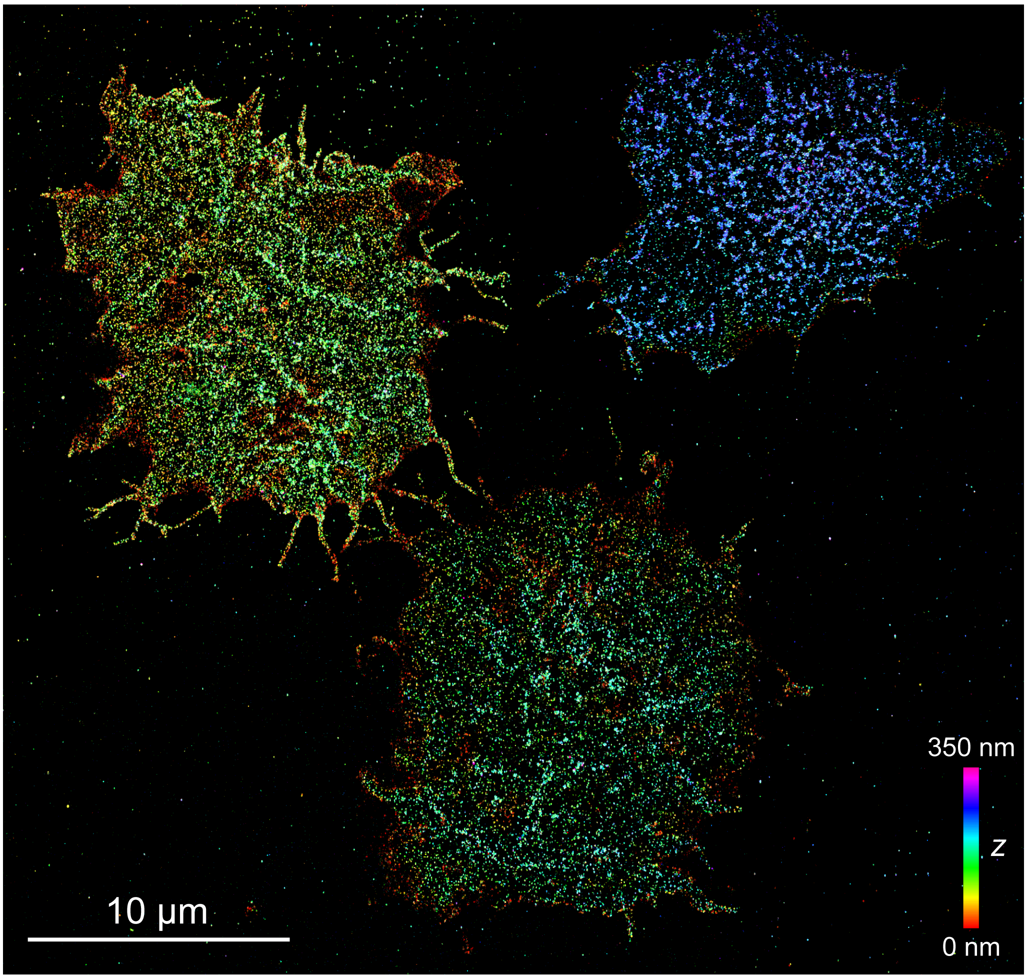

Figure 4.12: Three-dimensional imaging of wild-type CD4 in Jurkat cells utilizing direct TRABI-BP. CD4 on the basal membrane of Jurkat exhibits a wide variety of three-dimensional structures, ranging from ring like nanodomains in the $\geqslant$100 nm scale (upper right cell) to almost filamentous structures of CD4 assemblies away from the adhesion plane (upper left cell).

Intensity based Biplane

TRABI-BP has been established as high-quality quantitative 3D imaging tool. The general procedure comprised fixed FWHM PSF fitting, a subsequent TRABI analysis and a final z-coordinate allocation via the channel- and lookup-table assignment.

Here we suggest an advanced version of TRABI-BP, directly using the intensity measure from both channels, originating from the fixed FWHM PSF fitting. By then relating the raw intensity value to each other similar to Eq. (3.3) in principle the same result can be achieved as by using the TRABI percentage values. This is feasible, since TRABI robustly estimates the total intensity in each channel, which is evenly split. The total intensity is subsequently canceled out in Eq. (3.3).

We benchmarked this procedure by reanalyzing the microtubules data from the original work with the new approach and got equal axial localization precisions (data not shown). There are several advantages of the new approach, e.g. the processing speed is dramatically reduced by omitting the TRABI step. Also, this procedure allows for higher effective localization densities and improves the axial range of the method by $\approx 20\%$.

An impressive example of the new approach is illustrated in Fig. 4.13, where the three-dimensional layering of the CD4 labeled plasma membrane of Jurkat cells is revealed. In some of the observed cells, we discovered CD4 nano-domains that are ring-shaped and in the 100 nm scale. Those are axially clearly separated from another membrane layer, exhibiting very homogeneous CD4 signal.

Interestingly enough, the two functional CD4 mutants show no clear sign of the ring-shaped nano-domains, which is currently under further investigation. Clearly, this distinction could not be made in a conventional 2D *d*STORM setup, although the overall thickness of the layer is only ≈ 200 nm.

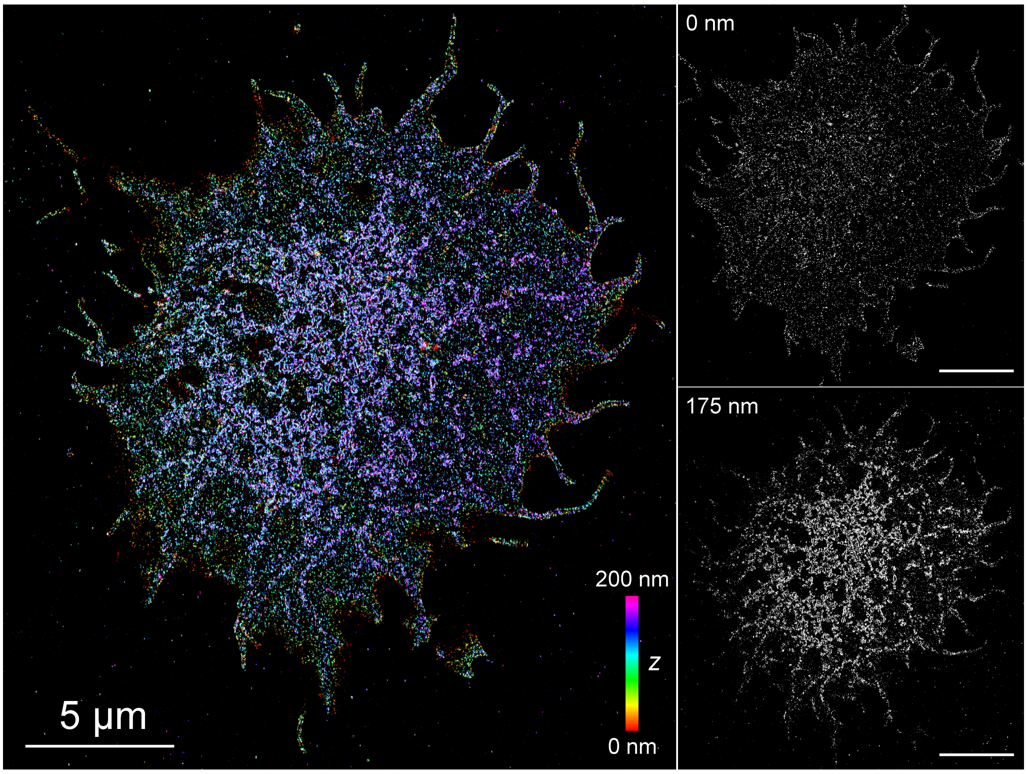

Figure 4.13: Layering of CD4 wild-type on the basal membrane of Jurkat cells, labeled with Alexa647, imaged by Intensity based Biplane. *Left*: Three-dimensional representation of CD4, with two axially distinct structural arrangements, i.e. one homogeneous layer of CD4 (*right top*) and a layer including ring-shaped nano-domains of CD4 in the ⩾100 nm range (*right bottom*). Scale bars 5 µm.

Fiducial-Free axial Drift Correction

When dealing with three-dimensional data imaged over an extensive time period (in case of the displayed data in Figs. 4.12 & 4.13 ≈ 60 minutes) a certain amount of axial drift or shift is unavoidable.

Here, we propose a novel, fiducial free approach, to subsequently determine the precise drift progression and correct for it.

We reckon, that in a thin sample layer the spatio-temporal distribution of active emitters should be constant over time. Therefore, one can calculate the time-dependent axial median coordinate of the whole sample and trace it, as is shown in Fig. 4.14.

For a perfectly stationary sample, this curve would be then a flat-line. Otherwise, the axial median would exhibit a gradient. By fitting this curve with a polynomial function (usually of the fifth order) one can model the often times nonlinear axial drift and linearize the according coordinate. As Fig. 4.14 illustrates, this procedure can be applied to quantitative (Fig. 4.14 A,B) as well as virtual axial coordinates (C,D).

A more refined approach, where only a small, very flat region of the sample is used could lead to even more precise axial correction and would be also applicable to axially extensive structures. Comparative measurements of axial drift correction in various samples utilizing the whole or just parts of the sample are currently in progress.

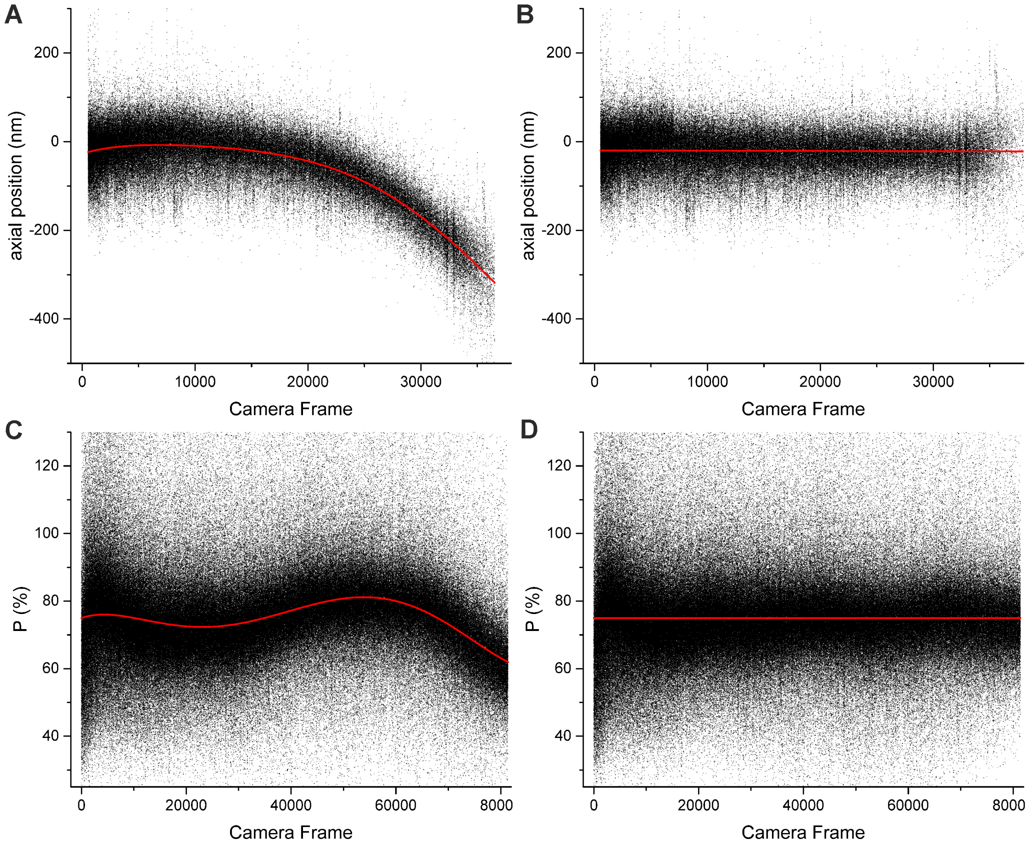

Figure 4.14: Fiducial free axial drift correction. A, C: The time dependent axial ensemble coordinate is tracked and fitted with a polynomial function. B, D: By linearizing and backtracking, the axial drift can be corrected robustly. The approach works well for quantitative (A, B) and virtual (C, D) three-dimensional coordinates.

4.3.3 Further Concepts

Additionally to the presented 3D imaging modes, we realized the calibrated single-plane TRABI approach, suggested in the original TRABI manuscript. Therefore, we set the focal plane slightly under the basal membrane. With that, the ambiguity of P values above and under the focal plane is canceled out, and an unique axial coordinate can be allocated by relating the single plane calibration curve to the data, similar to the TRABI-BP approach. Especially researchers without any conventional 3D capability could therefore instantly profit from that straight forward approach.

Our data suggests, that axial resolutions of $\leqslant$100 nm are achievable, while the lateral localization precision in the 10 nm range is largely preserved, when the defocus is slight and handled carefully.

5 Further Outlook and Conclusion

5.1 Generalization of Post-Localization Algorithms

Although quantification approaches in SMLM seem to be logical and straight forward, the field is far away from consistency. When one deals with biological target structures, as almost always in SMLM no two samples are alike. Clearly, there are conceptual and structural similarities, especially in the field of clustering proteins, but still after over a decade of SMLM no gold standard on how to analyze disperse or clustered localization data has been established.

Furthermore, the very basic idea of how to determine localization precision or the actual spatial resolution in a given SMLM data set is far from being generalized.

To truly claim SMLM as the prime candidate for *quantitative* super-resolution microscopy, standards have to be defined and adhered to. Naturally, not the dogmatic predefinition of the methods exclusively allowed for post-localization analysis purposes has to be the goal, but rather the minimally required techniques. As an example, there should be an agreement on what analysis steps are at least required to make statements about the nature of nanodomains, or clusters, with a standardized way to perform the analysis *and* report the results. Surely every more sophisticated step afterwards is welcome, once the minimum is fulfilled.

Furthermore, in the case of meta-analysis and particle-averaging methods, the community should think about equal requirements on methodical standards like sample sizes and data quality preconditions on when it is warranted to perform such analyses. As long as different users reach diverging conclusions when analyzing the exact same data sets, one cannot truly speak of a quantitative science.

5.2 Screening the SMLM Archives for hidden Gems

Since the release of TRABI there was a small but steady input from researchers across the globe who had inquiries about specific applications of the algorithm to their, mostly already existing, SMLM data. So it seems fair to assume that TRABI is actually applied to at least some two-dimensional SMLM data sets.

Taken into account how fast the field of super-resolution in general and SMLM in particular has grown during the last decade with over 2500 and 1500 published manuscripts respectively (see Fig. 5.1 [99][100]) it is conceivable that in the tens of thousands of (un-) published 2D SMLM data sets some concealed gems of structural information are existing.

Reanalyzing a promising fraction of those data sets could untangle valuable 3D information, previously flatly projected, leading to a complete new interpretation of the data and the underlying structure.

Furthermore, if nothing else, the awareness of researchers for the inherently three-dimensional nature of almost every biological structure could be enhanced, resulting in more sensible treatment of samples and data in SMLM.

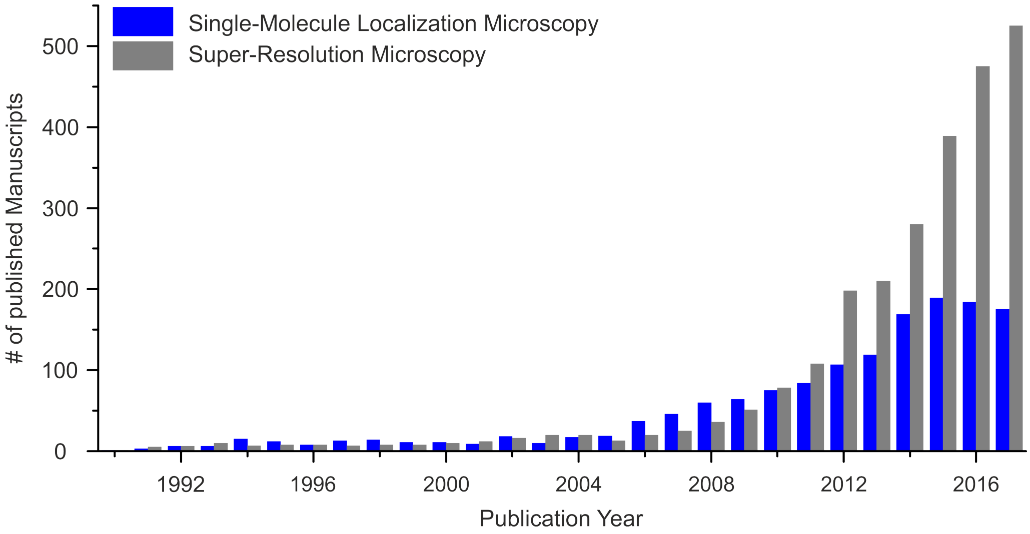

Figure 5.1: Progression of the fields of super-resolution (grey) in general and single-molecule localization microscopy (blue) in particular, regarding the number of papers published each year since 1990 on the basis of a thematic key word search [99][100].

5.3 TRABI combined with *soft* Astigmatism

As I discussed in chapter 3.2 and is shown in **P6**, TRABI can be advantageously combined with a Biplane imaging scheme to break the symmetry around the focal plane in the P-curve and thereby obtain unique, quantitative axial coordinates.

Another relatively straight forward approach would be to combine single plane TRABI imaging with a weak cylindrical lens in the detection path, hence introducing a slight astigmatism to the PSF. As discussed in chapter 1.1.2, astigmatism is commonly used in SMLM to create a z-dependent PSF shape divergence. Since single plane TRABI is already more axially sensitive as the FWHM based approaches, the additional ellipticity information could be used to solely determine wether a fluorophore is above or below the focal plane, or even in correlative combination of both independently calculated z positions (from TRABI and astigmatism) to achieve an improved axial precision and range.

Preliminary results show that the TRABI performance is not affected by the asymmetry of astigmatic PSFs, which is to be expected since the intensity estimation process does not rely on fitting or shape determination.

One could also think of aperture shapes that are not circles or other (a-)symmetrical patterns, therefore further encoding the photon redistribution out of focus, e.g. induced by astigmatism.
In that context, it seems logical also to explore combinatory approaches with other, more sophisticated PSF engineering techniques to further broaden the scope of TRABI and photometric SMLM. Also, direct analytical fitting of the complex shape of $out\ of\ focus$ PSFs could be beneficial for 3D SMLM if computationally sensible (see section 5.5).

5.4 Understanding the SMLM PSF

The PSF of a microscope does not follow a Gaussian. Naturally this fact is very well known, but still, in the field of SMLM it is largely assumed, that fitting an easy to handle two-dimensional Gaussian to the emission pattern provides a sufficient measure of its center of mass. Especially when dealing with more or less *in focus* signal, the centroid coordinate of a PSF can be derived with a two-dimensional Gaussian with very high precision and accuracy [27].
Nevertheless, TRABI has revealed, that even *in focus* PSFs exhibit substantial photonic deviation from a 2D-Gaussian. Furthermore, a master student of mine, Franz Xaver Engelmayer, working on the characterization of TRABI, showed that especially in the range of ±500 nm around the focal plane the experimental PSF can be better approximated by the superposition of two dependent Gaussians [101].

Additionally we are investigating the effects of EMCCD and sCMOS cameras, commonly used for SMLM, where complex noise distributions and A/D conversions can possibly affect the overall PSF.
For instance Jörg Enderlein (Universität Göttingen) suggested to us the possibility of the build up of strong coulomb potentials in the center of the PSF and of weaker in the PSF-exteriors, leading to an effective re-distribution of photons and therefore PSF reshaping. While this is currently under investigation, preliminary results indeed hint at a slight nonlinearity in lower photon regimes of EMCCD cameras.

Finally, we got additional insights in the *in focus* PSF of high NA microscopes very recently in collaboration with Bernd Rieger and Sjoerd Stallinga (Delft University of Technology). They are in the process of compiling a sophisticated PSF model, to precisely reconstruct the experimentally measured PSF, which diverges substantially from common theoretical models. Those simulations could be key to test AP, TRABI and Gaussian fitting with realistic *ground truth* data and also revealed a possible incompleteness of the simulations implemented for the original TRABI characterization.

As discussed in chapter 3.2.4, the analytical form of a PSF model was discretized and transformed to a two-dimensional pixel-coordinate distribution for random pseudo photon allocation. Due to practical working memory limitations the completely simulated PSF was hereby cut off after the second side minimum, preventing photons from entering further away region. When analyzing the unrestrained PSFs provided by Bernd and Sjoerd with AP, we could not reproduce a P value of 100% , at least not with the same radii as suggested, due to the broader distribution of photons in the exteriors of the PSF, but remained with a slight offset of ≈5% between ground truth and AP result.

At the time of conclusion of this thesis it remains to be seen how big of an impact this fact has on the overall performance of AP and TRABI, which is currently under investigation. Albeit, the P value originating from TRABI with reasonable radii settings might not reflect the *true* photon count of the entire emission distribution on the camera, but still remains closer to the truth in experimental data than intensity values from Gaussian fitting. Further, contrary to common Guassian fitters, TRABI gives robust z-independent intensity values. Also one has to consider the experimental limitations concerning the definition of a spot or PSF respectively. Photons might occur several micrometers away from the center of mass of an emission pattern, but cannot be allocated assuredly in a crowded photonic environment like a densely labeled biological sample.

Furthermore, the utilization of TRABI as a tool for three-dimensional imaging in general is not affected negatively by these findings, but rather will be further improved by any deeper understanding of the single-molecule PSF.

Finally, the model PSF still deviates substantially from experimentally measured emission patterns of isolated fluorophores in many ways, which will be subject of future investigations.

5.5 Customized Fitting Algorithms for photometric 3D Imaging

In light of the previous sections, it is worth mentioning that there is still much potential and need for improvement for modern day localization algorithms. This statement is valid both in itself and especially regarding photometric three-dimensional imaging and beyond. One consequence of the TRABI findings for me is the need for a customized fitting algorithm, which deviates substantially from the status quo of SMLM, i.e. fitting *one* singular Gaussian to every PSF to obtain its position in space.

Having shown that TRABI based on fixed FWHM fitting with standard software produces the best results in terms of three-dimensional localization precision and resolution, it seems straight forward to imagine an approach where at any spot a multitude of fits with a whole array of different parameter settings could be performed.

The simplest example would be fitting two independent Gaussian functions with fixed FWHMs to the exact same spot, where one would serve as the inner and the other as the outer *aperture* for intensity determination. To date, this simple approach is not straight forward to achieve with existing localization software, without sequentially plugging the parameter set into the software and relating the results afterwards.

Approaches with three or even more apertures ([35][102]), here based on fixed FWHM fitting, are only consequential to accurately scale the PSF photometrically with any degree of detail.

Another, already existing, idea would be the exact approximation of spots by complicated PSF models, thereby either directly fitting all three spatial coordinates to the spot, or obtaining a precise photometric value for the whole PSF. Recent work has shown, that more convenient fitting models like cubic splines can capture the shape of any PSF with great accuracy, while being computationally much cheaper than fully analytical PSF models [103].

There are many possibilities to choose from when fitting functions to emission patterns, whether complicated full analytical models or simplistic shapes as cones, cylinders or slightly more funky ones like urns or vases. All could lead to an improvement in axial range or intensity determination precision in the end. Surely, it will be seen which approaches emerge as best compromise between applicability, range and precision.

5.6 Closing Remarks

"Alles sehen ist perspektivisches Sehen."

Today, super-resolution microscopy provides one of the most versatile and powerful toolboxes to investigate biological questions on an array of scales, from whole animal studies to nanometer protein assemblies.
SMLM protrudes within the growing realm of non-diffraction limited microscopic techniques because it exclusively allocates molecular information *per definitionem*. As a consequence, SMLM can be utilized as high resolution imaging tool as well as instrument for truly quantitative microscopy.

In this thesis I presented a variety of different approaches to quantitative SMLM, ranging from straight forward isolated cluster analyses to multi-level meta-analyses of large scale multi-protein complexes.
As I have shown repeatedly, crafty post-localization algorithms can reveal structural information beyond the superior resolution capabilities of SMLM as well as providing an unbiased perspective of the information content of localization data.
The analysis of the SMLM PSF is far from conclusion and it will spawn novel and superior techniques to scale the four-dimensional single molecule space in biological samples.

Nevertheless, absolute quantification of protein numbers and spatial organization of emitters remains challenging and is often casually done. The more sensitive the interpretation of single-molecule data and their biological consequences are, the more tedious the control experiments and analyses have to be. SMLM gives researchers the unique possibility to get molecular information with high spatio-temporal resolution and will therefore remain among the prime techniques for biological research.

However, since there is no absolute, but rather only circumstantial truth, SMLM results have to be reported as a snapshot from the parametric space in which they reside in. If we accomplish a measure of generalization on minimal standards for sample preparation, imaging proceedings and data analysis, we could clear the way for true quantitative super-resolution.

Appendices

A Acronyms & Abbreviations

2D	Two-Dimensional
3D	Three-Dimensional
ADC	Analog to Digital converter Counts
ADT	Anderson Darling Test
AP	Aperture Photometry
BG	Background
BP	Biplane
CE	Central Element
CEmD	Critical Emitter Density
CED	Canny Edge Detector
CLEM	Correlative Light and Electron Microscopy
CLSM	Confocal Laser Scanning Microscopy
CMOS	Complementary Metal-Oxide-Semiconductor
DBSCAN	Density-Based Spatial Clustering of Applications with Noise
DLA	Diffraction Limited Area

***d*STORM**	*direct* Stochastic Optical Reconstruction Microscopy
EM	Electron Microscopy
EMCCD	Electron Multiplying Charge-Coupled Device
EZ	Exclusion Zone
FMM	Functional Membrane Micro-domains
FRET	Förster Resonance Energy Transfer
FW	Fit Window
FWHM	Full Width at Half Maximum
JIF	Jeff's Image Format
LE	Lateral Element
MCA	Mean Component Analysis
NA	Numerical Aperture
NN	Nearest Neighbor
NPC	Nuclear Pore Complex
PAFP	Photo-Activatable Fluorescent Protein
PALM	Photoactivated Localization Microscopy
PBS	Phosphate Buffer Saline
PSF	Point Spread Function
sCMOS	Scientific CMOS
SEM	Scanning Electron Microscopy

SIM	Structured Illumination Microscopy
SMLM	Single-Molecule Localization Microscopy
SNC	Synaptonemal Complex
STED	Stimulated Emission Depletion
STORM	Stochastic Optical Reconstruction Microscopy
TF	Transversal Filament
TRABI	Temporal Radial Aperture Based Intensity estimation
UV	Ultraviolet
WGA	Wheat Germ Agglutinin

B Manuscripts

In the following section all published manuscripts are reproduced in the original typeset from the publishing journal, together with the accordance form from every co-author.

Dipl. – Phys. Christian Franke
Lehrstuhl für Biotechnologie und Biophysik
Biozentrum, Am Hubland
97074 Würzburg
Germany

Würzburg, 4th July 2017

Manuscript:

Sebastian van de Linde, Sarah Aufmkolk, Christian Franke, Thorge Holm, Teresa Klein, Anna Löschberger, Sven Proppert, Steve Wolter, and Markus Sauer.

Investigating cellular structures at the nanoscale with organic fluorophores.

Chemistry & Biology, 20(1):8-18, 2013.

The contributions of the PhD candidate Christian Franke to the above manuscript involved:

- Compilation and supplementation of raw data
- Discussion of the manuscript draw

Christian Franke

Sebastian van de Linde

Sarah Aufmkolk

Thorge Holm

T. Klein

Teresa Klein

Löschberger

Anna Löschberger

Sven G. Propp

Sven Proppert

Steve Wolter

Markus Sauer

Chemistry & Biology
Review

Investigating Cellular Structures at the Nanoscale with Organic Fluorophores

Sebastian van de Linde,[1] Sarah Aufmkolk,[1] Christian Franke,[1] Thorge Holm,[1] Teresa Klein,[1] Anna Löschberger,[1] Sven Proppert,[1] Steve Wolter,[1] and Markus Sauer[1,*]
[1]Department of Biotechnology and Biophysics, Biozentrum, Julius-Maximilians-University Würzburg, Am Hubland, 97074 Würzburg, Germany
*Correspondence: m.sauer@uni-wuerzburg.de
http://dx.doi.org/10.1016/j.chembiol.2012.11.004

Super-resolution fluorescence imaging can provide insights into cellular structure and organization with a spatial resolution approaching virtually electron microscopy. Among all the different super-resolution methods single-molecule-based localization microscopy could play an exceptional role in the future because it can provide quantitative information, for example, the absolute number of biomolecules interacting in space and time. Here, small organic fluorophores are a decisive factor because they exhibit high fluorescence quantum yields and photostabilities, thus enabling their localization with nanometer precision. Besides past progress, problems with high-density and specific labeling, especially in living cells, and the lack of suited standards and long-term continuous imaging methods with minimal photodamage render the exploitation of the full potential of the method currently challenging.

Single-Molecule-Based Localization Microscopies with Organic Fluorophores

Since the first synthesis of fluorescein by Baeyer in 1871 (Baeyer, 1871) organic fluorophores have been successfully used in different disciplines and continuously advanced highly sensitive fluorescence microscopy and spectroscopy techniques. Organic fluorophores are small, chemically modifiable, and can be used for stoichiometric labeling of almost any protein even in living cells (Fernández-Suárez and Ting, 2008; Giepmans et al., 2006; Miller and Cornish, 2005). Although the optical resolution is limited (Abbe, 1873), fluorescence microscopy is the method of choice to study cellular architecture and dynamics in a comparatively noninvasive way.

Increasing detection sensitivity enabled single-molecule fluorescence spectroscopy and imaging experiments, which revealed spectroscopic phenomena that had previously been hidden in ensemble experiments because of averaging. One of the most surprising results of early single-molecule spectroscopy experiments was fluorescence intermittency or blinking (Moerner and Orrit, 1999; Tinnefeld and Sauer, 2005), that is, the random interruption of fluorescence emission of a single fluorophore as a direct consequence of the observation of a single quantum system with discrete fluorescent and nonfluorescent states. Simultaneously, it became clear that the position of single fluorophores can be determined by fitting the emission pattern with suitable model functions at which the localization precision depends mainly on the number of collected photons N and on the standard deviation of the PSF (σ), and can be roughly approximated by $\sigma/N^{1/2}$ for negligible background (Mortensen et al., 2010; Thompson et al., 2002). Because of the high brightness and photostability, typically thousands of photons can be detected from an individual organic fluorophore before it photobleaches, thus allowing its localization with nanometer accuracy (Yildiz and Selvin, 2005). Through this, it became possible to perform ultra-high-resolution colocalization studies of two fluorophores exhibiting distinctive spectroscopic characteristics, for example, fluorescence spectra or lifetime (Churchman et al., 2005; Heilemann et al., 2002; Lacoste et al., 2000; Pertsinidis et al., 2010).

Single-molecule-based localization microscopy methods, such as photoactivated localization microscopy (PALM) (Betzig et al., 2006; Shroff et al., 2008), fluorescence photoactivation localization microscopy (FPALM) (Hess et al., 2006), stochastic optical reconstruction microscopy (STORM) (Bates et al., 2007; Rust et al., 2006), and *direct* STORM (*d*STORM) (Heilemann et al., 2008; van de Linde et al., 2011b), use wide-field microscopes equipped with laser light sources for irradiation and sensitive detectors, for example, charge-coupled device cameras for fluorescence detection. Fundamentally, these methods live on the temporal separation of fluorescence emission of single fluorophores, for which reason the utilization of photoswitches is a prerequisite. Whereas in PALM and FPALM experiments the fluorophores are photoconverted from an initially dark or blue-shifted state, in STORM and *d*STORM all bright fluorophores must be transferred to a reversible OFF state at the beginning of the experiment. The primary information readout lies in stochastic activation and detection of individual fluorophores, for example, upon irradiation with light of appropriate wavelength and intensity. If the probability of activation is sufficiently low, the majority of activated fluorophores residing in their fluorescent ON state are spaced further apart than the diffraction limit and their positions can be precisely localized. This cycle of photoactivation and readout is repeated to record thousands of images in time. A super-resolution image is finally reconstructed from all single-molecule localizations (typically several ten thousands to millions of localizations) (Figure 1). Although PALM and FPALM use photoactivatable or photoconvertible fluorescent proteins, STORM and *d*STORM as originally introduced, exploit reversible photoswitching of carbocyanine dyes, such as Cy5 and Alexa Fluor 647 (hereafter denoted as Alexa647), between an ON and OFF state with (Rust et al., 2006) or without (Heilemann et al., 2008) a second activator

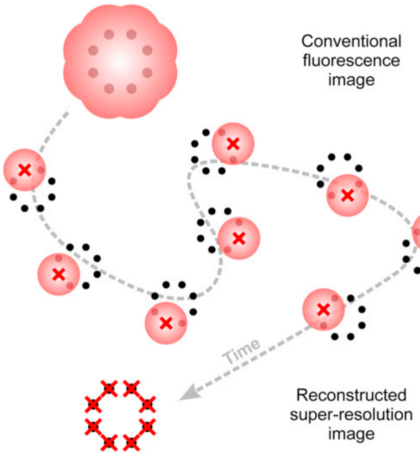

Figure 1. Principle of Localization Microscopy Using Photoswitchable Organic Fluorophores

A structure of interest (black dots) is labeled with photoswitchable fluorophores. The point-spread-functions (red) of the fluorophores overlap and generate a conventional fluorescence image of the structure. The majority of fluorophores is then transferred to a reversible OFF state, and only a sparse subset of fluorophores, optionally activated by light of the appropriate wavelength, is switched on stochastically and thus spatially separated in time. Ideally, every fluorophore is switched on and localized individually at least once. Finally, a super-resolution image is reconstructed from all single-molecule localizations.

dye (e.g., Cy3) in the presence of millimolar concentrations of thiols.

An alternative, elegant method of single-molecule-based localization microcopy is points accumulation for imaging in nanoscale topography (PAINT) (Sharonov and Hochstrasser, 2006) or universal PAINT (uPAINT) (Giannone et al., 2010). Here, transient binding events of single fluorescent probes to a structure are detected, localized, and finally used for reconstruction of a super-resolved reactivity map. Furthermore, single catalytic conversions of fluorogenic probes at active sites of a catalyst (termed NASCA, i.e., nanometer accuracy by stochastic catalytic reactions microscopy) have been exploited successfully to reconstruct diffraction unlimited reactivity maps of catalytic particles (Roeffaers et al., 2009).

Before stochastic single-molecule localization methods evolved, far-field super-resolution imaging was already achieved in a deterministic way, that is, by illuminating a sample with a defined light pattern, such as in stimulated emission depletion (STED) (Klar et al., 2000) or in structured illumination microscopy (SIM) (Gustafsson, 2000). Both methods were successfully used for live-cell subdiffraction resolution imaging with impressive temporal resolution (Kner et al., 2009; Nägerl et al., 2008). To get an overview of all the different methods and aspects of super-resolution fluorescence imaging, we would like to refer the reader to some recent excellent reviews and general guides (Diaspro, 2010; Flors, 2011; Galbraith and Galbraith, 2011; Heilemann et al., 2009a; Hell, 2009; Henriques et al., 2011; Huang et al., 2010; Ji et al., 2008; Patterson et al., 2010; Schermelleh et al., 2010; Toomre and Bewersdorf, 2010; van de Linde et al., 2012; Vogelsang et al., 2010). Here, we limit our report and discussion to organic fluorophores, their photoswitching mechanism, and advantageous use in localization microscopy in fixed and living cells and the potential use of localization microscopy for quantification of biomolecules, including the necessity of efficient reference structures. We conclude with an outlook on future developments, such as improved labeling methods, which are required to fully exploit the potential of single-molecule-based localization microscopy methods.

Photoswitching of Organic Fluorophores

One of the central cornerstones of single-molecule-based localization microscopy is the transfer of the majority of organic fluorophores—residing initially in their fluorescent ON state—to the OFF state, meanwhile guaranteeing that every fluorophore is separately localized at a particular time during data acquisition. As a rule of thumb, localization microscopy requires that the OFF state has to be substantially longer than the average ON state lifetime of the fluorophores (Heilemann et al., 2009b; Vogelsang et al., 2010). The more complex the structure, the more fluorophores are needed to accurately resolve the structure, that is, the more fluorophores have to reside simultaneously in the OFF state, implicating that the ratio of ON/OFF lifetimes has to be adapted accordingly. Hence, complex structures require easily OFF state lifetimes in the range of hundreds of milliseconds to several seconds.

Because semiconductor nanocrystals (so-called quantum dots) show excitation intensity-dependent blinking, they have been used in first localization microscopy experiments (Lidke et al., 2005). However, although the blinking process of quantum dots can be assumed to be statistically independent, their blinking characteristics occur on fast timescales, that is, their ON/OFF ratio renders super-resolution imaging based on single-molecule localizations complicated. Similarly, the triplet state of organic fluorophores with lifetimes of a few microseconds (Drexhage, 1973; Sauer et al., 2011) under physiological conditions cannot be used as OFF state for super-resolution imaging. To prevent quenching of the triplet state by molecular oxygen and increase the lifetime of the OFF state, organic fluorophores can be embedded in polyvinyl alcohol (PVA), which is known to exhibit a low oxygen permeability (Zondervan et al., 2003). Under these conditions, 94% of all Cy5 molecules of a sample could be transferred to an OFF state at a time enabling super-resolution imaging of the microtubule network in fixed cells (Bock et al., 2007). This concept has later been successfully transferred to other organic fluorophores and termed ground state depletion microscopy followed by individual molecule return (GSDIM) (Fölling et al., 2008).

A significant breakthrough in photoswitching of organic fluorophores was achieved in 2005 when two groups reported independently that carbocyanine fluorophores, such as Cy5 and Alexa647, can be switched between a bright ON and a long-lasting nonfluorescent OFF state upon irradiation with different wavelengths in the absence (Heilemann et al., 2005) (Figure 2) or presence of a second activator fluorophore (Bates et al., 2005). In these first photoswitching reports of organic fluorophores, the addition of millimolar concentrations of β-mercaptoethylamine (MEA) and oxygen removal using an enzymatic oxygen scavenging system was described as mandatory to achieve reversible photoswitching. The demonstration that

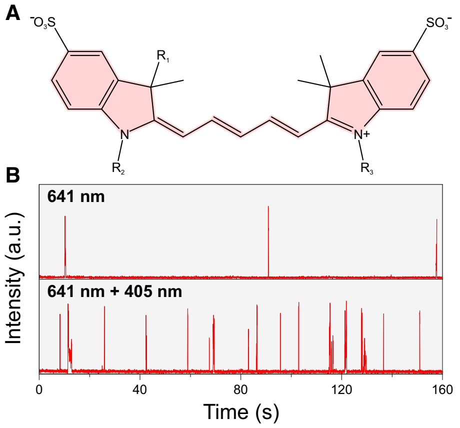

Figure 2. Photoswitching of Cyanine Dyes
(A) Basic chemical structure of carbocyanine dyes, such as Cy5 and Alexa647, which were the first conventional organic dyes used for photoswitching. Cy5-COOH: $R_1 = CH_3$, $R_2 = C_2H_5$, $R_3 = (CH_2)_5COOH$; Alexa647-COOH: $R_1 = (CH_2)_5COOH$, $R_{2,3} = (CH_2)_4SO_3^-$ (Terpetschnig et al., 2004).
(B) Fluorescence time traces of a single antibody labeled with Alexa647 under photoswitching conditions, that is, oxygen-depleted solution, 100 mM MEA (pH 7.4). Top: direct photoswitching of Alexa647 only with the readout wavelength at 641 nm. Bottom: direct photoswitching of Alexa647 with irradiation at 641 nm and with additional activation at 405 nm.

single Cy5 molecules can be cycled between an ON and OFF state more than 100 times with a reproducibility of over 90% at room temperature, ultimately formed the basis for the successful introduction of localization microscopy methods, such as STORM and *d*STORM.

As shown later (Heilemann et al., 2009b; Vogelsang et al., 2009) photoswitching under reducing conditions can be transferred to many other commercial standard fluorophores (Figure 3). The direct photoswitching behavior of organic fluorophores in the presence of millimolar concentrations of thiols in aqueous solution is caused by the redox properties of the fluorophores. That is, they share similar redox potentials and can therefore be reduced by thiols upon excitation entering a stable reduced OFF state with a lifetime easily exceeding several seconds. Importantly, the first excited singlet state of the fluorophores is not reduced (quenched) by thiols. It is the deprotonated form of thiols (i.e., thiolates) that can selectively reduce the triplet state of organic fluorophores forming a radical anion with absorption maxima at ~400–500 nm and possibly the fully reduced leuco form of the fluorophore (van de Linde et al., 2011a).

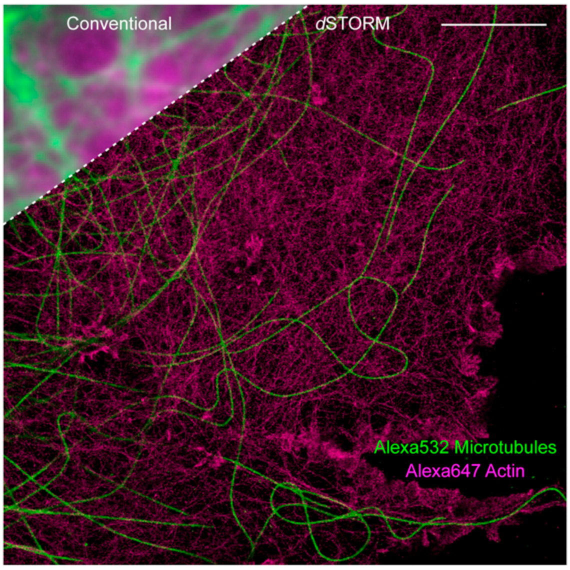

Figure 3. Dual-Color *d*STORM in Fixed Cells
Fixed COS-7 cells were labeled with primary mouse antibodies against β-tubulin and Alexa532-labeled goat anti-mouse secondary antibodies (green). Actin was labeled using Alexa647 phalloidin (magenta). Sequential *d*STORM imaging was performed in 100 mM MEA (pH 8.3). Direct photoswitching of Alexa647 and Alexa532 was performed by irradiating the fluorophores with ~5 kW cm^{-2} at 641 nm and 532 nm, respectively. No additional activation at a shorter wavelength was used. Channel alignment was performed with 100 nm multifluorescent beads (TetraSpeck, Invitrogen, Carlsbad, CA, USA). The upper left corner shows a part of the conventional wide-field fluorescence image. Scale bar: 5 μm.

This underlying photoswitching process can be described by the following mechanism (Figure 4): upon excitation, the fluorophore cycles between the singlet ground-state and the first excited singlet state and emits fluorescence photons dependent on its fluorescence quantum yield. Once intersystem crossing occurs, the resulting triplet state can be either quenched by molecular oxygen producing singlet oxygen and repopulating the singlet ground state or by the thiolate generating the thiyl radical and corresponding fluorophore radical anion. The efficiency of the reactions is controlled by the redox properties of the fluorophore, the thiol and oxygen concentration, and the pH value of the solvent. Here, it is beneficial if the fluorophore is cycled several times between singlet ground, excited singlet, and triplet state in order to enable the detection of as many photons as possible before the triplet state is reduced by the thiolate and a very stable OFF state with lifetime of seconds to minutes is generated. Some fluorophores with pronounced electron affinity, such as methylene blue, or some oxazine dyes, such as ATTO 655 or ATTO 680, have the tendency to accept a second electron and form the colorless fully reduced leuco dye (Kottke et al., 2010; van de Linde et al., 2011a). The photoswitching cycle is finally completed and the singlet ground state recovered upon oxidation of the reduced fluorophore with molecular oxygen. Thus, molecular oxygen plays two important roles through (1) quenching the triplet state, enabling the detection of enough photons for precise localization, and (2) oxidizing the radical anion or leuco dye and recovering the fluorescent ON state. In addition, recovery of the ON state is also promoted by direct excitation of the radical anion at, for example, 405 nm (van de Linde et al., 2011a, 2011b). Furthermore, it has to be considered that several efficient oxygen consuming steps are involved in the reaction mechanism for radical anion formation and decomposition.

These very sensitive dependencies of the photoswitching rates on pH and oxygen and thiol concentration might also explain discrepancies reported in super-resolution imaging experiments using the same fluorophore attached to different

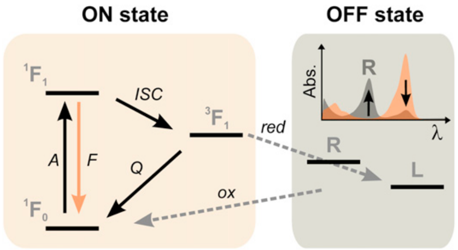

Figure 4. Photoswitching of Organic Fluorophores under Reducing Conditions
Upon irradiation, the fluorophore is cycled between the singlet ground $^1F_0$ and first excited state $^1F_1$. (A, absorption; F, fluorescence emission). Through intersystem crossing (ISC) the triplet state ($^3F_1$) is populated, which can be quenched by either molecular oxygen (Q) or appropiate reducing agents (red), such as thiols, and a reduced fluorophore radical (R) is generated. Some fluorophores can accept a second electron to create the fully reduced leuco form (L). Both can be oxidized again to the singlet ground state of the fluorophore (ox). Upper right corner: if a fluorophore radical is formed, an additional blue-shifted absorption band appears around 400 nm for most rhodamine derivatives (Abs., absorbance; λ, wavelength).

antibodies or cellular structures or under different buffer conditions. Unfortunately, the described mechanism cannot explain all possible reaction pathways, for example, the possibility of the formation of a carbocyanine thiol-adduct (Dempsey et al., 2009). However, if a thiol-adduct or leuco dye is formed the chromophoric system of the fluorophore is interrupted and absorption at ~400–500 nm disappears completely. Fluorophore radical anions, on the other hand, show strong and broad absorption bands at these wavelengths, justifying light-induced switchability in both directions. Moreover, one has to consider that mechanistic photophysical studies at the ensemble level are performed under lower irradiation intensities, whereas localization microscopy experiments are typically performed with high excitation intensities of several kW cm^{-2}, which might influence the dark state formation mechanism at the single-molecule level.

Because the OFF state exhibits a broad absorption band, recovery of the ON state succeeds also upon direct excitation of the fluorophore, for example, Cy5 at 640 nm albeit with low efficiency (Figure 2). Hence, one should always keep in mind that the use of high readout irradiation intensities likewise promotes recovery of the ON state. Furthermore, the emission of one fluorophore can also have a low probability to recover adjacent fluorophores residing in the OFF state, especially in densely labeled samples. Early STORM experiments always used a shorter wavelength absorbing fluorophore as activator tagged in close proximity (~2 nm) to the photoswitchable reporter fluorophore Cy5 or Alexa647 (Bates et al., 2007; Rust et al., 2006). Upon direct excitation of the activator fluorophore excited-state energy can potentially be transferred radiationless to the OFF state of the reporter fluorophore located in close proximity whereby the ON state is recovered. Direct photoswitching without the use of an activator dye, such as in *d*STORM, necessitates slightly higher but still very low irradiation intensity at ~400–500 nm of typically a few hundred μW to recover the fluorescent ON state (Heilemann et al., 2008). Both approaches have their advantage; *d*STORM eases label procedures (Heilemann et al., 2008; van de Linde et al., 2011b), whereas STORM with different activator-reporter dye pairs can be used for chromatic aberration-free multicolor super-resolution imaging as long as unspecific reactivation events of the reporter dye are excluded (Dani et al., 2010).

In summary the photoswitching mechanism can be very likely described by excitation of fluorophores and population of their triplet states, followed by reduction, for example, with thiols to generate a stable radical anion and subsequent (photo-induced) oxidation to recover the ground state, for example, with molecular oxygen. Hence, from the mechanistic point of view, the underlying photoswitching mechanism can be well generalized under the acronym RESOLFT, which stands for reversible saturable optical fluorescence transitions (Hell, 2007; Hofmann et al., 2005). From the chemical point of view, photoswitching of organic fluorophores as used in localization microscopy is best described by the reducing and oxidizing system (ROXS), originally introduced to minimize blinking and photobleaching of organic fluorophores in single-molecule fluorescence microscopy experiments (Vogelsang et al., 2008). Using ROXS, the time the fluorophore spends in the triplet state is first shortened, and a reduced radical is formed, which is subsequently oxidized to efficiently recover the singlet ground state. Thus, the fluorophore is predominantly cycled between singlet ground and first excited singlet-state, and by collecting as many photons as possible, stable fluorescence emission is obtained. This can be achieved by the addition of a reducing agent, such as ascorbic acid, and an oxidizing agent, such as methylviologen, in an oxygen-depleted solution. However, through the fine adjustment of the concentration of oxidizing and reducing agents, prolonged OFF state lifetimes can be created, which are suitable for localization microscopy (introduced as ‘‘blink microscopy’’) (Ha and Tinnefeld, 2012; Steinhauer et al., 2008; Vogelsang et al., 2009). Accordingly, the term ‘‘active-control’’ of the photoswitching behavior of fluorophores represents an unifying description of the different localization microscopy methods (Thompson et al., 2012).

Live-Cell Localization Microscopy with Organic Fluorophores

The photoswitchability of many organic fluorophores in living cells is caused by the cellular redox environment, particularly due to the presence of the most abundant redox couple, the glutathione disulfide (GSSG)-glutathione (GSH) couple. On average, the GSH concentration in the cytosol is 1–11 mM, which is far higher than that of most other redox-active compounds (Schafer and Buettner, 2001; Smith et al., 1996). That is, living cells naturally contain a redox cocktail for photoswitching of organic fluorophores (van de Linde et al., 2012; Wombacher et al., 2010). In addition, the redox potential not only varies between different cell lines but also differs within structures in a cell with the mitochondria containing the most reductive GSH/GSSG pool (Jones, 2010).

Because fluorescent proteins (FPs) can be genetically fused to target proteins and thus provide straightforward access to specific and stoichiometric labeling, photoactivatable FPs were the first choice of fluorophores for live-cell localization microscopy (Biteen et al., 2008; Hess et al., 2007; Manley et al., 2008; Shroff et al., 2008). On the other hand, FPs have in general a lower fluorescence quantum yield and photostability than organic fluorophores for which reason so far only a few suitable photoactivatable FPs, such as PAGFP, PAmCherry, PAtagRFP, and EosFP, have been used successfully for (multicolor) live-cell localization microscopy (Cella Zanacchi et al., 2011; Hess et al., 2007; Shroff et al., 2007; Subach et al., 2009, 2010). Organic fluorophores exhibit important photophysical advantages over FPs for molecular localization microscopy, such as they emit orders of magnitude more photons because they survive under moderate excitation conditions for prolonged time periods, exhibit tunable photoswitching rates, and can be imaged repeatedly. Unfortunately, specific and stoichiometric labeling of proteins in living cells with organic fluorophores is more demanding.

Even though genetic tags enable the fusion of a genetically encoded polypeptide to a protein of interest that can subsequently be labeled with organic fluorophore ligands (Fernández-Suárez and Ting, 2008; Keppler et al., 2003; Miller and Cornish, 2005), specific binding of fluorophore-labeled ligands to fusion proteins in living cells remains challenging and requires careful optimization and control experiments. However, the convenient combination of genetic tag, organic fluorophore, and target protein enables live-cell localization microscopy. First demonstrations of live-cell experiments include super-resolution imaging and tracking of H2B histone proteins with trimethoprim tags (TMP-ATTO 655) (Wombacher et al., 2010) and SNAP-tags (SNAP-Cell TMR-Star and SNAP-Cell 505) in various cell lines (Klein et al., 2011), transferrin with the fluorophore pair Alexa405-Alexa647, and clathrin light chain with SNAP-tag (Alexa647) (Jones et al., 2011). Because Alexa647 exhibits no cell permeability, the SNAP substrate BG-Alexa647 has been delivered by electroporation. Imaging has been performed by adding β-mercaptoethanol to support photoswitching and an oxygen scavenger system to reduce photobleaching of the carbocyanine dye (Jones et al., 2011). The irradiation intensities at the sample used in these first successful realizations of live-cell localization microscopy varied between 2 kW cm^{-2} (Klein et al., 2011) and 15 kW cm^{-2} (Jones et al., 2011). For multicolor live-cell super-resolution imaging and tracking experiments different combinations of genetically encoded tags (SNAP-, Halo-, CLIP-tags) (Figure 5) and organic fluorophores (Alexa488, Dy-488, Oregon Green, TMR, Dy-547, Alexa647, Dy-647) have been successfully used also in combination with photoactivatable FPs (Appelhans et al., 2012; Benke et al., 2012; Klein et al., 2012; Wilmes et al., 2012).

Here, it has to be pointed out that inefficient or nonspecific labeling often observed in super-resolution imaging experiments with organic fluorophores and genetic tags are mainly caused by the structure of the organic fluorophores. Dependent on their charge and water solubility, they exhibit different cell permeability and tend to agglomerate or stick nonspecifically to cellular organelles. For example, negatively charged organic fluorophores, such as fluorescein, Alexa488, Cy5, or Alexa647, exhibit satisfactory water solubility but almost no cell permeability, hence restricting their use to cell membrane labeling. Or alternatively, for inside cell labeling electroporation techniques have to be applied (Jones et al., 2011). On the other hand, the sticking of positively charged rhodamine derivatives can be used advantageously as "MitoTracker" and "LysoTracker" for nonspecific labeling of mitochondria and lysosomes, respectively, in living cells. Therefore, dynamic super-resolution imaging of organelles in living cells is possible with many standard membrane probes (Shim et al., 2012).

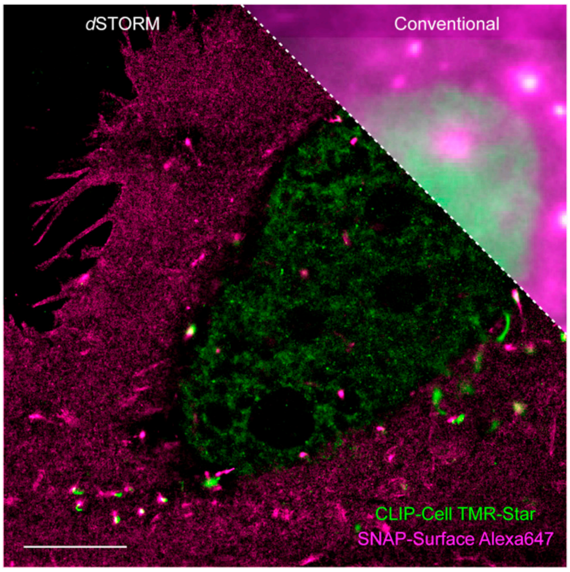

Figure 5. Live-Cell Dual-Color *d*STORM Using SNAP- and CLIP-Tags
U2OS cells were transiently transfected with pSNAPf-ADRβ2 (β-2 adrenergic receptor, magenta) and pCLIPf-H2B (core histone protein, green) and stained with SNAP-Surface Alexa Fluor 647 and CLIP-Cell TMR-Star. To allow switching of Alexa647 outside of the membrane, the medium was exchanged to 100 mM reduced glutathione, 5% glucose, 4 units/ml glucose oxidase, and 80 units/ml catalase (pH 7.9). Excitation intensities of ~1 kW cm^{-2} at 641 nm and 532 nm were used for sequential imaging of Alexa647 and TMR, respectively. The upper right part shows the conventional wide-field fluorescence image. Alignment of the two channels was performed with 100 nm multifluorescent beads. Scale bar: 5 μm. Reproduced from Klein et al. (2012) with permission, © Wiley-VCH Verlag GmbH & Co. KGaA, 2012.

Resolving fast cellular dynamics with high spatial resolution can only succeed if the number of truly localized fluorophores per time is high enough (Shroff et al., 2008). According to information theory, the required density of fluorescent probes must be high enough to satisfy the Nyquist-Shannon sampling theorem (Patterson et al., 2010; Shannon, 1949; Shroff et al., 2008). A single-molecule data stack (e.g., 10,000 frames acquired in 100 s) is usually divided in time interval subgroups. Thus, the size defines the temporal resolution at which a cellular process can be observed (e.g., 1,000 frames corresponding to 10 s temporal resolution). Reducing this time interval will increase the temporal resolution, but to obtain the same spatial resolution an equal amount of molecules must be localized. This can be achieved through accelerating the fluorophores ON/OFF cycle by applying higher laser intensities for readout and activation at the risk of photodamage (Shroff et al., 2008). Alternatively, the fluorophore density can be increased. Importantly, the performance of most single-molecule localization algorithms depends heavily on the emitter density with a throughput well below one molecule per μm^2 per frame (Wolter et al., 2011). Increasing the emitter density therefore results in erroneously analyzed overlapping PSFs. These localization errors are included as artifacts in the final super-resolution image and can lead to unresolved features and misinterpretation. Current promising approaches try to analyze overlapping PSFs, such as DAOSTORM (Holden et al., 2011) and compressed sensing (Zhu et al., 2012), thus increasing the total tolerable fluorophore density up to 10 molecules per μm^2.

Quantification and Reference Structures for Super-Resolution Imaging

What distinguishes localization microscopy from other imaging techniques is the fact that it builds up super-resolved images literally molecule-by-molecule. At first glance, one might intuitively suppose that localization microscopy allows counting the number of molecules in time and space and thus might revolutionize the field of molecular biology by quantitative understanding of cellular processes. Consequently, the fidelity of localization microscopy must be examined, which has only quite recently moved into the center of attention (Annibale et al., 2011; Bar-On et al., 2012; Gunzenhäuser et al., 2012; Itano et al., 2012; Lando et al., 2012; Owen et al., 2012; Sengupta et al., 2011; Veatch et al., 2012). Therefore, essential questions should be addressed concerning the label efficiency, the number of localizations per fluorophore, and the fraction of missing fluorophores.

A key factor of localization microscopy is to ensure that each fluorophore is detected individually above a certain threshold and thus precisely localized. Unfortunately, it is difficult to quantify the percentage of fluorophores we miss using a certain photon threshold due to, for example, fast photobleaching of the fluorophore. However, if the photon threshold is lowered excessively, the number of falsely identified localizations increases. These considerations argue for the use of organic fluorophores, which typically are brighter and more photostable than FPs. On the other hand, organic fluorophores complicate quantification because they are localized multiple times, whereas photoactivatable FPs are expected to be irreversibly bleached after photoactivation. But, even FPs can transiently switch off after activation and then later switch on again, a phenomenon that can lead to recounting of the same fluorophore (Annibale et al., 2010; McKinney et al., 2009). Because it is known that fluorophores change their switching performance dependent on environmental conditions (Endesfelder et al., 2011), ON/OFF switching control experiments with the aim to count the average number of localizations per fluorescent probe have to be performed in the same nanoenvironment, that is, in the same cellular compartment, but with very low numbers of active fluorophores to ensure the localization of individual fluorophores. Another factor that can confound quantification is that a single molecule is detected typically over more than one frame.

A possible strategy to account for these factors is to take advantage of the time dependence of photoswitching. This can be done by analyzing and adjusting the number of frames in which no fluorescent molecule appears within an area before events are counted as separate molecules (Annibale et al., 2011). Using techniques such as pair correlation, the blinking can also be directly factored into the analysis method (Sengupta et al., 2011; Veatch et al., 2012). Very recently, a procedure for counting of the centromere-specific histone H3 variant CENP-A^{Cnp1} by PALM in fission yeast has been developed. The study grouped multiple localizations and accounted for ON/OFF blinking demonstrating that each mEos2-tagged protein is localized on average twice under the applied experimental conditions (Lando et al., 2012).

Moreover, quantitative labeling of proteins has to be considered. Using classical immunocytochemistry with fluorophore-labeled antibodies for quantification of endogenous wild-type proteins is hampered by the fact that we usually do not know the binding constant of primary antibodies and the accessibility of proteins in their native environment. Furthermore, commercially available fluorophore-labeled antibodies generally exhibit a degree of labeling >1, and the number of secondary antibodies binding per primary antibody is unknown. Nevertheless, most unknown parameters, including the average number of localizations measured per fluorophore-labeled antibody, are accessible by elaborated control experiments.

FPs clearly have the edge over organic fluorophores because they can be genetically fused to the protein of interest. However, endogenous protein tagging has to demonstrate wild-type viability of cells, and uncertainties remain concerning the problem of maturation. Previous studies indicate that a certain fraction of FPs (~20%) remains dark or nonfluorescent because of missfolding (Garcia-Parajo et al., 2001; Ulbrich and Isacoff, 2007).

Although achieving super-resolution is now routine, quantitative data interpretation requires refined strategies and robust test samples to harness the full potential of localization microscopy. Test samples should allow us to measure the labeling efficiency and the percentage of detected molecules ideally in the same cellular environment and under identical experimental conditions. The development of test samples is of invaluable importance for calibration of super-resolution imaging microscopes and optimization of buffer conditions used to induce photoswitching of organic fluorophores. Suited test samples comprise DNA origami carrying fluorophores at well-defined positions (Steinhauer et al., 2009) as well as the single-molecule assembled patterns generated by cut-and-paste technology (SMCP) (Kufer et al., 2008, 2009). Recently, it has been shown that SMCP is well suited to generate artificial reference patterns with a defined number of emitters per diffraction limited region, for example, line patterns, which can be used to test the switching performance of organic dyes (Cordes et al., 2010).

Very recently, the nuclear pore complex (NPC) with its subdiffraction dimensions and 8-fold symmetry has been introduced as valuable biological test sample (Löschberger et al., 2012) (Figure 6). Using *d*STORM the 8-fold radial distribution of the integral membrane protein gp210 was resolved with an average diameter of 164 nm as well as the central channel with a diameter of 41 nm. This demonstrates that localization microscopy can achieve results that are comparable with those obtained by electron microscopy, although being less invasive. The combination of efficient antibodies and photoswitching of organic fluorophores proved to be highly reliable by confirming the 8-fold radial symmetry for the majority of all NPCs detected. Moreover, two-color super-resolution imaging experiments emphasize the highly symmetric NPCs as ideal model structures to control the quality of chromatic aberration corrections.

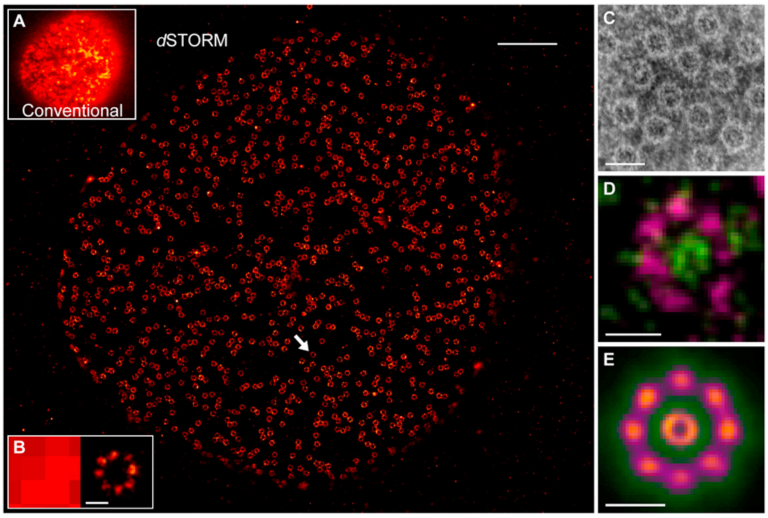

Figure 6. The Nuclear Pore Complex as Biological Reference Structure for Super-Resolution Microscopy
(A) The NPC anchoring proteins gp210 in *Xenopus laevis* A6 cells were labeled with the primary antibody Asc222a2 and Alexa647 goat anti-mouse F(ab')$_2$-fragments. Imaging was performed in oxygen-depleted solution containing 100 mM MEA (pH 7.8). A conventional fluorescence image of the bottom side of the nucleus is shown (inset).
(B) Magnified view of a single nuclear pore as marked in (A).
(C–E) NPCs in *X. laevis* oocytes. (C) NPCs as seen by electron microscopy using negative staining.
(D) Dual-color *d*STORM images of the NPC (gp210, magenta; central channel, green) using Alexa647-labeled antibodies and WGA-ATTO 520.
(E) Image analysis of accumulated NPC *d*STORM data from several hundred ring structures (gp210 and central channel). Scale bars: 2 μm (A), 100 nm (B), 150 nm (C), and 100 nm (D and E). (C)–(E) are reproduced from Löschberger et al. (2012) with permission, © Journal of Cell Science, 2012.

The Future Challenges of Molecular Localization Microscopy

Whereas the localization precision of single fluorophores is determined by the number of collected photons, the achievable resolution of complex biological structures is determined by the labeling density. That is, the higher the labeling density, the better the attainble structural resolution. With a size of ~1 nm, organic fluorophores are smaller than FPs but, unfortunately, require a chemical-labeling procedure. Frequently, immunofluorescence is used to label cellular structures in fixed cells using primary and fluorophore-labeled secondary antibodies. This method profits from a large repertoire of commercially available labeled secondary antibodies but has severe restrictions considering the size of immunoglobulin G antibodies of ~10 nm (Weber et al., 1978).

For standard fluorescence microscopy insignificant, the size of the fluorescent probe (e.g., antibody or pair of antibodies) can distort the size of cellular structures measured by localization microscopy. For example, the diameter of microtubules has often been determined to 40–50 nm using classical immunofluorescence labeling (Bates et al., 2007; Heilemann et al., 2008), much larger than the actual microtubule diameter of 25 nm (Weber et al., 1978). That is, the resolution of localization microscopy is so high that the size of the fluoresent probe has to be considered. Concerning the achievable structural resolution, a rough estimation illustrates the labeling challenge we have to accept: in accordance with the Nyquist-Shannon sampling theorem, a fluorophore-labeled antibody with a size of ~10 nm has to be attached directly side-by-side to a structure to ensure super-resolution imaging with a lateral resolution of 20 nm. Here, direct labeling of the primary antibody or the use of very small labeled camelid antibodies (nanobodies) directed against a green fluorescent protein (GFP) can improve the situation (Ries et al., 2012). However, FPs are also relatively large, with a typical size of 2–5 nm and a mass of ~27 kDa for most monomeric derivatives of GFP (Ormö et al., 1996). In addition, genetically encoded tags can cause significant perturbations to a protein's structure and have no direct extension to other classes of biomolecules, including lipids, nucleic acids, glycans, and secondary metabolites.

The ideal labeling method for super-resolution imaging uses small, bright, and photostable fluorophores, preferably attached directly to the molecule of interest. In recent years, an alternative tool for tagging molecules has emerged involving the incorporation of unique chemical functionality into a target molecule using the cell's own biosynthesis machinery (Prescher and Bertozzi, 2005). This so-called bio-orthogonal click chemistry has led to an explosion of interest in selective covalent labeling of molecules in cells and living organisms (Kolb et al., 2001; Laughlin et al., 2008; Prescher and Bertozzi, 2005). The labeling technology is founded upon a copper-catalyzed azide-alkyne cycloaddition but can also be used copper-free by employing ring strains as an alternative means for alkyne activation to improve biocompatibility (Agard et al., 2004). The two-step labeling process starts with the genetic or metabolic incorporation of azide or alkyne modified nucleotides, nucleosides, amino acids, monosaccharides, or fatty acids by living cells or organisms. Next, the reaction partner, that is, the complementary alkyne or azide linked to a fluorophore is "clicked" into place. The small size of azide and alkyne tags allows the functionalized substrates and fluorophores to be readily processed by enzymes, such as nucelotide polymerases and aminoacyl tRNA synthetases, and enables likewise a high labeling density as the key requirement for super-resolution imaging. First successful applications combined 5-Ethynyl-2′-deoxyuridine (EdU) labeling and *d*STORM for super-resolution imaging of DNA (Zessin et al., 2012).

Another problem that still needs to be sorted out to harness the full potential of localization microscopy is the three-dimensional (3D) reconstruction of whole cells or organisms. To minimize background signals, conventional methods localize individual fluorophores in a thin axial section predefined by the illumination method using either total internal reflection fluorescence (TIRF) microscopy to restrict excitation close to the coverslip or a highly inclined and laminated optical sheet (HILO) to generate an axially confined inclined beam for intracellular imaging (Tokunaga et al., 2008). In combination with defocusing approaches, such as dual or multi-focal-plane imaging or astigmatism localization, microscopy achieves an axial resolution of 50–80 nm over an axial range of $\sim$1 μm (Huang et al., 2008; Juette et al., 2008). Therefore, such 3D super-resolution images visualize always only a section of the cell's current biomolecule or flurophore distribution, respectively. In order to map the distribution of labeled biomolecules in whole cells or nuclei, long-term continuous imaging methods with minimal photodamage, such as selective plane illumination microscopy (SPIM) (Huisken et al., 2004) or Bessel beam plane illumination (Planchon et al., 2011), combined with localization microscopy techniques (Cella Zanacchi et al., 2011) have to be used. By moving the cell through the beam or the beam through the cell, respectively, the sample can be sectioned into axial areas suitable for 3D localization microscopy and a whole-cell super-resolution image can finally be reconstructed. Alternatively, confined activation of axial sections by two-photon laser scanning in combination with suited photoactivatable fluorophores can be applied to achieve whole-cell super-resolution imaging (Fölling et al., 2007; York et al., 2011). Such methods—efficient labeling with small fluorophores and quantitative localization—can truly revolutionize our current understanding of developmental biology processes, for example, stem cell differentiation or synaptic plasticity and usher in a new molecular era by counting the numbers of proteins or biomolecules present at different cell stages or upon stimulation, respectively.

However, we should always bear in mind that super-resolution images are today still difficult to validate because of our lacking experience. Cellular structures and biomolecule distributions have never before been observed with single-molecule sensitivity and resolution. All the knowledge, which has been collected so far about the molecular structure of cells, stems from electron microscopy images. To resolve all doubt about the significance of the measured data, we must perform correlative electron and localization microscopy experiments (Betzig et al., 2006). Furthermore, unspecific labeling of target proteins as well as the inappropriate acquisition and analysis of the single-molecule data stack can introduce artifacts in super-resolution images, which hamper the interpretation of so far unknown protein distributions. Hence, careful control experiments with biologically suited reference structures, such as the nuclear pore complex (Löschberger et al., 2012), have to be used for benchmarking localization microscopy data.

ACKNOWLEDGMENTS

We thank Georg Krohne for providing the Asc222a2 antibody and Michael Reil for preparing the A6 cells. Financial support from the Biophotonics Initiative of the Bundesministerium für Bildung und Forschung (BMBF; grant 13N11019) and the Deutsche Forschungsgemeinschaft (DFG; grant SA 829/8-1) is gratefully acknowledged.

REFERENCES

Abbe, E. (1873). Theorie des Mikroskops und der mikroskopischen Wahrnehmung. Arch. Mikr. Anat. *9*, 413–468.

Agard, N.J., Prescher, J.A., and Bertozzi, C.R. (2004). A strain-promoted [3 + 2] azide-alkyne cycloaddition for covalent modification of biomolecules in living systems. J. Am. Chem. Soc. *126*, 15046–15047.

Annibale, P., Scarselli, M., Kodiyan, A., and Radenovic, A. (2010). Photoactivatable fluorescent protein mEos2 displays repeated photoactivation after a long-lived dark state in the red photoconverted form. J. Phys. Chem. Lett. *1*, 1506–1510.

Annibale, P., Vanni, S., Scarselli, M., Rothlisberger, U., and Radenovic, A. (2011). Quantitative photo activated localization microscopy: unraveling the effects of photoblinking. PLoS ONE *6*, e22678.

Appelhans, T., Richter, C.P., Wilkens, V., Hess, S.T., Piehler, J., and Busch, K.B. (2012). Nanoscale organization of mitochondrial microcompartments revealed by combining tracking and localization microscopy. Nano Lett. *12*, 610–616.

Baeyer, A. (1871). Ueber eine neue Klasse von Farbstoffen. Ber. Dtsch. Chem. Ges. *4*, 555–558.

Bar-On, D., Wolter, S., van de Linde, S., Heilemann, M., Nudelman, G., Nachliel, E., Gutman, M., Sauer, M., and Ashery, U. (2012). Super-resolution imaging reveals the internal architecture of nano-sized syntaxin clusters. J. Biol. Chem. *287*, 27158–27167.

Bates, M., Blosser, T.R., and Zhuang, X.W. (2005). Short-range spectroscopic ruler based on a single-molecule optical switch. Phys. Rev. Lett. *94*, 108101.

Bates, M., Huang, B., Dempsey, G.T., and Zhuang, X.W. (2007). Multicolor super-resolution imaging with photo-switchable fluorescent probes. Science *317*, 1749–1753.

Benke, A., Olivier, N., Gunzenhäuser, J., and Manley, S. (2012). Multicolor single molecule tracking of stochastically active synthetic dyes. Nano Lett. *12*, 2619–2624.

Betzig, E., Patterson, G.H., Sougrat, R., Lindwasser, O.W., Olenych, S., Bonifacino, J.S., Davidson, M.W., Lippincott-Schwartz, J., and Hess, H.F. (2006). Imaging intracellular fluorescent proteins at nanometer resolution. Science *313*, 1642–1645.

Biteen, J.S., Thompson, M.A., Tselentis, N.K., Bowman, G.R., Shapiro, L., and Moerner, W.E. (2008). Super-resolution imaging in live Caulobacter crescentus cells using photoswitchable EYFP. Nat. Methods *5*, 947–949.

Bock, H., Geisler, C., Wurm, C.A., Von Middendorff, C., Jakobs, S., Schonle, A., Egner, A., Hell, S.W., and Eggeling, C. (2007). Two-color far-field fluorescence nanoscopy based on photoswitchable emitters. Appl. Phys. B *88*, 161–165.

Cella Zanacchi, F., Lavagnino, Z., Perrone Donnorso, M., Del Bue, A., Furia, L., Faretta, M., and Diaspro, A. (2011). Live-cell 3D super-resolution imaging in thick biological samples. Nat. Methods *8*, 1047–1049.

Churchman, L.S., Okten, Z., Rock, R.S., Dawson, J.F., and Spudich, J.A. (2005). Single molecule high-resolution colocalization of Cy3 and Cy5 attached to macromolecules measures intramolecular distances through time. Proc. Natl. Acad. Sci. USA *102*, 1419–1423.

Cordes, T., Strackharn, M., Stahl, S.W., Summerer, W., Steinhauer, C., Forthmann, C., Puchner, E.M., Vogelsang, J., Gaub, H.E., and Tinnefeld, P. (2010). Resolving single-molecule assembled patterns with superresolution blink-microscopy. Nano Lett. *10*, 645–651.

Dani, A., Huang, B., Bergan, J., Dulac, C., and Zhuang, X. (2010). Superresolution imaging of chemical synapses in the brain. Neuron *68*, 843–856.

Dempsey, G.T., Bates, M., Kowtoniuk, W.E., Liu, D.R., Tsien, R.Y., and Zhuang, X. (2009). Photoswitching mechanism of cyanine dyes. J. Am. Chem. Soc. *131*, 18192–18193.

Diaspro A., ed. (2010). Nanoscopy and Multidimensional Optical Fluorescence Microscopy (Boca Raton, FL: Chapman and Hall/CRC).

Drexhage, K.H. (1973). Structure and properties of laser dyes. In Topics in Applied Physics, Vol 1 Dye Lasers, F.P. Schäfer, ed. (Berlin: Springer-Verlag), pp. 144–193.

Endesfelder, U., Malkusch, S., Flottmann, B., Mondry, J., Liguzinski, P., Verveer, P.J., and Heilemann, M. (2011). Chemically induced photoswitching of fluorescent probes—a general concept for super-resolution microscopy. Molecules *16*, 3106–3118.

Fernández-Suárez, M., and Ting, A.Y. (2008). Fluorescent probes for super-resolution imaging in living cells. Nat. Rev. Mol. Cell Biol. *9*, 929–943.

Flors, C. (2011). DNA and chromatin imaging with super-resolution fluorescence microscopy based on single-molecule localization. Biopolymers *95*, 290–297.

Fölling, J., Belov, V., Kunetsky, R., Medda, R., Schönle, A., Egner, A., Eggeling, C., Bossi, M., and Hell, S.W. (2007). Photochromic rhodamines provide nanoscopy with optical sectioning. Angew. Chem. Int. Ed. Engl. *46*, 6266–6270.

Fölling, J., Bossi, M., Bock, H., Medda, R., Wurm, C.A., Hein, B., Jakobs, S., Eggeling, C., and Hell, S.W. (2008). Fluorescence nanoscopy by ground-state depletion and single-molecule return. Nat. Methods *5*, 943–945.

Galbraith, C.G., and Galbraith, J.A. (2011). Super-resolution microscopy at a glance. J. Cell Sci. *124*, 1607–1611.

Garcia-Parajo, M.F., Koopman, M., van Dijk, E.M., Subramaniam, V., and van Hulst, N.F. (2001). The nature of fluorescence emission in the red fluorescent protein DsRed, revealed by single-molecule detection. Proc. Natl. Acad. Sci. USA *98*, 14392–14397.

Giannone, G., Hosy, E., Levet, F., Constals, A., Schulze, K., Sobolevsky, A.I., Rosconi, M.P., Gouaux, E., Tampé, R., Choquet, D., and Cognet, L. (2010). Dynamic superresolution imaging of endogenous proteins on living cells at ultra-high density. Biophys. J. *99*, 1303–1310.

Giepmans, B.N.G., Adams, S.R., Ellisman, M.H., and Tsien, R.Y. (2006). The fluorescent toolbox for assessing protein location and function. Science *312*, 217–224.

Gunzenhäuser, J., Olivier, N., Pengo, T., and Manley, S. (2012). Quantitative super-resolution imaging reveals protein stoichiometry and nanoscale morphology of assembling HIV-Gag virions. Nano Lett. *12*, 4705–4710.

Gustafsson, M.G. (2000). Surpassing the lateral resolution limit by a factor of two using structured illumination microscopy. J. Microsc. *198*, 82–87.

Ha, T., and Tinnefeld, P. (2012). Photophysics of fluorescent probes for single-molecule biophysics and super-resolution imaging. Annu. Rev. Phys. Chem. *63*, 595–617.

Heilemann, M., Herten, D.P., Heintzmann, R., Cremer, C., Muller, C., Tinnefeld, P., Weston, K.D., Wolfrum, J., and Sauer, M. (2002). High-resolution colocalization of single dye molecules by fluorescence lifetime imaging microscopy. Anal. Chem. *74*, 3511–3517.

Heilemann, M., Margeat, E., Kasper, R., Sauer, M., and Tinnefeld, P. (2005). Carbocyanine dyes as efficient reversible single-molecule optical switch. J. Am. Chem. Soc. *127*, 3801–3806.

Heilemann, M., van de Linde, S., Schüttpelz, M., Kasper, R., Seefeldt, B., Mukherjee, A., Tinnefeld, P., and Sauer, M. (2008). Subdiffraction-resolution fluorescence imaging with conventional fluorescent probes. Angew. Chem. Int. Ed. Engl. *47*, 6172–6176.

Heilemann, M., Dedecker, P., Hofkens, J., and Sauer, M. (2009a). Photoswitches: key molecules for subdiffraction-resolution fluorescence imaging and molecular quantification. Laser & Photon. Rev. *3*, 180–202.

Heilemann, M., van de Linde, S., Mukherjee, A., and Sauer, M. (2009b). Super-resolution imaging with small organic fluorophores. Angew. Chem. Int. Ed. Engl. *48*, 6903–6908.

Hell, S.W. (2007). Far-field optical nanoscopy. Science *316*, 1153–1158.

Hell, S.W. (2009). Microscopy and its focal switch. Nat. Methods *6*, 24–32.

Henriques, R., Griffiths, C., Hesper Rego, E., and Mhlanga, M.M. (2011). PALM and STORM: unlocking live-cell super-resolution. Biopolymers *95*, 322–331.

Hess, S.T., Girirajan, T.P., and Mason, M.D. (2006). Ultra-high resolution imaging by fluorescence photoactivation localization microscopy. Biophys. J. *91*, 4258–4272.

Hess, S.T., Gould, T.J., Gudheti, M.V., Maas, S.A., Mills, K.D., and Zimmerberg, J. (2007). Dynamic clustered distribution of hemagglutinin resolved at 40 nm in living cell membranes discriminates between raft theories. Proc. Natl. Acad. Sci. USA *104*, 17370–17375.

Hofmann, M., Eggeling, C., Jakobs, S., and Hell, S.W. (2005). Breaking the diffraction barrier in fluorescence microscopy at low light intensities by using reversibly photoswitchable proteins. Proc. Natl. Acad. Sci. USA *102*, 17565–17569.

Holden, S.J., Uphoff, S., and Kapanidis, A.N. (2011). DAOSTORM: an algorithm for high- density super-resolution microscopy. Nat. Methods *8*, 279–280.

Huang, B., Wang, W.Q., Bates, M., and Zhuang, X.W. (2008). Three-dimensional super-resolution imaging by stochastic optical reconstruction microscopy. Science *319*, 810–813.

Huang, B., Babcock, H., and Zhuang, X. (2010). Breaking the diffraction barrier: super-resolution imaging of cells. Cell *143*, 1047–1058.

Huisken, J., Swoger, J., Del Bene, F., Wittbrodt, J., and Stelzer, E.H. (2004). Optical sectioning deep inside live embryos by selective plane illumination microscopy. Science *305*, 1007–1009.

Itano, M.S., Steinhauer, C., Schmied, J.J., Forthmann, C., Liu, P., Neumann, A.K., Thompson, N.L., Tinnefeld, P., and Jacobson, K. (2012). Super-resolution imaging of C-type lectin and influenza hemagglutinin nanodomains on plasma membranes using blink microscopy. Biophys. J. *102*, 1534–1542.

Ji, N., Shroff, H., Zhong, H., and Betzig, E. (2008). Advances in the speed and resolution of light microscopy. Curr. Opin. Neurobiol. *18*, 605–616.

Jones, D.P. (2010). Redox sensing: orthogonal control in cell cycle and apoptosis signalling. J. Intern. Med. *268*, 432–448.

Jones, S.A., Shim, S.H., He, J., and Zhuang, X. (2011). Fast, three-dimensional super-resolution imaging of live cells. Nat. Methods *8*, 499–508.

Juette, M.F., Gould, T.J., Lessard, M.D., Mlodzianoski, M.J., Nagpure, B.S., Bennett, B.T., Hess, S.T., and Bewersdorf, J. (2008). Three-dimensional sub-100 nm resolution fluorescence microscopy of thick samples. Nat. Methods *5*, 527–529.

Keppler, A., Gendreizig, S., Gronemeyer, T., Pick, H., Vogel, H., and Johnsson, K. (2003). A general method for the covalent labeling of fusion proteins with small molecules in vivo. Nat. Biotechnol. *21*, 86–89.

Klar, T.A., Jakobs, S., Dyba, M., Egner, A., and Hell, S.W. (2000). Fluorescence microscopy with diffraction resolution barrier broken by stimulated emission. Proc. Natl. Acad. Sci. USA *97*, 8206–8210.

Klein, T., Löschberger, A., Proppert, S., Wolter, S., van de Linde, S., and Sauer, M. (2011). Live-cell dSTORM with SNAP-tag fusion proteins. Nat. Methods *8*, 7–9.

Klein, T., van de Linde, S., and Sauer, M. (2012). Live-cell super-resolution imaging goes multicolor. ChemBioChem *13*, 1861–1863.

Kner, P., Chhun, B.B., Griffis, E.R., Winoto, L., and Gustafsson, M.G. (2009). Super-resolution video microscopy of live cells by structured illumination. Nat. Methods *6*, 339–342.

Kolb, H.C., Finn, M.G., and Sharpless, K.B. (2001). Click Chemistry: Diverse Chemical Function from a Few Good Reactions. Angew. Chem. Int. Ed. Engl. *40*, 2004–2021.

Kottke, T., van de Linde, S., Sauer, M., Kakorin, S., and Heilemann, M. (2010). Identification of the product of photoswitching of an oxazine fluorophore using Fourier transform infrared difference spectroscopy. J. Phys. Chem. Lett. *1*, 3156–3159.

Kufer, S.K., Puchner, E.M., Gumpp, H., Liedl, T., and Gaub, H.E. (2008). Single-molecule cut-and-paste surface assembly. Science *319*, 594–596.

Kufer, S.K., Strackharn, M., Stahl, S.W., Gumpp, H., Puchner, E.M., and Gaub, H.E. (2009). Optically monitoring the mechanical assembly of single molecules. Nat. Nanotechnol. *4*, 45–49.

Lacoste, T.D., Michalet, X., Pinaud, F., Chemla, D.S., Alivisatos, A.P., and Weiss, S. (2000). Ultrahigh-resolution multicolor colocalization of single fluorescent probes. Proc. Natl. Acad. Sci. USA *97*, 9461–9466.

Lando, D., Endesfelder, U., Berger, H., Subramanian, L., Dunne, P.D., McColl, J., Klenerman, D., Carr, A.M., Sauer, M., Allshire, R.C., et al. (2012). Quantitative single-molecule microscopy reveals that CENP-A(Cnp1) deposition occurs during G2 in fission yeast. Open Biol. *2*, 120078.

Laughlin, S.T., Baskin, J.M., Amacher, S.L., and Bertozzi, C.R. (2008). In vivo imaging of membrane-associated glycans in developing zebrafish. Science *320*, 664–667.

Lidke, K., Rieger, B., Jovin, T., and Heintzmann, R. (2005). Superresolution by localization of quantum dots using blinking statistics. Opt. Express *13*, 7052–7062.

Löschberger, A., van de Linde, S., Dabauvalle, M.C., Rieger, B., Heilemann, M., Krohne, G., and Sauer, M. (2012). Super-resolution imaging visualizes the eightfold symmetry of gp210 proteins around the nuclear pore complex and resolves the central channel with nanometer resolution. J. Cell Sci. *125*, 570–575.

Manley, S., Gillette, J.M., Patterson, G.H., Shroff, H., Hess, H.F., Betzig, E., and Lippincott-Schwartz, J. (2008). High-density mapping of single-molecule trajectories with photoactivated localization microscopy. Nat. Methods *5*, 155–157.

McKinney, S.A., Murphy, C.S., Hazelwood, K.L., Davidson, M.W., and Looger, L.L. (2009). A bright and photostable photoconvertible fluorescent protein. Nat. Methods *6*, 131–133.

Miller, L.W., and Cornish, V.W. (2005). Selective chemical labeling of proteins in living cells. Curr. Opin. Chem. Biol. *9*, 56–61.

Moerner, W.E., and Orrit, M. (1999). Illuminating single molecules in condensed matter. Science *283*, 1670–1676.

Mortensen, K.I., Churchman, L.S., Spudich, J.A., and Flyvbjerg, H. (2010). Optimized localization analysis for single-molecule tracking and super-resolution microscopy. Nat. Methods *7*, 377–381.

Nägerl, U.V., Willig, K.I., Hein, B., Hell, S.W., and Bonhoeffer, T. (2008). Live-cell imaging of dendritic spines by STED microscopy. Proc. Natl. Acad. Sci. USA *105*, 18982–18987.

Ormö, M., Cubitt, A.B., Kallio, K., Gross, L.A., Tsien, R.Y., and Remington, S.J. (1996). Crystal structure of the Aequorea victoria green fluorescent protein. Science *273*, 1392–1395.

Owen, D.M., Sauer, M., and Gaus, K. (2012). Fluorescence localization microscopy: The transition from concept to biological research tool. Commun. Integr. Biol. *5*, 345–349.

Patterson, G., Davidson, M., Manley, S., and Lippincott-Schwartz, J. (2010). Superresolution imaging using single-molecule localization. Annu. Rev. Phys. Chem. *61*, 345–367.

Pertsinidis, A., Zhang, Y., and Chu, S. (2010). Subnanometre single-molecule localization, registration and distance measurements. Nature *466*, 647–651.

Planchon, T.A., Gao, L., Milkie, D.E., Davidson, M.W., Galbraith, J.A., Galbraith, C.G., and Betzig, E. (2011). Rapid three-dimensional isotropic imaging of living cells using Bessel beam plane illumination. Nat. Methods *8*, 417–423.

Prescher, J.A., and Bertozzi, C.R. (2005). Chemistry in living systems. Nat. Chem. Biol. *1*, 13–21.

Ries, J., Kaplan, C., Platonova, E., Eghlidi, H., and Ewers, H. (2012). A simple, versatile method for GFP-based super-resolution microscopy via nanobodies. Nat. Methods *9*, 582–584.

Roeffaers, M.B., De Cremer, G., Libeert, J., Ameloot, R., Dedecker, P., Bons, A.J., Bückins, M., Martens, J.A., Sels, B.F., De Vos, D.E., and Hofkens, J. (2009). Super-resolution reactivity mapping of nanostructured catalyst particles. Angew. Chem. Int. Ed. Engl. *48*, 9285–9289.

Rust, M.J., Bates, M., and Zhuang, X.W. (2006). Sub-diffraction-limit imaging by stochastic optical reconstruction microscopy (STORM). Nat. Methods *3*, 793–795.

Sauer, M., Hofkens, J., and Enderlein, J. (2011). Handbook of Fluorescence Spectroscopy and Imaging: From Ensemble to Single Molecules, First Edition (Weilheim, Germany: Wiley).

Schafer, F.Q., and Buettner, G.R. (2001). Redox environment of the cell as viewed through the redox state of the glutathione disulfide/glutathione couple. Free Radic. Biol. Med. *30*, 1191–1212.

Schermelleh, L., Heintzmann, R., and Leonhardt, H. (2010). A guide to super-resolution fluorescence microscopy. J. Cell Biol. *190*, 165–175.

Sengupta, P., Jovanovic-Talisman, T., Skoko, D., Renz, M., Veatch, S.L., and Lippincott-Schwartz, J. (2011). Probing protein heterogeneity in the plasma membrane using PALM and pair correlation analysis. Nat. Methods *8*, 969–975.

Shannon, C.E. (1949). Communication in the presence of noise. Proc. IRE *37*, 10–21.

Sharonov, A., and Hochstrasser, R.M. (2006). Wide-field subdiffraction imaging by accumulated binding of diffusing probes. Proc. Natl. Acad. Sci. USA *103*, 18911–18916.

Shim, S.H., Xia, C., Zhong, G., Babcock, H.P., Vaughan, J.C., Huang, B., Wang, X., Xu, C., Bi, G.Q., and Zhuang, X. (2012). Super-resolution fluorescence imaging of organelles in live cells with photoswitchable membrane probes. Proc. Natl. Acad. Sci. USA *109*, 13978–13983.

Shroff, H., Galbraith, C.G., Galbraith, J.A., White, H., Gillette, J., Olenych, S., Davidson, M.W., and Betzig, E. (2007). Dual-color superresolution imaging of genetically expressed probes within individual adhesion complexes. Proc. Natl. Acad. Sci. USA *104*, 20308–20313.

Shroff, H., Galbraith, C.G., Galbraith, J.A., and Betzig, E. (2008). Live-cell photoactivated localization microscopy of nanoscale adhesion dynamics. Nat. Methods *5*, 417–423.

Smith, C.V., Jones, D.P., Guenthner, T.M., Lash, L.H., and Lauterburg, B.H. (1996). Compartmentation of glutathione: implications for the study of toxicity and disease. Toxicol. Appl. Pharmacol. *140*, 1–12.

Steinhauer, C., Forthmann, C., Vogelsang, J., and Tinnefeld, P. (2008). Superresolution microscopy on the basis of engineered dark states. J. Am. Chem. Soc. *130*, 16840–16841.

Steinhauer, C., Jungmann, R., Sobey, T.L., Simmel, F.C., and Tinnefeld, P. (2009). DNA origami as a nanoscopic ruler for super-resolution microscopy. Angew. Chem. Int. Ed. Engl. *48*, 8870–8873.

Subach, F.V., Patterson, G.H., Manley, S., Gillette, J.M., Lippincott-Schwartz, J., and Verkhusha, V.V. (2009). Photoactivatable mCherry for high-resolution two-color fluorescence microscopy. Nat. Methods *6*, 153–159.

Subach, F.V., Patterson, G.H., Renz, M., Lippincott-Schwartz, J., and Verkhusha, V.V. (2010). Bright monomeric photoactivatable red fluorescent protein for two-color super-resolution sptPALM of live cells. J. Am. Chem. Soc. *132*, 6481–6491.

Terpetschnig, E.A., Patsenker, L.D., and Tatarets, A. (August 2004). U.S. Patent 20040166515.

Thompson, M.A., Lew, M.D., and Moerner, W.E. (2012). Extending microscopic resolution with single-molecule imaging and active control. Ann. Rev. Biophys. *41*, 321–342.

Thompson, R.E., Larson, D.R., and Webb, W.W. (2002). Precise nanometer localization analysis for individual fluorescent probes. Biophys. J. *82*, 2775–2783.

Tinnefeld, P., and Sauer, M. (2005). Branching out of single-molecule fluorescence spectroscopy: challenges for chemistry and influence on biology. Angew. Chem. Int. Ed. Engl. *44*, 2642–2671.

Tokunaga, M., Imamoto, N., and Sakata-Sogawa, K. (2008). Highly inclined thin illumination enables clear single-molecule imaging in cells. Nat. Methods *5*, 159–161.

Toomre, D., and Bewersdorf, J. (2010). A new wave of cellular imaging. Annu. Rev. Cell Dev. Biol. *26*, 285–314.

Ulbrich, M.H., and Isacoff, E.Y. (2007). Subunit counting in membrane-bound proteins. Nat. Methods *4*, 319–321.

van de Linde, S., Krstić, I., Prisner, T., Doose, S., Heilemann, M., and Sauer, M. (2011a). Photoinduced formation of reversible dye radicals and their impact on super-resolution imaging. Photochem. Photobiol. Sci. *10*, 499–506.

van de Linde, S., Löschberger, A., Klein, T., Heidbreder, M., Wolter, S., Heilemann, M., and Sauer, M. (2011b). Direct stochastic optical reconstruction microscopy with standard fluorescent probes. Nat. Protoc. *6*, 991–1009.

van de Linde, S., Heilemann, M., and Sauer, M. (2012). Live-cell super-resolution imaging with synthetic fluorophores. Annu. Rev. Phys. Chem. *63*, 519–540.

Veatch, S.L., Machta, B.B., Shelby, S.A., Chiang, E.N., Holowka, D.A., and Baird, B.A. (2012). Correlation functions quantify super-resolution images and estimate apparent clustering due to over-counting. PLoS ONE *7*, e31457.

Vogelsang, J., Kasper, R., Steinhauer, C., Person, B., Heilemann, M., Sauer, M., and Tinnefeld, P. (2008). A reducing and oxidizing system minimizes photobleaching and blinking of fluorescent dyes. Angew. Chem. Int. Ed. Engl. *47*, 5465–5469.

Vogelsang, J., Cordes, T., Forthmann, C., Steinhauer, C., and Tinnefeld, P. (2009). Controlling the fluorescence of ordinary oxazine dyes for single-molecule switching and superresolution microscopy. Proc. Natl. Acad. Sci. USA *106*, 8107–8112.

Vogelsang, J., Steinhauer, C., Forthmann, C., Stein, I.H., Person-Skegro, B., Cordes, T., and Tinnefeld, P. (2010). Make them blink: probes for super-resolution microscopy. ChemPhysChem *11*, 2475–2490.

Weber, K., Rathke, P.C., and Osborn, M. (1978). Cytoplasmic microtubular images in glutaraldehyde-fixed tissue culture cells by electron microscopy and by immunofluorescence microscopy. Proc. Natl. Acad. Sci. USA *75*, 1820–1824.

Wilmes, S., Staufenbiel, M., Lisse, D., Richter, C.P., Beutel, O., Busch, K.B., Hess, S.T., and Piehler, J. (2012). Triple-color super-resolution imaging of live cells: resolving submicroscopic receptor organization in the plasma membrane. Angew. Chem. Int. Ed. Engl. *51*, 4868–4871.

Wolter, S., Endesfelder, U., van de Linde, S., Heilemann, M., and Sauer, M. (2011). Measuring localization performance of super-resolution algorithms on very active samples. Opt. Express *19*, 7020–7033.

Wombacher, R., Heidbreder, M., van de Linde, S., Sheetz, M.P., Heilemann, M., Cornish, V.W., and Sauer, M. (2010). Live-cell super-resolution imaging with trimethoprim conjugates. Nat. Methods *7*, 717–719.

Yildiz, A., and Selvin, P.R. (2005). Fluorescence imaging with one nanometer accuracy: application to molecular motors. Acc. Chem. Res. *38*, 574–582.

York, A.G., Ghitani, A., Vaziri, A., Davidson, M.W., and Shroff, H. (2011). Confined activation and subdiffractive localization enables whole-cell PALM with genetically expressed probes. Nat. Methods *8*, 327–333.

Zessin, P.J., Finan, K., and Heilemann, M. (2012). Super-resolution fluorescence imaging of chromosomal DNA. J. Struct. Biol. *177*, 344–348.

Zhu, L., Zhang, W., Elnatan, D., and Huang, B. (2012). Faster STORM using compressed sensing. Nat. Methods *9*, 721–723.

Zondervan, R., Kulzer, F., Orlinskii, S.B., and Orrit, M. (2003). Photoblinking of Rhodamine 6G in poly(vinyl alcohol): radical dark state formed through the triplet. J. Phys. Chem. A *107*, 6770–6776.

Dipl. – Phys. Christian Franke
Lehrstuhl für Biotechnologie und Biophysik
Biozentrum, Am Hubland
97074 Würzburg
Germany

Würzburg, 4th July 2017

Manuscript:

Anna Löschberger, Christian Franke, Georg Krohne, Sebastian van de Linde, and Markus Sauer.

Correlative super-resolution fluorescence and electron microscopy of the nuclear pore complex with molecular resolution.

J Cell Sci, 127(20):4351-4355, 2014

The contributions of the PhD candidate Christian Franke to the above manuscript involved:

- Conceptual design, implementation and execution of the described quantification approach
- Analysis of gp210 localization data
- Contribution to the manuscript draft, especially Figure 3 and section 'Quantification of *d*STORM data'

Christian Franke

Löschberger
Anna Löschberger

Georg Krohne
Georg Krohne

Sebastian van de Linde

Markus Sauer

© 2014. Published by The Company of Biologists Ltd | Journal of Cell Science (2014) 127, 4351–4355 doi:10.1242/jcs.156620

SHORT REPORT

Correlative super-resolution fluorescence and electron microscopy of the nuclear pore complex with molecular resolution

Anna Löschberger[1], Christian Franke[1], Georg Krohne[2], Sebastian van de Linde[1] and Markus Sauer[1,*]

ABSTRACT

Here, we combine super-resolution fluorescence localization microscopy with scanning electron microscopy to map the position of proteins of nuclear pore complexes in isolated *Xenopus laevis* oocyte nuclear envelopes with molecular resolution in both imaging modes. We use the periodic molecular structure of the nuclear pore complex to superimpose direct stochastic optical reconstruction microscopy images with a precision of <20 nm on electron micrographs. The correlative images demonstrate quantitative molecular labeling and localization of nuclear pore complex proteins by standard immunocytochemistry with primary and secondary antibodies and reveal that the nuclear pore complex is composed of eight gp210 (also known as NUP210) protein homodimers. In addition, we find subpopulations of nuclear pore complexes with ninefold symmetry, which are found occasionally among the more typical eightfold symmetrical structures.

KEY WORDS: Correlative electron and super-resolution fluorescence microscopy, Nuclear pore complex, *d*STORM, Localization microscopy, Quantification

INTRODUCTION

Electron microscopy (EM) and electron tomography have been extensively used to elucidate cellular ultrastructure and architecture of large multiprotein complexes. An impressive example of the resolution power of these methods is the determination of the three-dimensional (3D) structure of the nuclear pore complex (NPC), a gigantic molecular machine assembled from ~30 different nuclear proteins with a molecular mass of over 100 MDa, with a resolution of a few nanometers (Beck et al., 2007; Maimon et al., 2012). However, conventional fixation and staining protocols for EM and electron tomography are optimized to provide optimal preservation of cellular ultrastructure and not to provide specific molecular labeling. Immunolabeling EM with gold-conjugated antibodies can reveal localizations of cellular components with nanometer resolution but is limited by the quality of fixation and the inaccessibility of antigens, and it can obscure structural details beneath it. Even under optimized conditions (i.e. with the availability of high-affinity antibodies and mild fixation and staining protocols) only a subset of target molecules is likely to be successfully detected (Morphew, 2007). Hence, the determination of the molecular composition of large biological complexes, such as the NPC, remains challenging.

Correlative light and electron microscopy (Müller-Reichert et al., 2007; Kukulski et al., 2011) can be used advantageously for imaging of proteins or organelles within cells because fluorescence microscopy allows specific molecular labeling and, in combination with new super-resolution fluorescence microscopy methods, spatial resolutions well below the diffraction barrier. Super-resolution fluorescence imaging by single-molecule photoactivation or photoswitching and position determination (localization microscopy) (Betzig et al., 2006; Hess et al., 2006; Rust et al., 2006; Heilemann et al., 2008, Sauer, 2013) can localize fluorescently labeled molecules at virtually molecular resolution. Furthermore, super-resolution fluorescence imaging enables higher labeling efficiencies than immunogold EM using fluorophore-tagged antibodies, which facilitates structure determination by localization microscopy. Thus, localization microscopy and EM are complementary methods that can be combined to determine molecular positions in the context of the cellular ultrastructure provided by EM with nanometer resolution (Betzig et al., 2006; Watanabe et al., 2011; Kopek et al., 2012; Nanguneri et al., 2012; Suleiman et al., 2013; Sochacki et al., 2014; Perkovic et al., 2014). In order to perform correlative localization and electron microscopy, several methodological requirements have to be fulfilled. First, protein fluorescence damage and autofluorescent background due to fixation and staining required to preserve good ultrastructure has to be kept to a minimum (Tsien, 1998; Watanabe et al., 2011). Second, protein positions determined by localization microscopy have to be located within the EM image across large areas with a precision in the nanometer range. This demand is impeded by a lack of suitable alignment markers that are stationary at the nanoscale range and exhibit good contrast in the two imaging modes (Watanabe et al., 2011; Kopek et al., 2012; Sochacki et al., 2014; Perkovic et al., 2014). Even when such types of markers are available, structural deformations occurring between the two imaging modes can aggravate the overlay of the two images with molecular precision.

Finally, one should bear in mind that localization microscopy can provide quantitative molecular information about molecular distributions and, appropriate controls assumed, absolute numbers of proteins present. Therefore, it has to be guaranteed that each protein of interest is labeled with an ‘active’ fluorophore and that its fluorescence is detected above a certain photon threshold (Sauer, 2013; Lando et al., 2012). This task is particularly demanding when using fluorophore-labeled antibodies for specific labeling.

Here, we demonstrate the use of correlative scanning electron (SEM) and direct stochastic optical reconstruction microscopy (*d*STORM) (Heilemann et al., 2008; van de Linde et al., 2011;

---

[1]Department of Biotechnology and Biophysics, Biozentrum, Julius Maximilian University Würzburg, Am Hubland, 97074 Würzburg, Germany. [2]Department of Electron Microscopy, Biozentrum, Julius Maximilian University Würzburg, Am Hubland, 97074 Würzburg, Germany.

*Author for correspondence (m.sauer@uni-wuerzburg.de)

Received 15 May 2014; Accepted 6 August 2014

Löschberger et al., 2012) to image proteins of NPCs in isolated *Xenopus laevis* oocyte nuclear envelopes with molecular resolution in both imaging modes. Instead of using alignment markers, we use the periodic molecular structure of the NPC to localize proteins in *d*STORM and corresponding SEM images to overlay them with nanometer precision. Our results demonstrate quantitative molecular labeling of the NPC protein gp210 (also known as NUP210) (Favreau et al., 2001; Gerace et al., 1982; Gajewski et al., 1996) by standard immunocytochemistry with primary and secondary antibodies, and that the NPC contains eight gp210 homodimers. In addition, *d*STORM reveals subpopulations of NPCs with ninefold symmetry that are found occasionally among the more typical eightfold symmetrical structures (Hinshaw and Milligan, 2003).

RESULTS AND DISCUSSION

Recently, the NPC has been introduced as a suitable reference structure for verification of super-resolution imaging data. Two-color *d*STORM images recorded either consecutively or simultaneously by spectrally resolved imaging in combination with particle averaging demonstrated that the organization of NPC proteins can be visualized with nanometer resolution (Löschberger et al., 2012, Wolter et al., 2012). In order to shed light on the heterogeneity of NPC composition and quantify the labeling efficiency, we set out to localize the integral membrane protein gp210 (Favreau et al., 2001; Gerace et al., 1982) and *N*-acetylglucosamine-modified nucleoporins of the central channel of NPCs by correlative SEM and *d*STORM. Isolated *Xenopus laevis* oocyte nuclear envelopes were prepared on chambered cover glass without correlative markers (Fig. 1). The nuclear envelopes were labeled using a primary antibody directed against an epitope in the luminal side of gp210 (Gajewski et al., 1996), and Alexa Fluor 647 (Alexa 647)-labeled $F(ab')_2$ fragments or Alexa-647-labeled wheat germ agglutinin (WGA) binding to modified nucleoporins of the central channel (Davis and Blobel, 1987).

At this point, it has to be indicated that correlative imaging of NPCs in isolated nuclear envelopes with molecular resolution is challenging because sample preparation generates a situation in which the cytoplasmatic NPC side, with the anchoring proteins, is oriented in the direction of the coverglass, but SEM imaging is restricted to the nucleoplasmatic, nuclear-basket-containing side (Fig. 1A). Accidentally, we realized sample areas where the nuclear envelope folded back during preparation, hence, also enabling SEM of the cytoplasmatic NPC side (Fig. 1B). However, it is impossible to identify such folded areas in fluorescence images. Therefore, in the majority of preparations the cytoplasmatic side of the NPC is invisible in the SEM images. By contrast, the central channel and the integral membrane protein gp210 can be visualized from the cytoplasmatic and nucleoplasmatic side by fluorescence imaging.

In localization microscopy, single-molecule coordinates are generally visualized as a histogram by using sub-pixel binning (Wolter at al., 2012; Wolter et al., 2010). To determine the influence of pixel binning on resolution, we reconstructed *d*STORM images of the central NPC channel at different pixel size (Fig. 1C). The resulting super-resolution images clearly demonstrate that the central channel of the NPC with a diameter of ∼40 nm did not become visible until the pixel size was reduced below 20 nm. This finding demonstrates that we achieved a spatial resolution considerably better than 20 nm for imaging of the central channel in NPCs (Fig. 1C). The high spatial resolution is due to the large number of photons detected per Alexa 647, ∼3.500 photons/frame, and the small size of a WGA dimer, of ∼5 nm (Schwefel et al., 2010), used to label the nucleoporins of the central channel. In accordance with this finding, we determined a localization precision of ∼6 nm (s.d., in the lateral direction) using localizations of unspecifically bound isolated WGA–Alexa-647 molecules in the sample.

Next, we mapped the *xy* positions of gp210 labeled with Alexa 647 antibody and WGA–Alexa-647-labeled nucleoporins onto the SEM image (Fig. 2). Image alignment was performed without markers, exploiting the highly symmetric circular structure of the NPC (supplementary material Figs S1, S2). The *xy* positions of Alexa 647 in the *d*STORM images matched the shapes of the

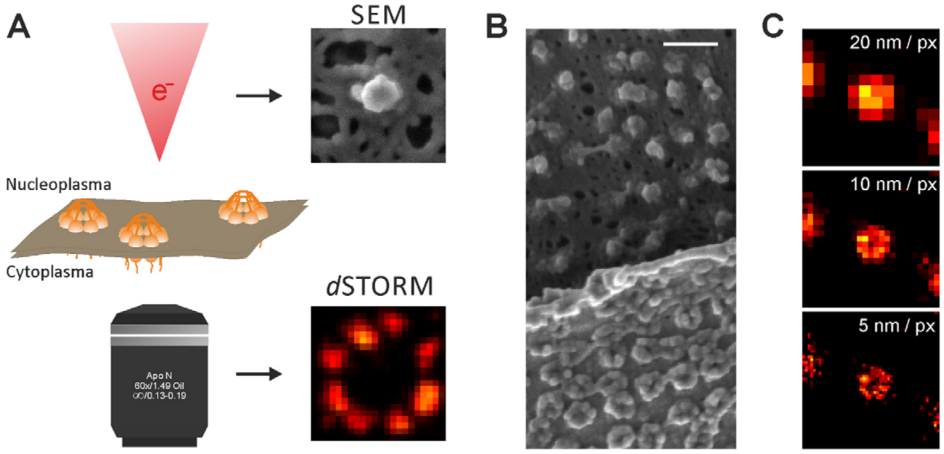

Fig. 1. Imaging the nuclear envelope by SEM and *d*STORM. (A) SEM imaging is restricted to the nucleoplasmatic, nuclear-basket-containing, side, whereas *d*STORM imaging is performed from the cytoplasmatic side, where the anchoring proteins are oriented in the direction of the coverglass. Schematically, an electron beam and an objective are depicted to symbolize SEM and *d*STORM imaging, respectively. (B) SEM image of a folded nuclear envelope. (C) Influence of the pixel binning used to reconstruct the super-resolved *d*STORM image on resolution, that is, the visualization of the central channel of the NPC. Scale bar: 200 nm.

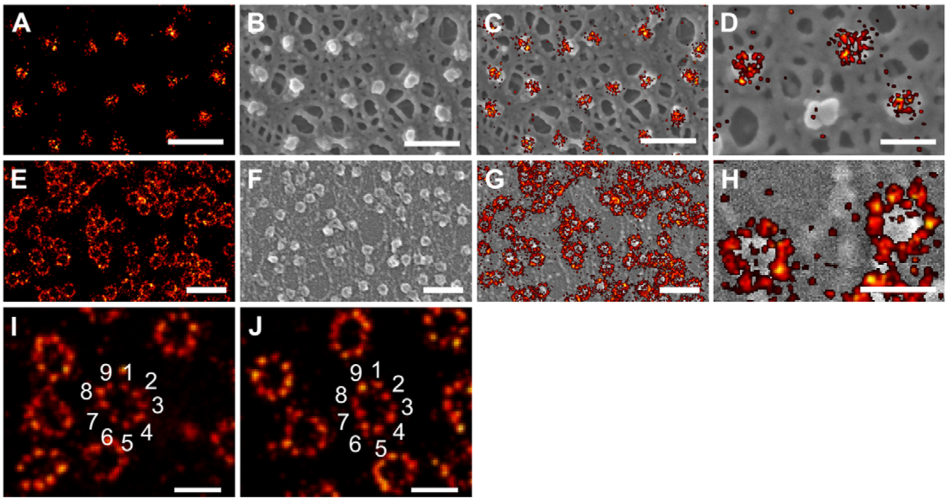

Fig. 2. Correlative *d*STORM-SEM of NPCs. (A) *d*STORM image of the central channel labeled with WGA–Alexa-647, (B) corresponding SEM image of the nucleoplasmatic side of the nuclear envelope and (C) overlay of the *d*STORM and SEM images. (D) Detailed overlay of a different area, highlighting that some NPCs are not labeled by WGA–Alexa-647. (E) The integral membrane protein gp210 was labeled using immunofluorescence with Alexa 647. (F) Corresponding SEM image, (G) overlay of *d*STORM and SEM image and (H) overlay of the detailed eightfold structure of the outer gp210 ring. (I,J) Examples of NPCs revealing a ninefold symmetrical structure of gp210 proteins (Hinshaw and Milligan, 2003). Scale bars: 250 nm (A–C), 100 nm (D), 500 nm (E–G), 200 nm (H–J).

NPC structures in SEM (Fig. 2). The majority of WGA–Alexa-647-labeled NPCs showed the central channel perfectly superimposed with the SEM structures (Fig. 2A–D). Even in large correlative *d*STORM-SEM images, the overlay error remained smaller than the spatial optical resolution (supplementary material Fig. S3).

By contrast, gp210 proteins were labeled by an antibody complex, which limited the overlay accuracy to ~20 nm. In addition, the *d*STORM structures were generally larger than the corresponding SEM structures. However, because the overlay of the two images was not based on direct protein assignment but on the center of the NPC structures in *d*STORM and SEM images, we also expect a smaller overlay error for the gp210 structure. Whether the simple overlay of the center of mass of localization microscopy and EM data also works for unsymmetrical structures needs to be tested.

The majority of gp210-labeled NPCs showed an eightfold symmetric arrangement surrounding the central channel (Fig. 2E–H). Some of the gp210 eightfold structures appeared slightly distorted, which arises from the spreading of the nuclear envelope on the coverglass. Only very rarely (<1%) could completely unlabeled NPCs be identified in *d*STORM-SEM images (Fig. 2D). The same applies to the central channel labeled by WGA–Alexa-647. The infrequent appearance of completely unlabeled NPCs cannot be explained by labeling statistics but must be ascribed to incomplete compositions of NPCs or incomplete maturated or erroneously folded proteins.

Interestingly, we also discovered some (<0.1%) NPCs featuring a ninefold rotational symmetry of gp210 proteins (Fig. 2I,J). Subpopulations of ninefold and tenfold symmetrical NPCs with slightly larger diameter have previously been found in preparations of *Xenopus oocyte* nuclei by EM, suggesting that the assembly process of NPCs can be influenced by local nuclear envelope inhomogeneity, e.g. curved membranes that favor the formation of larger NPCs due to packing constraints (Hinshaw and Milligan, 2003).

Taking advantage of the specific and efficient labeling properties of the anti-gp210 antibodies used (Gajewski et al., 1996) and the high detection and localization probability of Alexa 647, we set out to quantify the number of gp210 proteins surrounding the central channel of the NPC. So far, it is unclear whether eight or 16 gp210 proteins are arranged as monomers or homodimers around the central channel (Favreau et al., 2001; Gerace et al., 1982). Analysis of localization data of 318 NPCs revealed values of 274±4 (mean±s.e.m.) localizations per NPC (median, 253) and 35.1±0.5 (mean±s.e.m.) localizations per protein domain (median, 32) forming the eightfold NPC structure (Fig. 3A,B). This demonstrates that on average 7.9 domains are labeled and identified per NPC. For isolated fluorescence signals detected within the circular NPC structure, we determined a value of 8.1±0.2 (mean±s.e.m.) localizations per Alexa-647-labeled $F(ab')_2$ fragment (median, 5.5) (Fig. 3C).

With the assumption that the isolated signals resulted from single Alexa-647-labeled $F(ab')_2$ fragments, we estimate that on average more than four Alexa-647-labeled $F(ab')_2$ fragments bind per gp210 domain. Given that the probability for binding of more than 4 $F(ab')_2$ fragments per primary antibody is negligibly low and it is known that the primary antibody X222 binds to a single epitope of the gp210 protein (Gajewski et al., 1996), our data provide evidence that each domain contains a gp210 homodimer labeled on average with two monoclonal X222 antibodies and four to six Alexa-647-labeled $F(ab')_2$ fragments. Control localization experiments with non-specifically adsorbed Alexa-647-labeled $F(ab')_2$ fragments on nuclear envelopes in the absence of the primary antibody directed against gp210 protein corroborated our finding that more than four Alexa-647-labeled $F(ab')_2$ fragments bound per gp210 domain (supplementary material Fig. S4).

To summarize, our data convincingly demonstrate that localization microscopy with standard fluorescent probes, such as fluorescently tagged antibodies, can map the position of

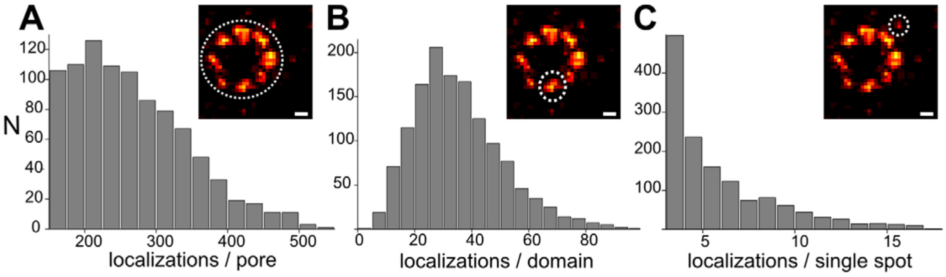

Fig. 3. Localization statistic of gp210 proteins labeled with a primary antibody and a secondary Alexa-647-labeled F(ab′)$_2$ fragment. The mean localization number was determined as 274±4 for whole NPCs (an example is shown in the inset) (A), 35.1±0.5 for single domains (dashed ring in inset) within the eightfold NPC structure (B), and 8.1±0.2 for isolated fluorescence signals (spots, dashed ring in inset) found in NPCs corresponding to an individual F(ab′)$_2$ fragment (C) (mean±s.e.m.). Scale bars, 20 nm.

proteins in the context of the ultrastructure of large multiprotein complexes provided by EM with nanometer resolution and can reveal subpopulations with slightly altered characteristics that are washed out by particle averaging methods (Löschberger et al., 2012; Szymborska et al., 2013). In addition, correlative *d*STORM-SEM showed that NPCs were only rarely invisible in the fluorescence imaging mode but appear perfectly assembled in the EM imaging mode. These results emphasize the complementarity of the two imaging modes and also provide evidence for the reliability of *d*STORM when applied in combination with highly specific antibodies for quantitative super-resolution imaging. In combination with correlative focused ion beam scanning electron microscopy (FIB-SEM), *d*STORM can potentially be used also for 3D quantitative super-resolution imaging. Alternatively, the sample can be imaged with two-dimensional tiling and at multiple angles to create 3D tomograms in transmission electron microscopy (TEM) (Sochacki et al., 2014)

MATERIALS AND METHODS

Sample preparation for *d*STORM

Nuclear envelopes of *Xenopus laevis* oocytes were isolated as previously described (Löschberger et al., 2012). They were fixed for 20 min with 2% paraformaldehyde in phosphate-buffered saline (PBS). After a short washing step in PBS, they were saturated with 0.5% BSA (Serva) in PBS for 5 min. The envelopes were labeled with X222 antibodies (Gajewski et al., 1996) directed against gp210 for 45 min, washed for 10 min in PBS and incubated with Alexa-647-labeled F(ab′)$_2$ fragments [Life Technologies, A-21237; degree of labeling (DOL) of ~3.5] of goat anti-mouse-IgG antibody for 30 min. Finally, a washing step of at least 20 min in PBS was performed. For WGA staining, the nuclear envelopes were incubated in 1 µg/ml WGA–Alexa-647 (Sigma) in PBS for 10 min. Samples were stored in PBS with 0.2% sodium azide.

Localization microscopy

*d*STORM imaging was performed as described previously (van de Linde et al., 2011; Löschberger et al., 2012). Briefly, we used an inverted microscope (Olympus IX-71) equipped with an oil-immersion objective (APO N, ×60, NA 1.49; Olympus). Irradiation at 640 nm was provided by a Genesis MX 639-1000 laser (Coherent). Typically, 20,000 frames were acquired with a frame rate of 105 Hz at excitation intensities of 1–10 kW cm^{-2} using an inclined illumination scheme (van de Linde et al., 2011). *d*STORM images were reconstructed and analyzed with the open source software rapi*d*STORM 3.2 (Wolter et al., 2010; Wolter et al., 2012). Only fluorescent spots containing more than 1000 photons were analyzed. By analyzing their ellipticity, multi-fluorophore events were discarded from further analysis (Wolter et al., 2010; Wolter et al., 2012). Typically, 3500 photons were detected per Alexa 647 molecule and frame. Localizations of 845 unspecifically bound, isolated WGA–Alexa-647 molecules were aligned to their center of mass and binned into one histogram. The localization precision (s.d.) was determined as 6.41±0.03 nm (s.e.m. of data fit) by fitting a two-dimensional Gaussian function to the data.

Scanning electron microscopy

After finishing the *d*STORM analysis, nuclear envelopes were fixed for 24 h at 4°C with 2.5% glutaraldehyde (50 mM sodium cacodylate pH 7.2, 50 mM KCl, 2.5 mM $MgCl_2$) and washed three times each for 3 min with 50 mM sodium cacodylate (pH 7.2). Specimens were then fixed for 2 h at 4°C with 2% OsO_4 buffered with 50 mM sodium cacodylate (pH 7.2), washed with distilled H_2O, dehydrated stepwise with acetone and dried using a critical point dryer (CPD 030; BAL-TEC, Liechtenstein). Dried specimens were carbon coated (MED 010 BAL-TEC, Liechtenstein) and analyzed with a JEOL field emission scanning electron microscope (JSM-7500F) at 1 kV using the modus gentle beam high at a working distance of 4.5–5 mm. Overview images were used to recognize the previously super-resolved areas (supplementary material Fig. S3).

Image alignment

Thanks to their highly symmetrical structure, NPCs can be used for intrinsic image alignment. The center of the gp210 or WGA ring structure in *d*STORM and SEM images that matched were identified manually (supplementary material Fig. S4) and used as reference points (landmarks). bUnwarpJ was used for image registration (Arganda-Carreras et al., 2006). Typically, six landmarks in different parts of the *d*STORM and SEM images were used for transformation of a 2.5×2.5 µm^2 image area. Briefly, bUnwarpJ calculates a B-spline transformation for registering two images. GIMP 2.8.10 was used to make the *d*STORM images transparent before correlative overlay with the SEM images.

Quantification of *d*STORM data

First, single NPCs were separated by applying a canny edge filter to the *d*STORM image. The vertices of the resulting mask were used to crop localization sets of single NPCs from the data provided by rapi*d*STORM (Wolter et al., 2010; Wolter et al., 2012). To allocate the whole NPC into single gp210 domains, a multilevel *k*-means algorithm was applied to the localization cloud. Using the known spatial features of the gp210 ring (i.e. the existence of a maximum of eight separated domains and their circular symmetry), starting points for the *k*-means clustering can be provided, minimizing the usual difficulties with *k*-means clustering. First, a mean component analysis (MCA) was performed on the x and y coordinates of all localizations of the single NPC candidate. NPCs exhibiting a ratio of the absolute values of the resulting eigenvectors larger than two were discarded to exclude overlapping pores and other artifacts from the canny edge filter. Afterwards an ellipse was fitted to the localization ring, again using the eigenvectors resulting from the MCA. Starting points were then set by distributing the intended number of domains, N, randomly but (angularly) equidistant along the ellipse. It appeared that lower starting values than five domains were not necessary. A second set of starting points was generated by turning the first set by $N^{-1}\times\alpha$, where α is the angle between two neighboring domains. This procedure is repeated for $N\times[5,6,7,8]$. Subsequently each candidate domain in the current subset was subjected to an Anderson–Darling test (Hamerly and Elkan, 2004) to evaluate whether the current separation was sufficient or not. Briefly, every candidate domain was tested for whether their spatial localization distribution in x and y, respectively, is Gaussian like. If this is not the case for at least one candidate, the current separation state is rejected, and the next parameter set is tried. If there is no successful test for the last parameter set, which is usually the 'eight turned starting points' configuration, the candidate is discarded. This might be the case for candidates that were cropped faulty from the canny edge detector or had insufficient spatial resolution, causing the domains to overlap significantly. Both cases were very rarely apparent. All further analyzing steps following the separation process, for example, production of histograms and localization counts, were conducted directly by additional PYTHON scripts or in OriginPro 8.5 (OriginLab).

Acknowledgements

We thank Christian Stigloher and Thomas Niehörster for help with sample preparation and discussion.

Competing interests

The authors declare no competing interests.

Author contributions

A.L., G.K., S.v.d.L., C.F. and M.S. conceived of and designed the experiments; A.L. and G.K. performed the experiments; C.F. and S.v.d.L. analyzed the data; M.S wrote the paper.

Funding

This work was supported by the Biophotonics Initiative of the Bundesministerium für Bildung und Forschung [grant numbers 13N11019 and 13N12781].

Supplementary material

Supplementary material available online at
http://jcs.biologists.org/lookup/suppl/doi:10.1242/jcs.156620/-/DC1

References

Arganda-Carreras, C., Sánchez Sorzano, Ó., Marabini, R., Carazo, J. M., Ortiz-de Solorzano, C. and Kybic, J. (2006). Consistent and elastic registration of histological sections using vector-spline regularization. *Computer Vision Approaches to Medical Image Analysis* **4241**, 85-95.

Beck, M., Lucić, V., Förster, F., Baumeister, W. and Medalia, O. (2007). Snapshots of nuclear pore complexes in action captured by cryo-electron tomography. *Nature* **449**, 611-615.

Betzig, E., Patterson, G. H., Sougrat, R., Lindwasser, O. W., Olenych, S., Bonifacino, J. S., Davidson, M. W., Lippincott-Schwartz, J. and Hess, H. F. (2006). Imaging intracellular fluorescent proteins at nanometer resolution. *Science* **313**, 1642-1645.

Davis, L. I. and Blobel, G. (1987). Nuclear pore complex contains a family of glycoproteins that includes p62: glycosylation through a previously unidentified cellular pathway. *Proc. Natl. Acad. Sci. USA* **84**, 7552-7556.

Favreau, C., Bastos, R., Cartaud, J., Courvalin, J. C. and Mustonen, P. (2001). Biochemical characterization of nuclear pore complex protein gp210 oligomers. *Eur. J. Biochem.* **268**, 3883-3889.

Gajewski, A., Lourim, D. and Krohne, G. (1996). An antibody against a glycosylated integral membrane protein of the Xenopus laevis nuclear pore complex: a tool for the study of pore complex membranes. *Eur. J. Cell Biol.* **71**, 14-21.

Gerace, L., Ottaviano, Y. and Kondor-Koch, C. (1982). Identification of a major polypeptide of the nuclear pore complex. *J. Cell Biol.* **95**, 826-837.

Hamerly, G. and Elkan, C. (2004). Learning the k in k-means. *Adv. Neural Inf. Process. Syst.* **16**, 281-288.

Heilemann, M., van de Linde, S., Schüttpelz, M., Kasper, R., Seefeldt, B., Mukherjee, A., Tinnefeld, P. and Sauer, M. (2008). Subdiffraction-resolution fluorescence imaging with conventional fluorescent probes. *Angew. Chem. Int. Ed. Engl.* **47**, 6172-6176.

Hess, S. T., Girirajan, T. P. and Mason, M. D. (2006). Ultra-high resolution imaging by fluorescence photoactivation localization microscopy. *Biophys. J.* **91**, 4258-4272.

Hinshaw, J. E. and Milligan, R. A. (2003). Nuclear pore complexes exceeding eightfold rotational symmetry. *J. Struct. Biol.* **141**, 259-268.

Kopek, B. G., Shtengel, G., Xu, C. S., Clayton, D. A. and Hess, H. F. (2012). Correlative 3D superresolution fluorescence and electron microscopy reveal the relationship of mitochondrial nucleoids to membranes. *Proc. Natl. Acad. Sci. USA* **109**, 6136-6141.

Kukulski, W., Schorb, M., Welsch, S., Picco, A., Kaksonen, M. and Briggs, J. A. G. (2011). Correlated fluorescence and 3D electron microscopy with high sensitivity and spatial precision. *J. Cell Biol.* **192**, 111-119.

Lando, D., Endesfelder, U., Berger, H., Subramanian, L., Dunne, P. D., McColl, J., Klenerman, D., Carr, A. M., Sauer, M., Allshire, R. C. et al. (2012). Quantitative single-molecule microscopy reveals that CENP-A(Cnp1) deposition occurs during G2 in fission yeast. *Open Biol.* **2**, 120078.

Löschberger, A., van de Linde, S., Dabauvalle, M. C., Rieger, B., Heilemann, M., Krohne, G. and Sauer, M. (2012). Super-resolution imaging visualizes the eightfold symmetry of gp210 proteins around the nuclear pore complex and resolves the central channel with nanometer resolution. *J. Cell Sci.* **125**, 570-575.

Maimon, T., Elad, N., Dahan, I. and Medalia, O. (2012). The human nuclear pore complex as revealed by cryo-electron tomography. *Structure* **20**, 998-1006.

Morphew, M. K. (2007). 3D immunolocalization with plastic sections. *Methods Cell Biol.* **79**, 493-513.

Müller-Reichert, T., Srayko, M., Hyman, A., O'Toole, E. T. and McDonald, K. (2007). Correlative light and electron microscopy of early Caenorhabditis elegans embryos in mitosis. *Methods Cell Biol.* **79**, 101-119.

Nanguneri, S., Flottmann, B., Horstmann, H., Heilemann, M. and Kuner, T. (2012). Three-dimensional, tomographic super-resolution fluorescence imaging of serially sectioned thick samples. *PLoS ONE* **7**, e38098.

Perkovic, M., Kunz, M., Endesfelder, U., Bunse, S., Wigge, C., Yu, Z., Hodirnau, V.-V., Scheffer, M. P., Seybert, A., Malkusch, S. et al. (2014). Correlative light- and electron microscopy with chemical tags. *J. Struct. Biol.* **186**, 205-213.

Rust, M. J., Bates, M. and Zhuang, X. (2006). Sub-diffraction-limit imaging by stochastic optical reconstruction microscopy (STORM). *Nat. Methods* **3**, 793-796.

Sauer, M. (2013). Localization microscopy coming of age: from concepts to biological impact. *J. Cell Sci.* **126**, 3505-3513.

Schwefel, D., Maierhofer, C., Beck, J. G., Seeberger, S., Diederichs, K., Möller, H. M., Welte, W. and Wittmann, V. (2010). Structural basis of multivalent binding to wheat germ agglutinin. *J. Am. Chem. Soc.* **132**, 8704-8719.

Sochacki, K. A., Shtengel, G., van Engelenburg, S. B., Hess, H. F. and Taraska, J. W. (2014). Correlative super-resolution fluorescence and metal-replica transmission electron microscopy. *Nat. Methods* **11**, 305-308.

Suleiman, H., Zhang, L., Roth, R., Heuser, J. E., Miner, J. H., Shaw, A. S. and Dani, A. (2013). Nanoscale protein architecture of the kidney glomerular basement membrane. *eLife* **2**, e01149.

Szymborska, A., de Marco, A., Daigle, N., Cordes, V. C., Briggs, J. A. G. and Ellenberg, J. (2013). Nuclear pore scaffold structure analyzed by super-resolution microscopy and particle averaging. *Science* **341**, 655-658.

Tsien, R. Y. (1998). The green fluorescent protein. *Annu. Rev. Biochem.* **67**, 509-544.

van de Linde, S., Löschberger, A., Klein, T., Heidbreder, M., Wolter, S., Heilemann, M. and Sauer, M. (2011). Direct stochastic optical reconstruction microscopy with standard fluorescent probes. *Nat. Protoc.* **6**, 991-1009.

Watanabe, S., Punge, A., Hollopeter, G., Willig, K. I., Hobson, R. J., Davis, M. W., Hell, S. W. and Jorgensen, E. M. (2011). Protein localization in electron micrographs using fluorescence nanoscopy. *Nat. Methods* **8**, 80-84.

Wolter, S., Schüttpelz, M., Tscherepanow, M., VAN DE Linde, S., Heilemann, M. and Sauer, M. (2010). Real-time computation of subdiffraction-resolution fluorescence images. *J. Microsc.* **237**, 12-22.

Wolter, S., Löschberger, A., Holm, T., Aufmkolk, S., Dabauvalle, M.-C., van de Linde, S. and Sauer, M. (2012). rapid*STORM*: accurate, fast open-source software for localization microscopy. *Nat. Methods* **9**, 1040-1041.

Dipl. – Phys. Christian Franke
Lehrstuhl für Biotechnologie und Biophysik
Biozentrum, Am Hubland
97074 Würzburg
Germany

Würzburg, 4th July 2017

Manuscript:

Sebastian Letschert, Antonia Göhler, Christian Franke, Nadja Bertleff-Zieschang, Elisabeth Memmel, Sören Doose, Jürgen Seibel, and Markus Sauer.

Super-Resolution Imaging of Plasma Membrane Glycans

Angewandte Chemie International Edition, 53(41):10921-10924, 2014

The contributions of the PhD candidate Christian Franke to the above manuscript involved:

- Design and implementation of early stage data analysis tools
- Analysis and discussion of preliminary results

Christian Franke

S. Letschert
Sebastian Letschert

Antonia Göhler

Nadja Bertleff-Zieschang
i. A. Seibel

Elisabeth Memmel
i.A. Seibel

S. Doose
Sören Doose

Jürgen Seibel

Markus Sauer

Angewandte
Chemie

DOI: 10.1002/ange.201406045

Bioorthogonal Chemistry | Hot Paper

Super-Resolution Imaging of Plasma Membrane Glycans**

Sebastian Letschert, Antonia Göhler, Christian Franke, Nadja Bertleff-Zieschang, Elisabeth Memmel, Sören Doose, Jürgen Seibel,* and Markus Sauer**

Abstract: *Much of the physiology of cells is controlled by the spatial organization of the plasma membrane and the glycosylation patterns of its components, however, studying the distribution, size, and composition of these components remains challenging. A bioorthogonal chemical reporter strategy was used for the efficient and specific labeling of membrane-associated glycoconjugates with modified monosaccharide precursors and organic fluorophores. Super-resolution fluorescence imaging was used to visualize plasma membrane glycans with single-molecule sensitivity. Our results demonstrate a homogeneous distribution of N-acetylmannosamine (ManNAc)-, N-acetylgalactosamine (GalNAc)-, and O-linked N-acetylglucosamine (O-GlcNAc)-modified plasma membrane proteins in different cell lines with densities of several million glycans on each cell surface.*

The glycosylation state of proteins controls their function, localization, and stability.[1,2] Cell-surface glycans are involved in many cell–cell recognition processes, as well as tumor development, and they reflect the developmental stage and the transformation state of a cell.[3–5] Visualization of the glycoprotein patterns in plasma membranes with regard to diseases could thus pave the way for the development of refined diagnostic tools.

However, until now two obstacles have impeded the exploitation of quantitative data concerning the architecture of membrane-associated glycoproteins: the difficulty of selective and efficient labeling of glycosylated membrane proteins, and the resolution limit of optical microscopy. This is of special importance considering the existence of confined plasma membrane compartments, that is, nanodomains or clusters with a supposed size of 5–300 nm that are required for subcompartmentalization and associated functions.[6–10] Recently, the difficulty in labeling glycans by traditional molecular and cell biology techniques has been overcome by the introduction of a bioorthogonal chemical reporter strategy termed "click chemistry".[11]

Herein, the tolerance of mammalian cells to small modifications of monosaccharide precursors is exploited. Upon cellular uptake, azido- or alkyne-modified monosaccharides are covalently incorporated by the biosynthetic machinery into the substrates of glycosyltransferases to create non-native glycans. Once incorporated into components of the cell surface, these azido- or alkyne-modified glycans can be covalently labeled with alkyne- or azido-modified fluorophores, respectively, to form triazole-linked products for the in vitro and in vivo imaging of various glycoproteins.[12–14]

In our study, we combined click chemistry for labeling and super-resolution fluorescence microscopy for visualization of membrane-associated glycoproteins with subdiffraction resolution. For the metabolic labeling of sialic acid containing and mucin-type O-linked glycans, we used analogues of their biosynthetic precursors *N*-acetylmannosamine (ManNAc), and *N*-acetylgalactosamine (GalNAc), respectively; O-GlcNAc-modified plasma membrane proteins were labeled by using a GlcNAc analogue in human osteosarcoma (U2OS) and neuroblastoma (SK-M-NC) cell lines. For subdiffraction resolution fluorescence imaging with single-molecule sensitivity, we used *direct* stochastic optical reconstruction microscopy (*d*STORM).[15–17]

Since the biosynthetic machinery tolerates the addition of chemical reporters to the N-acyl group, we fed cells with the peracetylated monosaccharides *N*-azidoacetylmannosamine (Ac$_4$ManNAz), *N*-azidoacetylgalactosamine (Ac$_4$GalNAz), and *N*-azidoacetylglucosamine (Ac$_4$GlcNAz), which are incorporated into cell-surface glycans upon cell permeation and deacetylation.[12–14] Ac$_4$ManNAz and Ac$_4$GalNAz have been used to visualize sialic acids and mucin-type O-linked glycans in different cell types as well as in living mice and zebrafish.[12–14] Ac$_4$GlcNAz is modified by the GlcNAc salvage pathway enzymes to give uridine diphosphate (UDP)-GlcNAz, which is used as a substrate by the intracellular cytosolic O-GlcNAc transferase (OGT). The resulting modification with O-GlcNAc modulates signaling and regulates protein expression, degradation, and trafficking.[12–14] O-GlcNAc addition is catalyzed by a recently discovered epidermal growth factor (EGF) domain specific O-linked GlcNAc transferase (EOGT).

In a first set of experiments, we optimized the labeling of neuroblastoma cells with different azidoacetyl monosaccharides and alkyne-bearing Alexa Fluor 647 by applying Cu$^{\text{I}}$-catalyzed azide–alkyne cycloaddition in the absence and

---

[*] S. Letschert, Dr. A. Göhler, C. Franke, Priv.-Doz. Dr. S. Doose, Prof. Dr. M. Sauer
Department of Biotechnology & Biophysics
Julius Maximilian University Wuerzburg
Am Hubland, 97074 Würzburg (Germany)
E-mail: soeren.doose@uni-wuerzburg.de
m.sauer@uni-wuerzburg.de
Homepage: http://www.super-resolution.de

N. Bertleff-Zieschang, E. Memmel, Prof. Dr. J. Seibel
Institute of Organic Chemistry
Julius Maximilian University Wuerzburg
Am Hubland, 97074 Würzburg (Germany)
E-mail: seibel@chemie.uni-wuerzburg.de

[**] We thank L. Pliess and P. Geßner for assistance in cell culture. This work was supported by the Biophotonics Initiative of the Bundesministerium für Bildung und Forschung (grants 13N11019 and 13N12507, M.S.), the Deutsche Forschungsgemeinschaft (DFG SA829/13-1 to M.S. and DFG Se 1410/6-1 to J.S.) and the Universität Bayern e.V. (E.M.), FCI (N.B.-Z.), ISF and IRG (S.D.).

Supporting information for this article is available on the WWW under http://dx.doi.org/10.1002/anie.201406045.

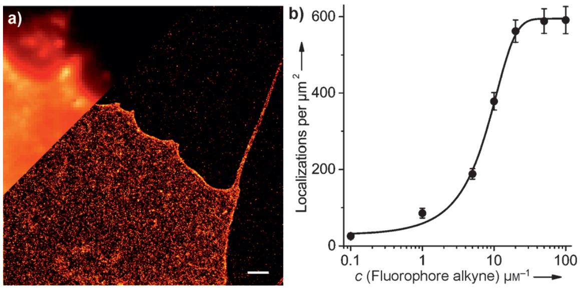

Figure 1. Membrane glycans of SK-N-MC neuroblastoma cells stained through the metabolic incorporation of azido-sugar analogues followed by copper-catalyzed azide–alkyne cycloaddition (CuAAC). a) A standard fluorescence image (upper left corner) and a high-resolution *d*STORM image (main image) of Ac$_4$GalNAz-treated neuroblastoma cells stained with alkyne-bearing Alexa Fluor 647. b) Localization densities of Ac$_4$GlcNAz-treated neuroblastoma cells for different alkyne–fluorophore concentrations. At an alkyne–fluorophore concentration of about 20 µM, the number of localizations per unit of membrane area as determined by *d*STORM becomes saturated. Scale bar: 1 µm.

presence of Cu^{I} and the Cu^{I}-stabilizing reagent Tris(3-hydroxypropyltriazolylmethyl)amine (THPTA). Cells were incubated with 25 µM aqueous solutions of modified monosaccharides in their culture medium for two days and then labeled and fixed in 4% formaldehyde with 0.2% glutaraldehyde at 25°C to minimize the lateral diffusion of membrane molecules (Figure 1, and Figures S1, S2 in the Supporting Information).[18] A fluorophore concentration of 20 µM and an incubation time of 5 min proved to be sufficient for efficient labeling in the presence of Cu^{I} and THPTA (Figure 1 b). Higher fluorophore concentrations do not result in higher labeling efficiencies.

The resulting *d*STORM images of Ac$_4$ManNAz-, Ac$_4$GalNAz-, and Ac$_4$GlcNAz-derivatized plasma membrane proteins demonstrate substantially improved resolution compared to widefield fluorescence images and reveal the localization of single glycans homogeneously distributed over the entire basal plasma membrane of U2OS and SK-*N*-MC cells (Figure 1, Figure 2, and Figure S3 in the Supporting Information). The use of blocking agents (e.g., bovine serum albumin) to reduce unspecific binding of the fluorophores to the surface was not necessary. In control experiments, the number of non-specific localizations was found to be less than 1% (Figure S4 in the Supporting Information). To exclude the influence of the addition of copper ions and THPTA on the distribution of glycoconjugates on the basal plasma membrane, we performed copper-free experiments with Alexa Fluor 647 conjugated to dibenzocyclooctyne (DIBO) for strain-promoted azide–alkyne cycloaddition. Furthermore, we imaged the apical membrane of cells by *d*STORM to investigate the influence of the proximal coverslip. The resulting *d*STORM images appear identical and display homogeneously distributed glycans in the apical plasma membrane as well (Figure S5 in the Supporting Information). To extract reliable estimates for localization densities, 12–32 cells were imaged in all experiments and averaged data are presented (Figure 2 a). Interestingly, we do not see any characteristic glycan nanodomains or clusters as have been identified in recent super-resolution imaging studies of membrane proteins.[9,10,19–21] The calculation of Ripley's K-function and nearest-neighbor distance distributions only reveals characteristic clusters on the 25 nm length scale that originate from the repeated localization of a single fluorophores (Figure S6 in the Supporting Information). Ripley's K-function might indicate some more clustering for GalNAz and ManNAz glycoconjugates when compared with simulated data for complete spatial randomness. However, no characteristic length scale could reproducibly be identified either visually or by statistical analysis (Figure S6 in the Supporting Information).

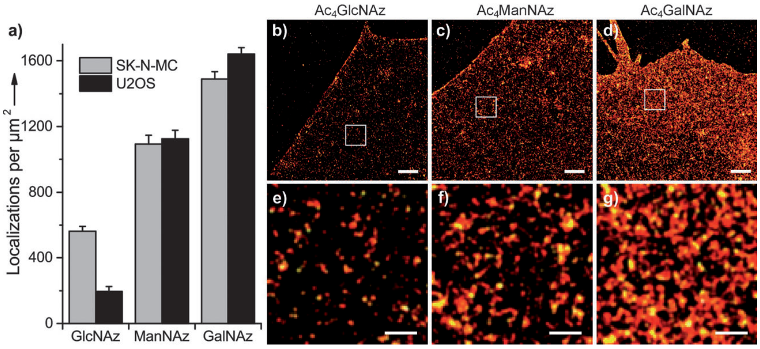

Figure 2. Super-resolution imaging and analysis of cell-surface glycoproteins. SK-N-MC neuroblastoma cells and U2OS cells were fed with one of the reactive azido sugars (Ac$_4$GlcNAz, Ac$_4$ManNAz, or Ac$_4$GalNAz) and then visualized and analyzed by click chemistry and *d*STORM. a) Localization density of membrane-associated glycans labeled with Alexa Fluor 647 (20 µM). Error bars represent the standard error of the mean of 12–32 imaged cells. b–d) *d*STORM images of glycoconjugates in the basal membrane of SK-*N*-MC neuroblastoma cells. Enlarged images of the sections in white boxes are shown in the lower panels (e–g). Scale bars: 1 µm (b–d) and 200 nm (e–g).

Our *d*STORM images further demonstrate that the plasma membranes of neuroblastoma and osteosarcoma cells exhibit the highest density of labeled glycans for GalNAz glycoconjugates, with 1500–1700 localizations per µm^2, followed by ManNAz-derived glycoconjugates, with approximately 1100 localizations per µm^2 (Figure 2 a). GlcNAz glycoconjugates show the lowest density with a peculiar dependence on the investigated cell type (Figure 2 a). For neuroblastoma cells, we find on average approximately 600 localizations per µm^2, whereas in osteosarcoma cells (U2OS), the density is substantially lower (Figure 2 a). While Ac$_4$GalNAz and Ac$_4$ManNAz modify various glycoproteins and glycolipids, Ac$_4$GlcNAz modifies the extracellular epidermal growth factor (EGF)-like domain of just a handful of membrane proteins,[22,23] thus explaining the lower localization density.

To estimate the number of localizations per fluorophore, spots with repeated localizations of isolated fluorophore-labeled glycans were grouped by using the tracking function of rapi*d*STORM.[24,25] To ensure that only single fluorophores were analyzed, we decreased the fluorophore concentration to 10 nM to give a very low labeling density (< 20 localizations μm^{-2}). Fluorescent spots that were switched on for longer than 10 frames were discarded from further analysis. The remaining spatially isolated fluorescent spots were tracked over the whole image stack (15000 frames) within a defined area (tracking radius) to determine the number of localizations per spot. In order to determine the optimal tracking radius, we varied the tracking radius between 0 and 200 nm. By using the mean values of the resulting distributions under saturation conditions, we extracted 2.7 ± 0.4 localizations per isolated fluorescent spot (Figure 3a and Figure S7 in the Supporting Information). By aligning the coordinates of the localizations for each isolated fluorescent spot to its center of mass, we generated a 2D histogram of all localizations, which resembles a Gauss distribution. The standard deviation of the Gauss function fitted to the projection in the *xy* plane reveals an average localization precision of 10.7 ± 0.1 nm (Figure 3b).

By using the value of 2.7 ± 0.4 localizations per isolated fluorescent spot, we can now estimate the density of GalNAz and ManNAz glycans on the basal plasma membrane to be approximately 600 μm^{-2} and 400 μm^{-2}, respectively. Accordingly, we estimate there to be approximately 220 μm^{-2} and 70 μm^{-2} GlcNAz glycans on the basal plasma membrane of neuroblastoma and osteosarcoma cells, respectively. With a basal plasma membrane area of approximately 2000 μm^2, these values correspond to around 5×10^6 fluorophore-labeled plasma membrane glycans per neuroblastoma cell (considering all three glycan modifications and including the apical and basal sides of the cell). Considering other studies, in which it has been estimated that derivatives of azidoacetyl monosaccharides replace only 4–56 % of their natural analogues depending on the cell line used,[26,27] the plasma membrane of a single cell may easily contain over 10 million glycans.[28]

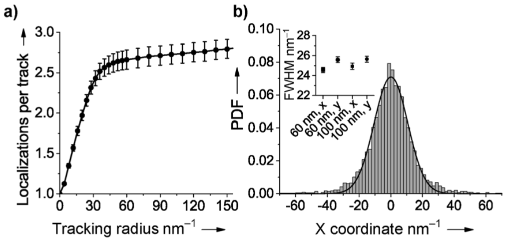

Figure 3. Quantitative analysis of *d*STORM data. a) Spots from isolated fluorophore-labeled glycans were tracked with different tracking radii over all frames. To be sure that only single fluorophores were analyzed, $Ac_4GlcNAz$ treated SK-N-MC cells were incubated with only 10 nM alkyne-bearing Alexa Fluor 647. The curve saturates at a level of 2.68 ± 0.12 ($\pm$SEM, $n = 12$ cells), which is the mean number of localizations per track. b) Probability density function (PDF) of all localizations belonging to a fluorescent spot, that is, an isolated fluorophore-labeled glycan, with a full width at half maximum (FWHM) of 25.2 ± 0.3 nm (mean ± standard error from the four estimates, inset), which corresponds to a localization precision (σ) of 10.7 ± 0.1 nm.

To conclude, our data demonstrate that the cell surface of mammalian cells is homogeneously covered with several million glycans. None of the glycoconjugates form plasma membrane clusters or nanodomains on the length scale of ten to several hundred nanometers. Since the spatial and temporal organization and functions of all of these mammalian glycans is diverse, super-resolution imaging methods in combination with click chemistry hold promise for a refined understanding of the essential cellular functions associated with cell-surface glycans.

Received: June 10, 2014

Keywords: bioorthogonal chemistry · click chemistry · membrane glycans · microscopy · super-resolution imaging

---

[1] H. H. Freeze, *Nat. Rev.* **2006**, *7*, 537–549.
[2] G. W. Hart, M. P. Housley, C. Slawson, *Nature* **2007**, *446*, 1017–1022.
[3] K. Ohtsubo, J. D. Marth, *Cell* **2006**, *126*, 855–867.
[4] R. S. Haltiwanger, J. B. Lowe, *Annu. Rev. Biochem.* **2004**, *73*, 491–537.
[5] M. M. Fuster, J. D. Esko, *Nat. Rev. Cancer* **2005**, *5*, 526–542.
[6] K. Simons, M. J. Gerl, *Nat. Rev. Mol. Cell Biol.* **2010**, *11*, 688–699.
[7] A. Kusumi, T. K. Fujiwara, R. Chadda, M. Xie, T. A. Tsunoyama, Z. Kalay, R. S. Kasai, K. G. N. Suzuki, *Annu. Rev. Cell Dev. Biol.* **2012**, *28*, 215–250.
[8] B. F. Lillemeier, J. R. Pfeiffer, Z. Surviladze, B. S. Wilson, M. M. Davis, *Proc. Natl. Acad. Sci. USA* **2006**, *103*, 18992–18997.
[9] C. Eggeling, C. Ringemann, R. Medda, G. Schwarzmann, K. Sandhoff, S. Polyakova, V. N. Belov, B. Hein, C. von Middendorf, A. Schönle, S. W. Hell, *Nature* **2009**, *457*, 1159–1162.
[10] G. van den Bogaart, K. Meyenberg, H. J. Risselada, H. Amin, K. I. Willig, B. E. Hubrich, M. Dier, S. W. Hell, H. Grubmüller, U. Diederichsen, R. Jahn, *Nature* **2011**, *479*, 552–555.
[11] M. Boyce, C. R. Bertozzi, *Nat. Methods* **2011**, *8*, 638–642.
[12] S. T. Laughlin, C. R. Bertozzi, *Proc. Natl. Acad. Sci. USA* **2009**, *106*, 12–17.
[13] J. A. Prescher, D. H. Dube, C. R. Bertozzi, *Nature* **2004**, *430*, 873–877.
[14] S. T. Laughlin, J. M. Baskin, S. L. Amacher, C. R. Bertozzi, *Science* **2008**, *320*, 664–667.
[15] M. Heilemann, S. van de Linde, M. Schüttpelz, R. Kasper, B. Seefeldt, A. Mukherjee, P. Tinnefeld, M. Sauer, *Angew. Chem.* **2008**, *120*, 6266–6271; *Angew. Chem. Int. Ed.* **2008**, *47*, 6172–6176.
[16] S. van de Linde, A. Löschberger, T. Klein, M. Heidbreder, S. Wolter, M. Heilemann, M. Sauer, *Nat. Protoc.* **2011**, *6*, 991–1009.
[17] P. Zessin, K. Finan, M. Heilemann, *J. Struct. Biol.* **2012**, *177*, 344–348.
[18] K. A. K. Tanaka, K. G. N. Suzuki, Y. M. Shirai, S. T. Shibutani, M. S. M. Miyahara, H. Tsuboi, M. Yahara, A. Yoshimura, S. Mayor, T. K. Fujiwara, A. Kusumi, *Nat. Methods* **2010**, *11*, 865–866.

[19] J. J. Sieber, K. I. Willig, C. Kutzner, C. Gerding-Reimers, B. Harke, G. Donnert, B. Rammner, C. Eggeling, S. W. Hell, H. Grubmüller, Th. Lang, *Science* **2007**, *317*, 1072 – 1076.

[20] H. Mizuno, M. Abe, P. Dedecker, A. Makino, S. Rocha, Y. Ohno-Iwashita, J. Hofkens, T. Kobayashi, T. Miyawaki, *Chem. Sci.* **2011**, *2*, 1548 – 1553.

[21] D. J. Williamson, D. M. Owen, J. Rossy, A. Magenau, M. Wehrmann, J. J. Gooding, K. Gaus, *Nat. Immunol.* **2011**, *12*, 655 – 662.

[22] Y. Sakaidani, T. Nomura, A. Matsuura, M. Ito, E. Suzuki, K. Murakami, D. Nadano, T. Matsuda, K. Furukawa, T. Okajima, *Nat. Commun.* **2011**, *2*, 583.

[23] J. F. Alfaro, C.-X. Gong, M. E. Monroe, J. T. Aldrich, T. R. W. Clauss, S. O. Purvine, Z. Wang, D. G. Camp, J. Shabanowitz, P. Stanley, G. W. Hart, D. F. Hunt, F. Yang, R. D. Smith, *Proc. Natl. Acad. Sci. USA* **2012**, *109*, 7280 – 7285.

[24] S. Wolter, M. Schüttpelz, M. Tscherepanow, S. van de Linde, M. Heilemann, M. Sauer, *J. Microsc.* **2010**, *237*, 12 – 22.

[25] S. Wolter, A. Löschberger, T. Holm, S. Aufmkolk, M.-C. Dabauvalle, S. van de Linde, M. Sauer, *Nat. Methods* **2012**, *9*, 1040 – 1041.

[26] S. J. Luchansky, S. Argade, B. K. Hayes, C. R. Bertozzi, *Biochemistry* **2004**, *43*, 12358 – 12366.

[27] P. V. Chang, X. Chen, C. Smyrniotis, A. Xenakis, T. Hu, C. R. Bertozzi, P. Wu, *Angew. Chem.* **2009**, *121*, 4090 – 4093; *Angew. Chem. Int. Ed.* **2009**, *48*, 4030 – 4033.

[28] R. D. Cummings, J. M. Pierce, *Chem. Biol.* **2014**, *21*, 1 – 15.

Dipl. – Phys. Christian Franke
Lehrstuhl für Biotechnologie und Biophysik
Biozentrum, Am Hubland
97074 Würzburg
Germany

Würzburg, 4th July 2017

Manuscript:

Katharina Schücker, Thorge Holm, Christian Franke, Markus Sauer, and Ricardo Benavente.

Elucidation of synaptonemal complex organization by superresolution imaging with isotropic resolution

Proceedings of the National Academy of Sciences, 112(7):2029-2033, 2015

The contributions of the PhD candidate Christian Franke to the above manuscript involved:

- Conceptual design and execution of the described quantification approach
- Implementation of the used software
- Meta-analysis of all reported 6 SNC component localization data
- Contribution to the manuscript draft, especially Figure 4 and section 'Postprocessing of *d*STORM Data for Average Protein Position Determination'

Christian Franke

Katharina Schücker

Thorge Holm

Markus Sauer

Ricardo Benavente

Elucidation of synaptonemal complex organization by super-resolution imaging with isotropic resolution

Katharina Schücker[a,1], Thorge Holm[b,1], Christian Franke[b], Markus Sauer[b,2], and Ricardo Benavente[a,2]

Departments of [a]Cell and Developmental Biology and [b]Biotechnology and Biophysics, Biocenter, University of Würzburg, 97074 Würzburg, Germany

Edited* by Jennifer Lippincott-Schwartz, National Institutes of Health, Bethesda, MD, and approved December 19, 2014 (received for review August 2, 2014)

Synaptonemal complexes (SCs) are meiosis-specific multiprotein complexes that are essential for synapsis, recombination, and segregation of homologous chromosomes, but the molecular organization of SCs remains unclear. We used immunofluorescence labeling in combination with super-resolution imaging and average position determination to investigate the molecular architecture of SCs. Combination of 2D super-resolution images recorded from different areas of the helical ladder-like structure allowed us to reconstruct the 3D molecular organization of the mammalian SC with isotropic resolution. The central element is composed of two parallel cables at a distance of ∼100 nm, which are oriented perpendicular to two parallel cables of the lateral element arranged at a distance of ∼220 nm. The two parallel cable elements form twisted helical structures that are connected by transversal filaments by their N and C termini. A single-cell preparation generates sufficient localizations to compile a 3D model of the SC with nanometer precision.

super-resolution imaging | synaptonemal complex | *d*STORM | meiosis | average position determination

The synaptonemal complex (SC) is a well-preserved meiosis-specific protein complex among different species (1, 2). As revealed by transmission electron microscopy (TEM), when fully assembled, SCs are 200-nm-wide, ribbon-like structures that extend all along a chromosome bivalent (3, 4). SCs have a characteristic ladder-like organization that is highly conserved through evolution and consists of two lateral elements (LEs), at which chromatin of homologous chromosomes is attached, and a central region (CR). The CR holds the homologous chromosomes together and is made up of numerous transversal filaments (TFs) and the central element (CE).

At present, seven protein components of the synaptonemal complex have been identified in mammals, namely, the LE proteins SYCP2 and SYCP3 (5, 6); the TF protein SYCP1 (7); and the CE-specific proteins SYCE1, SYCE2, SYCE3, and TEX12 (8–10) (Figs. S1 and S2). However, in addition to the identification of SC protein components and the investigation of interaction partners, the establishment of a model of the molecular architecture remains indispensable for the understanding of its function and assembly process. Due to the resolution limit of conventional fluorescence microscopy, information about the molecular organization of SCs has been mainly obtained by immunogold EM (11). In standard immunogold EM preparations, gold particles are localized with nanometer resolution and the localization precision is mainly limited by the size of the primary and secondary IgG antibodies and the gold signal density (12–14). However, sample preparation is time-consuming and quantitative analysis of the signal is tedious because of the low binding efficiency of gold-labeled antibodies. Because the structural resolution is also determined by the labeling density (15), immunogold EM cannot visualize the different SC proteins as continuous structures. Therefore, the construction of localization maps of different proteins within the SC by immunogold EM remains challenging.

Recent advances in super-resolution imaging based on single-molecule localization (16, 17) provide spatial resolutions that are well below the diffraction limit, approaching virtually molecular resolution. In addition, fluorophore-labeled antibodies exhibit a higher binding affinity enabling the visualization of SC proteins as continuous structures. Hence, in combination with particle averaging methods, single-molecule localization microscopy can deliver localization maps of different proteins of multiprotein complexes with high precision (18, 19).

Because meiotic germ cells can be prepared for microscopic analysis and highly specific antibodies directed against the different components are available, the SC is predestinated for structure determination using single-molecule localization microscopy. In this work, we used one- and two-color single-molecule localization microscopy by *direct* stochastic optical reconstruction microscopy (*d*STORM) (20, 21) to elucidate the molecular organization of the helical SC structure with isotropic nanometer precision.

Results and Discussion

***d*STORM Can Resolve Single Protein Strands of the SC with Nanometer Precision.** As demonstrated in previous studies, SC substructures (LEs and CR) cannot be resolved as individual structures in confocal laser scanning microscopy images. Different SC proteins appear to colocalize on a single strand (Fig. 1 *A–D*). In clear contrast, LEs and the CR are easily resolved as separate strands using SYCP3- and SYCP1-specific antibodies and *d*STORM (Fig. 1 *E–L*). Notably, *d*STORM can resolve the different spatial positions of the N and C termini of the TF protein SYCP1 (Fig. 2 *M–P*). TFs are built up of SYCP1 homodimers, and previous experiments have indicated that the C-terminal ends of SYCP1 dimers localize in LEs, whereas the N termini of SYCP1 dimers interact in the CE (7, 15, 22, 23). Our data confirm that the N termini localize in the CE. Furthermore, the C termini localize to

Significance

Synaptonemal complexes (SCs) are meiosis-specific, 200-nm-wide, ladder-like structures that are essential for synapsis, recombination, and segregation of homologous chromosomes. Despite its importance for the spatial organization of individual components during meiosis, the molecular architecture of the SC is still unknown. We used super-resolution imaging by *direct* stochastic optical reconstruction microscopy (*d*STORM), which provides subdiffraction resolution for structural investigation of the SC. The helical ladder-like structure allowed us to reconstruct the 3D molecular organization of the mammalian SC from 2D “frontal” and “lateral” views with isotropic resolution. In combination with particle averaging, we managed to elucidate the molecular organization of the mammalian SC with nanometer precision and unraveled previously unknown details of its molecular architecture.

Author contributions: M.S. and R.B. designed research; K.S. and T.H. performed research; K.S., T.H., and C.F. analyzed data; and K.S., T.H., C.F., M.S., and R.B. wrote the paper.

The authors declare no conflict of interest.

*This Direct Submission article had a prearranged editor.

[1] K.S. and T.H. contributed equally to this work.

[2] To whom correspondence may be addressed. Email: m.sauer@uni-wuerzburg.de or benavente@biozentrum.uni-wuerzburg.de.

This article contains supporting information online at www.pnas.org/lookup/suppl/doi:10.1073/pnas.1414814112/-/DCSupplemental.

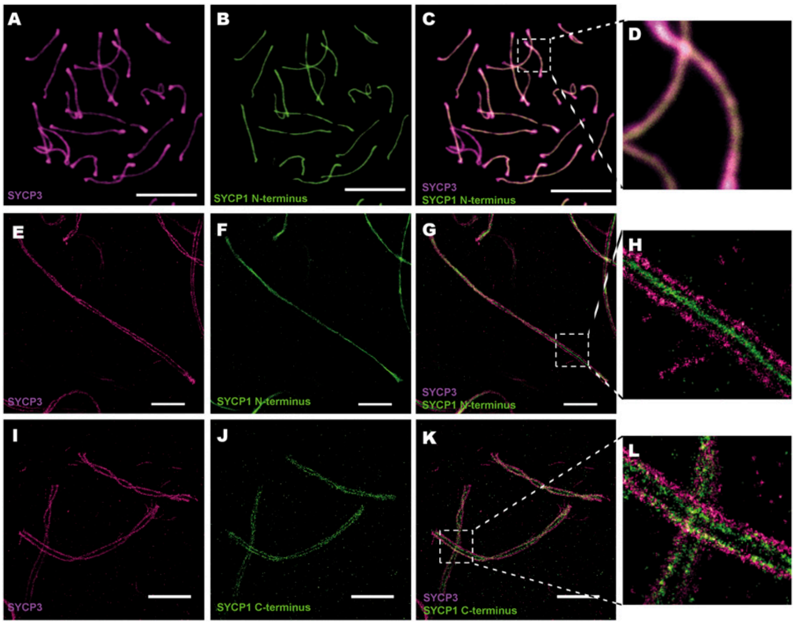

Fig. 1. Fluorescence imaging of SCs by standard and super-resolution imaging. Confocal laser scanning microscopy images (*A*–*D*) and *d*STORM images (*E*–*L*) are shown. (*A*) SYCP3 labeled with Texas Red. (*B*) SYCP1 N terminus labeled with Al488. (*C* and *D*) Overlay of *A* and *B* plus a magnified view. (*E*) SYCP3 labeled with Al647. (*F*) SYCP1 N terminus labeled with Al532. (*G* and *H*) Overlay of *E* and *F* plus a magnified view. (*I*) SYCP3 labeled with Al647. (*J*) SYCP1 C terminus labeled with Al532. (*K* and *L*) Overlay of *I* and *J* plus a magnified view. (Scale bars: *A*–*C*, 10 μm; *E*–*G* and *I*–*K*, 2 μm.)

the inner edge of the LEs (Fig. 1 *E*–*L*), indicating that the interaction of TFs with LE components takes place close to here and not deep in the LE. Consistent with immunogold EM and biochemical approaches, SYCP1 N termini overlap in the CE (15, 22, 23).

Our data also provide previously unidentified information about the molecular organization of proteins in the respective SC substructures. Regarding LEs, previous immunogold EM data suggested that SYCP2 is not homogeneously distributed in the LEs, as is the case for SYCP3, but enriched toward the inner edge of the LEs (22, 24). However, with the resolution provided by *d*STORM, the two proteins SYCP2 and SYCP3 appear to colocalize along the axial LE structures (Fig. 2 *A*–*D*).

To elucidate the molecular organization of the SC with nanometer precision and compile a molecular model, we determined the average positions of fluorescent probes with respect to the center of the helical structure (Fig. S3). To obtain 3D information about the spatial and axial localization of the different SC proteins, we did not use astigmatic (25) or biplane (26) imaging but took advantage of the fact that the SC shows a twisted helical structure. Imaging of the twisted and nontwisted areas allows the reconstruction of 3D protein maps from "frontal" and "lateral" 2D *d*STORM images, respectively, with isotropic resolution (Figs. 2 and 3). For quantitative analysis of the frontal and lateral distribution of SC proteins, one-color *d*STORM experiments were used exploiting the fact that the experimental conditions can be optimized for one fluorophore, Alexa Fluor 647 (Al647) in this case (20, 21). This approach allowed us to detect, on average, ∼2,200 fluorescence photons per frame and single fluorescent probe, resulting in a localization precision of <10 nm.

Advanced 3D Model Emerges from *d*STORM Analysis. Advantageously, a single-cell preparation generates sufficient localizations to compile a 3D model of SC proteins with isotropic nanometer precision (Fig. 4 and Movie S1). The *d*STORM images of SC frontal views show a narrow monomodal signal distribution for the SYCP1 N termini with a width of 39.8 ± 1.1 nm (SD) (Fig. 4*A* and Fig. S4*I*), which is consistent with the notion that the SYCP1 N termini are localized to the very center of the CR (Figs. 1*H*, 2*P*, and 3 *D*–*F*). Available data suggest that SYCE3 binds directly to SYCP1, although the binding site is not known (10, 11). The SYCE3 signal distribution (Figs. 2 *H* and *L* and 3 *A*–*C*) is also monomodal, but wider [67.8 ± 2.1 nm (SD)] than the signal distribution of SYCP1 N termini (dotted lines of SYCP1 N termini and SYCE3 localizations in the frontal view are shown in Fig. 4*A* and Fig. S4*I*). This observation is in agreement with immunogold EM data (10) and might imply that SYCE3 binding to SYCP1 is not restricted to its N terminus. The signal distribution of SYCE2 [63.3 ± 2.1 nm (SD)] is slightly, but significantly, more narrow compared with SYCE3 and overlaps with the SYCP1 N terminus signal in agreement with previous coimmunoprecipitation experiments (9, 11) (Fig. 4 and Fig. S4*H*). The signal distribution of SYCE1 is 54.8 ± 2.8 nm (i.e., still narrower compared with SYCE2) (Fig. S4*G*). However, because the localization distributions clearly overlap, SYCE1 can interconnect with other CE proteins (Fig. 4).

The *d*STORM images of the twisted areas (lateral views) revealed bubbles (i.e., areas with bimodal distributions of SYCE1, SYCE2, SYCE3, and SYCP1 N termini) (Figs. 3 and 4*B* and Fig. S4). At these sites, the signals split into two parallel lines separated by a small interspace (Figs. 2*L*, 3, and 4*B*). The distribution of SYCP1 N termini and SYCE3, SYCE2, and SYCE1 localizations depicts two helical cables separated by 99.1 ± 4.8 nm (SD), 105.5 ± 5.3 nm (SD), 107.0 ± 4.6 nm (SD), and 96.7 ± 8.8 nm (SD), respectively, in lateral views (Fig. 4*B* and Fig. S4). The parallel cables of the CE are oriented perpendicular to the parallel cables of the LE. Here, it has to be pointed out that the degree of the dip in the bimodal distributions of these CE proteins can be affected by the size of the antibodies and the corresponding restricted accessibility of protein epitopes. The appearance of a bimodal distribution of all central proteins in lateral views independent of their relative positions (Fig. 4*B*) demonstrates the existence of at least two longitudinal cables in the CE composed of SYCP1,

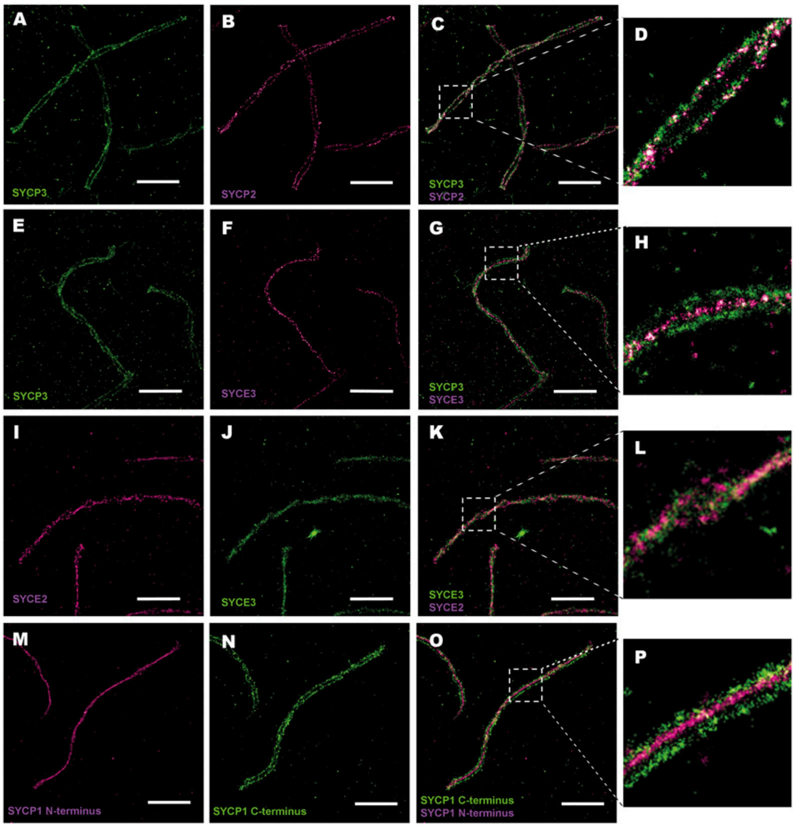

Fig. 2. Two-color *d*STORM images of the SC. (*A*) SYCP3 labeled with Al532. (*B*) SYCP2 labeled with Al647. (*C* and *D*) Overlay of *A* and *B* and a magnified view. (*E*) SYCP3 labeled with Al532. (*F*) SYCE3 labeled with Al647. (*G* and *H*) Overlay of *E* and *F* and a magnified view. (*I*) SYCE2 labeled with Al647. (*J*) SYCE3 labeled with Al532. (*K* and *L*) Overlay of *I* and *J* and a magnified view. (*M*) SYCP1 N terminus labeled with Al647. (*N*) SYCP1 C terminus labeled with Al532. (*O* and *P*) Overlay of *M* and *N* and a magnified view. (Scale bars: 2 μm.)

SYCE3, SYCE2, and SYCE1 that overlap axially in *d*STORM images taken from frontal views of the SC (Figs. 2 *I–L*, 3, and 4 and Fig. S4). In previous immunogold EM studies, no indication for a bimodal distribution of either of these proteins has ever been obtained. However, our results are in agreement with previous TEM data showing that TFs are organized in more than one layer (3, 4, 8–10, 15, 23, 27) (Fig. S2).

Both proteins of the LEs, SYCP3 and SYCP2, are arranged as two cables separated by 221.6 ± 6.1 nm (SD) and 218.5 ± 6.4 nm (SD), respectively (Figs. 2 *A–D* and 4*A*). SYCP3 and SYCP2, showing distribution widths of 55.8 ± 2.3 nm (SD) and 51.2 ± 1.2 nm (SD), respectively, colocalize on the LEs (Fig. 4*A* and Fig. S4 *B* and *D*). The helical LE structure surrounds the CR proteins SYCP1, SYCE3, SYCE2, and SYCE1, which are also arranged as two vertical twisted cables. Overall, the CR exhibits a width of 148.2 ± 2.6 nm (SD), as defined by the average positions of the two SYCP1 C-terminal signals (Fig. 4*A*). The C-terminal SYCP1 signal distribution shows a width of 45.2 ± 1.5 nm (SD) (Fig. 4*A*). With typical data sizes of five to seven SCs investigated per prepared cell nucleus, the SE of position determination is in the range of 0.6–2.4 nm.

Our study demonstrates that the SC represents ideal requirements for 3D molecular structure investigation by single-molecule localization microscopy (Fig. 4*C* and Movie S1). It shows a helical structure allowing position determination with isotropic resolution, it can easily be prepared on coverslips, its protein components can specifically be labeled by antibodies with low background, and a single preparation delivers enough data for model compilation with low statistical error. We predict that future single-molecule localization microscopy studies using selected combinations of antibodies will allow even deeper insights into the molecular organization of the SC and its interaction with other multiprotein complexes of the recombination machinery and the nuclear envelope.

Materials and Methods

Details on material and methods can be found in *SI Material and Methods*. Animal care was approved by the regulatory agency of the city of Würzburg (reference FB VVL 568/300-1870/13; according to §11/1 no. 1 of the German Animal Welfare Act, German Ministry of Agriculture, Health and Economics Cooperation).

Murine Spermatocyte Cell Spread Preparation. For cell spreading, we dissected testes from WT mice and followed the protocol described by de Boer et al. (28). For *d*STORM analysis, we used coverslips (24 × 60 mm) that we coated with 0.01% (wt/vol) poly-L-lysine for 5 min. We preferred coverslips instead of slides for SC spreading, because coverslips allow the use of total internal reflection fluorescence (TIRF) or highly inclined and laminated optical sheet (HILO) illumination schemes (29).

Photoswitching Buffer. For photoswitching, a 100 mM β-mercaptoethylamine buffer (MEA; Sigma) in PBS with a pH of 7.4–7.7 for one-color measurements (Al647) and a pH of 8.4–8.5 for two-color experiments (Al647 and Al532) was used. For recordings that were used for distance measurements, an oxygen scavenger system containing 10% (wt/vol) glucose and 0.5 mg/mL glucose oxidase was used.

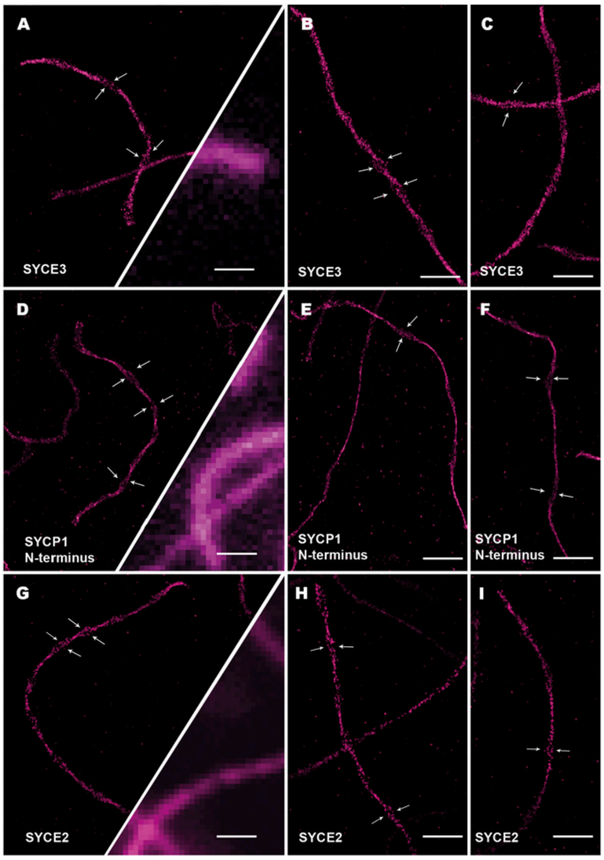

Fig. 3. Lateral view *d*STORM images of SYCE3, SYCP1, and SYCE2 reveal two parallel lines separated by ~100 nm. SYCE3 (*A*–*C*), the SYCP1 N terminus (*D*–*F*), and SYCE2 (*G*–*I*) were labeled with Al647. In *A* (*Lower Right*), *D* (*Lower Right*), and *G* (*Lower Right*), conventional TIRF wide-field fluorescence images are shown for resolution comparison. The arrows illustrate regions where the SC is twisted and seen from the side (lateral views). (Scale bars: 1 μm.)

Super-resolution Imaging. Super-resolution imaging by *d*STORM was performed using an inverted wide-field fluorescence microscope as described in more detail by van de Linde et al. (21). Briefly, for excitation of Al647 and Al532, a 639-nm OPSLaser-Diode System (Genesis MX639-1000 STM; Coherent) and a 514-nm OPSLaser-Diode System (Genesis MX514 STM; Coherent) were used. Al647 was always imaged before Al532 to minimize photobleaching. Lasers were spectrally cleaned by bandpass filters (FF01-642/10-25; Semrock or ZET 514/10; Chroma) and overlaid by a LaserMUX filter (LM01-552; Semrock). Laser beams were widened and focused onto the back focal plane of the microscope objective (APON 60XOTIRF; Olympus) by a lens system assembled with 25-mm (G322284000; Qioptiq) and 120-mm (G322303000; Qioptiq) focal length achromatic lens. The laser beam is directed into the back port of the inverse microscope (IX71; Olympus) by a broad-band dielectric mirror (KCB2 and BB2-E02; Thorlabs) and is reflected into the objective by a triple-band dichroic beam splitter (FF425/532/656-Di01; Semrock). The lens system and the dielectric mirror are mounted on a custom-made linear translation stage to switch between EPI (illumination and detection on one side), HILO, and TIRF illumination. To minimize sample drift, the objective and the sample are mounted onto the nosepiece stage (IX2-NPS; Olympus). The fluorescent light from the sample is collected by the same objective and is transmitted by the dichroic beam splitter and a triple-band detection filter (Em01-R442/514/647; Semrock). Images of the yellow Al532 and red Al647 dyes are separated and spectrally filtered by a dichroic beam splitter (630dcxr; Chroma) and dichroic bandpass filters (FF01-582/75 and FF01-697/75; Semrock) mounted to a dual-camera adaptor (TuCam; Andor) onto two EM CCD cameras (iXon Ultra 897; Andor).

Conventional wide-field fluorescence images were taken at low laser intensities to prevent photoswitching and at exposure times depending on fluorescence intensities between 10 and 1,000 ms. For *d*STORM imaging, data stacks consisting of 15,000–30,000 images were recorded with frame rates of 50–100 frames per second and 10- to 20-ms exposure times, respectively, at excitation intensities of 1–3 kW·cm^{-2}.

Image Reconstruction and Alignment of Two-Color Imaging. Images were reconstructed using rapid*d*STORM 3.2 (30, 31). The *d*STORM images are shown with a pixel size of 10 nm. For two-color imaging, Al647 was recorded first and both cameras were aligned using multifluorescent beads. The image generated by Al532 was transformed onto the image of Al647 using landmarks (bUnwapJ; Fiji) (32). Chromatic shift between the two images of the two cameras was corrected using cross-correlations/elastic transformations.

Postprocessing of *d*STORM Data for Average Protein Position Determination. To gain quantitative information on the diameter of single strands, as well as the distance of potential double strands, an in-house written python routine was exercised (Fig. S3). First, candidates for single complexes were separated by applying a canny edge filter to the superresolved picture. The vertices of the resulting mask were used to crop localization sets of these candidates out of the rapid*d*STORM output. Candidates consisting of crossing complexes or featuring extreme curvature, close to a full circle, proved inaccessible to further analysis. Using a mean component analysis of the *x* and *y* components of the localization set, those candidates were discarded, exhibiting a ratio of the absolute values of both eigenvectors smaller than 3. Next,

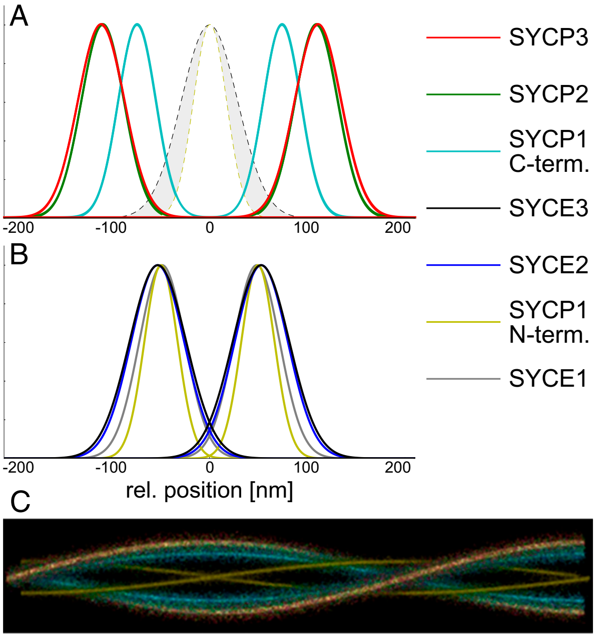

Fig. 4. Localization distributions and 3D reconstruction of the SC as revealed by *d*STORM and particle averaging. (*A*) Frontal view showing the bimodal distribution of the LE proteins SYCP2 and SYCP3 and the SYCP1 C terminus in continuous lines. The monomodal distributions of the CE protein SYCE3 and the SYCP1 N terminus are plotted in dotted lines. (*B*) Lateral view showing the bimodal distributions of CE proteins SYCE1, SYCE2, and SYCE3, as well as the SYCP1 N terminus. (*C*) Three-dimensional model of protein distributions of SYCP3 (red), SYCP2 (green), the SYCP1 C terminus (cyan), and the SYCP1 N terminus (yellow). Solid cables show averaged protein positions with the width of the SD of the averaged position (6.07 nm for SYCP3, 6.39 nm for SYCP2, 2.58 nm for the SYCP1 C terminus, and 4.84 nm for the SYCP1 N terminus). Cloudy dots indicate measured FWHM of single-molecule localization distributions (55.8 nm for SYCP3, 51.1 nm for SYCP2, 45.2 nm for the SYCP1 C terminus, and 39.8 nm for the SYCP1 N terminus).

a high-order ($n > 10$) polynomial was fitted to the data. Using this polynomial as a guideline, a sliding window algorithm was applied. The edge length parallel to the polynomial was thereby 50 nm, and the vertical edge length was chosen to be sufficiently larger than the expected double-strand distance (~1,000 μm). For each step, this window was moved 25 nm along the polynomial, providing a 25-nm overlap to the previous and next segments. For each segment, all distances between all inlying localizations were determined and histogrammed after projecting the distances perpendicular to the current slope of the polynomial. This histogram is then the basis for the calculation of strand diameter and double-strand distance. First, a fit of a bi-Gaussian distribution is attempted, and if successful, both peak values are stored. Thereby, the larger peak value stands for the mean distance of the two strands and the smaller peak value stands for the SD of localizations within the single strands in the current segment. If the bi-Gaussian fitting is unsuccessful, a mono-Gaussian model is applied to determine the spatial SD of the current segment, representing the diameter. To avoid falsifications due to unclean signals at the tail sections of the complexes, 100- to 500-nm segments from both sides of the complex were usually excluded from the final analysis. The left entirety of all diameter/distance values (originating from each segment) along the strand is then again histogrammed to determine the mean values for a single complex (via a bi- or mono-Gaussian fit of the final histogram). For each species, 30–50 complete complexes were processed, resulting in overall mean values of double-strand distance (if existing) as well as the FWHM of single strands (derived from the SD) for each protein (Fig. 4 *A* and *B* and Fig. S4). If not stated otherwise, all stated error margins are the SD of the individual protein statistic.

ACKNOWLEDGMENTS. We thank Howard Cooke (Medical Research Council Human Genetics Unit) for the provision of the antibody guinea pig anti-SYCE2 and rabbit anti-SYCE1. This work was supported by a grant of the Deutsche Forschungsgemeinschaft, Priority Program 1384–Mechanisms of Genome Haploidization (to R.B.). M.S. acknowledges the financial support of the Biophotonics Initiative of the Bundesministerium für Bildung und Forschung (Grants 13N11019 and 13N12507).

1. von Wettstein D, Rasmussen SW, Holm PB (1984) The synaptonemal complex in genetic segregation. *Annu Rev Genet* 18:331–413.
2. Zickler D, Kleckner N (1998) The leptotene-zygotene transition of meiosis. *Annu Rev Genet* 32:619–697.
3. Moses MJ (1968) Synaptinemal complex. *Annu Rev Genet* 2:363–412.
4. Wettstein R, Sotelo JR (1971) The molecular architecture of synaptonemal complexes. *Adv Mol Cell Biol* 1:109–152.
5. Lammers JH, et al. (1994) The gene encoding a major component of the lateral elements of synaptonemal complexes of the rat is related to X-linked lymphocyte-regulated genes. *Mol Cell Biol* 14(2):1137–1146.
6. Offenberg HH, et al. (1998) SCP2: A major protein component of the axial elements of synaptonemal complexes of the rat. *Nucleic Acids Res* 26(11):2572–2579.
7. Meuwissen RL, et al. (1992) A coiled-coil related protein specific for synapsed regions of meiotic prophase chromosomes. *EMBO J* 11(13):5091–5100.
8. Costa Y, et al. (2005) Two novel proteins recruited by synaptonemal complex protein 1 (SYCP1) are at the centre of meiosis. *J Cell Sci* 118(Pt 12):2755–2762.
9. Hamer G, et al. (2006) Characterization of a novel meiosis-specific protein within the central element of the synaptonemal complex. *J Cell Sci* 119(Pt 19):4025–4032.
10. Schramm S, et al. (2011) A novel mouse synaptonemal complex protein is essential for loading of central element proteins, recombination, and fertility. *PLoS Genet* 7(5): e1002088.
11. Fraune J, Schramm S, Alsheimer M, Benavente R (2012) The mammalian synaptonemal complex: Protein components, assembly and role in meiotic recombination. *Exp Cell Res* 318(12):1340–1346.
12. Weber K, Rathke PC, Osborn M (1978) Cytoplasmic microtubular images in glutaraldehyde-fixed tissue culture cells by electron microscopy and by immunofluorescence microscopy. *Proc Natl Acad Sci USA* 75(4):1820–1824.
13. Baschong W, Wrigley NG (1990) Small colloidal gold conjugated to Fab fragments or to immunoglobulin G as high-resolution labels for electron microscopy: A technical overview. *J Electron Microsc Tech* 14(4):313–323.
14. Schmekel K, et al. (1996) Organization of SCP1 protein molecules within synaptonemal complexes of the rat. *Exp Cell Res* 226(1):20–30.
15. Shannon CE (1949) Communication in the presence of noise. *Proc IEEE Inst Electr Electron Eng* 37:10–21.
16. Patterson G, Davidson M, Manley S, Lippincott-Schwartz J (2010) Superresolution imaging using single-molecule localization. *Annu Rev Phys Chem* 61:345–367.
17. Sauer M (2013) Localization microscopy coming of age: From concepts to biological impact. *J Cell Sci* 126(Pt 16):3505–3513.
18. Löschberger A, et al. (2012) Super-resolution imaging visualizes the eightfold symmetry of gp210 proteins around the nuclear pore complex and resolves the central channel with nanometer resolution. *J Cell Sci* 125(Pt 3):570–575.
19. Szymborska A, et al. (2013) Nuclear pore scaffold structure analyzed by super-resolution microscopy and particle averaging. *Science* 341(6146):655–658.
20. Heilemann M, et al. (2008) Subdiffraction-resolution fluorescence imaging with conventional fluorescent probes. *Angew Chem Int Ed Engl* 47(33):6172–6176.
21. van de Linde S, et al. (2011) Direct stochastic optical reconstruction microscopy with standard fluorescent probes. *Nat Protoc* 6(7):991–1009.
22. Winkel K, Alsheimer M, Öllinger R, Benavente R (2009) Protein SYCP2 provides a link between transverse filaments and lateral elements of mammalian synaptonemal complexes. *Chromosoma* 118(2):259–267.
23. Liu JG, et al. (1996) Localization of the N-terminus of SCP1 to the central element of the synaptonemal complex and evidence for direct interactions between the N-termini of SCP1 molecules organized head-to-head. *Exp Cell Res* 226(1):11–19.
24. Tarsounas M, Pearlman RE, Gasser PJ, Park MS, Moens PB (1997) Protein-protein interactions in the synaptonemal complex. *Mol Biol Cell* 8(8):1405–1414.
25. Huang B, Wang W, Bates M, Zhuang X (2008) Three-dimensional super-resolution imaging by stochastic optical reconstruction microscopy. *Science* 319(5864):810–813.
26. Juette MF, et al. (2008) Three-dimensional sub-100 nm resolution fluorescence microscopy of thick samples. *Nat Methods* 5(6):527–529.
27. Öllinger R, Alsheimer M, Benavente R (2005) Mammalian protein SCP1 forms synaptonemal complex-like structures in the absence of meiotic chromosomes. *Mol Biol Cell* 16(1):212–217.
28. de Boer E, Lhuissier FG, Heyting C (2009) Cytological analysis of interference in mouse meiosis. *Methods Mol Biol* 558:355–382.
29. Tokunaga M, Imamoto N, Sakata-Sogawa K (2008) Highly inclined thin illumination enables clear single-molecule imaging in cells. *Nat Methods* 5(2):159–161.
30. Wolter S, et al. (2010) Real-time computation of subdiffraction-resolution fluorescence images. *J Microsc* 237(1):12–22.
31. Wolter S, et al. (2012) rapidSTORM: Accurate, fast open-source software for localization microscopy. *Nat Methods* 9(11):1040–1041.
32. Arganda-Carreras I, et al. (2006) Consistent and elastic registration of histological sections using vector-spline regularization. *Lecture Notes in Computer Science* 4241: 85–95.

Dipl. – Phys. Christian Franke
Lehrstuhl für Biotechnologie und Biophysik
Biozentrum, Am Hubland
97074 Würzburg
Germany

Würzburg, 4th July 2017

Manuscript:

Johannes Schneider, Teresa Klein, Benjamin Mielich-Süss, Gudrun Koch, Christian Franke, Oscar P Kuipers, Akos T Kovacs, Markus Sauer, and Daniel Lopez.

Spatio-temporal remodeling of functional membrane microdomains organizes the signaling networks of a bacterium

PLoS genetics, 11(4):e1005140, 2015.

The contributions of the PhD candidate Christian Franke to the above manuscript involved:

- Conceptual design, implementation and execution of the described quantification approach of SMLM data
- Analysis of SMLM data
- Minor contribution to the manuscript draft; Figures 3 and 4E; section 'Photoactivated localization microscopy'

Christian Franke

Johannes Schneider

Teresa Klein

Benjamin Mielich-Süß

Benjamin Mielich-Süss

Koch

Gudrun Koch

Oscar P Kuipers

Akos T Kovacs

Markus Sauer

Daniel Lopez

PLOS | GENETICS

RESEARCH ARTICLE

Spatio-temporal Remodeling of Functional Membrane Microdomains Organizes the Signaling Networks of a Bacterium

Johannes Schneider[1], **Teresa Klein**[2], **Benjamin Mielich-Süss**[1], **Gudrun Koch**[1], **Christian Franke**[2], **Oscar P. Kuipers**[3], **Ákos T. Kovács**[4], **Markus Sauer**[2], **Daniel Lopez**[1]*

1 Research Center for Infectious Diseases ZINF, University of Würzburg, Würzburg, Germany, **2** Department of Biotechnology and Biophysics, University of Würzburg, Würzburg, Germany, **3** Molecular Genetics Group, Groningen Biomolecular Sciences and Biotechnology Institute, University of Groningen, Groningen, The Netherlands, **4** Terrestrial Biofilms Group, Institute of Microbiology, Friedrich Schiller University of Jena, Jena, Germany

* Daniel.Lopez@uni-wuerzburg.de

OPEN ACCESS

Citation: Schneider J, Klein T, Mielich-Süss B, Koch G, Franke C, Kuipers OP, et al. (2015) Spatio-temporal Remodeling of Functional Membrane Microdomains Organizes the Signaling Networks of a Bacterium. PLoS Genet 11(4): e1005140. doi:10.1371/journal.pgen.1005140

Editor: Josep Casadesús, Universidad de Sevilla, Spain

Received: September 22, 2014

Accepted: March 11, 2015

Published: April 24, 2015

Data Availability Statement: Our transcriptomic data is deposited at Gene Expression Omnibus (GEO): Accession database number GSE47918.

Funding: This work was funded by the European Research Council ERC-Starting Grant ERC335568 (DL) and German Federal Ministry of Education and Research (BMBF) grant number 13N11019 (MS). This publication was funded by the German Research Foundation (DFG) and the University of Wuerzburg in the funding programme Open Access Publishing. The funders had no role in study design,

Abstract

Lipid rafts are membrane microdomains specialized in the regulation of numerous cellular processes related to membrane organization, as diverse as signal transduction, protein sorting, membrane trafficking or pathogen invasion. It has been proposed that this functional diversity would require a heterogeneous population of raft domains with varying compositions. However, a mechanism for such diversification is not known. We recently discovered that bacterial membranes organize their signal transduction pathways in functional membrane microdomains (FMMs) that are structurally and functionally similar to the eukaryotic lipid rafts. In this report, we took advantage of the tractability of the prokaryotic model *Bacillus subtilis* to provide evidence for the coexistence of two distinct families of FMMs in bacterial membranes, displaying a distinctive distribution of proteins specialized in different biological processes. One family of microdomains harbors the scaffolding flotillin protein FloA that selectively tethers proteins specialized in regulating cell envelope turnover and primary metabolism. A second population of microdomains containing the two scaffolding flotillins, FloA and FloT, arises exclusively at later stages of cell growth and specializes in adaptation of cells to stationary phase. Importantly, the diversification of membrane microdomains does not occur arbitrarily. We discovered that bacterial cells control the spatio-temporal remodeling of microdomains by restricting the activation of FloT expression to stationary phase. This regulation ensures a sequential assembly of functionally specialized membrane microdomains to strategically organize signaling networks at the right time during the lifespan of a bacterium.

Author Summary

Cellular membranes organize proteins related to signal transduction, protein sorting and membrane trafficking into the so-called lipid rafts. It has been proposed that the functional

data collection and analysis, decision to publish, or preparation of the manuscript.

Competing Interests: The authors have declared that no competing interests exist.

diversity of lipid rafts would require a heterogeneous population of raft domains with varying compositions. However, a mechanism for such diversification is not known due in part to the complexity that entails the manipulation of eukaryotic cells. The recent discovery that bacteria organize many cellular processes in membrane microdomains (FMMs), functionally similar to the eukaryotic lipid rafts, prompted us to explore FMMs diversity in the bacterial model *Bacillus subtilis*. We show that diversification of FMMs occurs in cells and gives rise to functionally distinct microdomains, which compartmentalize distinct signal transduction pathways and regulate the expression of different genetic programs. We discovered that FMMs diversification does not occur randomly. Cells sequentially regulate the specialization of the FMMs during cell growth to ensure an effective and diverse activation of signaling processes.

Introduction

Cells typically compartmentalize their cellular processes into subcellular structures (e.g. organelles) to optimize their efficiency and improve their activity. One of the most interesting concepts in cellular compartmentalization is the proposed existence of *lipid rafts* in the membranes of eukaryotic cells [1]. Eukaryotic membranes organize a large number of proteins related to signal transduction, protein sorting and membrane trafficking into discrete nanoscale domains termed lipid rafts [1,2]. The functional diversity of lipid rafts is currently attributed to a different lipid and protein composition, as compelling evidence suggests that a heterogeneous population of lipid rafts could exist on a given cell [3–5]. Yet, the molecular mechanisms by which cells generate and regulate raft heterogeneity are still unclear. In eukaryotic systems, it is known that the integrity of lipid rafts requires the activity of two different raft-associated proteins termed flotillins (FLO-1 and FLO-2) [6,7]. Flotillins are scaffolding proteins, which may redundantly act as chaperones in recruiting the protein cargo to lipid rafts and interact with the recruited proteins that activate the signal transduction processes [8–10]. Consequently, the perturbation of the activity of flotillins causes serious defects in several signal transduction and membrane trafficking processes, which seems to be intimately related to the occurrence of severe human diseases, such as Alzheimer's disease, Parkinson's disease or muscular dystrophy (reviewed in [11]).

The spatial organization of signaling networks in lipid rafts has been considered a hallmark in cellular complexity because their existence is exclusively associated with eukaryotic cells. However, we recently discovered that bacteria organize many proteins related to signal transduction in functional membrane microdomains (FMMs) that are structurally and functionally similar to the lipid rafts of eukaryotic cells [12]. Bacterial flotillins are important components for the organization and the maintenance of the architecture of FMMs. Similar to the eukaryotic flotillins, bacterial flotillins probably act as scaffolding proteins in tethering protein components to the FMMs, thereby facilitating their efficient interaction and oligomerization and to mediate the efficient activation of signal transduction pathways harbored in FMMs. Consequently, mutants lacking flotillins show a severe defect in FMM-localized signaling pathways concomitantly with a severe dysfunction of diverse physiological processes, such as biofilm formation, natural competence or sporulation [12–17].

The FMMs of the bacterial model *Bacillus subtilis* contain two different flotillin-like proteins, FloA and FloT [12]. FloA and FloT flotillins physically interact [13] and presumably play a redundant role because the dysfunction of specific FMM-associated physiological processes, like biofilm formation, only occurs in the Δ*floA* Δ*floT* defective mutant and is not observed in either of the Δ*floA* or Δ*floT* single mutants [17]. Likewise, the overexpression of both *floA* and *floT* causes pleiotropic effects in cell division and cell differentiation but this effect is not observed in cells that overexpress one single flotillin gene [16]. In this respect, bacterial flotillins seem to behave similarly to human flotillins FLO-1 and FLO-2, given that both FLO-1 and FLO-2 are associated with each other in hetero-oligomeric complexes and have a strong regulatory correlation [18–20]. These experimental evidences led to the general assumption that both flotillins play a redundant function in both eukaryotic lipid rafts and bacterial FMMs.

In this report, we provide evidence that a heterogeneous population of membrane microdomains coexists on bacterial cells. We show that FloA and FloT are two functionally different flotillins that physically interact but unevenly distribute within the FMMs of bacterial cells. FloA and FloT act as specific scaffold proteins that tether a defined group of FMMs-associated proteins. This generates functionally distinct microdomains, which compartmentalize distinct signal transduction pathways and regulate different genetic programs. Importantly, we show that cells sequentially regulate the functional specialization of the FMMs during cell growth. Cells restrict the expression of the *floT* gene to stationary phase to ensure an effective activation of signaling processes at specific times during the lifespan of the bacterium.

Results

FloA and FloT are differentially regulated in *B*. *subtilis*

While exploring flotillin redundancy in the FMMs of *B*. *subtilis*, we discovered that the expression of FloA and FloT is controlled by different genetic programs, which could indicate that these are two functionally different flotillins. We came across this finding by examining the expression profiles of *floA* and *floT* genes in the 249 different growing conditions that are published in [21,22], and are available in SubtiExpress (http://subtiwiki.uni-goettingen.de/apps/expression). By doing this, we consistently found high expression of *floA* in all the growing conditions tested, including LB and MSgg growth media, the two growth media that we normally used in the laboratory to grow *B*. *subtilis* (S1A Fig) [23]. However, the expression of *floT* showed more variability among the growth conditions tested and exhibited an important difference in gene expression between LB (lower expression of *floT*) and MSgg (higher expression of *floT*). To test this in the laboratory, we constructed *B*. *subtilis* strains harboring the P_{floA}-*yfp* and P_{floT}-*yfp* transcriptional fusions (YFP is yellow fluorescence protein) and grew them in LB and MSgg media [23]. Our laboratory uses the chemically-defined medium MSgg to induce sporulation and the formation of robust biofilms in *B*. *subtilis* cultures and differs to LB medium in which *B*. *subtilis* did not show any of the developmental characteristics of MSgg [24]. By growing *B*. *subtilis* cells in these two growth conditions, we detected an activation of *floT* expression in MSgg (S1A Fig), while LB medium showed poor activation of *floT* expression (S1B Fig). In contrast, *floA* was equally expressed in both MSgg and LB media. Furthermore, we generated strains labeled with the FloA-GFP and FloT-GFP translational fusions (GFP is green fluorescence protein) to visualize and quantify flotillin protein production using flow cytometry. The FloT-GFP labeled strain showed a reduction of the fluorescence signal when grown in LB medium while FloA-GFP was equally expressed in both MSgg and LB media (S1C Fig).

To investigate whether the differential production of FloA and FloT is a cell-regulated process, the strains labeled with P_{floA}-*yfp* and P_{floT}-*yfp* transcriptional fusions were used to systematically inactivate regulatory genes of *B*. *subtilis* and search for mutants capable of altering the expression of *floT* in MSgg medium (S1D Fig). We detected a uniform expression of *floA* in all mutants tested. However, we discovered that cells lacking the *abrB* gene showed increased expression of *floT*. Additionally, we found inhibition of *floT* expression in cells when the *spo0A* gene was deleted. Importantly, *spo0A* and *abrB* belong to the same signaling pathway. AbrB is

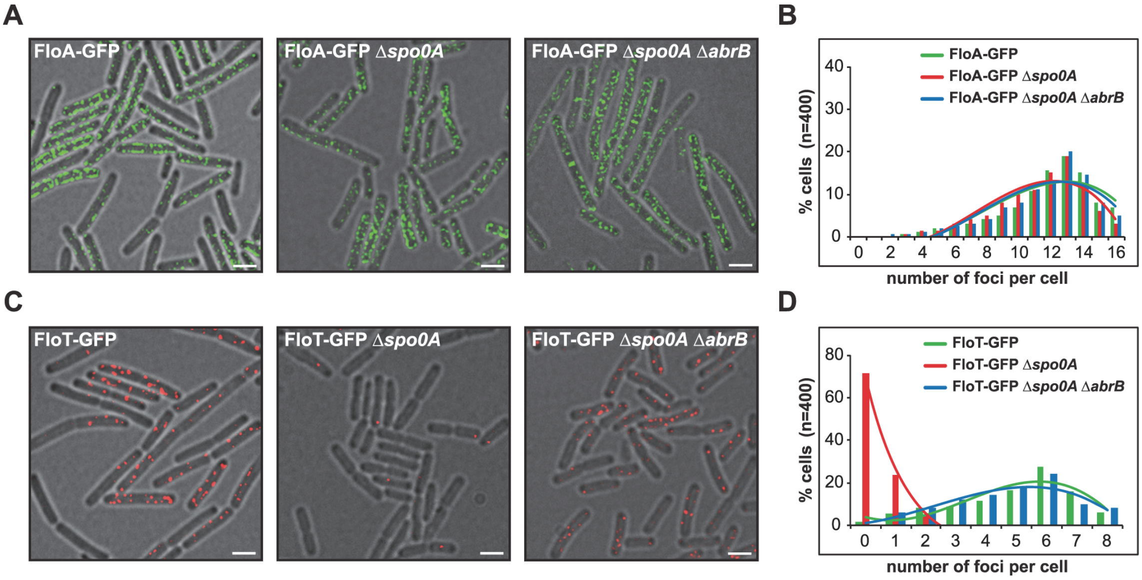

Fig 1. Spo0A regulates *floT* and not *floA* expression via inhibition of AbrB. (A) Fluorescence microscopy pictures of different strains expressing FloA-GFP translational fusion (Fluorescence signal in green). Scale bars are 2 μm. **(B)** Quantification of fluorescence foci of different strains expressing FloA-GFP translational fusion. **(C)** Fluorescence microscopy pictures of different strains expressing FloT-GFP translational fusion (Fluorescence signal in red). Scale bars are 2 μm. **(D)** Quantification of fluorescence foci of different strains expressing FloT-GFP translational fusion. Cells were grown in MSgg medium at 37°C until stationary phase.

doi:10.1371/journal.pgen.1005140.g001

a repressor of biofilm formation among other processes [25] and its expression is negatively regulated by Spo0A [26]. Spo0A is a master regulatory protein necessary for the activation of many physiological processes related to stationary phase [27]. Therefore, this provides epistatic evidence that Spo0A positively regulates *floT* expression at stationary phase via inhibition of *abrB* and that this genetic cascade does not affect the expression of *floA*. To test this hypothesis, we deleted *spo0A* and/or *abrB* genes in FloA-GFP and FloT-GFP labeled strains and monitored the subcellular distribution pattern of flotillins using fluorescence microscopy and applying a deconvolution algorithm to eliminate out-of-focus signal and to improve their correct visualization (see material and methods section) (Fig 1). Indeed, Δ*spo0A* or Δ*spo0A* Δ*abrB* mutants showed no variation in the distribution pattern of fluorescence foci that were generated by FloA (Fig 1A and 1B). In contrast, Δ*spo0A* mutant showed a severe reduction of fluorescence foci that were generated by FloT, which could be reconstituted in the Δ*spo0A* Δ*abrB* double mutant (Fig 1C and 1D).

Activation of Spo0A (Spo0A~P) occurs at stationary phase due in part to the activation of the histidine kinase C (KinC) [28,29], which is driven by the action of the self-produced signaling molecule surfactin. Thus, FloA-GFP and FloT-GFP labeled strains were grown in LB medium and complemented with exogenously added surfactin (5 μM) (S2A and S2C Fig). FloA-GFP labeled cells showed no alteration of the fluorescence signal but FloT-GFP labeled cells showed an increase in the number of foci (S2A–S2D Fig). This is a Spo0A-depedent effect because the *spo0A* deficient strain showed no recovery of FloT expression upon addition of surfactin (S2E and S2F Fig). Altogether, these results show an upregulation of FloT production at stationary phase in a Spo0A-dependent manner likely via AbrB. In contrast, the production of FloA is not influenced by this regulatory cascade.

Flotillins distribute unevenly within the FMMs of *B*. *subtilis*

The distinct regulatory programs for FloA and FloT production led us to hypothesize that FloA and FloT may play different roles in *B. subtilis* cells. To investigate this hypothesis, we first explored whether FloA and FloT show any structural difference. FloT is a larger protein (509 aa) that has an extended C-terminal region compared to FloA (331 aa) (Figs 2A and S3A). To determine if these structural differences are associated with a different subcellular distribution pattern, we used strains labeled with the FloA-GFP and FloT-GFP translational fusions to visualize and quantify the number of fluorescent foci (n = 400) using fluorescence microscopy. On average, FloA distributed in 13 foci per cell while FloT distributed approximately in 6 foci (Figs 2B, 2C and S3B). These results are consistent with the number of foci that we detected in the genetic analysis that are shown in Fig 1. However, to validate that these results were not a consequence of clustering artifacts [30], we compared their distribution pattern using non-dimerizing monomeric red fluorescence protein mCherry (mCh) in a total of 400 cells. Likewise, FloA distributed in 13 foci per cell while FloT distributed in 6 foci, as previously observed (Figs 2B, 2C and S3B). Importantly, the subcellular localization of flotillins consistently showed that FloA distributed in more foci per cell than FloT. To gain more insight about the differential distribution pattern of flotillins, we performed co-localization experiments using FloA-GFP, FloT-mCh and FloA-mCh, FloT-GFP double-labeled strains. Co-localization of both signals was detected by fluorescence microscopy, showing colocalization of FloT with FloA in all cells examined (Fig 2D), which adds to the previous notion that FloA and FloT physically interact [12,13,17]. However, the obvious differences in the number of foci between FloA and FloT resulted in the colocalization of both FloA and FloT signals only in a subset of foci (Pearson's correlation coefficient $R^2 = 0.81$). This diversified the pool of FMMs of a given cell into two different types of microdomains: one family of microdomains that contains solely FloA signal and a second type of microdomains in which both FloA and FloT signals converge. We performed time-lapse fluorescence microscopy experiments using a FloA-GFP FloT-mCherry double-labeled strain to investigate the dynamics of the subcellular co-localization. A series of images were taken at one-second time interval (Fig 2E). The fluorescence signal attributable to FloA and FloT reorganized dynamically within the membrane and consistently showed co-localization of signals from FloA and FloT.

The asymmetrical distribution pattern of FloA and FloT was further examined at higher resolution using super-resolution imaging by PALM [31,32]. To this end, FloA and FloT were labeled with the photoactivatable monomeric protein mEOS2 and expressed in *B. subtilis* cells. FloA-mEOS2 and FloT-mEOS2 proteins were activated by low intensity irradiation at 405 nm. Photoactivated proteins were excited at 568 nm, imaged and bleached before the next cycle of photoactivation. Individual protein positions were determined (localized) in each image frame and used to reconstruct a high-resolution PALM image (Fig 3A and 3B). Clusters candidates were defined by either one connected pixel area in image-based analysis or by a cloud of scattered localizations with spatial coherence in localization based analysis. Spatial coherence implies that the increase local density of localizations follows a Gaussian distribution within the cluster, which is indicative of the nonrandom distribution of localizations. Using the raw localization data and the corresponding super-resolved image, we generated a mask to define possible cluster candidates and separate them from the localization pseudo background. By using this technique, we confirmed that FloA assembled in 13 small clusters per cell (Diameter = 46.73 ± 1.35 nm). FloT however, assembled in approximately 6 larger clusters per cell (Diameter = 63.39 ± 2.28 nm) with a higher content of proteins (Fig 3C–3F). To validate these results, we also monitored the distribution pattern of FloA and FloT when fused to photoactivatable monomeric PAmCherry using PALM (S4A and S4B Fig). The statistical analysis of the

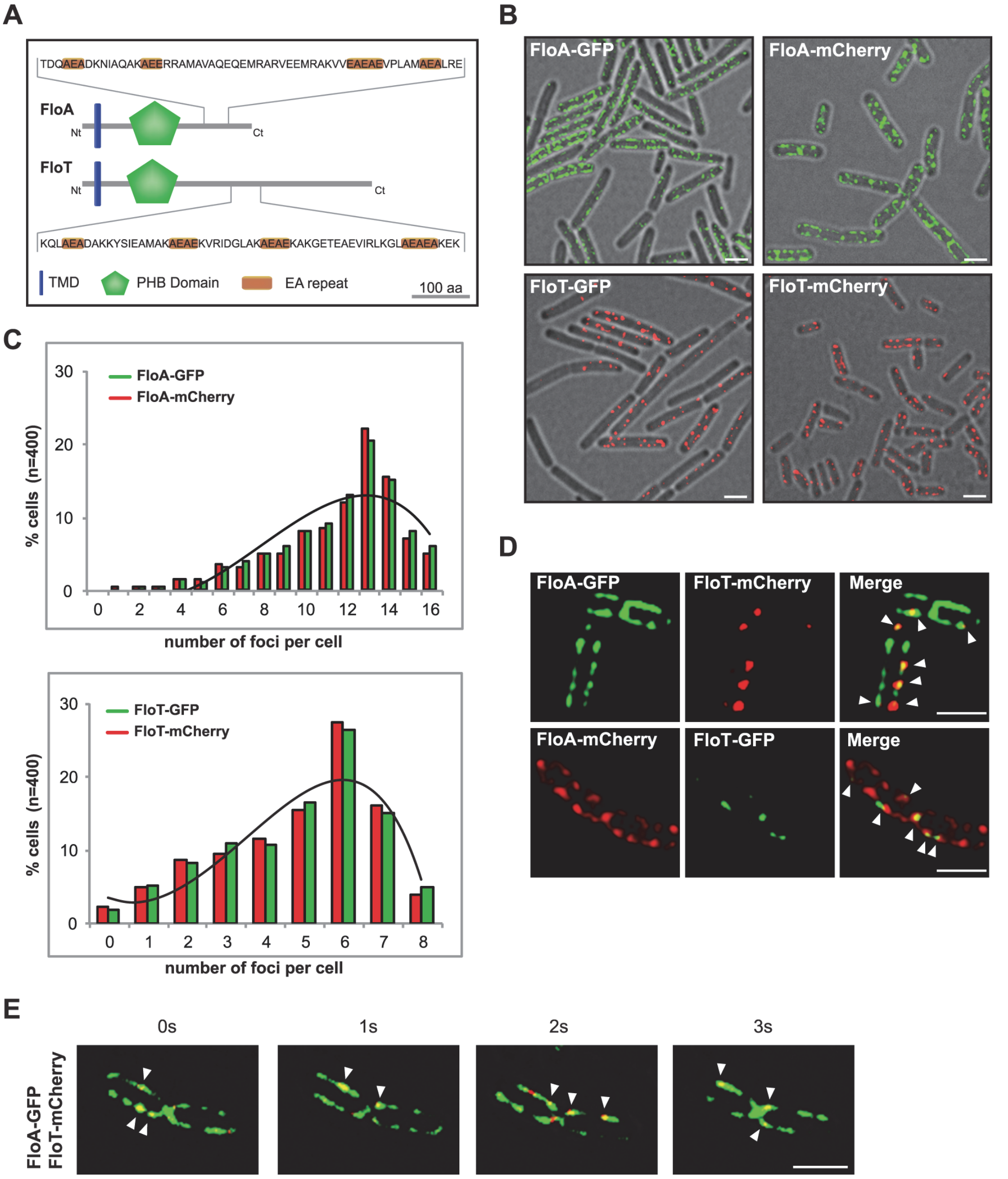

Fig 2. FloA and FloT are two distinct flotillins. **(A)** Comparative diagram of FloA and FloT protein structures. The membrane-anchored region is represented in blue. The PHB domain is represented in green and the coil-coiled region is magnified and EA repeats are labeled in orange. Scale bar is 100 amino acids. **(B)** Fluorescence microscopy pictures of cells labeled with FloA-GFP, FloA-mCherry (upper panel), FloT-GFP and FloT-mCherry (lower panel) translational fusions. Fluorescence signal associated with FloA is represented in green and fluorescence signal associated with FloT is represented in red. Cultures were grown in MSgg medium at 37°C until stationary phase. Scale bars are 2 μm. **(C)** Quantification of the number of foci per cell (n = 400). **(D)** Fluorescence microscopy pictures of double-labeled strains. Cultures were grown in MSgg medium at 37°C until stationary phase. GFP signal is represented in green and mCherry signal is represented in red. Right panel shows the merge of the two fluorescence signals, which is visualized as yellow fluorescence signal. Scale bars are 2 μm. **(E)** Time lapse fluorescence microscopy analysis of cells expressing FloA-GFP (green signal) and FloT-mCherry (red signal) translational fusions. Signal was monitored within the same cells at 1 sec intervals. Cultures were grown in MSgg medium at 37°C until stationary phase. Scale bar is 2 μm.

doi:10.1371/journal.pgen.1005140.g002

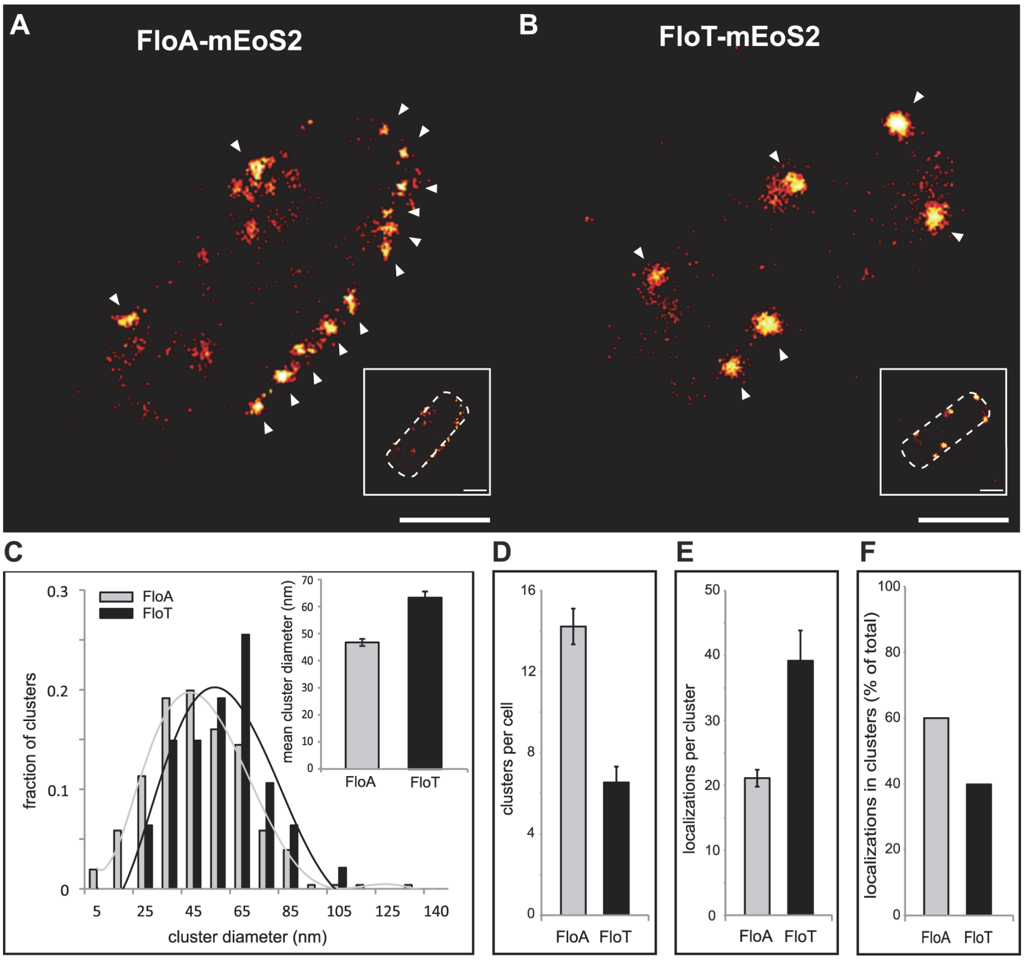

Fig 3. FloA and FloT distribute differently within the bacterial microdomains. (A and B) PALM images of cells labeled with FloA-mEoS2 (A) or FloT-mEoS2 (B) translational fusions grown to stationary phase and fixed with PFA (4%). With increasing localization density the color code changes from red to yellow. White arrows indicate the localization of a cluster. Scale bars are 500 nm. Detail of the right bottom of each panel shows a dashed-line decorated PALM picture as a general indicator of the cell outline. Scale bar is 500 nm. **(C)** Comparative graph of the diameter of the clusters that were generated by FloA-mEoS2 and FloT-mEoS2 fluorescence signal. The upper right corner shows a graph with the mean of the diameter of the FloA and FloT clusters. **(D)** Comparative graph of the number of clusters detected in FloA-mEoS2 and FloT-mEoS2 labeled cells. **(E)** Comparative graph of the number of FloA and FloT localizations per cluster. **(F)** Comparative graph of the percentage of localizations that organized in clusters.

doi:10.1371/journal.pgen.1005140.g003

signals detected by PALM and further validation by western blot analysis suggested that FloT is more abundant than FloA in cells and yet, based on our results, is concentrated in a lower number of foci (S4C and S4D Fig).

Spatial organization of flotillin distribution is driven by flotillin interaction

The molecular basis of the asymmetrical distribution of FloA and FloT was explored by monitoring the intra- and inter-specific interactions that occur between FloA and FloT flotillins. To do this, we used a bacterial two-hybrid (BTH) assay, in which FloA and FloT were tagged to T25 or T18 catalytic domains of an adenylate cyclase that reconstitute the enzyme upon interaction of two proteins [33]. A fully active adenylate cyclase produces cAMP, which accumulates in the cytoplasm and triggers the expression of a cAMP-inducible *lacZ* reporter gene [33]. Using this assay, we detected a strong interaction signal with FloA alone (Fig 4A) (Instructions of the manufacturer define a positive signal if above the threshold of 700 Miller Units [33]). Likewise, a strong interaction signal was detected with FloT (Fig 4A). This is indicative of the capacity of FloA and FloT to form homo-oligomers. However, when we assayed the interactions between FloA and FloT, the interaction signal was less prominent in comparison to the FloA-FloA and FloT-FloT interactions, suggesting that flotillins are prone to form homo-oligomers while hetero-oligomerization occurs to a lesser extent (Fig 4A). The propensity to form homo-oligomers suggests different interaction properties between FloA and FloT, which is probably a determinant in the generation of distinct subcellular distribution patterns.

Both FloA and FloT have a N-terminal region that anchors the protein to the membrane and the SPFH domain that is characteristic of this protein family (for stomatin, prohibitin, flotillin and HflK/C) [34,35]. However, the C-terminal region, which is the most variable region between FloA and FloT, contains four glutamate-alanine repeats (EA repeats) that are responsible for the oligomerization of human FLO-1 and FLO-2 (Figs 2A and S3A) [36] and are probably important in determining the interactions between FloA and FloT. We performed site-directed mutagenesis of the C-terminal region of each flotillin, which generated several variants of FloA and FloT, in which each one of the four EA repeats was replaced (EA→GL) (S5B Fig). We assayed the interaction properties of each one of the resultant variants using a BTH approach. FloA-FloA and FloT-FloT interactions did not occur when we altered the EA2 or EA4 repeats ($\leq$ 700 Miller Units). Additionally, FloA-FloA interaction was abrogated when EA1 was mutated ($\leq$ 700 Miller Units) while EA3 seemed to minimally affect the homo-oligomerization of both FloA and FloT ($\geq$ 700 Miller Units) (Fig 4B). Moreover, the localization pattern of GFP-labeled variants was examined. Variants with EA2 and EA4 altered repeats showed poor aggregation and a severe decrease in the number of foci (Fig 4C and 4D). Alterations in EA1 affected severely the oligomerization of FloA while the variants with altered EA3 showed mild alterations in their distribution pattern (Fig 4C and 4D). None of the distribution patterns were appreciably altered in the absence of the alternative flotillin, suggesting that additional interaction motifs may exist to facilitate hetero-oligomerization (S5C Fig). Since the expression of the altered variants was still detected by western blot analysis (S5D Fig), it is possible that they become dispersed throughout the cellular membrane. Thus, we constructed a mEOS2--tagged version of FloA(EA4) and FloT(EA2) to study their subcellular distribution pattern using PALM microscopy. By using this approach, we detected a large number of single fluorescent proteins randomly dispersed across the cellular membrane (Fig 4E and 4F) rather than organized in foci.

The abovementioned results suggest that FloA and FloT display distinct subcellular distribution pattern, due in part to their different oligomerization affinities, which are determined by the specific interactions that occurred at the C-terminal region of each flotillin. We confirmed these observations by generating a chimeric version of FloA that contains the C-terminal region of FloT ($FloA_T$) and a chimeric version of FloT that contains the C-terminal region of FloA ($FloT_A$). GFP-fused versions of these proteins were generated to examine their subcellular distribution pattern (Fig 5). Using this approach, we consistently observed that the distribution pattern of $FloA_T$ resulted different from wild-type FloA and resembled the distribution pattern of wild-type FloT. Likewise, the distribution pattern of $FloT_A$ resulted very different from the wild-type FloT pattern, showing approximately 13 smaller foci per cell, which is similar to the distribution of wild-type FloA. These results are in agreement with what is shown in Fig 4 and confirmed that the c-termini regions confer specific oligomerization properties to each flotillin.

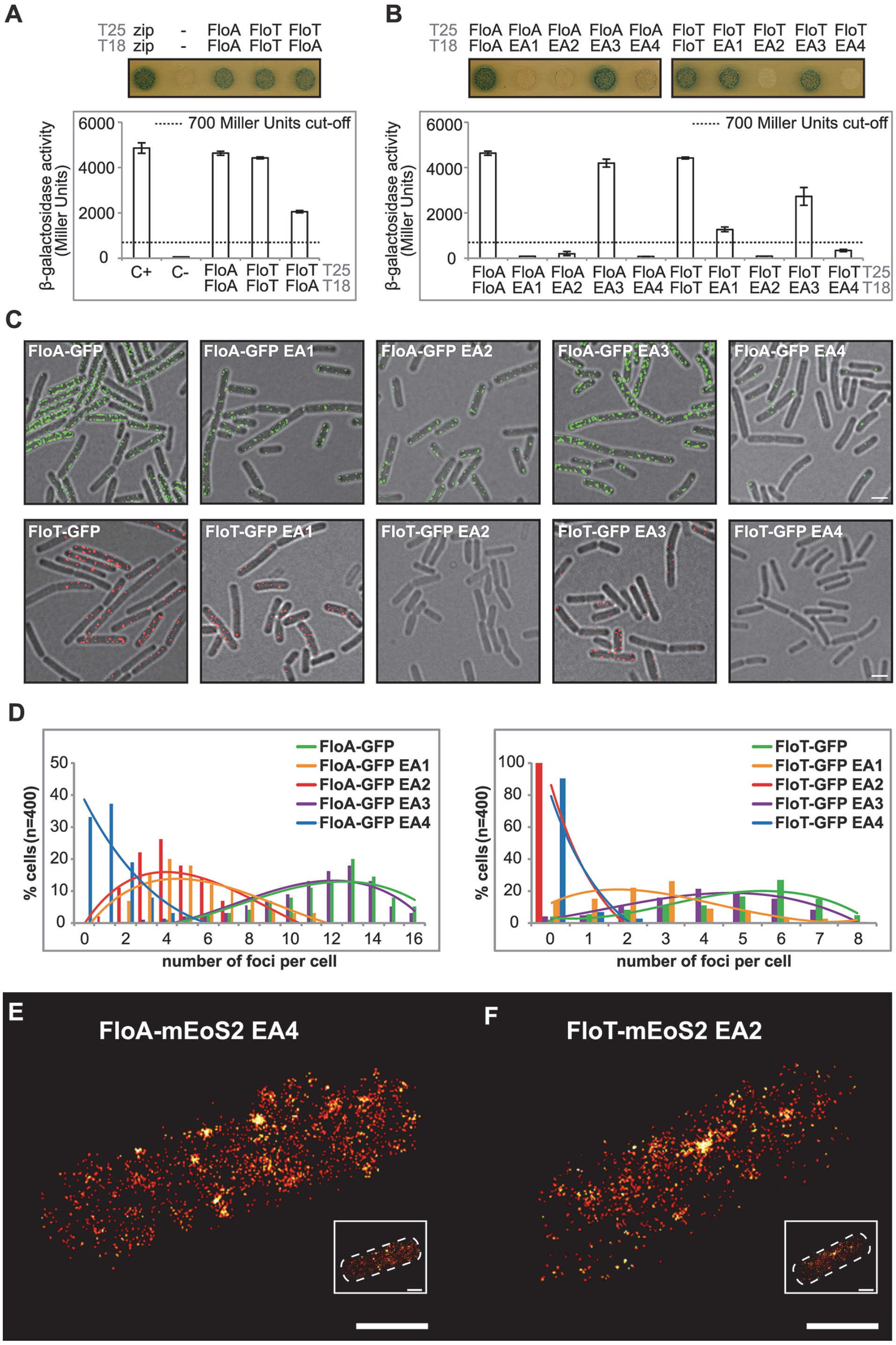
A
T25 zip - FloA FloT FloT
T18 zip - FloA FloT FloA
β-galactosidase activity (Miller Units)
700 Miller Units cut-off
6000
4000
2000
0
C+ C- FloA FloA FloT FloT FloT FloA T25 T18
B
T25 FloA FloA FloA FloA FloA FloT FloT FloT FloT FloT
T18 FloA EA1 EA2 EA3 EA4 FloT EA1 EA2 EA3 EA4
C
FloA-GFP
FloA-GFP EA1
FloA-GFP EA2
FloA-GFP EA3
FloA-GFP EA4
FloT-GFP
FloT-GFP EA1
FloT-GFP EA2
FloT-GFP EA3
FloT-GFP EA4
D
% cells (n=400)
number of foci per cell
0 2 4 6 8 10 12 14 16
0 10 20 30 40 50
0 1 2 3 4 5 6 7 8
0 20 40 60 80 100
E
FloA-mEoS2 EA4
F
FloT-mEoS2 EA2

Fig 4. Oligomerization properties of FloA and FloT. (A) BTH analysis to study the interactions between FloA and FloT. Interaction activates *lacZ* and this degrades X-Gal (blue). The two cytoplasmic domains of a leucine-zipper represent a positive control (pKT25-zip + pUT18C-zip). The negative control is represented by the *E. coli* strains harboring empty plasmids (pKNT25 + pUT18). Plasmids containing FloA, FloT and EA variants are pKNT25 (T25) or pUT18 (T18). Dashed line indicates the threshold limit of 700 Miller Units that defines a positive (≥ 700 Miller Units) and a negative interaction signal (≤ 700 Miller Units) according to the instructions of the manufacturer. **(B)** BTH analysis between the EA1 to EA4 variants of FloA and FloT. Positive controls are wild type FloA and FloT. Dashed line indicates the threshold limit of 700 Miller Units that defines a positive and a negative interaction signal. **(C)** Fluorescence microscopy of cells expressing GFP-tagged versions of EA variants of FloA (Upper row). Fluorescence microscopy of cells expressing GFP-tagged versions of EA variants of FloT (Bottom row). Scale bar is 2 μm. (D) Quantification of the number of foci per cell (n = 400) of the distinct GFP-tagged versions of EA variants of FloA (left panel) and FloT (right panel). **(E and F)** PALM images of cells expressing the EA4 variant of FloA-mEoS2 (E) and EA2 variant of FloT-mEoS2 (F). Scale bars are 500 nm. Detail of the right bottom of each panel shows a dashed-line decorated PALM picture as a general indicator of the cell outline. Scale bar is 500 nm.

doi:10.1371/journal.pgen.1005140.g004

FloA and FloT tether distinct signal transduction pathways

We were interested in exploring the biological significance of cells expressing two different flotillins with distinct spatio-temporal distribution patterns. We hypothesized that this may occur because these are two functionally different flotillins and therefore, they serve as scaffold in tethering the components of distinct signal transduction pathways in *B. subtilis*. We explored this hypothesis by first identifying the proteins that distinctively bind to either FloA or FloT. To do this, His^6-tagged versions of FloA and FloT were expressed in *B. subtilis* cells. The membrane fraction was resolved by blue-native PAGE (BN-PAGE) to allow the separation of the membrane protein complexes in their natural oligomeric states [37]. Our BN-PAGE assays used a polyacrylamide gradient of 4%–20%, which allows the resolution of membrane-bound

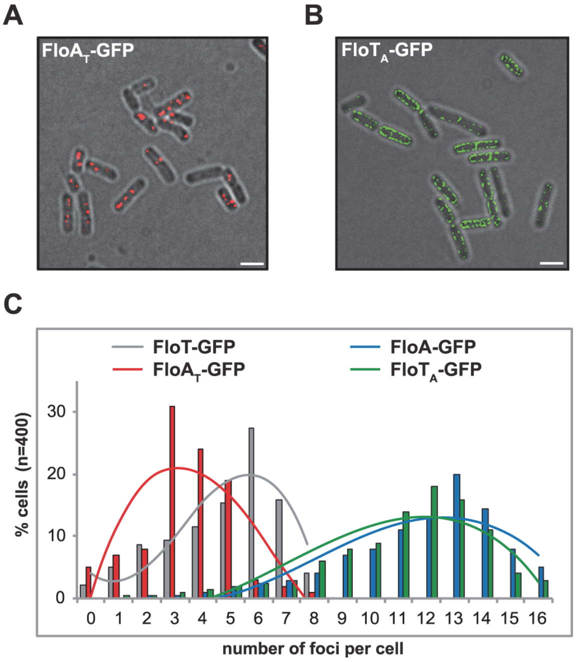

Fig 5. C-terminal region of FloA and FloT plays a role in their oligomerization properties. (A) Fluorescence microscopy image of cells expressing a GFP-tagged version of FloA$_{T}$. Fluorescence signal is represented in red (scale bar is 2 μm) **(B)** Fluorescence microscopy image of cells expressing a GFP-tagged version of FloT$_{A}$. Fluorescence signal is represented in green (scale bar is 2 μm). **(C)** Quantification of the number of foci per cell (n = 400) in different genetic backgrounds.

doi:10.1371/journal.pgen.1005140.g005

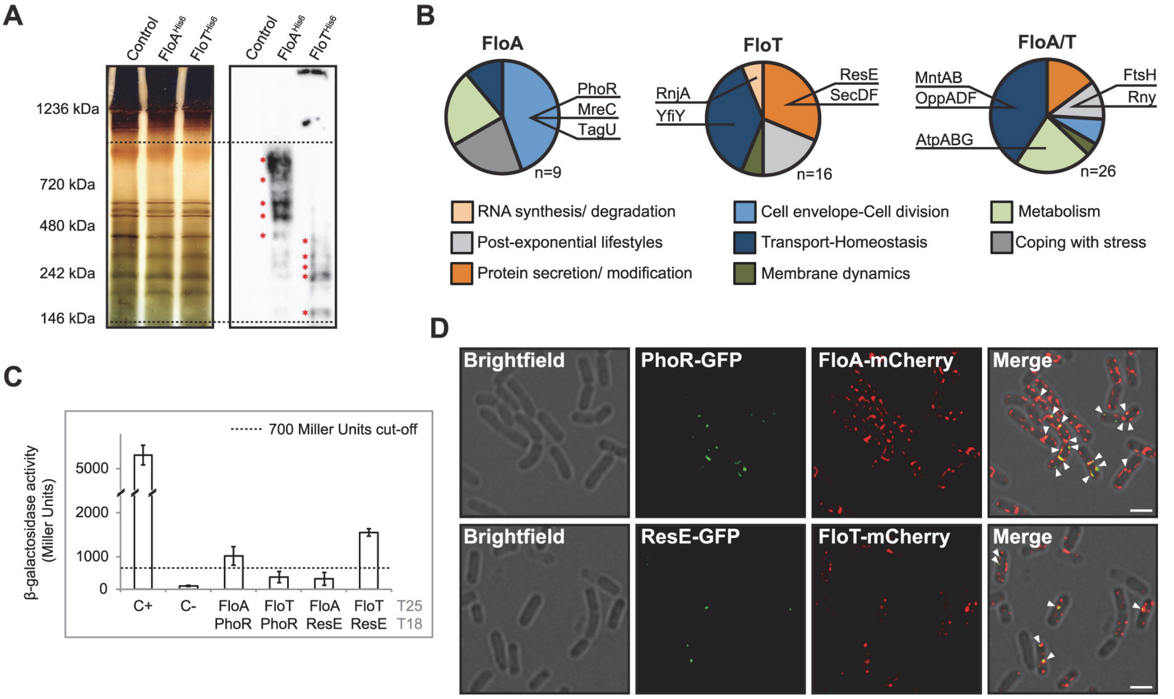

Fig 6. Physiological processes associated with FloA or FloT. (A) Silver-stained BN-PAGE that resolves the protein complexes from the membrane fraction of different strains (left panel). Western blot assay, using antibodies against His^6, to detect flotillin-interacting protein complexes on the BN-PAGE (right panel). Dashed lines define the higher (1000 KDa) and lower (100 KDa) resolution limit of protein complexes in a 4%-20% BN-PAGE. Red asterisks denote the bands that were analyzed by MS. **(B)** Functional classification of the proteins identified in association FloA (left), FloT (centre) or both FloA and FloT (right). Dashed lines define the higher (1,000 KDa) and lower (100 KDa) resolution limit of protein complexes in a 4%-20% BN-PAGE. Red asterisks denote the bands that were analyzed by MS. **(C)** BTH assay to study the interactions between FloA or FloT and the PhoR and ResE flotillin-associated kinases. Dashed line indicates the threshold limit of 700 Miller Units that defines a positive (≥ 700 Miller Units) and a negative interaction signal (≤ 700 Miller Units) according to the instructions of the manufacturer. **(D)** Fluorescence microscopy images of colocalization of fluorescence signals. Upper row shows a double-labeled strain expressing PhoR-GFP and FloA-mCherry translational fusions. Fluorescence signals are represented in green and red, respectively. Colocalization of both green and red fluorescence signals merges in a yellow signal (indicated with a white arrow). Scale bar is 2 μm. Bottom row shows a double-labeled strain expressing ResE-GFP and FloT-mCherry translational fusions. Fluorescence signals are represented in green and red, respectively. Colocalization of both green and red fluorescence signal merges in a yellow signal (indicated with a white arrow). Scale bar is 2 μm.

doi:10.1371/journal.pgen.1005140.g006

protein complexes with a molecular weight between 100 kDa and 1000 kDa. BN-PAGE coupled to immunoblotting, using antibodies against the His^6 tag, was used to identify a number of membrane-associated protein complexes that exclusively interacted with FloA or FloT (Fig 6A and S3 Table). The corresponding bands were identified by mass spectrometry (MS) and validated as components of the protein cargo of the FMMs previously identified in analyses of the DRM fraction [12,13,17] (S3 Table).

MS analysis identified nine membrane proteins exclusively associated with FloA (Fig 6B). Their functional classification suggested their active participation in processes related to cell envelope regulation and cell division regulation. Those include the cytoskeletal-associated proteins MreC and PBP1A/1B or proteins related to cell wall remodeling, such as TagU and PhoR [38] (Fig 6B). We were particularly interested in the PhoR-FloA interaction, as this is a signaling kinase that activates a cascade that is related to cell wall organization [39] and is probably representative of the contribution of FloA to the FMMs. Using a BTH assay, we confirmed a specific interaction between PhoR and FloA (≥ 700 Miller Units) that was not observed between PhoR and FloT ($\leq$ 700 Miller Units) (Fig 6C). In contrast, a total number of sixteen proteins were identified in exclusive association with FloT and their functional classification suggested an important role in adaptation to stationary phase (Fig 6B). This is the case for YclQ, YhfQ or YfiY proteins involved in siderophore uptake (reviewed in [40]); the protein secretion components SecA, SecDF and YacD, which have been correlated to FloT in previous studies [13] and the membrane-bound sensor kinase ResE, required for antibiotic, siderophore production and adaptation to oxygen-limiting conditions [41]. BTH analysis confirmed the interaction of ResE and FloT ($\geq$ 700 Miller Units) that was not observed between ResE and FloA ($\leq$ 700 Miller Units) (Fig 6C). We also identified a group of twenty-six proteins that interacted with both FloA and FloT (Fig 6B). The functional classification of this group is more diverse but generally related to cell differentiation processes. This includes the metalloprotease FtsH, required for the activation of Spo0A and thus, biofilm formation and sporulation [42] and known to interact with FloA and FloT from previous studies [13,16,17] and the OppABCDF oligopeptide permease, responsible for importing peptidic signals to activate biofilm formation or natural competence [43].

To investigate in more detail the interactions between FloA-PhoR and FloT-ResE that we discovered in the BN-PAGE and the bacterial two-hybrid analysis, we performed co-localization experiments using FloA-mCherry, PhoR-GFP and FloT-mCherry, ResE-GFP double-labeled strains. We confirmed by RT-PCR analyses that PhoR-GFP and ResE-GFP translational fusions complemented Δ*phoR* and Δ*resE* mutants respectively, which suggested that the translational fusions were functional (S6 Fig). Co-localization of FloA and PhoR signals was detected by fluorescence microscopy. Likewise, we also detected co-localization of the FloT and ResE signals (Fig 6D). Colocalization of PhoR and ResE with their respective flotillin was detected in all cells examined (Pearson's correlation coefficients $R^2 = 0.82$ and $R^2 = 0.85$, respectively). These results suggest that FloA-PhoR and FloT-ResE are spatially correlated and support our hypothesis that FloA-PhoR and FloT-ResE physically interact. The specific interaction detected between PhoR and ResE sensor kinases and their respective flotillins was explored in further experiments to better understand how the scaffold activity of bacterial flotillins physically influences the activity of their signaling partners. The most direct hypothesis is that scaffold proteins facilitate signal transduction through tethering of signaling partners, because they enforce proximity and increase the likelihood of their interaction [44]. Thus, we investigated the effect of increasing concentrations of the scaffold flotillins on the interaction and activity of PhoR and ResE. PhoR and ResE belong to the PhoPR and ResDE two-component systems (TCS), which comprise a receptor histidine kinase and their cognate response regulator (PhoP and ResD). Histidine kinases are activated by forming homodimers, autophosphorylate and generate a phosphotransfer reaction to their response regulators. First, we generated a BTH assay to quantitatively monitor the homo-dimerization of PhoR and ResE (Fig 7A). This assay was complemented with a pSEVA modulable vector system [45], to generate different strains that produced lower, medium and higher levels of their respective flotillins that were further validated by immunoblotting (Fig 7A). These strains were used to quantitatively monitor the homo-dimerization efficiency of PhoR and ResE kinases with different concentrations of FloA and FloT, respectively. Both PhoR and ResE kinases responded similarly to increasing concentrations of their respective flotillins. A slight improvement in their interaction efficiency was observed with lower concentration of flotillins, which improved with medium concentration of the flotillins. Importantly, the BTH assay that produced higher concentration of the flotillins showed a decrease in the interaction efficiency of both kinases. This is consistent with the typical limitation of scaffold proteins, in that higher concentrations of the scaffold titrate signaling partners into separate complexes, thus inhibiting their interaction [46] (Fig 7B), as it has been experimentally shown in the scaffold protein Ste5 in yeast [47]

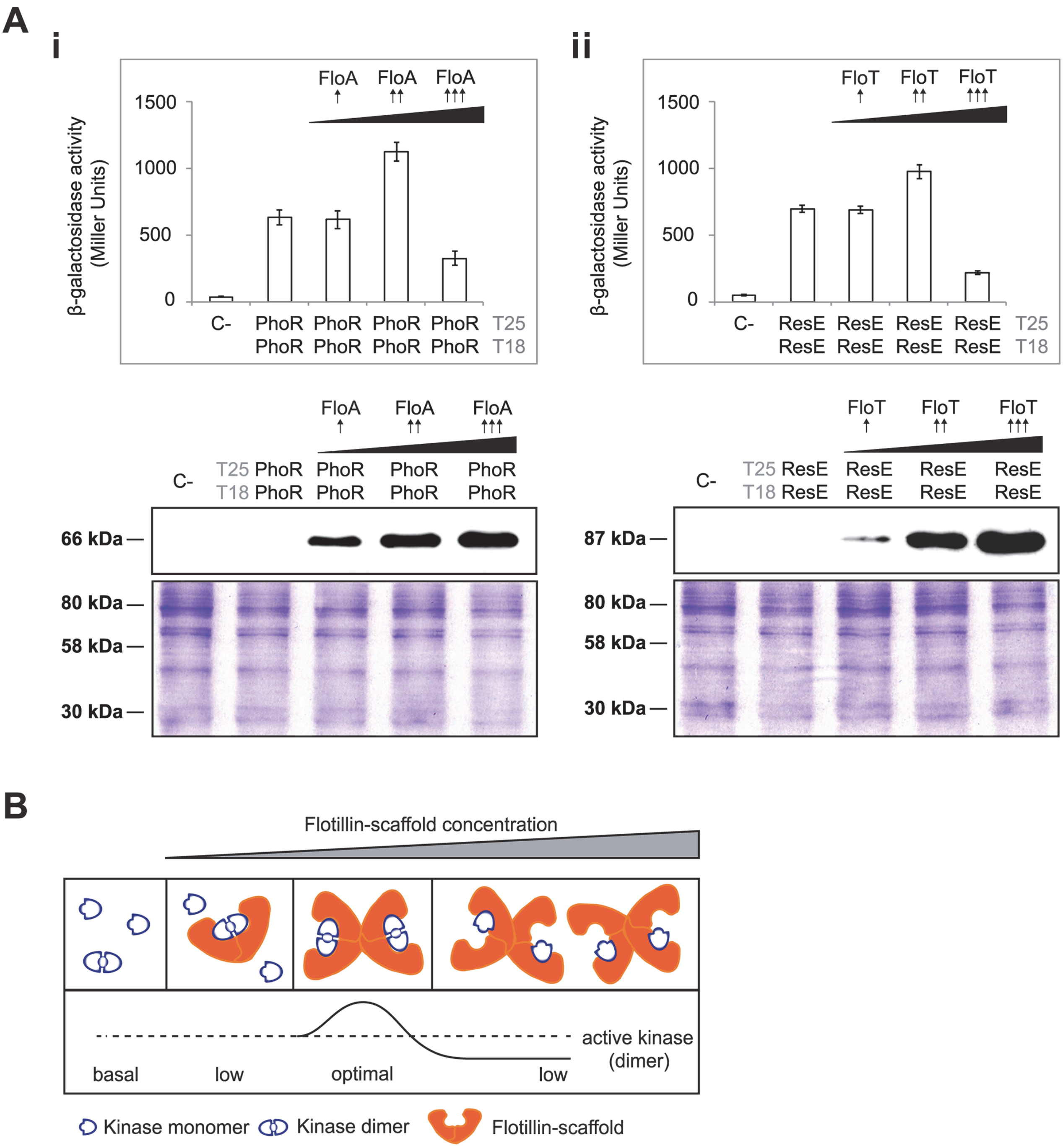

Fig 7. Tethering of signaling partners mediated by flotillins. (A) BTH assay to quantify the interaction of PhoR (i) and ResE (ii) under different concentrations of flotillins (upper panels). Dashed line indicates the threshold limit of 700 Miller Units that defines a positive (≥ 700 Miller Units) and a negative interaction signal (≤ 700 Miller Units) according to the instructions of the manufacturer. Lower- (pSEVA-621), medium- (pSEVA-631) and high-copy (pSEVA-641) plasmids expressing His^6-tagged FloA and FloT rendered lower (↑), medium (↑↑) and higher (↑↑↑) concentration of flotillin in the BTH assay,

respectively, according to immunoblot analysis (lower panels). SDS-PAGE are shown as loading control. **(B)** Inhibition of the activity of a protein complex by scaffold titration. Protein assembly by scaffold proteins has potential drawbacks. At high concentrations, scaffolds may titrate enzyme and substrate away from each other.

doi:10.1371/journal.pgen.1005140.g007

and the JIP1 scaffold human cells [48]. This suggests that bacterial flotillins act as scaffold proteins to specifically facilitate signal transduction through tethering of signaling partners.

To investigate the influence of flotillins in the activation of PhoPR and ResDE TCS, we performed qRT-PCR analysis to quantify the transcription of genes which expression is strongly controlled by PhoP and ResD regulators (Fig 8A and 8B). We detected that the expression of the PhoP-regulated genes *glpQ* and *tuaB* involved in cell envelope metabolism [49,50] were reduced in a strain lacking the kinase PhoR and a strain lacking FloA. Likewise, the expression of the ResD-regulated gene *sboX*, responsible for the production of the antibiotic subtilosin [51], and *yclJ*, a gene that encodes for a regulatory protein [52] was reduced in a strain lacking the kinase ResE and a strain lacking FloT (Fig 8A and 8B). Control strains producing tagged versions of the cognate regulators (PhoP-3xFlag and ResD-3xFlag) showed comparable level of the regulators among the different strains, suggesting that the deletion of the respective flotillin specifically affects the activity of each cognate regulator, which in turn inhibits the expression of regulated genes.

Activation of the cognate regulators promotes a conformational change that impacts gene expression. Thus, the protein-protein interaction experiments were coupled to an in-depth analysis of the transcriptional profile of *B. subtilis* cells lacking *floA* or *floT* genes. The Δ*floA* and Δ*floT* mutants were grown to stationary phase. Total RNA was purified and used to perform microarray analysis using whole-genome *B. subtilis* genechips. Experiments were performed in triplicate and genes were considered differentially expressed when $\geq$2 fold in expression was detected in all replicates. Our microarray analysis indicated 123 genes to be differentially expressed (S4–S6 Tables and GEO database accession number GSE47918). 77 of these genes belong to different signaling regulons of *B. subtilis*, which were organized in a Voronoi treemap (Fig 8C). Each sector of the Voronoi treemap represents a gene and is labeled with the name of the gene that it represents. Each section is labeled in a two-color code to denote upregulated genes (in green) and downregulated genes (in red). There is no biological significance associated with the different shapes that are assigned to each sector. The magnitude of the fold change can be examined in supplemental S4–S6 Tables. This categorization revealed a group of genes whose expression depended on *floA* expression and a second group whose expression depended on *floT* expression. For instance, cells lacking *floA* showed induction of a large number of genes related to cell envelope metabolism, represented by *sigM* and *yhdl*, *yhdK*, *yfml* and *csbB* and *ytrGABCDEF sigM*-induced genes [53]. Additional genes related to cell wall reorganization were also detected (*ytgP*, *dnaA*, *scpA* and *scpB*), including *tagAB* and *tagDEFGH* operons, which are known of being repressed by PhoPR. Cells lacking *floT* displayed a strong inhibition of the genes that constitute the ResDE regulon (*qcrABC*, *ykuNOP*, *dhbABCEF*, *hmp*, *nasDE and sboXA*-*albABCDEFG*) [54]. Their expression is particularly prominent at stationary phase, when the production of the antibiotic subtilosin (*sboXA-albABCDEFG*) [51] and the siderophore bacillibactin (*dhbABCEF*) [55] is necessary. To validate the results obtained by microarray analysis, we performed qRT-PCR gene expression analysis on several genes that belong to the different regulons that are represented in the Voronoi treemap. qRT-PCR analysis showed comparable results to microarray analysis (Fig 8D).

The differential regulation of gene expression that is caused by the activity of FloA and FloT was manifested at the physiological level. We detected phenotypic differences in the Δ*floA* and the Δ*floT* mutants that may be related to the different expression of the controlled genes. For

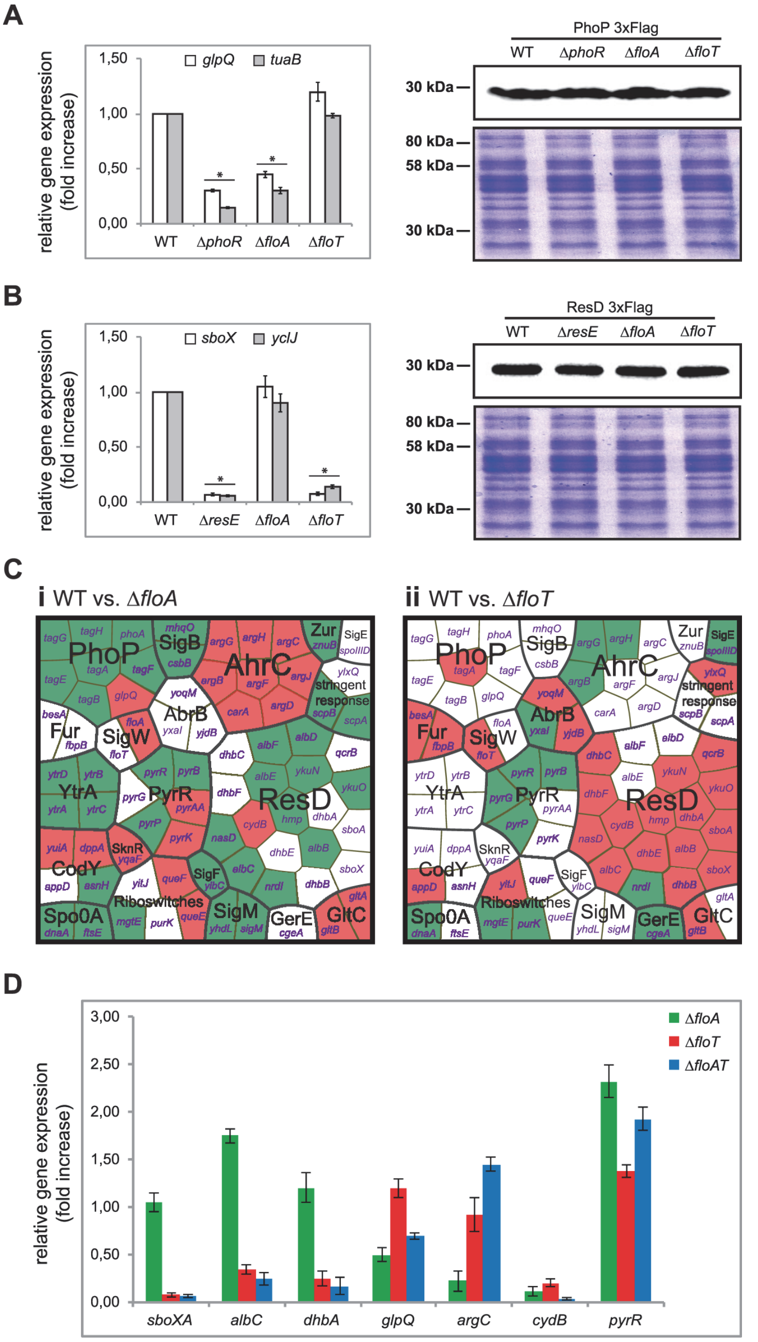

Fig 8. Flotillins influence kinase-dependent activation of PhoP and ResD regulators. (A) Left panel shows qRT-PCR of the PhoP-regulated genes *glpQ* and *tuaB* in different genetic backgrounds. Statistically significant differences are marked with an asterisk (Student's t-test $p \leq 0.05$). Right panel shows immunoblot assay to detect PhoP-3xFlag in different genetic backgrounds. **(B)** Left panel shows qRT-PCR of the ResD-regulated genes *sboX* and *yclJ* in different genetic backgrounds (Student's t-test $p \leq 0.05$). Right panel shows immunoblot assay to detect ResD-3xFlag in different genetic backgrounds (right panel). **(C)** Genome-

wide gene expression analysis of flotillin-regulated genes. Voronoi treemaps represent upregulated genes (green sectors) and downregulated genes (red sectors) in the Δ*floA* mutant (i) and Δ*floT* mutant (ii) in comparison to the wild-type strain. Genes whose expression was altered are represented and functionally classified in regulons. Each section is labeled with the name of the genes that represents. **(D)** qRT-PCR analysis of selected genes from the genome-wide gene expression analysis to validate the microarray data.

doi:10.1371/journal.pgen.1005140.g008

instance, when mutants were grown in Fe^{2+}-containing growth medium, only the Δ*floA* mutant accumulated the extracellular red pigment pulcherrimin (Fig 9A), resulting from the condensation of Fe^{2+} with the dipeptide pulcherriminic acid (Leu-Leu) (abs 420 nm) [56]. Pulcherriminic acid accumulates and is released into the medium in response to an excess of amino acid residues that decorate peptidoglycan precursors of bacterial cell wall synthesis, which is usually indicative of a defective cell wall metabolism [56–59]. This suggest that Δ*floA* mutant is defective in cell wall turnover and is consistent to our proteomic and transcriptomic analyses, suggesting that FloA plays a role in the regulation of cell wall metabolism. Moreover, the Δ*floA* mutant showed reduced sensitivity to the antibiotic vancomycin (Fig 9B), similar to other cases in which reduced sensitivity to vancomycin has been observed in cell-wall deficient strains. Vancomycin binds to the C-terminal D-Ala-D-Ala sequence of the pentapeptide peptidoglycan, thereby preventing the integration of peptidoglycan subunits into the cell wall. Cells that show a defective peptidoglycan turnover also show a reduced number of targets to the action of vancomycin and therefore, reduced sensitivity to the action of this antibiotic [60–62]. However, a defective cell wall often implies a less efficient barrier against the diffusion of other antibiotics [63–65], as is the case of the membrane pore-former sublancin [66]. Accordingly, the Δ*floA* mutant shows a higher sensitivity to the glycopeptide sublancin [67].

Likewise, we tested the capacity of the Δ*floA* and Δ*floT* mutants to adapt to stress-related conditions that are typically associated with cultures that undergo stationary phase. When we grew the Δ*floA* and Δ*floT* mutants under oxygen-limiting conditions, only the Δ*floT* mutant displayed a defective growth (Fig 9C). In contrast, the Δ*floA* mutant was able to grow at similar rate to the wild-type strain. The incapacity of the Δ*floT* mutant to adapt to oxygen-limiting conditions could be attributed to a defective activation of the ResDE regulon, as the activation of this regulon is necessary to allow nitrate respiration and thus, cell growth in oxygen-limiting conditions. Our data shows that this mechanism seemed defective only in the Δ*floT* mutant, which grew poorly in oxygen-limiting conditions (Fig 9D). This is consistent with the role that FloT plays in the regulation of stationary phase and stress-related cellular processes, including the activation of the ResDE regulon, which we have detected in our proteomic and transcriptomic data. Taken together, Fig 9E shows a tentative model that integrates our proteomic, transcriptomic and physiological data. This model shows how FloA and FloT scaffold tether distinct signal transduction pathways, which ultimately control different cellular processes in *B. subtilis*. Furthermore, this model illustrates how functionally different FMMs regulate different genetic networks in a bacterial cell, which leads to the activation of different physiological processes.

Discussion

There is growing recognition of the importance of eukaryotic lipid rafts in numerous cellular processes as diverse as protein sorting, membrane trafficking, compartmentalizing signaling cascades or pathogen entry [2,68]. This functional diversity is currently attributed to a different lipid and protein composition of lipid rafts, as it is hypothesized that a heterogeneous population of lipid rafts could exist on cellular membranes specialized on different biological processes [3–5]. Yet, the molecular mechanisms by which cells generate and regulate raft

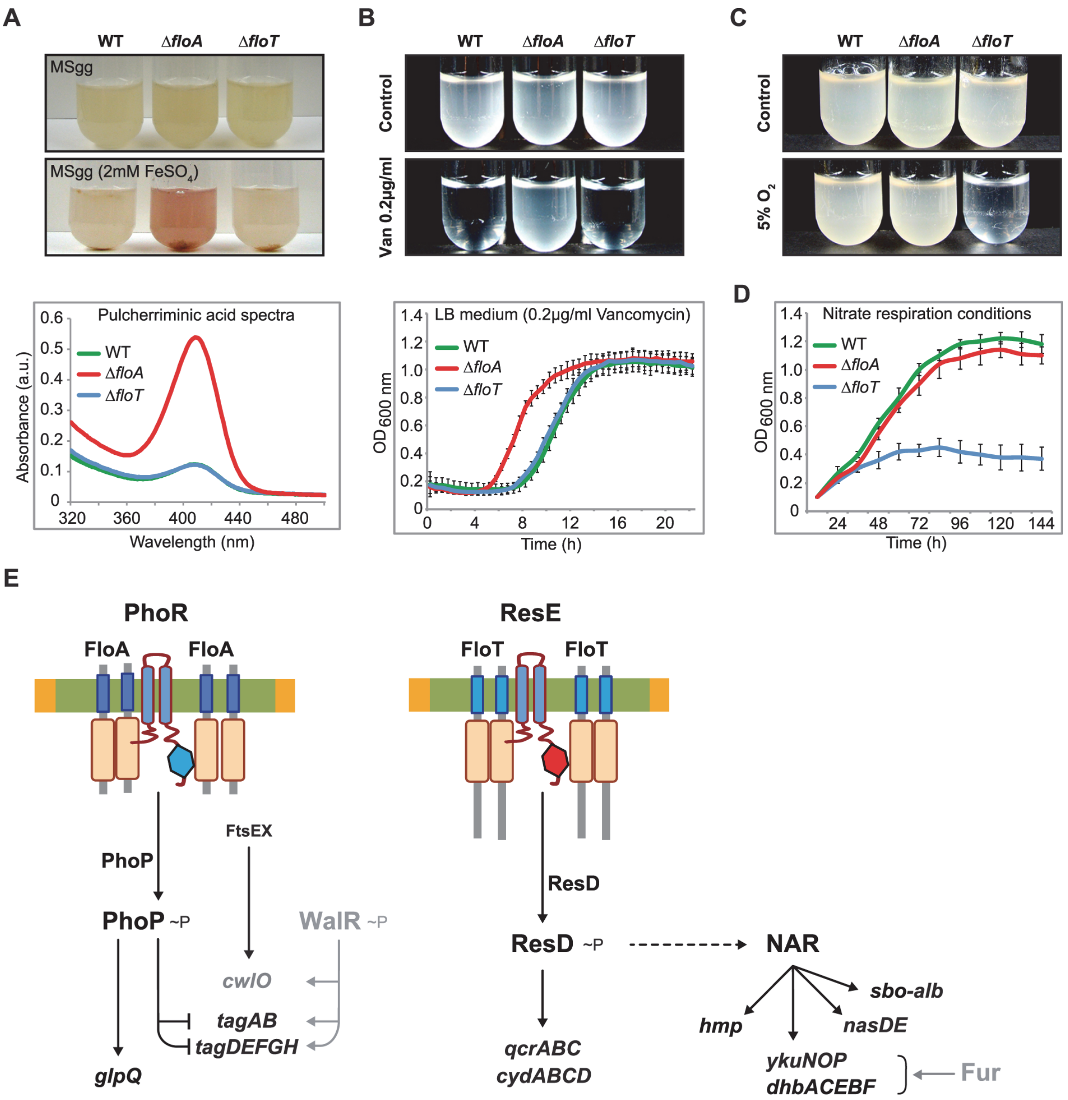

Fig 9. FloA and FloT flotillins influence different physiological processes. (A) Upper panel shows different strains grown in liquid MSgg medium and MSgg supplemented with 2mM FeSO$_4$ to stationary phase. Bottom panel shows the spectrum of pulcherriminic acid that was measured in cell extracts. **(B)** Upper panel shows the pictures of cultures of different strains that were grown with or without vancomycin (0,2 μg/ml) (MSgg liquid medium). Bottom panel shows their growth curve in the presence of vancomycin (0,2 μg/ml) (LB liquid medium). **(C)** Pictures of cultures of different strains that were grown in MSgg liquid medium in regular atmosphere or under oxygen-limiting conditions. Cells were incubated at 30°C for 72h. **(D)** Growth of the different strains in the absence of oxygen. MSgg medium was modified by replacing glutamate and glycerol with glucose 1% and NaNO$_3$ 0,2% **(E)** Schematic representation of the specific signaling pathways that are associated with FloA or FloT. Genes detected in the microarray analysis whose expression was influenced by flotillins are represented in black.

doi:10.1371/journal.pgen.1005140.g009

heterogeneity are still unclear. Nevertheless, it is assumed that cells likely regulate the process of raft diversification, to avoid the assembly of membrane signaling platforms that could simultaneously send distinct and conflicting signals to the cell. Here we use a bacterial model to show that *B. subtilis* cells are able to diversify FMMs into distinct families of signaling platforms, which are specialized in regulating distinct cellular processes, supporting the current hypothesis that a heterogeneous population of functionally specialized microdomains could exist on cellular membranes.

The discovery of the existence of FMMs adds to other examples of compartmentalization of macromolecules in bacteria, which demonstrate that bacteria are sophisticated organisms with an intricate cellular organization [69,70]. The biological significance of bacterial FMMs could be similar to the role of lipid rafts in eukaryotic cells. One possible function of FMMs could be the generation of a specific microenvironment to protect certain biological processes from inadequate conditions and non-specific interactions. For instance, spatial separation of signal transduction pathways may benefit their interaction specificity. Another plausible role for FMMs is to serve as platforms that control the assembly of membrane-bound protein complexes. By accumulating functionally related proteins in subcellular compartments, the likelihood of interaction increases and thus protein-protein interactions can be efficiently organized in space and time [2,11]. This phenomenon is facilitated by the activity of flotillins, which are FMMs-localized scaffold proteins that coordinate the physical assembly of protein interaction partners [44].

FloA and FloT seem to behave like other scaffold proteins that were described in eukaryotic cells, by specifically tethering signaling partners at lower concentrations or titrating, and thereby inhibiting their interaction at higher concentrations [44,46–48]. We show in this report that FloA and FloT self-interact and distinctively distribute within the FMMs of *B. subtilis*. Furthermore, FloA and FloT bind to and facilitate the interaction of different protein components and thus, activate different signal transduction cascades. The main force involved in generating raft heterogeneity is the uneven spatio-temporal distribution of two distinct flotillins FloA and FloT, Similarly, there are two flotillin paralogs in metazoans, FLO-1 and FLO-2, which show differential expression in distinct tissues, suggesting that these proteins may display certain level of specialization in scaffolding distinct cellular processes [71]. Based on this, it is possible that distinct families of lipid rafts may exist in the membrane of eukaryotic cells as well, yet this hypothesis still needs to be experimentally addressed.

Why do cells need or use different rafts? Cells may use this strategy to deliberately activate diverse cellular processes in time to ultimately dictate cell fate [3,72]. Here we show an example in which FMM remodeling occurs during bacterial growth using differential regulatory programs for flotillin expression. While FloA is constitutively expressed, the expression of FloT is restricted to stationary phase. Bacteria could use this mechanism to restrict the assembly and activation of particular protein components to stationary phase. Furthermore, the expression of a different scaffolding protein at stationary phase could help to rapidly adapt the signal transduction networks to face new environmental conditions. Bacteria possibly use this strategy to deliberately activate diverse cellular processes in time to ultimately ensure an effective activation of signaling processes during the lifespan of a bacterium [3,72].

Cells control the expression of each flotillin to restrict their expression to the growth stage in which their functionality is necessary. FloA preferentially tethers protein components associated with cell wall turnover and primary metabolism. Consequently, the Δ*floA* mutant shows a defect in cell wall turnover. In contrast to FloA, FloT is responsible for tethering protein components that are related to adaptation to stationary phase, such as production of siderophores and antibiotics. In addition to this, we found several proteins associated with the FMMs that interact with both FloA and FloT and are related to biofilm formation and sporulation (see Fig 4). An example of this is the membrane-bound protease FtsH that is required for biofilm formation and sporulation [42], which has been shown to interact with FloA and FloT [13,16,17], as we confirmed in this report. Based on these results, it is likely that the Δ*floA* Δ*floT* double mutant shows additional and more pleiotropic defects in signal transduction than the Δ*floA* and Δ*floT* single mutants [17]. Likewise, a pleiotropic defect in cell division and biofilm formation has been associated with the overproduction of both FloA and FloT, which is not observable with the overproduction of either FloA or FloT separately [16].

The differential distribution of flotillin within lipid rafts opens additional questions as to whether other structural components of the lipid rafts, like for instance the constituent lipids, show a different spatio-temporal distribution pattern and thus, may also contribute to raft heterogeneity. All these questions were hindered by the difficulty to characterize subcellular structures in the past. However, the development of recent technologies is changing our knowledge about the structure and function of subcellular structures, including lipid rafts [73,74]. The development of super-resolution microscopes and corresponding data analysis methods may well ease the study of bacteria and offer a tractable model to study the role of membrane microdomains, which is rather complicated in their eukaryotic counterparts. The finding that bacteria organize membrane microdomains functionally and structurally equivalent to lipid rafts represents a remarkable level of sophistication in the organization of bacterial signaling networks that allow prokaryotes to amplify and integrate diverse stimuli. Overall, the spatio-temporal organization of signaling networks in bacteria evidences that bacteria are more complex organisms than previously appreciated.

Materials and Methods

Strains, media and growth conditions

Bacillus subtilis undomesticated wild type NCIB 3610 was used as parental strain in this study [23]. *Escherichia coli* DH5α and *B. subtilis* 168 strains were used for standard cloning and transformation procedures. A full strain list is shown in S1 Table. Selective LB agar was supplemented with antibiotics at final concentrations of: ampicillin 100 μg/ml; spectinomycin 100 μg/ml; erythromycin 2 μg/ml and lincomycin 25 μg/ml, tetracycline 5 μg/ml; chloramphenicol 3 μg/ml; kanamycin 50 μg/ml. When required, surfactin (Sigma, USA) was added from a stock solution to a final concentration of 5 μM. To maintain *B. subtilis* cells at exponential phase, cells were grown in shaking liquid LB cultures at 37° C overnight. Liquid LB medium was inoculated with 1:100 volume of the overnight culture and grown to OD600nm = 0.3 with vigorous shaking (200 rpm). To prolong growth at exponential phase, cells were repeatedly passed to fresh LB medium. Passaging was performed when cells reached OD600nm = 0.3. We repeated this procedure as described in [24] for approximately 20 generations prior to cell examination. To search for regulatory proteins that control the expression of *floA* and *floT* genes, the collection of mutants harboring the P_{floA}-*yfp* and P_{floT}-*yfp* transcriptional reporters were grown overnight in LB medium at 37°C with continuous agitation (200 rpm). After this, 2 μl of the overnight LB culture was spotted on MSgg agar plates and colonies were allowed to grow at 30°C for 72 h. Images were taken on a Nikon SMZ 1500 Zoom Stereomicroscope equipped with an AxioCam color (Zeiss, Germany). To monitor gene expression, YFP reporter signals were detected using a 520/20 excitation and BP535/30 emission filter. The excitation time was set to 5 s. Unlabeled wild type strain was used as negative control to determine the background.

Construction of strains

Deletion mutants were generated using long flanking homology PCR [75] (using the primers listed in S3 Table). Markerless gene deletions were used to generate the Δ*floA*, Δ*floT* and Δ*floA* Δ*floT* mutants. Upstream and downstream regions of the *floA* and *floT* genes were joined by long flanking homology PCR [75] and cloned into the vector pMAD [76]. Gene deletion occurs via a sequential process of double recombination. Isolation of the mutants was achieved by counterselection, as described in [76]. The strains harboring the P_{floA}-GFP and P_{floT}-GFP

Dipl. – Phys. Christian Franke
Lehrstuhl für Biotechnologie und Biophysik
Biozentrum, Am Hubland
97074 Würzburg
Germany

Würzburg, 4th July 2017

Manuscript:

Christian Franke, Markus Sauer, and Sebastian van de Linde.

Photometry unlocks 3D information from 2D localization microscopy data

Nat. Methods 14, 41{44, (2017), doi:10.1038/nmeth.4073

The contributions of the PhD candidate Christian Franke to the above manuscript involved:

- Idea, design, development and evaluation of the TRABI algorithm (collaboratively)
- Analysis of pre-published data concerning the *virtual 3D* method
- Preparation of samples (single molecule surfaces and microtubules)
- Design and execution of experiments
- Implementation, execution and evaluation of all Biplane post-processing steps
- Implementation, execution and evaluation of single molecule simulations
- Contribution to the manuscript draft and revision process

Christian Franke | Markus Sauer | Sebastian van de Linde

Photometry unlocks 3D information from 2D localization microscopy data

Christian Franke[1], Markus Sauer[1] &
Sebastian van de Linde[1,2]

We developed a straightforward photometric method, temporal, radial-aperture-based intensity estimation (TRABI), that allows users to extract 3D information from existing 2D localization microscopy data. TRABI uses the accurate determination of photon numbers in different regions of the emission pattern of single emitters to generate a *z*-dependent photometric parameter. This method can determine fluorophore positions up to 600 nm from the focal plane and can be combined with biplane detection to further improve axial localization.

Single-molecule localization microscopy (SMLM) methods, such as photoactivated localization microscopy (PALM)[1] and direct stochastic optical reconstruction microscopy (dSTORM)[2], have become widely used. To facilitate 3D cellular imaging with enhanced isotropic resolution, different methods for 3D imaging have been successfully introduced, such as astigmatism[3] or multiplane imaging[4,5], albeit at the cost of increased technical complexity[6–10].

We developed a simple 3D SMLM method that is based on photometric analysis of the fluorescence emission pattern of single emitters and uses an algorithm we refer to as TRABI. In combination with state-of-the-art localization software packages, it allowed the accurate determination of single-molecule intensities.

We reasoned that the photon distribution in a diffraction-limited image (spot) of a single fluorophore, recorded on standard SMLM setups, normalized to the total detected light could be used to extract its axial position. Using two circular apertures around the center of a spot with radii r_1 and r_2, with $r_1 > r_2$, we were able to determine the intensities in these areas and the photometric ratio $P = I_2\, I_1^{-1}$. Given a redistribution of photons by defocusing, P then becomes a function of the axial position of the fluorophore (**Fig. 1a**).

Thus, we first developed a method to accurately determine total photon numbers (TRABI), which was mainly inspired by classical aperture photometry (AP) (**Supplementary Note 1**)[11,12]. AP is based on subtracting the background from the total intensity signal to determine the fluorophore brightness. The background is estimated by analyzing the local area next to the emitter (**Supplementary Fig. 1**). TRABI advantageously uses fluorescent on-states and non-fluorescent off-states of photoswitchable or photoactivatable fluorophores (**Supplementary Figs. 2**–**4**). A circular aperture with radius r_1 and area A_1 encircles the center of the spot (**Fig. 1b**). The integrated signal in this aperture gives the raw intensity, $I_{\mathrm{raw},1}$. In contrast with AP, the same aperture is then used to determine the background intensity, I_{BG}, in a subsequent frame, when the fluorophore resides in its off-state (or bleached state). In this way, the local background can be accurately determined and the corrected intensity calculated, $I_1 = I_{\mathrm{raw},1} - I_{\mathrm{BG}}$, without the need to expand the aperture (**Supplementary Fig. 4**).

We implemented TRABI in ImageJ to analyze SMLM image stacks (**Supplementary Software** and **Supplementary Notes 1** and **2**). TRABI read the localization file of well-established localization software packages such as rapidSTORM[13] and output a new text file, which was extended by I_1 of the spot as well as background information. To avoid contributions from adjacent fluorophores to the background signal, we defined a circular exclusion zone around the spot with radius $2r_1$ and checked for the presence of other single-molecule coordinates (**Fig. 1b** and **Supplementary Fig. 2**). In the case of interference, the current frame was skipped and the next frame was analyzed in the same way to determine I_{BG}. TRABI also allowed averaging over multiple apertures in a number of successive frames, n_{BG}, to improve statistics for background estimation (**Supplementary Fig. 3**). The analysis was complemented by a second circular aperture covering only the central part of the emission pattern (I_2) (**Fig. 1a**). For each single-molecule spot, TRABI generated the photometric ratio $P = I_2\, I_1^{-1}$.

Using simulations, we determined optimal parameters to reliably measure total spot intensities at high precision, that is, $r_1 = 1.86 \times$ FHWM (full width at half maximum) and $n_{\mathrm{BG}} = 7$ (**Supplementary Fig. 3**). Over a range of 500–35,000 simulated photons per spot (I_{True}) and 1–50 noise photons (s.d.), TRABI provided accurate single-molecule intensities ($I_1 \approx I_{\mathrm{True}}$) (**Supplementary Fig. 4**).

TRABI was tested on experimental data originating from surface-immobilized Cy5-labeled DNA molecules. The total photon numbers (I_1) of five experimentally recorded spots were determined to be between 2,736 and 5,366 (**Fig. 1c**), exceeding alternative intensity estimations by AP and Gaussian fitting. Single-molecule intensities obtained by Gaussian fitting (I_{Fit}) were calculated by the localization software, and were significantly underestimated.

Next, we varied the distance of the objective from the single-molecule surface using a piezo scanner (**Fig. 1d**) and recorded 1,000 frames every 100 nm under dSTORM conditions. For every spot, the photometric ratio P was determined by $r_1 = 1.86 \times$ FWHM and $r_2 = 5/13 \times r_1$. We generated histograms of P for every data set and found a strong z dependence. When the sample was

---

[1]Department of Biotechnology and Biophysics, University of Würzburg, Würzburg, Germany. [2]Present address: Department of Physics, University of Strathclyde, Glasgow, UK. Correspondence should be addressed to S.v.d.L. (s.vandelinde@strath.ac.uk).

RECEIVED 15 JULY; ACCEPTED 16 OCTOBER; PUBLISHED ONLINE 21 NOVEMBER 2016 ; DOI:10.1038/NMETH.4073

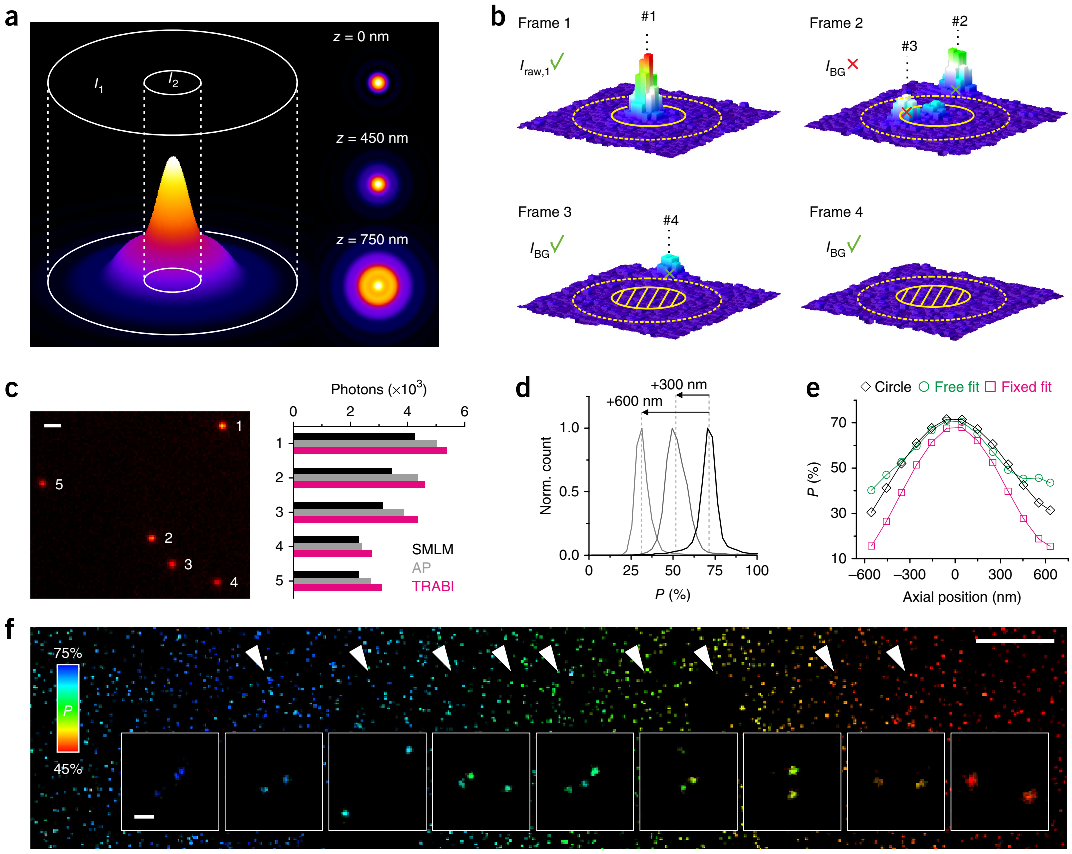

Figure 1 | Photometry-based 3D super-resolution imaging. (**a**) The z-dependent photometric parameter P is created by determining the intensities in two apertures of the molecule's emission pattern according to $P = I_2\, I_1^{-1}$. (**b**) Principle of TRABI, which uses a circular aperture with radius r_1 (solid circle) and an exclusion zone defined by $2r_1$ (dashed circle); I_1 is determined by subtracting background (I_{BG}) from raw intensity ($I_{raw,1}$); $I_{raw,1}$ and I_{BG} are not estimated in frames in which localizations from neighboring spots interfere. (**c**) Left, dSTORM imaging of surface-immobilized Cy5-labeled DNA. Right, number of photons obtained by fitting using rapidSTORM (free fit; black), classical AP (r_1 = 865 nm, r_2 = 1,131 nm; gray) and TRABI (r_1 = 865 nm, n_{BG} = 7; magenta). (**d**) Histograms of P for different axial positions of the single-molecule surface adjusted with a piezo-scanner. Dashed lines indicate the median of the distribution. (**e**) P as a function of the axial position. Dots represent the median of the distribution, solid lines are used to guide the eye; I_1 was determined by TRABI (r_1 = 865 nm), and I_2 was determined either by TRABI (r_2 = 333 nm, black curve) or through free (green) or fixed fitting (magenta, FWHM = 300 nm) in rapidSTORM. (**f**) Reconstructed dSTORM image of a single-molecule surface tilted by an angle of 0.56°, color-coded by P. Arrowheads indicate x positions of magnified single-molecule localization patterns (insets). Scale bars represent 1 μm (**c**), 5 μm (**f**, top) and 100 nm (**f**, insets).

sharply in focus, the median of the distribution was 71.4%, whereas placing the objective 300 nm and 600 nm further away yielded medians of 51.6% and 31.4%, respectively (**Fig. 1d**). Because experimentally determined P values were not normally distributed (**Supplementary Figs. 5** and **6**), we decided that the median was more robust as estimator and determined the median absolute deviation (MAD) as error. Despite the symmetry around the focus, the total working range either above or below the focal plane could be determined to at least 600 nm (**Fig. 1e**). To test our approach, we inclined the single-molecule surface by 0.56 ± 0.02°, thereby creating an axial difference of 668 ± 29 nm in the field of view (that is, 68.1 μm). Single-molecule events were robustly identified by their P values (**Fig. 1f**). Experimentally, we were able to reproduce the angle of the tilt to 0.52 ± 0.10° (**Supplementary Fig. 7**).

By using the intensity determined by Gaussian fitting ($I_2 = I_{Fit}$), we found a similar z dependence for P, albeit with reduced working range and enlarged relative error (MAD/median) (**Fig. 1e** and **Supplementary Fig. 8**). Here, Gaussian fitting was performed with the point-spread function (PSF) width as a free fit parameter where the 2D Gaussian is adapted to optimally fit the emission pattern. In other words, the size of the central aperture is erratic. Alternatively, we tested a stiff Gaussian fit with fixed width in rapidSTORM to determine I_2 (**Fig. 1e**), resulting in small relative errors of P and an extended working range of 750 nm (**Supplementary Figs. 8** and **9**). We reasoned that any geometric aperture could be used to determine I_2, including 2D fit functions such as Gaussians, which are less prone to pixelation artifacts. The effective working range is in principle limited by the analysis method, the position of the focal plane and the emitter brightness (**Supplementary Note 2**).

Although Gaussian fitting of well-established SMLM software underestimated single-molecule intensities in experimental data, it performed perfectly well on simulated data (**Supplementary Fig. 10**). The experimental deviation remained when imaging on microscope setups with different objectives and detector types (**Supplementary Fig. 11**). By averaging the single-molecule data into a single PSF, the deviation of intensity estimation was

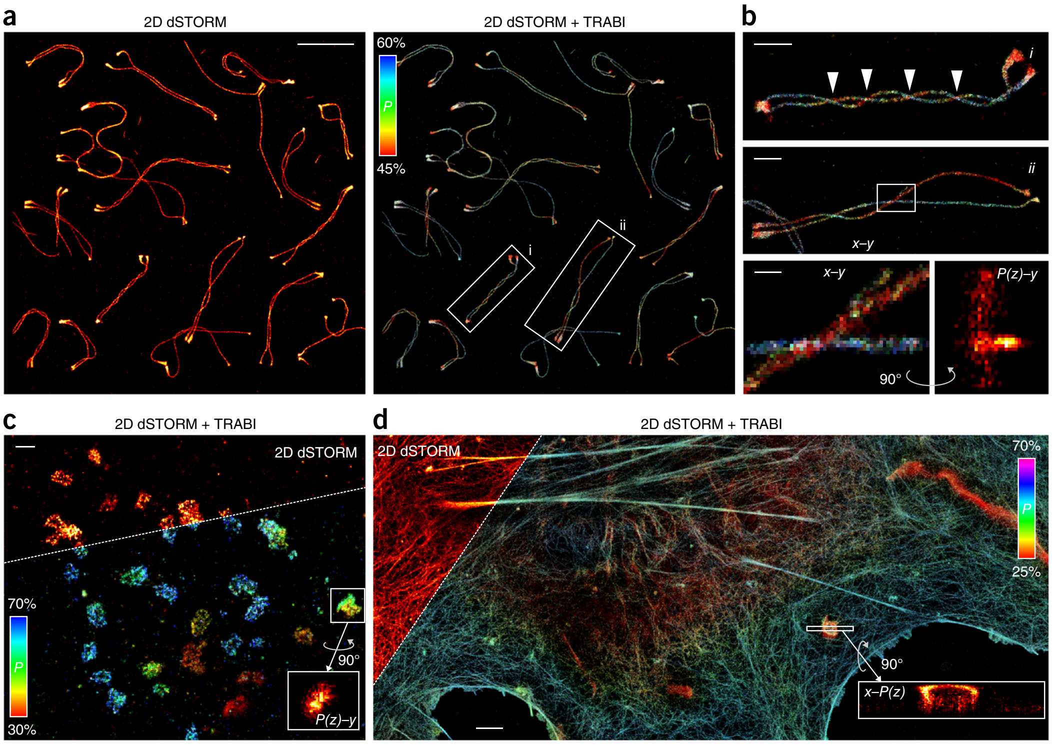

Figure 2 | Virtual 3D imaging obtained by TRABI from 2D dSTORM data on different structures. (**a**) Left, conventional 2D dSTORM image of the SC by staining SYCP3 with AF647-labeled antibodies[15]. Right, virtual 3D image, that is, *x–y–P(z)*, obtained by TRABI by analyzing the conventional 2D data. (**b**) Magnified views of insets (*i*, *ii*) shown in **a**; arrowheads indicate twists of the lateral element of the SC (*i*). Magnified views of *ii* are shown as *x–y* and *P(z)–y* projections (**Supplementary Video 1**). (**c**) 3D analysis of active zones in the neuromuscular junction of *Drosophila* larva, stained with Cy5-labeled antibodies, showing the presynaptic protein Bruchpilot in rab3 mutants[16] (**Supplementary Video 2**). Inset, *P(z)* projection of one active zone. Top left, corner shows the conventional dSTORM image. (**d**) 3D analysis of conventional 2D data on F-actin in COS-7 cells stained with Si-rhodamine-labeled phalloidin[17] (**Supplementary Video 3**). Top left, conventional dSTORM image. Scale bars represent 5 µm (**a**), 1 µm (**b**), 200 nm (**b**, bottom), 500 nm (**c**) and 2 µm (**d**).

significantly reduced with $P > 96\%$ (**Supplementary Fig. 12**). Researchers should therefore bear in mind that standard simulations, as well as more accurate models such as Gibson–Lanni[14] (**Supplementary Fig. 13**), might differ from experimentally recorded fluorescence spots as a result of optical aberrations that become noticeable by photometric analysis (**Supplementary Note 1**).

We used fixed PSF fitting (300 nm as fixed FWHM; **Supplementary Fig. 14**) to calculate P with TRABI. We applied TRABI on conventionally recorded 2D SMLM data and generated virtual 3D super-resolution images, color-coded in $P(z)$ (**Fig. 2** and **Supplementary Figs. 15** and **16**). Synaptonemal complexes (SCs), which are meiosis-specific multiprotein complexes that are essential for synapsis, recombination and segregation of homologous chromosomes, were recently studied using 2D dSTORM[15]. The SC protein component SYCP3 consists of two lateral elements, which are arranged as two cables separated by ~220 nm[15]. Using TRABI, the twist of the cables, in 2D seen as superposition (**Fig. 2a**), could axially be separated by using P (**Fig. 2b** and **Supplementary Video 1**). Furthermore, the bending of one cable surrounding the other became visible in the $P(z)$–y projection.

In addition, we reanalyzed 2D dSTORM data on the presynaptic protein Bruchpilot in *Drosophila* larva, which is a major functional component of the active zone cytomatrix[16]. The virtual 3D TRABI image clearly visualized the 3D organization of active zones in different layers, emphasizing the inclined axial arrangement of active zones that are not seen *en face* in 2D (**Fig. 2c** and **Supplementary Video 2**). Finally, we used TRABI on filamentous actin, which was imaged in a PALM-like imaging modality with caged near-infrared Si-rhodamine dyes[17]. The conventional 2D super-resolution image was successfully transformed into a virtual 3D image with additional axial information on the structural organization of F-actin (**Fig. 2d**, **Supplementary Fig. 15** and **Supplementary Video 3**). We propose that any 2D SMLM data in which the focal plane is predominantly set below or above the structure of interest can be reanalyzed with TRABI to create virtual 3D images (**Supplementary Note 2**). The FWHM information of spots, which is extractable by free fitting, could be used in a similar manner, but with substantial restrictions in terms of sensitivity (**Supplementary Figs. 8e** and **14e**).

To further increase the axial precision and scope of TRABI-based 3D imaging, we used a biplane scheme (BP)[4,5] to distinguish spots appearing above and below the focal plane, that is, $z = 0$ nm. We used an image splitter and separated the focal planes of the two channels by ~300 nm and measured a calibration curve with P as a function of z for each channel (**Supplementary Fig. 8**). We were able to retrieve absolute axial coordinates over a range of ~800 nm. We then imaged Alexa Fluor 647 (AF647)-labeled microtubules by dSTORM and analyzed both image stacks

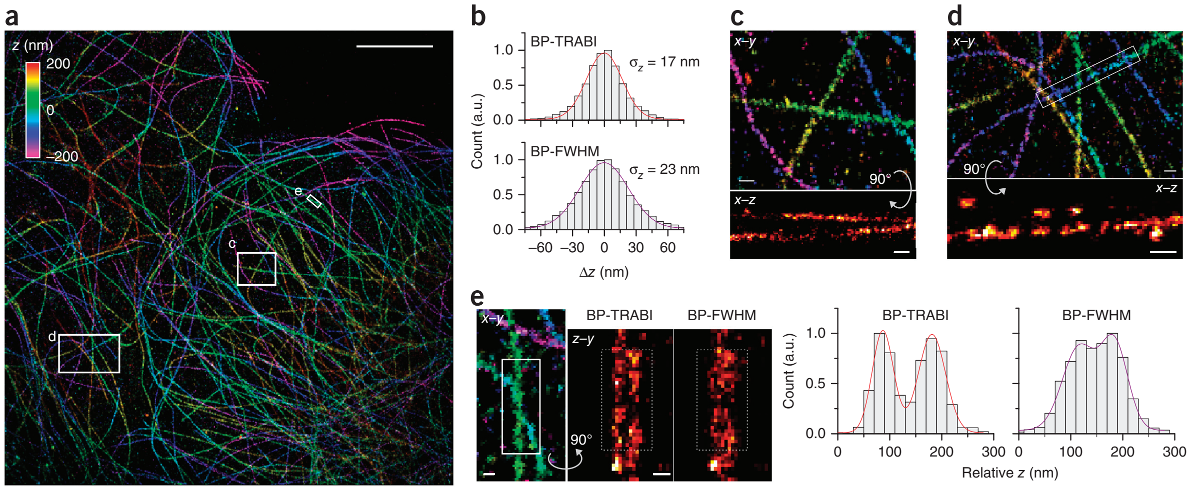

Figure 3 | 3D super-resolution imaging of microtubules in U2OS cells, stained with AF647-labeled antibodies. (**a**) 3D dSTORM image using BP-TRABI, color-coded in *z*. (**b**) Axial localization precision (s.d.) of BP-TRABI and BP-FWHM were determined to 17 nm and 23 nm, respectively. (**c**–**e**) Magnified views of insets shown in **a**. (**c**) *x*–*z* projection of the entire *x*–*y* view. (**d**) *x*–*z* projection of the boxed region of the *x*–*y* view. (**e**) *z*–*y* projection of the boxed region in *x*–*y*; cross-section profile of adjacent filaments as seen with BP-TRABI and BP-FWHM; solid lines indicate double Gaussian fits. Using BP-TRABI, indicated filaments were resolved with highest resolution and axially separated by 94 nm (averaged in *y* as indicated by dashed boxes). Regions shown in **c** and **d** are available as **Supplementary Videos 4** and **5**. Scale bars represent 5 μm (**a**), 200 nm (**c**,**d**) and 100 nm (**e**).

with rapidSTORM and TRABI. We sorted the localizations that appeared on both channels, derived the axial position of each molecule using the calibration curve, corrected the coordinates for the refractive index mismatch[3,18] and reconstructed a 3D dSTORM image (**Fig. 3a**). Enlarged regions and axial cross-section profiles of adjacent microtubule filaments clearly demonstrated improved resolution (**Fig. 3b**–**e** and **Supplementary Videos 4** and **5**). We determined the axial precision of BP-TRABI to 16.6 nm (s.d.). This precision could be further increased by applying higher photon thresholds to 12.6 nm, which is over 1.4-fold higher than classical biplane imaging using the FWHM information of the spots (BP-FWHM) (**Supplementary Fig. 17**). In contrast with BP-FWHM, we were able to fully separate adjacent filaments in axial direction at a distance of 94 nm (**Fig. 3e**). Depending on the sample, the overall increase in precision of BP-TRABI over BP-FWHM was even higher (**Supplementary Figs. 18** and **19**).

3D SMLM is a powerful research tool, but often requires complex calibration procedures. TRABI can be directly applied to any 2D SMLM data to unlock previously unused 3D information without additional optical instrumentation. This might offer new biological interpretations of many conventionally recorded data sets. TRABI can be used platform independently in ImageJ, but we expect that this algorithm can also be implemented easily in existing localization software packages to provide corrected spot intensities along with additional axial information. In addition to 3D imaging, TRABI will allow researchers to determine exact total photon numbers independent of the axial position, making it a versatile tool also for the characterization of new dyes and switching buffers.

METHODS

Methods, including statements of data availability and any associated accession codes and references, are available in the online version of the paper.

Note: Any Supplementary Information and Source Data files are available in the online version of the paper.

ACKNOWLEDGMENTS

We thank J. Enderlein (University of Göttingen) for providing us with software for the refractive index mismatch correction and D. Birch for critically reading the manuscript. We are very grateful to T. Klein, as well as to K. Schücker, R. Benavente (University of Würzburg) and L. Lavis (Janelia Research Campus) for the provision of raw data and to L. Ließ for support with cell culture.

AUTHOR CONTRIBUTIONS

C.F. and S.v.d.L. designed the TRABI algorithm, developed software, performed experiments and evaluated the data. C.F., M.S. and S.v.d.L. discussed results and commented on the manuscript. S.v.d.L. conceived the project and wrote the manuscript.

COMPETING FINANCIAL INTERESTS

The authors declare competing financial interests: details are available in the online version of the paper.

1. Betzig, E. *et al. Science* **313**, 1642–1645 (2006).
2. van de Linde, S. *et al. Nat. Protoc.* **6**, 991–1009 (2011).
3. Huang, B., Wang, W., Bates, M. & Zhuang, X. *Science* **319**, 810–813 (2008).
4. Ram, S., Prabhat, P., Chao, J., Ward, E.S. & Ober, R.J. *Biophys. J.* **95**, 6025–6043 (2008).
5. Juette, M.F. *et al. Nat. Methods* **5**, 527–529 (2008).
6. Pavani, S.R. *et al. Proc. Natl. Acad. Sci. USA* **106**, 2995–2999 (2009).
7. Shtengel, G. *et al. Proc. Natl. Acad. Sci. USA* **106**, 3125–3130 (2009).
8. Xu, K., Babcock, H.P. & Zhuang, X. *Nat. Methods* **9**, 185–188 (2012).
9. Bourg, N. *et al. Nat. Photonics* **9**, 587–593 (2015).
10. Deschamps, J., Mund, M. & Ries, J. *Opt. Express* **22**, 29081–29091 (2014).
11. Howell, S.B. *Publ. Astron. Soc. Pac.* **101**, 616–622 (1989).
12. Holden, S.J. *et al. Biophys. J.* **99**, 3102–3111 (2010).
13. Wolter, S. *et al. Nat. Methods* **9**, 1040–1041 (2012).
14. Gibson, S.F. & Lanni, F. *J. Opt. Soc. Am. A Opt. Image Sci. Vis.* **9**, 154–166 (1992).
15. Schücker, K., Holm, T., Franke, C., Sauer, M. & Benavente, R. *Proc. Natl. Acad. Sci. USA* **112**, 2029–2033 (2015).
16. Ehmann, N. *et al. Nat. Commun.* **5**, 4650 (2014).
17. Grimm, J.B. *et al. Angew. Chem. Int. Edn Engl.* **55**, 1723–1727 (2016).
18. Huang, B., Jones, S.A., Brandenburg, B. & Zhuang, X. *Nat. Methods* **5**, 1047–1052 (2008).

ONLINE METHODS

Code availability. TRABI is provided as **Supplementary Software**. Updates will be available from http://bcp.phys.strath.ac.uk/photophysics/super-resolution/software/.

Sample preparation. Single-molecule surfaces were prepared on LabTek chambered coverslips (Nunc) that were previously cleaned with 2% Hellmanex (Sigma) for 1 h by incubating each chamber with approximately 10 mg ml^{-1} bovine serum albumin (BSA) and 0.2 mg ml^{-1} biotinylated BSA (all from Sigma) overnight at 4 °C. Afterwards, chambers were treated with 0.2 mg ml^{-1} NeutrAvidin (Sigma) for 30 min. Finally, a DNA with the sequence 5′-ATC GTT ACC AAA GCA TCG TAA ATC GCA TAA TAG CAC GTT AAT TTA GCA CGG ACG ATC GCC-3′, modified with Cy5 and biotin at the 5′ and 3′ end, respectively[19], was hybridized with an unmodified antisense strand (IBA lifesciences) and used at a concentration of 10^{-7} and 10^{-10} M for a 1- to 5-min incubation period. Between each step, the sample was gently washed three times with PBS (Sigma). All solutions were prepared in PBS.

Immunostainings of microtubules, actin and the nuclear pore complex were performed as previously described[2,13,20,21]. Microtubules shown in **Figure 3** were labeled with mouse anti β-tubulin antibodies (QL2122823, Sigma) and AF647-labeled goat anti-mouse F(ab')$_2$ fragments (1692984, Invitrogen), both diluted at 1:200. Single-molecule surfaces and microtubule structures shown in **Figure 3** and **Supplementary Figures 18** and **19** were imaged in 100 mM mercaptoethylamine (MEA) at pH 7.4 applying an enzymatic oxygen scavenger system, that is, 5% (w/v) glucose, 10 U ml^{-1} glucose oxidase, 200 U ml^{-1} catalase[21]. Samples stained with Alexa Fluor 647 (AF647), AF488, AF532 and AF568 were embedded in PBS containing 100 mM MEA (Sigma) at pH 7.4–8.6 (**Supplementary Figs. 5** and **6**). COS-7 and U2OS were purchased from CLS Cell Lines Service GmbH.

Imaging. Single-molecule and dSTORM imaging was performed on a custom-built objective-type TIRF setup as described elsewhere[2,20,22], employing highly inclined illumination. We used an inverted microscope (IX71, Olympus) equipped with a nose-piece stage (IX2-NPS, Olympus) and a 60× oil objective (NA 1.45 PlanApo, Olympus). Biplane imaging was performed using a two-channel image splitter with twofold magnification (TwinCam, Cairn Research) equipped with a 50/50 beamsplitter (Cairn Research) and two EMCCD cameras (Ixon 897 and Ixon Ultra 897, Andor). Cameras were synchronized by a pulse generator (DG535, Stanford Research Systems). 3D calibration experiments were performed by moving the objective with a piezo scanner (Pifoc, Physik Instrumente) driven with a LVPZT servo controller (E-662, Physik Instrumente). The inclined surface was created by using three high precision coverslips with 170 µm ± 5 µm thickness (Carl Roth).

Comparative measurements on single-molecule surface were also performed on a Nikon Eclipse Ti-E with 100x PlanApo λ NA 1.45 oil immersion objective equipped with a sCMOS camera (Zyla, Andor) and a Zeiss-Observer Z1 with 63× LD C-Apochromat NA 1.15 water-immersion objective equipped with an EMCCD (iXon Ultra, Andor).

Simulations. Using a custom-written Python script, single-molecule spots were simulated by distributing photons randomly[23,24] on a pixel grid, according to a 2D probability distribution[25] according to the PSF of the microscope

$$\mathrm{PSF}(D)=\left(\frac{2J_1(D)}{D}\right)^2 \tag{1}$$

with $D(x, \lambda, n_1, n_2) = 2\pi n_1 x/(\lambda n_2)$, where J_1 is the Bessel function of first kind and first order, x the radial coordinate, n_1 and n_2 are the refractive indices of immersion and sample medium, respectively, and λ is the emission wavelength. For every frame, coordinates for single photons where drawn according to equation (1) with sub-nanometer precision until the target amplitude was reached. Then, the resulting emission pattern was subsequently binned into a 50 × 50 pixel-grid, where every pixel represented (100 nm)^2. Additional noise was added according to a Poisson distribution, where the target noise level was set as its mean value. To perform the TRABI analysis, a pseudo-realistic blinking behavior was achieved by inserting pure noise frames in between subsequent frames. Standard simulation parameters were $n_1 = 1.45$, $n_2 = 1.33$, and $\lambda = 670$ nm. For every amplitude-noise set 2,000 frames were simulated, consisting of each 1,000 emission and pure noise frames.

Three-dimensional emission patterns were simulated according to the Gibson-Lanni model[14] using ImageJ[26]. Parameters were set to $n_1 = 1.5$, $n_2 = 1.33$, lateral FWHM = 340 nm, NA = 1.45. The z-dependent PSF was used as probability density matrix while photons and noise were distributed as described above.

PSF averaging. Image stacks were processed with custom-written software in Python. Single spots were identified according to the localization file in rapidSTORM, centered within a 23- × 23-pixel region of interest around the pixel containing the molecule's center, cropped and binned into 1-nm sub-pixels. Each spot was then centered in the pixel-grid according to the rapidSTORM localization. Finally, all emitters were averaged into a single image, which was binned to 100 nm and 25 nm before photometric analysis.

Aperture photometry. AP was written and implemented in ImageJ and is described in **Supplementary Note 1.**

TRABI. TRABI was written and developed in ImageJ. For a detailed description see **Supplementary Notes 1** and **2** and **Supplementary Figure 2**.

Localization software. We used well-established single-molecule localization software packages[27], that is, rapidSTORM 3.3 (ref. 13), as stand-alone software as well as ThunderSTORM[28] and PeakFit[29] as up-to-date ImageJ plugins using standard settings. The PSF width was a free fit parameter in ThunderSTORM and PeakFit with fit window radii of 5.0 and 4.5 camera pixels, respectively. Fitting in rapidSTORM was performed with the PSF width (FWHM) either as free (free fit) or fixed parameter (fixed fit). If not otherwise stated a PSF FWHM of 300 nm was used for fixed fitting in rapidSTORM (**Figs. 1e**, **2** and **3**; **Supplementary Figs. 7–9**, **11**, **13** and **15–19**).

Calibrated 3D imaging with BP-TRABI and BP-FWHM. 3D calibration curves were generated by imaging a single-molecule surface under dSTORM conditions with a biplane detection scheme. Using a piezo scanner, we varied the relative axial position from −2 μm to +2 μm with a frequency of 0.00125-Hz at duty cycle of 0.999. Both cameras were triggered with a frequency of 20 Hz, thus generating a z-step width of 0.25 nm per camera frame.

Incoming fluorescence signal was split by a 50/50 beamsplitter, where the focal planes were separated by ~300 nm[5,30]. In the following, reflected and transmitted light are referred to as channel 1 and 2, respectively. Images of both channels were aligned by linear transformation.

dSTORM image stacks were analyzed in rapidSTORM. We used four different settings for 3D imaging.

1) The determination of I_1 and P with TRABI, where

a. I_2 was determined with a second circular aperture in TRABI,

b. I_2 was obtained through free PSF fitting in rapidSTORM,

c. I_2 was obtained through fixed PSF fitting in rapidSTORM.

2) The determination of the spot FWHM with rapidSTORM by free PSF fitting (classical biplane).

For 1a–c, we used the same aperture to calculate I_1. A fit window radius of 400 nm (3.0 px) was used for free fitting (1b), fixed fitting was performed with 300 nm FWHM and a fit window radius of 1,000 nm (1c), whereas for 3D biplane analysis a fit window radius of 1,500 nm (11.3 px) was applied (2) (**Supplementary Fig. 8**). For the data sets of 1b and 2, the localizations were processed with an additional filter of 200 nm < FWHM < 1,200 nm in rapidSTORM. Only values of $P > 0\%$ and $P < 100\%$ were analyzed. This filtering was also applied to the data shown in **Figures 2** and **3** and **Supplementary Figures 15**, **16**, **18** and **19**.

Because of its high precision and ease of operation we used TRABI on fixed PSF fitting to determine I_2 for the visualization of the data shown in **Figures 2** and **3** and **Supplementary Figures 15**, **16**, **18** and **19**.

Calibration curves were calculated from localizations that were found in both channels. This was done by a nearest neighbor analysis, that is, localizations further apart than 300 nm after channel transformation were discarded. For BP-TRABI, the percentage ratio $P_{1,2}$ from each localization pair was calculated as

$$P_{1,2} = \frac{P_1 - P_2}{P_1 + P_2},$$

where P_1 and P_2 stand for the photometric ratio determined with TRABI (P) for each spot in channels 1 and 2, respectively (**Supplementary Fig. 8**). Similarly, for BP-FWHM the ratio of spot widths ($w_{1,2}$) was calculated as

$$w_{1,2} = -\frac{w_1 - w_2}{w_1 + w_2},$$

where w_1 and w_2 are the FWHM of each spot in channel 1 and 2, respectively.

$P_{1,2}$ and $w_{1,2}$ were fitted with a fourth order polynomial to generate z-lookup tables with a z-resolution of 0.25 nm (**Supplementary Fig. 8d**).

Experimental data shown in **Figure 3** were analyzed according to the following protocol

1) rapidSTORM analysis (for BP-TRABI: 300 nm fixed PSF FWHM and 1,000-nm fit window radius; for BP-FWHM: PSF width as free fit parameter and 1,500-nm fit window radius).

2) TRABI evaluation of the data to determine P.

3) Nearest neighbor assignment of the two channels for both data sets, BP-TRABI and BP-FWHM, to calculate $P_{1,2}$ and $w_{1,2}$ of each localization, respectively.

4) Final z-coordinates were assigned from the lookup tables, corrected for the refractive index mismatch and visualized with rapidSTORM and ImageJ.

z-coordinates were corrected for the refractive index mismatch by a scaling factor of 0.71 (refractive index of buffer with 5% glucose $n_b = 1.34$ and substrate (glass) $n_s = 1.52$, numerical aperture of NA = 1.45, emission wavelength $\lambda_{em} = 680$ nm, assuming isotropic emission)[31,32].

Data availability. Data are available from the author upon reasonable request. Source data for **Figures 1**, **3** and **Supplementary Figures 1**, **3**, **4** and **10** are available online.

19. Heilemann, M., Kasper, R., Tinnefeld, P. & Sauer, M. *J. Am. Chem. Soc.* **128**, 16864–16875 (2006).
20. Löschberger, A. *et al. J. Cell Sci.* **125**, 570–575 (2012).
21. Schäfer, P., van de Linde, S., Lehmann, J., Sauer, M. & Doose, S. *Anal. Chem.* **85**, 3393–3400 (2013).
22. Mehlitz, A. *et al. Cell. Microbiol.* **16**, 1224–1243 (2014).
23. Ober, R.J., Ram, S. & Ward, E.S. *Biophys. J.* **86**, 1185–1200 (2004).
24. Small, A. & Stahlheber, S. *Nat. Methods* **11**, 267–279 (2014).
25. Parthasarathy, R. *Nat. Methods* **9**, 724–726 (2012).
26. Kirshner, H., Aguet, F., Sage, D. & Unser, M. *J. Microsc.* **249**, 13–25 (2013).
27. Sage, D. *et al. Nat. Methods* **12**, 717–724 (2015).
28. Ovesný, M., Křížek, P., Borkovec, J., Svindrych, Z. & Hagen, G.M. *Bioinformatics* **30**, 2389–2390 (2014).
29. Herbert, A. GDSC SMLM ImageJ Plugins http://www.sussex.ac.uk/gdsc/intranet/microscopy/imagej/smlm_plugins (2015).
30. Badieirostami, M., Lew, M.D., Thompson, M.A. & Moerner, W.E. *Appl. Phys. Lett.* **97**, 161103 (2010).
31. Böhmer, M. & Enderlein, J. *J. Opt. Soc. Am. B* **20**, 554–559 (2003).
32. Patra, D., Gregor, I. & Enderlein, J. *J. Phys. Chem. A* **108**, 6836–6841 (2004).

doi:10.1038/nmeth.4073

Bibliography

[1] August Köhler. *Mikrophotographische untersuchungen mit ultraviolettem licht*, volume 21. Zeitschrift für wissenschaftliche Mikroskopie und für mikroskopische Technik, 1904.

[2] Ernst Abbe. Beiträge zur theorie des mikroskops und der mikroskopischen wahrnehmung. *Archiv für mikroskopische Anatomie*, 9(1):413–418, 1873.

[3] William E Moerner and Lothar Kador. Optical detection and spectroscopy of single molecules in a solid. *Physical review letters*, 62(21):2535, 1989.

[4] Michel Orrit and J Bernard. Single pentacene molecules detected by fluorescence excitation in a p-terphenyl crystal. *Physical review letters*, 65(21):2716, 1990.

[5] E Brooks Shera, Newton K Seitzinger, Lloyd M Davis, Richard A Keller, and Steven A Soper. Detection of single fluorescent molecules. *Chemical Physics Letters*, 174(6):553–557, 1990.

[6] Stefan W Hell and Jan Wichmann. Breaking the diffraction resolution limit by stimulated emission: stimulated-emission-depletion fluorescence microscopy. *Optics letters*, 19(11):780–782, 1994.

[7] Eric Betzig. Proposed method for molecular optical imaging. *Optics letters*, 20(3):237–239, 1995.

[8] AM Van Oijen, J Köhler, J Schmidt, M Müller, and GJ Brakenhoff. 3-dimensional super-resolution by spectrally selective imaging. *Chemical Physics Letters*, 292(1):183–187, 1998.

[9] Mike Heilemann, Dirk P Herten, Rainer Heintzmann, Christoph Cremer, Christian Müller, Philip Tinnefeld, Kenneth D Weston, Jürgen Wolfrum, and Markus Sauer. High-resolution colocalization of single dye molecules by fluorescence lifetime imaging microscopy. *Analytical chemistry*, 74(14):3511–3517, 2002.

[10] Thomas A Klar, Stefan Jakobs, Marcus Dyba, Alexander Egner, and Stefan W Hell. Fluorescence microscopy with diffraction resolution barrier broken by stimulated emission. *Proceedings of the National Academy of Sciences*, 97(15):8206–8210, 2000.

[11] Rainer Heintzmann and Christoph G Cremer. Laterally modulated excitation microscopy: improvement of resolution by using a diffraction grating. In *BiOS Europe'98*, pages 185–196. International Society for Optics and Photonics, 1999.

[12] Mats GL Gustafsson. Surpassing the lateral resolution limit by a factor of two using structured illumination microscopy. *Journal of microscopy*, 198(2):82–87, 2000.

[13] Keith A Lidke, Bernd Rieger, Thomas M Jovin, and Rainer Heintzmann. Superresolution by localization of quantum dots using blinking statistics. *Optics express*, 13(18):7052–7062, 2005.

[14] Eric Betzig, George H Patterson, Rachid Sougrat, O Wolf Lindwasser, Scott Olenych, Juan S Bonifacino, Michael W Davidson, Jennifer Lippincott-Schwartz, and Harald F Hess. Imaging intracellular fluorescent proteins at nanometer resolution. *Science (New York, N.Y.)*, 313:1642–1645, September 2006.

[15] Samuel T Hess, Thanu P K Girirajan, and Michael D Mason. Ultra-high resolution imaging by fluorescence photoactivation localization microscopy. *Biophysical journal*, 91:4258–4272, December 2006.

[16] Michael J Rust, Mark Bates, and Xiaowei Zhuang. Sub-diffraction-limit imaging by stochastic optical reconstruction microscopy (storm). *Nature methods*, 3(10):793–795, 2006.

[17] Mike Heilemann, Sebastian van de Linde, Mark Schüttpelz, Robert Kasper, Britta Seefeldt, Anindita Mukherjee, Philip Tinnefeld, and Markus Sauer. Subdiffraction-resolution fluorescence imaging with conventional fluorescent probes. *Angewandte Chemie (International ed. in English)*, 47:6172–6176, 2008.

[18] Teresa Klein, Sven Proppert, and Markus Sauer. Eight years of single-molecule localization microscopy. *Histochemistry and cell biology*, 141:561–575, June 2014.

[19] Kim I Mortensen, L Stirling Churchman, James A Spudich, and Henrik Flyvbjerg. Optimized localization analysis for single-molecule tracking and super-resolution microscopy. *Nature methods*, 7(5):377–381, 2010.

[20] B Richards and E Wolf. Electromagnetic diffraction in optical systems. ii. structure of the image field in an aplanatic system. In *Proceedings of the Royal Society of London A: Mathematical, Physical and Engineering Sciences*, volume 253, pages 358–379. The Royal Society, 1959.

[21] Sarah Frisken Gibson and Frederick Lanni. Experimental test of an analytical model of aberration in an oil-immersion objective lens used in three-dimensional light microscopy. *JOSA A*, 8(10):1601–1613, 1991.

[22] Hagai Kirshner, Franois Aguet, Daniel Sage, and Michael Unser. 3-d psf fitting for fluorescence microscopy: implementation and localization application. *Journal of microscopy*, 249(1):13–25, 2013.

[23] Alex Small and Shane Stahlheber. Fluorophore localization algorithms for superresolution microscopy. *Nature methods*, 11(3):267–279, 2014.

[24] Steve Wolter, Anna Löschberger, Thorge Holm, Sarah Aufmkolk, Marie-Christine Dabauvalle, Sebastian Van De Linde, and Markus Sauer. rapidstorm: accurate, fast open-source software for localization microscopy. *Nature methods*, 9(11):1040–1041, 2012.

[25] Anish V Abraham, Sripad Ram, Jerry Chao, ES Ward, and Raimund J Ober. Quantitative study of single molecule location estimation techniques. *Optics express*, 17(26):23352–23373, 2009.

[26] Raimund J Ober, Sripad Ram, and E Sally Ward. Localization accuracy in single-molecule microscopy. *Biophysical journal*, 86(2):1185–1200, 2004.

[27] Sjoerd Stallinga and Bernd Rieger. Accuracy of the gaussian point spread function model in 2d localization microscopy. *Optics express*, 18(24):24461–24476, 2010.

[28] A Shivanandan, H Deschout, M Scarselli, and A Radenovic. Challenges in quantitative single molecule localization microscopy. *FEBS letters*, 588(19):3595–3602, 2014.

[29] Russell E Thompson, Daniel R Larson, and Watt W Webb. Precise nanometer localization analysis for individual fluorescent probes. *Biophysical journal*, 82(5):2775–2783, 2002.

[30] Mariano Bossi, Jonas Folling, Vladimir N Belov, Vadim P Boyarskiy, Rebecca Medda, Alexander Egner, Christian Eggeling, Andreas Schonle, and Stefan W Hell. Multicolor far-field fluorescence nanoscopy through isolated detection of distinct molecular species. *Nano letters*, 8(8):2463–2468, 2008.

[31] André Lampe, Volker Haucke, Stephan J Sigrist, Mike Heilemann, and Jan Schmoranzer. Multi-colour direct storm with red emitting carbocyanines. *Biology of the Cell*, 104(4):229–237, 2012.

[32] Gleb Shtengel, James A Galbraith, Catherine G Galbraith, Jennifer Lippincott-Schwartz, Jennifer M Gillette, Suliana Manley, Rachid Sougrat, Clare M Waterman, Pakorn Kanchanawong, Michael W Davidson, et al. Interferometric fluorescent super-resolution microscopy resolves 3d cellular ultrastructure. *Proceedings of the National Academy of Sciences*, 106(9):3125–3130, 2009.

[33] N Bourg, C Mayet, G Dupuis, T Barroca, P Bon, S Lécart, E Fort, and S Lévêque-Fort. Direct optical nanoscopy with axially localized detection. *Nature Photonics*, 9(9):587–593, 2015.

[34] Joran Deschamps, Markus Mund, and Jonas Ries. 3d superresolution microscopy by supercritical angle detection. *Optics express*, 22(23):29081–29091, 2014.

[35] Christian Franke, Markus Sauer, and Sebastian van de Linde. Photometry unlocks 3d information from 2d localization microscopy data. *Nature Methods*, 2016.

[36] Alex von Diezmann, Yoav Shechtman, and W E Moerner. Three-dimensional localization of single molecules for super-resolution imaging and single-particle tracking. *Chemical reviews*, February 2017.

[37] H Pin Kao and AS Verkman. Tracking of single fluorescent particles in three dimensions: use of cylindrical optics to encode particle position. *Biophysical journal*, 67(3):1291–1300, 1994.

[38] Bo Huang, Wenqin Wang, Mark Bates, and Xiaowei Zhuang. Three-dimensional super-resolution imaging by stochastic optical reconstruction microscopy. *Science*, 319(5864):810–813, 2008.

[39] Bo Huang, Sara A Jones, Boerries Brandenburg, and Xiaowei Zhuang. Whole-cell 3d storm reveals interactions between cellular structures with nanometer-scale resolution. *Nature methods*, 5(12):1047–1052, 2008.

[40] Ignacio Izeddin, Mohamed El Beheiry, Jordi Andilla, Daniel Ciepielewski, Xavier Darzacq, and Maxime Dahan. Psf shaping using adaptive optics for three-dimensional single-molecule super-resolution imaging and tracking. *Optics Express*, 20(5):4957–4967, 2012.

[41] Yoav Shechtman, Steffen J Sahl, Adam S Backer, and WE Moerner. Optimal point spread function design for 3d imaging. *Physical review letters*, 113(13):133902, 2014.

[42] Sri Rama Prasanna Pavani, Michael A Thompson, Julie S Biteen, Samuel J Lord, Na Liu, Robert J Twieg, Rafael Piestun, and WE Moerner. Three-dimensional, single-molecule fluorescence imaging beyond the diffraction limit by using a double-helix point spread function. *Proceedings of the National Academy of Sciences*, 106(9):2995–2999, 2009.

[43] Matthew D Lew, Steven F Lee, Majid Badieirostami, and WE Moerner. Corkscrew point spread function for far-field three-dimensional nanoscale localization of point-like objects. *Optics letters*, 36(2):202–204, 2011.

[44] Yoav Shechtman, Lucien E Weiss, Adam S Backer, Steffen J Sahl, and WE Moerner. Precise three-dimensional scan-free multiple-particle tracking over large axial ranges with tetrapod point spread functions. *Nano letters*, 15(6):4194–4199, 2015.

[45] Yoav Shechtman, Lucien E Weiss, Adam S Backer, Maurice Y Lee, and WE Moerner. Multicolour localization microscopy by point-spread-function engineering. *Nature photonics*, 10:590, 2016.

[46] Prashant Prabhat, Sripad Ram, E Sally Ward, and Raimund J Ober. Simultaneous imaging of different focal planes in fluorescence microscopy for the study of cellular dynamics in three dimensions. *IEEE transactions on nanobioscience*, 3:237–242, December 2004.

[47] Manuel F Juette, Travis J Gould, Mark D Lessard, Michael J Mlodzianoski, Bhupendra S Nagpure, Brian T Bennett, Samuel T Hess, and Joerg Bewersdorf. Three-dimensional sub–100 nm resolution fluorescence microscopy of thick samples. *Nature methods*, 5(6):527–529, 2008.

[48] Amir Tahmasbi, Sripad Ram, Jerry Chao, Anish V Abraham, Felix W Tang, E Sally Ward, and Raimund J Ober. Designing the focal plane spacing for multifocal plane microscopy. *Optics express*, 22:16706–16721, July 2014.

[49] Sripad Ram, Prashant Prabhat, Jerry Chao, E Sally Ward, and Raimund J Ober. High accuracy 3d quantum dot tracking with multifocal plane microscopy for the study of fast intracellular dynamics in live cells. *Biophysical journal*, 95(12):6025–6043, 2008.

[50] Sripad Ram, Dongyoung Kim, Raimund J Ober, and E Sally Ward. 3d single molecule tracking with multifocal plane microscopy reveals rapid intercellular transferrin transport at epithelial cell barriers. *Biophysical journal*, 103(7):1594–1603, 2012.

[51] Majid Badieirostami, Matthew D Lew, Michael A Thompson, and WE Moerner. Three-dimensional localization precision of the double-helix point spread function versus astigmatism and biplane. *Applied physics letters*, 97(16):161103, 2010.

[52] Bassam Hajj, Mohamed El Beheiry, and Maxime Dahan. Psf engineering in multifocus microscopy for increased depth volumetric imaging. *Biomedical optics express*, 7(3):726–731, 2016.

[53] Laura Oudjedi, Jean-Bernard Fiche, Sara Abrahamsson, Laurent Mazenq, Aurélie Lecestre, Pierre-François Calmon, Aline Cerf, and Marcelo Nöllmann. Astigmatic multifocus microscopy enables deep 3d super-resolved imaging. *Biomedical Optics Express*, 7(6):2163–2173, 2016.

[54] Philip E Bourne. Life is three-dimensional, and it begins with molecules. *PLoS biology*, 15:e2002041, March 2017.

[55] Paolo Annibale, Stefano Vanni, Marco Scarselli, Ursula Rothlisberger, and Aleksandra Radenovic. Quantitative photo activated localization microscopy: unraveling the effects of photoblinking. *PloS one*, 6(7):e22678, 2011.

[56] David Lando, Ulrike Endesfelder, Harald Berger, Lakxmi Subramanian, Paul D Dunne, James McColl, David Klenerman, Antony M Carr, Markus Sauer, Robin C Allshire, et al. Quantitative single-molecule microscopy reveals that cenp-acnp1 deposition occurs during g2 in fission yeast. *Open biology*, 2(7):120078, 2012.

[57] Anne Burgert, Sebastian Letschert, Sören Doose, and Markus Sauer. Artifacts in single-molecule localization microscopy. *Histochemistry and cell biology*, 144(2):123–131, 2015.

[58] Ulrike Endesfelder, Sebastian Malkusch, Benjamin Flottmann, Justine Mondry, Piotr Liguzinski, Peter J Verveer, and Mike Heilemann. Chemically induced photoswitching of fluorescent probes—a general concept for super-resolution microscopy. *Molecules*, 16(4):3106–3118, 2011.

[59] Ralf Jungmann, Maier S Avendaño, Mingjie Dai, Johannes B Woehrstein, Sarit S Agasti, Zachary Feiger, Avital Rodal, and Peng Yin. Quantitative super-resolution imaging with qpaint. *Nature methods*, 13(5):439–442, 2016.

[60] Anna Löschberger, Christian Franke, Georg Krohne, Sebastian van de Linde, and Markus Sauer. Correlative super-resolution fluorescence and electron microscopy of the nuclear pore complex with molecular resolution. *J Cell Sci*, 127(20):4351–4355, 2014.

[61] Nadine Ehmann, Sebastian Van De Linde, Amit Alon, Dmitrij Ljaschenko, Xi Zhen Keung, Thorge Holm, Annika Rings, Aaron DiAntonio, Stefan Hallermann, Uri Ashery, et al. Quantitative super-resolution imaging of bruchpilot distinguishes active zone states. *Nature communications*, 5, 2014.

[62] Philip R Nicovich, Dylan M Owen, and Katharina Gaus. Turning single-molecule localization microscopy into a quantitative bioanalytical tool. *Nature Protocols*, 12(3):453–460, 2017.

[63] David Baddeley, Mark B Cannell, and Christian Soeller. Visualization of localization microscopy data. *Microscopy and Microanalysis*, 16(01):64–72, 2010.

[64] Hudson H Freeze. Genetic defects in the human glycome. *Nature Reviews Genetics*, 7(7):537–551, 2006.

[65] Gerald W Hart, Michael P Housley, and Chad Slawson. Cycling of o-linked β-n-acetylglucosamine on nucleocytoplasmic proteins. *Nature*, 446(7139):1017–1022, 2007.

[66] Sebastian Letschert, Antonia Göhler, Christian Franke, Nadja Bertleff-Zieschang, Elisabeth Memmel, Sören Doose, Jürgen Seibel, and Markus Sauer. Super-resolution imaging of plasma membrane glycans. *Angewandte Chemie International Edition*, 53(41):10921–10924, 2014.

[67] Philip J Clark and Francis C Evans. Distance to nearest neighbor as a measure of spatial relationships in populations. *Ecology*, 35(4):445–453, 1954.

[68] Brian D Ripley. The second-order analysis of stationary point processes. *Journal of applied probability*, 13(2):255–266, 1976.

[69] Martin Ester, Hans-Peter Kriegel, Jörg Sander, Xiaowei Xu, et al. A density-based algorithm for discovering clusters in large spatial databases with noise. In *Kdd*, volume 96, pages 226–231, 1996.

[70] Patrick Rubin-Delanchy, Garth L Burn, Juliette Griffié, David J Williamson, Nicholas A Heard, Andrew P Cope, and Dylan M Owen. Bayesian cluster identification in single-molecule localization microscopy data. *Nature methods*, 2015.

[71] Florian Levet, Eric Hosy, Adel Kechkar, Corey Butler, Anne Beghin, Daniel Choquet, and Jean-Baptiste Sibarita. Sr-tesseler: a method to segment and quantify localization-based super-resolution microscopy data. *Nature methods*, 12(11):1065–1071, 2015.

[72] Stuart Lloyd. Least squares quantization in pcm. *IEEE transactions on information theory*, 28(2):129–137, 1982.

[73] Georg Krohne, Werner W Franke, and Ulrich Scheer. The major polypeptides of the nuclear pore complex. *Experimental cell research*, 116(1):85–102, 1978.

[74] Anna Löschberger, Sebastian van de Linde, Marie-Christine Dabauvalle, Bernd Rieger, Mike Heilemann, Georg Krohne, and Markus Sauer. Super-resolution imaging visualizes the eightfold symmetry of gp210 proteins around the nuclear pore complex and resolves the central channel with nanometer resolution. *J Cell Sci*, 125(3):570–575, 2012.

[75] Fabian Göttfert, Christian A Wurm, Veronika Mueller, Sebastian Berning, Volker C Cordes, Alf Honigmann, and Stefan W Hell. Coaligned dual-channel sted nanoscopy and molecular diffusion analysis at 20 nm resolution. *Biophysical journal*, 105(1):L01–L03, 2013.

[76] Tino Pleiner, Mark Bates, Sergei Trakhanov, Chung-Tien Lee, Jan Erik Schliep, Hema Chug, Marc Böhning, Holger Stark, Henning Urlaub, and Dirk Görlich. Nanobodies: site-specific labeling for super-resolution imaging, rapid epitope-mapping and native protein complex isolation. *Elife*, 4:e11349, 2015.

[77] Anna Szymborska, Alex de Marco, Nathalie Daigle, Volker C Cordes, John AG Briggs, and Jan Ellenberg. Nuclear pore scaffold structure analyzed by super-resolution microscopy and particle averaging. *Science*, 341(6146):655–658, 2013.

[78] Jiong Ma, Alexander Goryaynov, and Weidong Yang. Super-resolution 3d tomography of interactions and competition in the nuclear pore complex. *Nature structural & molecular biology*, 23(3):239–247, 2016.

[79] Rodolfo Wettstein and JR Sotelo. The molecular architecture of synaptonemal complexes. *Adv. Cell Mol. Biol*, 1:109–152, 1971.

[80] Montrose J Moses. Synaptinemal complex. *Annual review of genetics*, 2(1):363–412, 1968.

[81] Katharina Schücker, Thorge Holm, Christian Franke, Markus Sauer, and Ricardo Benavente. Elucidation of synaptonemal complex organization by super-resolution imaging with isotropic resolution. *Proceedings of the National Academy of Sciences*, 112(7):2029–2033, 2015.

[82] Sebastian van de Linde, Sarah Aufmkolk, Christian Franke, Thorge Holm, Teresa Klein, Anna Löschberger, Sven Proppert, Steve Wolter, and Markus Sauer. Investigating cellular structures at the nanoscale with organic fluorophores. *Chemistry & biology*, 20(1):8–18, 2013.

[83] Johannes Schneider, Teresa Klein, Benjamin Mielich-Süss, Gudrun Koch, Christian Franke, Oscar P Kuipers, Ákos T Kovács, Markus Sauer, and Daniel Lopez. Spatio-temporal remodeling of functional membrane microdomains organizes the signaling networks of a bacterium. *PLoS genetics*, 11(4):e1005140, 2015.

[84] John Canny. A computational approach to edge detection. *IEEE Transactions on pattern analysis and machine intelligence*, (6):679–698, 1986.

[85] Larry Gerace, Yvonne Ottaviano, and Claudia Kondor-Koch. Identification of a major polypeptide of the nuclear pore complex. *The Journal of Cell Biology*, 95(3):826–837, 1982.

[86] Catherine Favreau, Ricardo Bastos, Jean Cartaud, Jean-Claude Courvalin, and Pekka Mustonen. Biochemical characterization of nuclear pore complex protein gp210 oligomers. *European journal of biochemistry*, 268(14):3883–3889, 2001.

[87] Greg Hamerly and Charles Elkan. Learning the k in k-means. In *Advances in neural information processing systems*, pages 281–288, 2004.

[88] Steve B Howell. Two-dimensional aperture photometry: signal-to-noise ratio of point-source observations and optimal data-extraction techniques. *Publications of the Astronomical Society of the Pacific*, 101(640):616, 1989.

[89] Seamus J Holden, Stephan Uphoff, Johannes Hohlbein, David Yadin, Ludovic Le Reste, Oliver J Britton, and Achillefs N Kapanidis. Defining the limits of single-molecule fret resolution in tirf microscopy. *Biophysical journal*, 99(9):3102–3111, 2010.

[90] Steve Wolter, Ulrike Endesfelder, Sebastian van de Linde, Mike Heilemann, and Markus Sauer. Measuring localization performance of super-resolution algorithms on very active samples. *Optics Express*, 19(8):7020–7033, 2011.

[91] Raghuveer Parthasarathy. Rapid, accurate particle tracking by calculation of radial symmetry centers. *Nature Methods*, 9(7):724–726, 2012.

[92] Martin Ovesnỳ, Pavel Křížek, Josef Borkovec, Zdeněk Švindrych, and Guy M Hagen. Thunderstorm: a comprehensive imagej plug-in for palm and storm data analysis and super-resolution imaging. *Bioinformatics*, 30(16):2389–2390, 2014.

[93] Alex Herbert. Gdsc smlm imagej http://www.sussex.ac.uk/gdsc/intranet/microscopy/imagej, 2015.

[94] TRABI Ubdate Page. http://bcp.phys.strath.ac.uk/photophysics/super-resolution/software/, 2017.

[95] Iris K Jarsch, Frederic Daste, and Jennifer L Gallop. Membrane curvature in cell biology: An integration of molecular mechanisms. *J Cell Biol*, 214(4):375–387, 2016.

[96] Pablo Mateos-Gil, Sebastian Letschert, Sören Doose, and Markus Sauer. Super-resolution imaging of plasma membrane proteins with click chemistry. *Frontiers in cell and developmental biology*, 4, 2016.

[97] Anne Burgert, Jan Schlegel, Jérôme Bécam, Sören Doose, Erhard Bieberich, Alexandra Schubert-Unkmeir, and Markus Sauer. Characterization of plasma membrane ceramides by super-resolution microscopy. *Angewandte Chemie*, 129(22):6227–6231, 2017.

[98] Matthew B Stone, Sarah A Shelby, and Sarah L Veatch. Super-resolution microscopy: shedding light on the cellular plasma membrane. *Chemical Reviews*, 2017.

[99] webofknowledge. search for ”single-molecule localization microscopy”, https://apps.webofknowledge.com, version of 13.07.2017.

[100] webofknowledge. search for ”super-resolution microscopy”, https://apps.webofknowledge.com, version of 13.07.2017.

[101] Franz Xaver Engelmayer. Charakterisierung und anwendung der ”temporal radial-aperture-based intensity-estimation” zur akkuraten einzelmolekül-intensitätsbestimmung für die 3d-lokalisationsmikroskopie. Master’s thesis, Julius-Maximilians Universität Würzburg, 2017.

[102] Ramraj Velmurugan, Jerry Chao, Sripad Ram, E Sally Ward, and Raimund J Ober. Intensity-based axial localization approaches for multifocal plane microscopy. *Optics Express*, 25(4):3394–3410, 2017.

[103] Hazen P Babcock and Xiaowei Zhuang. Analyzing single molecule localization microscopy data using cubic splines. *Scientific Reports*, 7(1):552, 2017.

Acknowledgments

'Alone we can do so little; together we can do so much.'

I want to express my deep gratitude and thanks to everyone who had any share in the genesis of this thesis or supported me otherwise.

In particular, I want to thank Markus Sauer for creating an environment of opportunity, scientific freedom and familiarity in his group, that I will cherish and certainly miss. Thank you for giving me the opportunity to develop myself, and my own ideas and going after them and for your advice, support and enthusiasm all along the way.

For a great collaboration on the synaptonemal complex and his everlasting zest and positivism I want to thank Ricardo Benavente. Thank you for your patience, support and discussions and also for assuming the evaluation of my thesis.

When I first came to Markus' group, there was a guy they called *Sepp*. Later I found out, that his actual name is Sebastian van de Linde, to whom I owe a lot and more. Sepp, thank you for your boundless enthusiasm (some might call it *Affenpower*) and scientific curiosity, which was truly inspiring for me since day one. Thank you for being a supervisor, a colleague, an office mate, an accomplice, a köpi-companion and a friend.

I want to express my gratitude to all my collaboration partners over the years, giving me the opportunity to work in a truly interdisciplinary environment. Special thanks go to Jörg Enderlein for his expertise and prompt guidance and support. Further I want to thank Katharina Schücker for a great collaboration on the synaptonemal complex.

Great thanks to everyone in the department of Biotechnology and Biophysics for an excellent working environment, for a lot of fun and great times in- and outside the university and for letting me win at *kicker*.
My special thanks go to Teresa Tracy O'Neal Klein for her biological expertise from day one whenever I needed it and for her friendship.
For their technical support and expertise in creating fantastic custom made devices I want to thank Albert Gessner, Marcus Behringer, Oli Reichert and Willi Bauer.

For their help and guidance in all biology-related questions, especially cell-culture and labeling I want to express my gratitude to Petra Geßner and Lisa Behringer-Pließ.
I want to thank Vladimir Soukhoroukov for offering me my first glimpse into the department, all the interesting discussions and anecdotes and of course for our chess matches.
For a very enjoyable time and a lot of fun I want to thank all the people that I had the chance to share an office with over the years, starting with Simone, Claudia, Thorge, Thonie and others, over Tobi and Sepp (also known as the *Relentless* days) to Simone (again), Sina, Felix, Franzi and Andi.
I also want to thank my three master students, Dominik Pfaff, Andreas Kurz and Franz-Xaver Engelmayer, that I had the opportunity to supervise during my thesis. I learned alot from you guys, I hope it also went vice versa.

My deepest thanks go to Rolf, Joyce and Simone for their friend- and companionship in almost 11 years of Würzburg. It is fair to say, that without you, I would not be the one that I am today. Thank you for all the great times and experiences along the way, I wouldn't want to miss a thing.
Also, thank you Sarah as part of the memorable 'Würzburg experience' as well; isn't it curious, that we came and leave at the very same time?!

Finally, I want to thank family for their everlasting support and the massive foundation they built for me to always lean on. Thanks to my parents, grandparents, my siblings and the latest members of the Franke family Linda, Robin, Nicholas and Johannes for all the joy & warmth and the home that they altogether form.
Thank you Julie, for your unfailing support, patience, wit and love. Your contribution to this work cannot be expressed in words, but if there were listed contributions to this thesis, yours should say: "J.H. rescued C.F. many times from going crazy." Now it's your turn!

Erklärungen nach §4 Abs. 3 Satz 3, 5, 8 der Promotionsordnung der Fakultät für Biologie

Affidavit

I hereby declare that my thesis entitled: „Advancing Single-Molecule Localization Microscopy: Quantitative Analyses and Photometric Three-Dimensional Imaging” is the result of my own work.

I did not receive any help or support from commercial consultants. All sources and / or materials applied are listed and specified in the thesis.

Furthermore I verify that the thesis has not been submitted as part of another examination process neither in identical nor in similar form.

Eidesstattliche Erklärung

Hiermit erkläre ich an Eides statt, die Dissertation: „Advancing Single-Molecule Localization Microscopy: Quantitative Analyses and Photometric Three-Dimensional Imaging“, eigenständig, d. h. insbesondere selbständig und ohne Hilfe eines kommerziellen Promotionsberaters, angefertigt und keine anderen, als die von mir angegebenen Quellen und Hilfsmittel verwendet zu haben.

Ich erkläre außerdem, dass die Dissertation weder in gleicher noch in ähnlicher Form bereits in einem anderen Prüfungsverfahren vorgelegen hat.

Würzburg, August 2017 Christian Franke